Colloidal Gels under Oscillatory Shear

Paul Andrew Smith

Thesis submitted for the degree of Doctor of Philosophy

School of Physics

University of Edinburgh

2004

Abstract

The addition of polymer to a colloidal suspension induces an attraction between the colloid particles. If sufficient polymer is added to a colloidal suspension then the particles stick to each other forming a frozen network of clusters that fill the sample volume. The structure of these amorphous states is not well understood. In particular, intermediate colloid volume fractions ($\Phi \sim 0.4$) are hardly studied, falling in between the two limits of very low density fractal gels and high density attractive glasses. Such gels are a well characterised model system to gain fundamental physical insights into strongly bonded, dense colloidal systems. This is a computationally and theoretical difficult regime. It is also interesting to study their flow properties. While some experiments have been conducted on the macroscopic flow properties of colloidal gels, a microscopic picture of the gels' structural response to flow is lacking.

We have studied the quiescent structure of dense colloidal gels with varying strength of attraction with confocal microscopy. We have obtained high quality 3-D images that allow quantitative comparison of the different gels by the extraction of the 3-D particle coordinates and subsequent calculation of quantitative measures of the local particle structure. We have observed that the gels have a liquid-like, although frozen, inhomogeneous structure. We have found an increase in the average number of bonds per particle for decreasing attraction strength, accompanied by changes in the particle-free void regions.

We developed and tested several versions of a precision linear parallel-plate oscillatory shear cell for light scattering-echo and microscopy experiments. This allowed us to study in detail the response of gels with varying strength to low strain oscillatory shear at various frequencies with optical and confocal microscopy and light scattering-echo. We have found that the gels responds elastically below a critical strain that depends on frequency and depletion attraction potential. Above this critical strain the particles that make up the gel are found to rearrange. Surprisingly, shear induces a new type of colloidal structure in the gel. The shear induced structure of small frozen ordered regions separated by empty voids and disordered regions has never

been seen before in any colloidal system. The amount of ordering is found to depend on strain and frequency as well as on the colloid and polymer volume fractions of the gel. We found that the ordered regions are predominantly in 2-D planes and limited to small domains separated by defects, disordered particles or voids. Sufficient strain leads to interesting changes in the void distribution in both samples where particle ordering was observed and in those where it was not. Our results are interpreted by a simple theoretical model based on the timescale for a particle to escape from the potential well.

Acknowledgements

Firstly, I wish to thank my supervisors Stefan Egelhaaf and Wilson Poon for all their support and enthusiasm throughout my PhD.

Thanks to Mr Simpson and Mr Hawksford, the teachers who first opened my eyes to physics.

I am especially grateful to George Petekidis for his help and expertise with light scattering and all things sheared, to Andrew Downie for building all of the shear cells and making countless changes at a moments notice, to Andy Schofield for providing the colloids and Helen Sedgwick, Matt Jenkins, Khoa Pham and Mark Haw for many useful discussions.

Special thank all of my friends who I have spent time with in JCMB and beyond!

Finally, to my family for all their love and support and to Jemima for always being there.

Contents

Chapter 1

Introduction

1.1 Colloids

A colloid is formed by dispersing small pieces of a substance in a continuous medium. The size of the colloid is its defining feature. The constituents of the suspending medium must be small enough in comparison to the colloid for it to be treated as a continuous, homogeneous phase. As a consequence colloids are much larger in size than atoms and therefore quantum mechanical effects are negligible. The colloid must be sufficiently small for Brownian motion to dominate over the effect of gravitational settling. If a colloid is neutrally buoyant then it must be able to diffuse a reasonable distance due to Brownian motion in experimental timescales. Colloids span a length-scale from $\sim 10nm$ to $1\mu m$. Colloids can be found all around us in all combinations of states of matter. For example, milk is a liquid colloid (fat) suspended in a liquid medium (water). Solid pollen is found suspended in a gas medium (air). In this work we are only concerned with the case of solid colloids suspended in a liquid medium.

Colloids are part of a greater range of interesting substances brought together under the umbrella of "soft matter". A colloidal solid is very "soft" or weak in comparison to an atomic solid. This can be easily seen by estimating the yield stress for both kinds of material (of size R). The yield stress ($\propto 1/R^3$) is a measure of how much force is required per unit area to make a material flow. A colloidal solid is made up of colloid particles of size $R \leq 1\mu m$, giving a yield stress many orders of magnitude smaller than that of an atomic solid made up of atoms of typical size $R \sim 0.5nm$.

1.2 Why Study Colloids?

Colloids are found in a wide range of consumer and industrial products, for example paints and shampoos. A greater understanding of the underlying principals governing the behaviour and properties of these products is of great interest to the manufacturers. Many products are sold (and only useful) in metastable states, so their study is of particular interest.

Colloids can be thought of as large scale models of atomic systems. The thermodynamic properties of the colloid are formally the same as those for an atomic system with the same pair potential. There are several advantages of using colloids as experimental model systems. The colloidal length-scale is comparable to the wavelength of light making both light scattering and optical microscopy valuable research tools. It is possible to tune the size, and even the interactions, of colloid particles.

1.3 Motivation

This thesis presents a study of the oscillatory shear of colloidal gels. It was motivated by the need to understand how metastable aggregated states (gels), formed by attractive particles, respond to flow at the particle level. While some experiments have been conducted on the macroscopic flow properties of model colloidal gels, a microscopic picture of the gels structural response to flow is lacking. We wanted to see if it was possible to study the flow of colloidal gels at the microscopic level, both directly with optical microscopy and indirectly with the light scattering-echo, using a purpose built oscillatory shear cell suitable for use with both techniques. A subsidiary motivation was to gain some understanding of the quiescent micro-structure of the gels used in the shear experiments, which are long-lasting metastable states. The structure of these gels with strong attractions and high colloid volume fractions has been hardly studied, falling in between the two limits of very low density fractal gels and high-density attractive glasses. The study of the quiescent state is necessary in order to understand the structure after shear.

1.4 Thesis Layout

In this first chapter colloids are briefly introduced as well as some everyday examples. Chapter 2 contains firstly the relevant background on colloidal suspensions of hard spheres, colloid-polymer mixtures and non-equilibrium states focusing on gels. Secondly, it summarises the

published literature related to the micro-structure of colloidal gels and the behaviour of colloidal suspensions under shear flow. Thirdly, the key technical concepts related to the techniques of light scattering echo and optical microscopy are described.

Details of our model system are described in chapter 3, along with the experimental setups and methods used in the light scattering and microscopy experiments.

Chapter 4 describes the shear cells used in this work including the design, development and calibration methods. Note that the work described here represents a significant part of the original research contained in this thesis.

In chapter 5, the results of an optical and confocal microscopy study of the quiescent structure of dense colloidal gels is presented and discussed.

The results of a study into the oscillatory shear of colloidal gels conducted with light-scattering echo, optical and confocal microscopy are presented in chapter 6. The subsequent discussion centres on a model based on the timescale for a particle to escape from the potential well.

Finally, chapter 7 presents some conclusions which have been made based on this work, along with suggestions for future work.

Chapter 2

Background

2.1 Introduction

In this chapter we first introduce some theoretical background on colloidal suspensions of hard spheres, colloid-polymer mixtures and non-equilibrium states focusing on gels. Secondly, we summarise the published literature related to the micro-structure of colloidal gels and the behaviour of colloidal suspensions under shear flow. Thirdly, the key technical concepts related to the techniques of echo light scattering and optical microscopy are described.

2.2 Hard Sphere Colloids

2.2.1 Hard Sphere Model

Our starting point is the simplest system one can imagine. We consider a colloidal suspension in which the colloids behave as hard spheres of radius, R. There is no interaction between the spheres until they touch, where they experience an infinite repulsion (they behave as microscopic snooker balls). As can be seen in figure 2.1, the potential, $V(r)$ can be modelled as $V(0 < r < 2R) = \infty$ and $V(r > 2R) = 0$. Implicit in this model is that the particles are all exactly the same size; the particles are perfectly mono-disperse. Hard spheres have no energy scale so we need to only consider entropy to determine the phase behaviour [1]. We can thus characterise such a system by the number density of the particles alone. This is usually expressed as the colloid volume fraction Φ (see equation 2.1), where N is the number of particles of radius R in a suspension of volume V:

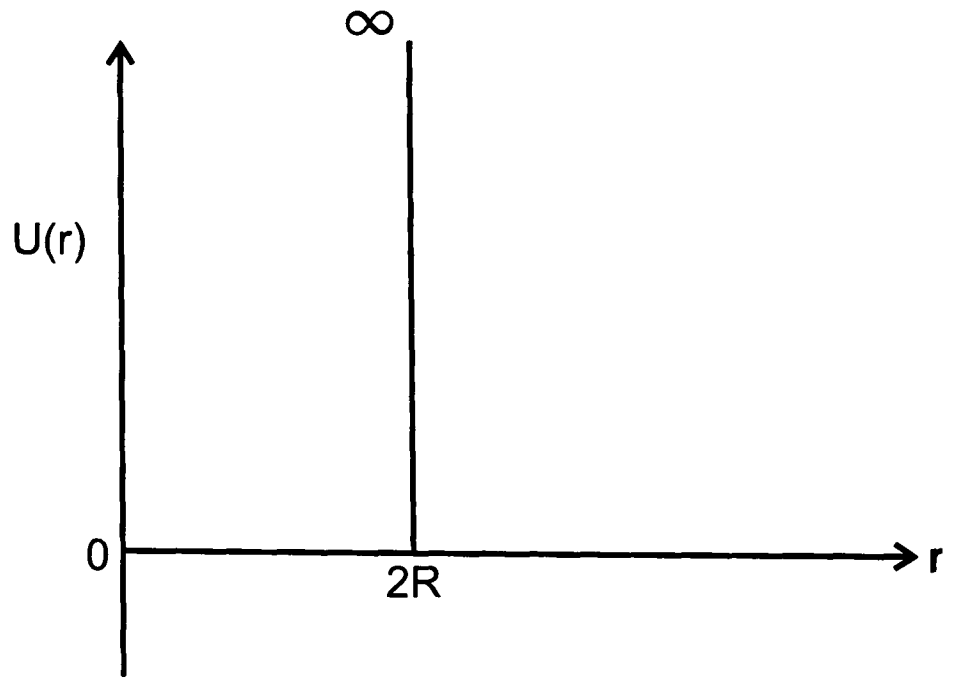

Figure 2.1: The pair potential $U(r)$ for a collection of hard sphere of uniform radius R and centre-to-centre separation r.

$$\Phi = \frac{4}{3}\pi R^3 \frac{N}{V} \tag{2.1}$$

2.2.2 Experimental Colloids

Most colloidal suspensions are very complex and very far removed from the hard sphere colloid presented above. We want to use an experimental model colloid that behaves as much like a hard sphere as possible. We will describe our particular system in detail later; here we will discuss how we can make real particles that act as much like hard spheres as possible.

Colloid Stabilization When we disperse some sufficiently small particles in a liquid we find that the particles stick together, rather than forming a stable model colloidal suspension. The van der Waals attraction between the particles causes them to aggregate (stick together) irreversibly. The van der Waals attraction is caused by fluctuations in the dipole moment of the atoms that make up the particle [2]. This quantum mechanical force is sufficiently long ranged for it to affect microscopic bodies such as a colloidal particle. This applies to neutral atoms and molecules aswell. The resulting attractive potential has a strength many times that of the thermal energy of the particles. It is important to stabilize the colloidal particle to prevent aggregation. This can be achieved by steric stabilization.

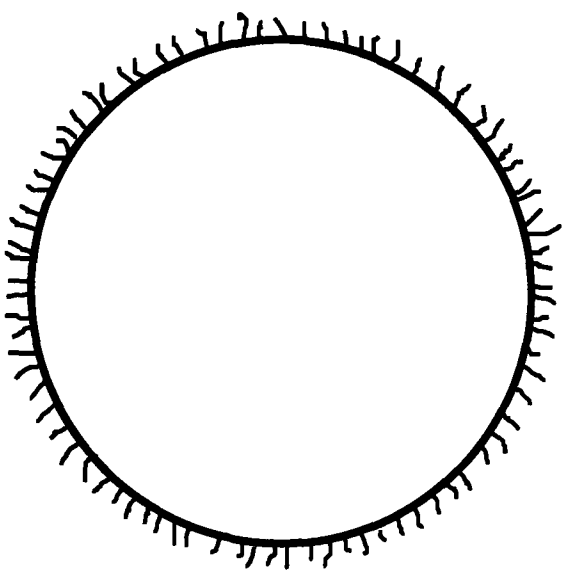

Figure 2.2: A schematic picture of a sterically stabilized colloid particle.

Steric Stabilization Polymer chains (length $\sim 10nm$) are grafted onto the surface of the colloidal particle as shown in figure 2.2. When two particles approach the polymer layers interpenetrate leading to a reduction in entropy. This causes a strong repulsion between the two polymer layers preventing the particles getting close enough for the van der Waals attraction to become significant and thus prevents the particles from sticking together. The resulting potential for particles stabilized in this way can be a good approximation to a hard sphere potential.

2.2.3 Phase Behaviour

In this section we describe the phase behaviour of a model hard sphere suspension and what these phases look like macroscopically.

The phase behaviour of a suspension of hard spheres has been predicted by computer simulation [3], [4] and is shown in figure 2.3. As mentioned before there is no energy scale for hard spheres so there is only a single parameter that completely determines the phase behaviour. This is the particle volume fraction, Φ. Below a freezing volume fraction of $\Phi_F = 0.494$ the particles form a fluid and are free to diffuse and explore the whole volume. Only short range local order is present. When viewed in a small glass sample cell the fluid is homogeneous in appearance.

Between $\Phi_F = 0.494$ and $\Phi_M = 0.545$ the system separates into coexisting fluid and crystal phases. In the case that the colloid radius is of the same length scale as visible light ($R \approx \lambda$) the crystal phase is easy to spot as iridescence (rainbow colours) is easily seen in a clearly

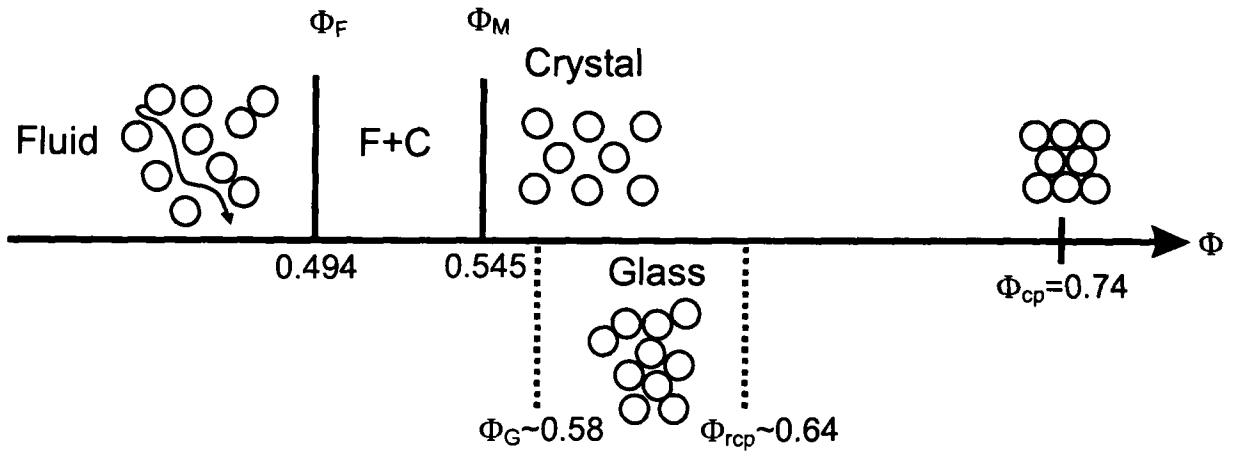

Figure 2.3: Phase behaviour of a suspension of mono-disperse hard-spheres.

separated layer at the bottom of the cell. The size of a unit cell (similar in size to a particle) is of the same length-scale as visible light so light is strongly scattered by the crystal leading to Bragg reflections (seen as iridescence). The whole sample shows iridescence when the sample is fully crystalline.

It is worth noting that in contrast to atomic crystals such as salt (NaCl), colloidal crystals are extremely weak and can be destroyed by gentle shaking of the sample cell. As the volume fraction is increased a greater proportion of the system exhibits long range order until at the melting volume fraction $\Phi_M = 0.545$ the system is fully crystalline. Increasing the volume fraction further results in a denser crystal. As hard spheres cannot fill space completely there is a maximum crystal volume fraction, $\Phi_{cp} = \frac{\pi}{3\sqrt{2}} (\approx 0.74)$. If the particles form a randomly ordered close packed arrangement then the maximum possible volume fraction is $\Phi_{rcp} \approx 0.64$.

It is not obvious that entropy considerations alone should result in an ordered arrangement of the particles. The reason is that a highly ordered arrangement as shown in figure 2.4 (B) gives freedom of movement of the particles about the lattice sites which gives high free volume entropy at the expense of configurational entropy [1]. Contrast this with a disordered state where the particles can be in a large number of distinguishable configurations but are very restricted in their movement due to the neighbouring particles, as shown in figure 2.4 (A). The particles will order when the entropy gained from being able to jiggle about exceeds that lost from being restricted to a single average position.

Hard spheres also exhibit non-equilibrium behaviour. At volume fractions above $\Phi_G \sim 0.58$ crystallisation is suppressed and an amorphous dynamically arrested solid is formed known as a glass [1]. In the sample cell, a glass appears homogeneous like a fluid but is much more viscous.

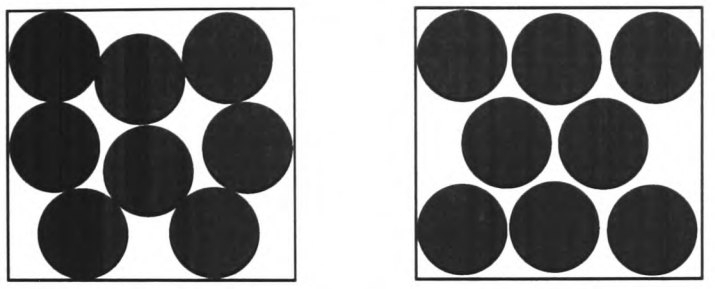

Figure 2.4: Schematic diagram of 2-D hard discs in a box showing how competition between configurational and free volume entropy can drive freezing. (A) a random configuration of discs has a high configurational entropy but low free volume entropy. (B) a crystalline arrangement of discs with low configurational entropy but high free volume entropy due to an increase in the local mobility of each disc.

2.3 Colloid-Polymer Mixtures

2.3.1 Depletion Potential

The addition of non-absorbing polymer to a suspension of colloids induces a tunable attraction between the colloidal particles. This is called the depletion effect and can cause phase separation. Figure 2.5 shows a schematic representation of a colloid-polymer mixture. The centre of a polymer coil is excluded from a region, the depletion zone, surrounding the impenetrable colloid of order r_g. The polymer coils are restricted to the free volume V_{free}, the region not occupied by the colloids and their respective depletion zones. The overlap of the depletion zones of adjacent colloids increases the free volume available to the polymer coils. This lowers the free energy by increasing the entropy of the polymer. Alternatively, the effect can be understood in terms of osmotic pressure. When the depletion zones of two particles overlap there is no polymer between them. This leads to an unbalanced osmotic pressure of the polymer which pushes the particles together, thus inducing an effective attraction between them.

This theoretical model was first proposed by Asakura and Oosawa [5], and independently by Vrij [6]. In their model the polymer coils are assumed to be spheres of radius r_g when interacting with the colloid particle that are hard spheres of radius R. However, the polymers can freely inter-penetrate each other. The attraction between the particles can be modeled by a pair potential $U_{dep}(r)$ which is shown in figure 2.6. The potential is given by:

$$U_{dep}(r) = \begin{cases} +\infty & : \quad r \leq 2R \\ -\Pi_p V_{overlap} & : \quad 2R < r \leq 2R + 2r_g \\ 0 & : \quad r > 2R + 2r_g \end{cases}$$

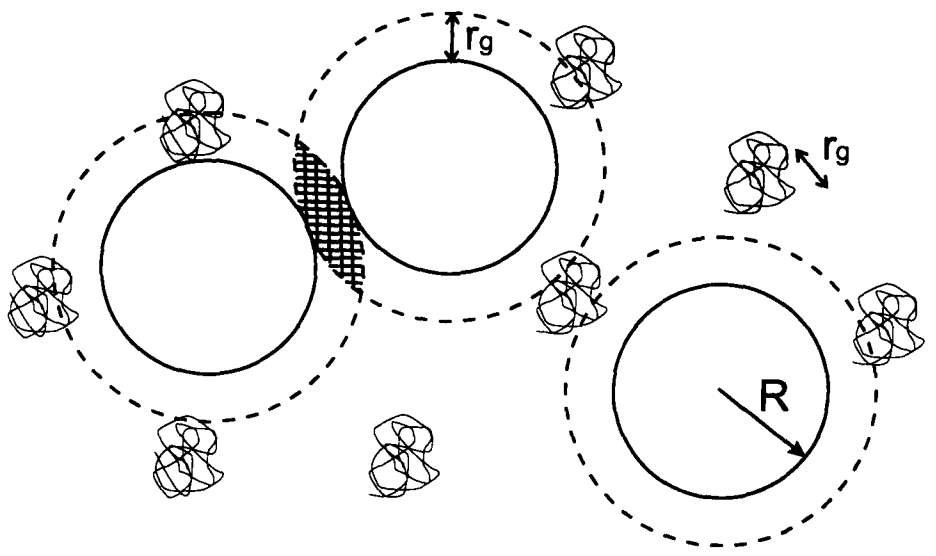

Figure 2.5: Diagram showing the depletion zone around each colloid particle, radius R. When the depletion zones overlap the random coil polymers, radius of gyration r_g, are depleted from the region between the particles.

where $V_{overlap}$ is the volume of the overlapping depletion regions between two particles separated by r. This volume is given by

$$V_{overlap} = \left(1 - \frac{3r}{4R(1+\xi)} + \frac{1}{2}\left(\frac{r}{2R(1+\xi)}\right)^3\right) \times \frac{\pi}{6}(2R)^3(1+\xi)^3 \qquad (2.2)$$

where ξ is the polymer-colloid size ratio, $\xi = r_g/R$.

We can also derive an expression for the osmotic pressure Π_p of the polymer solution using Van't Hoff's law. This relies on the assumption that the polymer solution behaves as an ideal gas. We will discuss later the effect of high polymer concentrations.

$$\Pi_p = \frac{N_p(k_B T)}{V_{\text{free}}} \qquad (2.3)$$

where N_p is the number of polymer coils and V_{free} is the free volume available to the polymer coils which is defined as

$$V_{\text{free}} = V - (V_c + V_{dep}) + V_{ol} \qquad (2.4)$$

where V is the total volume of the sample, V_c and V_{dep} are the volume occupied by the colloid particles and their depletion zones respectively. V_{ol} is the total volume of the overlapping depletion layers.

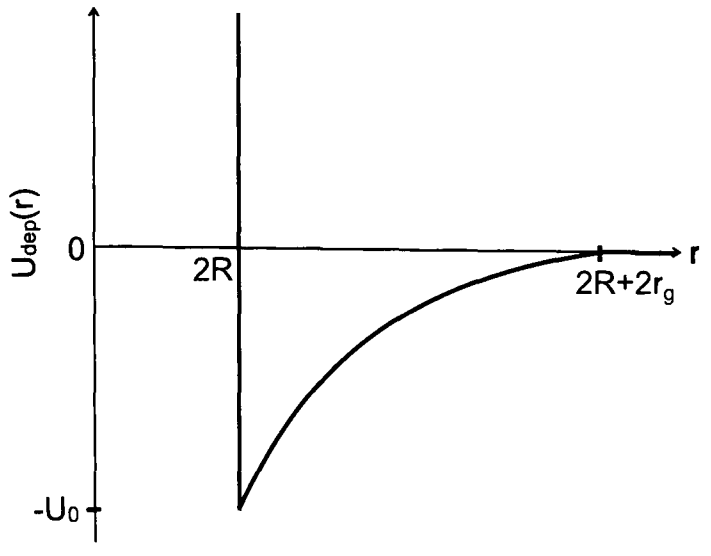

Figure 2.6: The pair potential $U_{dep}(r)$ for a colloid-polymer mixture of colloid particles of radius R and polymer coils with radius of gyration r_g.

The free volume is difficult to access in practice as it depends on the position of all the particles. We relate it to the total volume V by

$$V_{\text{free}} = \alpha V \tag{2.5}$$

where α is known as the free volume fraction. Using a simple mean field approximation and taking the average value of the free volume in the corresponding unperturbed colloidal system it is found that α depends only on the colloid volume fraction and ξ.

An approximate form for α may be obtained from scaled particle theory [7]

$$\alpha = (1 - \Phi)exp[-A\gamma - B\gamma^2 - C\gamma^3] \tag{2.6}$$

where $\gamma = \Phi/(1 - \Phi)$, $A = 3\xi + 3\xi^2 + \xi^3$, $B = 9\xi^2(2 + 3\xi^3)$ and $C = 3\xi^3$.

We can make contact with the experimental quantity, the polymer mass concentration C_p in the whole volume by rewriting equation 2.3 as

$$\frac{\Pi_p}{k_B T} = \frac{N_A}{M_w}\frac{m_p}{\alpha V} = \frac{N_A}{M_w} C_p^{\text{free}} \tag{2.7}$$

where N_A is Avogadro's number, M_w is the molecular mass of the polymer, m_p is the total mass of polymer in the system and C_p^{free} is the mass concentration of polymer in the free volume. C_p^{free} is defined as

$$C_p^{\text{free}} = \frac{m_p}{\alpha(\xi, \Phi)V} = \frac{C_p}{\alpha(\xi, \Phi)} \tag{2.8}$$

Corrections to AO Theory We can extend the A-O free volume theory by taking in account polymer coil-coil interactions [8]. The main change is that the size ratio ξ now depends on the free polymer concentration. We define a corrected size ratio:

$$\xi^* = \frac{\Delta}{R} \tag{2.9}$$

where Δ is now the depletion layer thickness ($\Delta = r_g$ in the uncorrected A-O theory). This gives us a corrected version of the free polymer concentration equation (2.8), where we have replaced ξ with $\xi^*(C_p^{\text{free}})$:

$$C_p^{\text{free}} = \frac{C_p}{\alpha(\xi^*(C_p^{\text{free}}), \Phi)} \tag{2.10}$$

In this equation $\xi^*(C_p^{\text{free}})$ incorporates two corrections to the thickness of the depletion layer Δ. Firstly, the effect of polymer concentration and secondly the effect of the presence of the spherical colloidal surface. The polymer concentration correction is significant as it is found that the depletion thickness decreases strongly as a function of the polymer concentration. The curvature correction has only a small effect on Δ unless the size ratio ξ is very large, where upon $\Delta \ll r_g$. Details of the method used to calculate Δ corrected for polymer concentration effects can be found in Appendix A.

To calculate the corrected depletion potential we need to use the corrected overlap volume and corrected osmotic pressure. The corrected equation for the overlap volume is:

$$V_{overlap} = \left(1 - \frac{3r}{4R(1+\xi^*)} + \frac{1}{2}(\frac{r}{2R(1+\xi^*)})^3\right) \times \frac{\pi}{6}(2R)^3(1+\xi^*)^3 \tag{2.11}$$

where $\xi^*(C_p^{\text{free}})$ replaces ξ.

The calculation of the osmotic pressure now uses $C_p^{\text{free}}(\xi^*)$. To calculate $\alpha(\xi^*(C_p^{\text{free}}), \Phi)$ we replace ξ with $\xi^*(C_p^{\text{free}})$ in equation 2.6. In addition, the osmotic pressure is no longer linear with respect to C_p^{free} for polymer dissolved in a good solvent (in contrast to equation 2.7) as excluded volume interactions between polymer segments have to be taken into account. There is a significant correction to the osmotic pressure which is calculated by integration of

an expression for the osmotic compressibility obtained from renormalisation group theory (see equation 3.10). The expression is for polymers in the full excluded volume limit.

The strength of the attraction between two colloid particles can be estimated by calculating U_{dep}, with $r = 2R$, when the particles are in contact. This is calculated in section 3.2.7.

2.3.2 Equilibrium Phase Behaviour

Here I will briefly summarise a method developed to predict the phase behaviour for a colloid-polymer mixture [9]. We must minimise the Helmholtz free energy. It can be shown that the best quantity to consider is the free energy density, f, and that this is only a function of the colloid volume fraction and the free polymer concentration, so $f = f(\Phi, C_p^{\text{free}})$. Using a mean field approach two different configurations of the colloids and polymers are considered. The "fluid" branch of the free energy diagram is found by having a disordered arrangement of polymers and colloids. The "crystal" branch is found by having an ordered arrangement of colloids with randomly placed polymer. These two branches are plotted on a free energy diagram with f against Φ for a fixed depletion strength in figure 2.7. The common tangent construction method is used to calculate the concentration of any coexisting phases [10]. This is a geometrical method that uses the two conditions for equilibrium, namely that the polymer chemical potential and the pressure of the two phases are equal. Using this method we can see from figure 2.7 that an initially homogeneous fluid with concentration Φ_i can lower its free energy density f_i by separating into a coexisting fluid phase with concentration Φ_f and crystal phase of concentration Φ_c. The relative volumes of the two phases are found from the lever rule [10] ($V_f/V_c = b/a$). To construct a complete phase diagram this process is repeated for a range of free polymer concentrations.

It is found that the predicted phase behaviour depends the polymer concentration and colloid volume fraction as well as on the range of the potential, which is determined by the size ratio $\xi = r_g/R$. When $\xi \lesssim 0.3$ the only effect of the polymer is to increase the size of the fluid-crystal coexistence region observed in the pure hard sphere colloid case. With higher size ratios a much richer range of phase behaviour is found. A critical point can be observed and distinct gas and liquid phases are predicted. This allows for three phase coexistence of gas, liquid and crystal.

In this work we only deal with the simpler case found at low size ratios. Figure 2.8 (A) shows a typical predicted phase diagram for a colloid-polymer mixture with size ratio, $\xi = 0.08$ in terms of free polymer volume fraction $\eta_p^{(R)}$ and Φ [11]. Figure 2.8 (B) shows the same

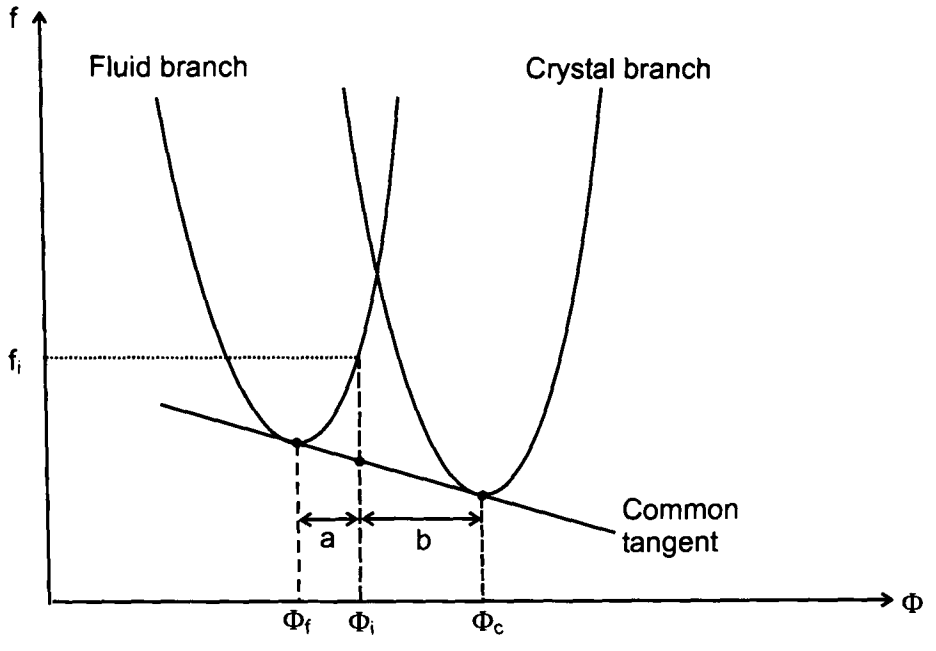

Figure 2.7: Schematic graph of the free energy density, f, as a function of colloid volume fraction Φ, for fixed free-volume polymer concentration, C_p^{free}. This figures shows how the common tangent construction may be used to determine the concentrations of the two coexisting phases; the lever rule giving the amounts of each phase we expect to find.

predicted phase diagram in terms of the experimental units of polymer volume fraction. Note that the tie-lines are now oblique, implying polymer partitioning between the fluid and crystal phases.

We want to know how the addition of polymer affects the hard-sphere phase behaviour at low size ratio compared with that predicted by theory. Many studies have found phase separation in colloidal suspension after the addition of non-absorbing polymer. The most relevant study to this work is [11]. Figure 2.8 (C) shows the experimentally determined the phase diagram for $\xi = 0.09$ using PMMA with non-absorbing polymer, the same system I consider. The experimental phase diagrams qualitatively fit the predicted phase diagram. On adding a small amount of polymer no change from the pure hard sphere colloid behaviour is found; fluid like behaviour is seen. Adding more polymer induces phase separation into coexisting fluid and crystal phases, this region is expanded as predicted by the theory.

2.3.3 Non-equilibrium Behaviour

However, at higher polymer concentrations crystallisation is suppressed and a range of non-equilibrium behaviour is observed. It is not surprising that this behaviour is not predicted by the equilibrium theory. We now go on to describe the non-equilibrium behaviour found in colloid-polymer systems and what is understood about their origins, for further information

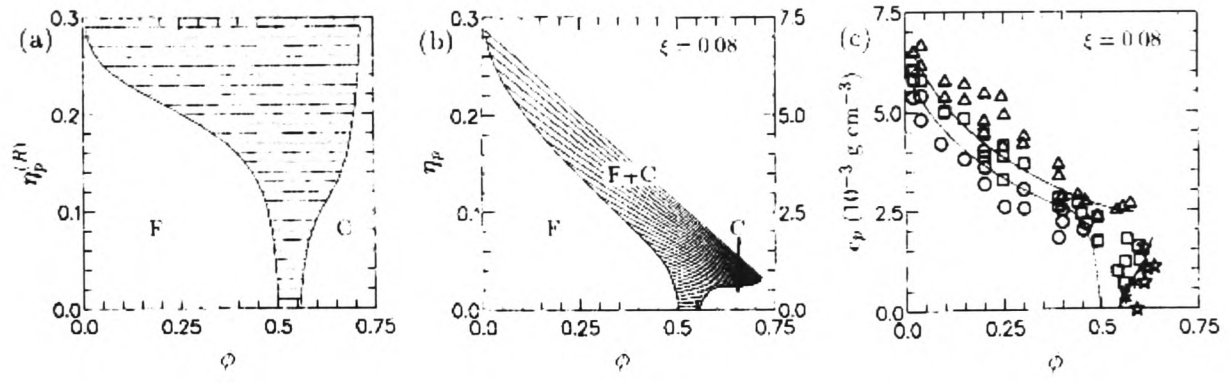

Figure 2.8: (A) Predicted phase diagram with free polymer volume fraction $\eta_p^{(R)}$ against colloid volume fraction, Φ for a mixture where $\xi = 0.08$. Tie-lines in the two phase region imply polymer partitioning between the fluid and crystal phases. (B) Same predicted phase diagram with experimentally relevant polymer volume fraction against colloid volume fraction. (C) Experimental phase diagram with polymer concentration C_p against colloid volume fraction, Φ for a PMMA-PS mixture where $\xi \sim 0.09$. (∘) homogeneous colloidal fluid, (□) fluid-crystal co-existing, (△) non-equilibrium aggregating state, (x) fully crystalline, and (⋆) glass. Solid lines are drawn to act as guides to the eye in identifying the position of phase boundaries. Figure reproduced from [11].

and references see the recent topical review by Poon [12]. Several different kinds of non-equilibrium behaviour have been found in a study of phase behaviour using small angle light scattering (SALS) [13], as summarised in figure 2.9.

Meta-stable Gas/Liquid It is thought that a meta-stable gas-liquid binodal buried in the equilibrium fluid-crystal coexistence region switches on non-equilibrium aggregation behaviour [12]. At high polymer concentrations the fluid branch of the free energy shows a "double minimum" structure, but for small polymers this gas-liquid binodal is hidden within the fluid-crystal coexistence region predicted by equilibrium thermodynamics. The non-equilibrium behaviour found fits in with this picture. The first form of non-equilibrium behaviour found above the fluid-crystal boundary is where density fluctuations give rise to areas with higher densities. As seen under the microscope disconnected aggregates form which are reminiscent of nucleation of droplets in classical fluids. Addition of more polymer gives rise to a meta-stable gas-liquid phase separation. Viewed under the microscope this would be seen as macroscopic regions of gas and likewise for liquid.

Transient Gels Transient gels are found at higher polymer concentrations than the previous two. The mechanism for the formation of these gels is complex due to the coupling with a spinodal decomposition and/or nucleation and growth phase separation. They can be easily recognised by either light scattering or direct observation [14], [15]. A ring of scattered light

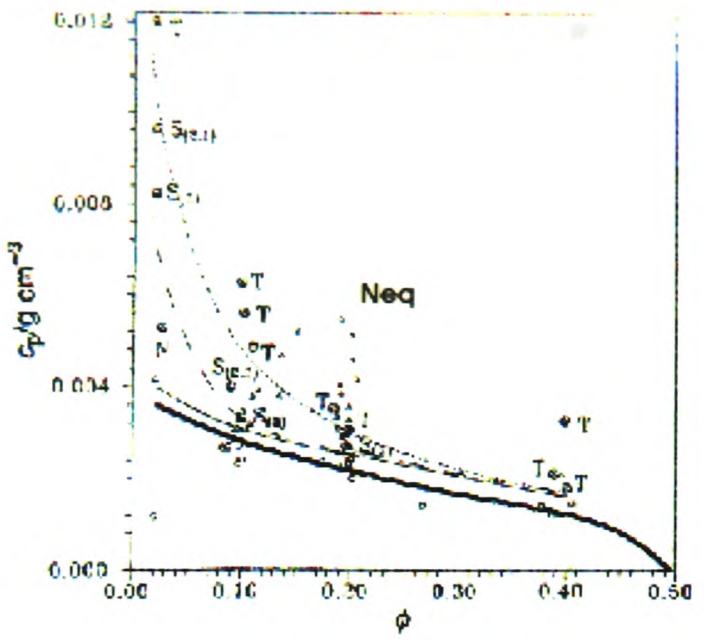

Figure 2.9: Experimental phase diagram expanded to include non-equilibrium "phases" for colloid-polymer mixtures with size ratio $\xi \sim 0.08$. Neq= non-equilibrium, T = transient gel, S = spinodal-like, N = Nucleation like. The marked boundaries are: fluid-crystal coexistence (lower solid line), non-equilibrium boundary (upper solid line), nucleation-spinodal boundary (long dashes) and transient gelation boundary (short dashes). Figure reproduced from [14]

appears at low angles, brightening and reducing in angle. After a few minutes, further collapse of the low angle ring is arrested, as are the fluctuations in the scattering pattern. After a period of time, the latency period τ_L, the ring suddenly collapses to zero angle and the rapid fluctuations resume.

Direct observation of the height of the colloid rich portion of the sample as a function of time give a characteristic "inverse sigmoidal" plot , as shown in figure 2.10. During τ_L (region A) sedimentation is very slow (or absent); then suddenly the sedimentation speeds up and a sediment is built up, this happens at the same time as the collapse of the small angle ring (region B); after this the sedimentation slows down again (region C). This phenomenon is called "Delayed Sedimentation".

Recent studies show that gravity and any residual charges on the particles can have significant effects on the behaviour seen at $\Phi \lesssim 0.2$ [16].

Dense Gels It has been found for dense colloidal suspensions with $\Phi \geq 0.4$ that the addition of polymer leads to a transition from colloidal fluid straight to a colloidal gel [17]. It is argued that the formation of the frozen structure of the gel is not related to the buried fluid-fluid spinodal or any metastable equilibrium phase boundary. Therefore it may be appropriate

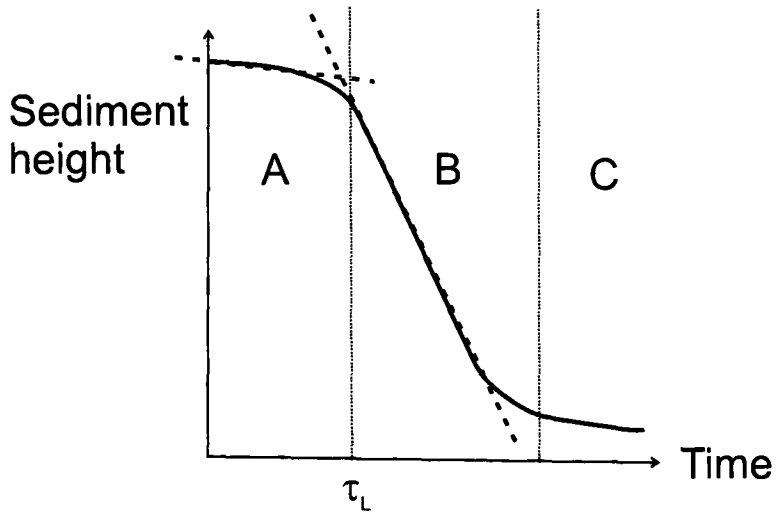

Figure 2.10: Schematic diagram showing the typical sedimentation profile of a suspension exibiting delayed sedimentation. Regions A, B and C represent the three phases of the settling process. τ_L is the delay time

to consider these gels as a different kind of gel from the transient gels studied at lower volume fractions for which the hidden spinodal is thought to play a role.

Repulsive and Attractive Glasses This is the high density limit for colloid polymer mixtures lying at the opposite extreme to very low volume fraction transient gels. The repulsive glass transition at $\Phi \sim 0.58$ is thought to be due to the caging of particles by their neighbours. Adding a little polymer "melts" the glass, and brings about crystallization. The caged particles in the hard sphere glass are given some space to rearrange and form crystals due to the weak clustering due to the small amount of polymer. The presence of even more polymer leads to cessation of crystallisation. This is interpreted as another glass transition, now attraction dominated. The addition of more polymer leads to an attraction so strong that all the particles are stuck to each other, once more giving structural arrest [18].

2.3.3.1 Gels in More Detail

Microscopic Structure of Gels The microscopic structure of gels depends on the colloid volume fraction and on the strength of the depletion attraction. Real space images of colloid-polymer gels at very low volume fraction ($\phi_c \leqslant 0.1$) [19] show that $\gtrsim 90\%$ of sample volume is empty space. The microscopic structure of the particles is less compact in samples with a stonger depletion attraction (more polymer), with fewer bonds per particle, forming more open chain-like clusters. Increasing the polymer concentration or colloid volume fraction monotonically reduced the number of bonds per particle. It is suggested that the stronger the

inter-particle attraction then the slower the compaction during aggregation.

For dense gels ($0.3 \lesssim \Phi_c \lesssim 0.5$), between 70% and 50% of the sample volume is empty space. The very short range structure of the gel is similar to that of a dense amorphous hard sphere system. At longer range the structure is different from a hard sphere system; long range structural heterogeneity i.e. voids are found. The voids have a broad volume distribution and can be many particle diameters in size (e.g. 10 particle diameters) [20]. Structural measurements with ultra-small-angle x-ray scattering on dense gels ($\phi_c \sim 0.4$) have been conducted by Shah et al [17]. They suggest from indirect measurements of the struture that the gel microstructure could be considered as being made up of small interpenetrating, polydisperse, percolated clusters of an average size 3-4 particle diameters with the surrounding voids having a characteristic length scale of 5-8 particle diameters.

The simple model of diffusion limited cluster aggregation (DLCA) [21] may be useful in understanding how gels form. Particles are assumed to be strongly attracted to each other; the limit of infinitely deep and zero range inter-particle attraction. Particles diffuse around but if they come into contact with another particle they stick together permanently. Clusters are formed that increase in size as they diffuse around. The clusters eventually fill space; forming a gel.

Clusters formed by DLCA have a fractal structure. This means that the number of particles in a cluster (proportional to mass) scales with cluster radius to some power d (which is known as the fractal dimension) which is smaller than the spatial dimension. In three dimensions DLCA produces a fractal dimension $d \sim 1.8$.

Reversible DLCA The DLCA model describes systems with very strong inter-particle attractions. In colloid-polymer gels the bond strength is finite; bonds can therefore be broken by the thermal energy of the particles, k_BT. So particle aggregation and thermal fluctuations compete. This is modelled by DLCA with finite bond energies known as "reversible DLCA" [22]. Particles still bond on contact but there is now a finite probability that the bond can be broken. The probability follows a Boltzmann distribution, $\sim exp(-U/k_BT)$.

Haw *et al* conducted computer simulations with reversible DLCA of particle aggregation in two-dimensions [23]. Figure 2.11 shows three "snap-shots" of particle aggregation from the simulations. In each image, black spots indicate the position of colloidal particles.

Three regimes were found:

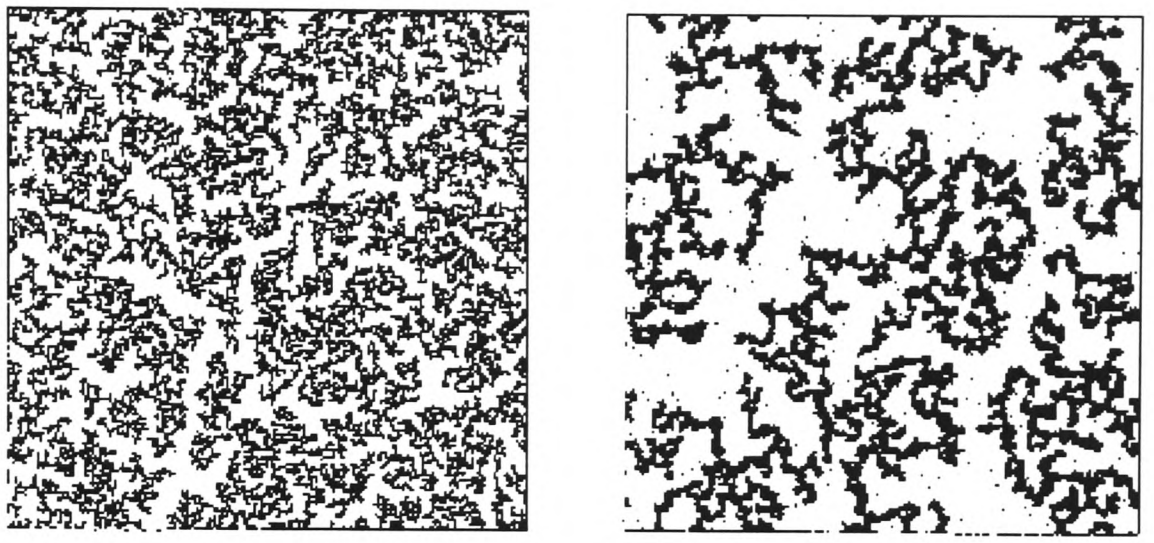

Figure 2.11: Two-dimensional Reversible DLCA simulation of particle aggregation with varying bond strength. (a) $U_{dep} \gg k_B T$, (b) $U_{dep} \sim 3k_B T$, (c) $U_{dep} \sim k_B T$. Figure reproduced from [23].

(a) For $U_{dep} \gg k_B T$. This is irreversible DLCA. The gel network formed is made of single particle links. Experimentally, this corresponds to very strong inter-particle attraction and no gravity.

(b) For lower bond strengths (reversible DLCA) the thermal fluctuations can break bonds leading to some compaction of the clusters on small length scales. The gel still forms quickly enough to span the system and form a gel. The arms of the gel network are fatter, being made up of multiply bonded particles.

(c) For even lower bond strengths, local restructuring becomes so fast that more or less compact clusters are formed.

Mechanism for Collapse of Transient Gels Gels continue to restructure after they have been formed, some of which will be driven by thermal fluctuations. In non-density matched samples, gravity-driven solvent flow as the gel slowly sediments may also play a role. Dark field imaging shows that such restructuring eventually opens up "channels" allowing rapid back flow of solvent, which in turn leads to the large-scale breakdown of the gel structure and the onset of rapid sedimentation [15].

2.4 Colloids Under Flow

Before looking at what happens to colloids under flow it is important to introduce some concepts related to rheology (study of flow and deformation) and the Peclet number which is used to compare the timescale associated with the flow to the timescale associated with the thermal motion of the colloid particles.

2.4.1 Rheology Background

Figure 2.12 shows an object being deformed by simple shear. The object, in this case a cuboid before deformation can be thought of as being made up of many, thin horizontal slices of thickness δy. Each slice is displaced sidewise relative to its neighbour below by an amount δx, resulting in the distortion of the cuboid into a rhomboid.

Shear distortion is quantified by the shear strain, γ, where

$$\gamma = \frac{\delta x}{\delta y} \tag{2.12}$$

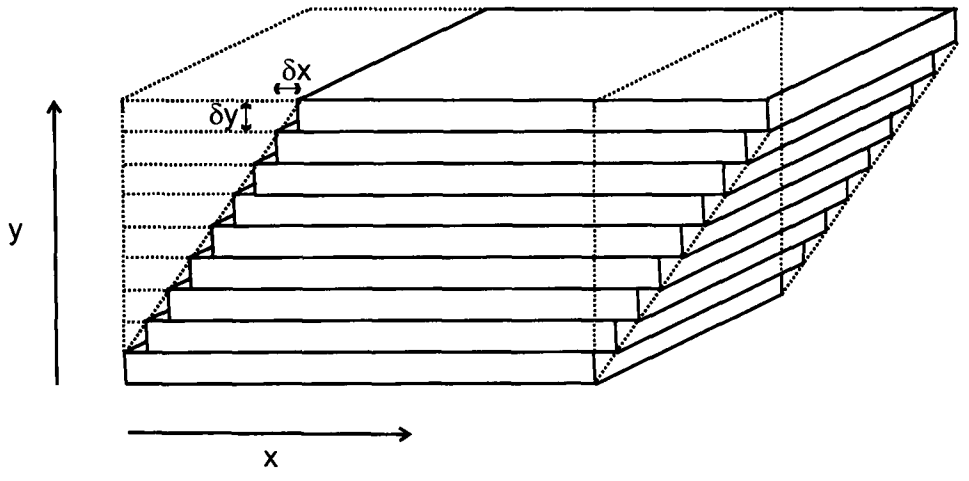

Figure 2.12: Simple shear deformation

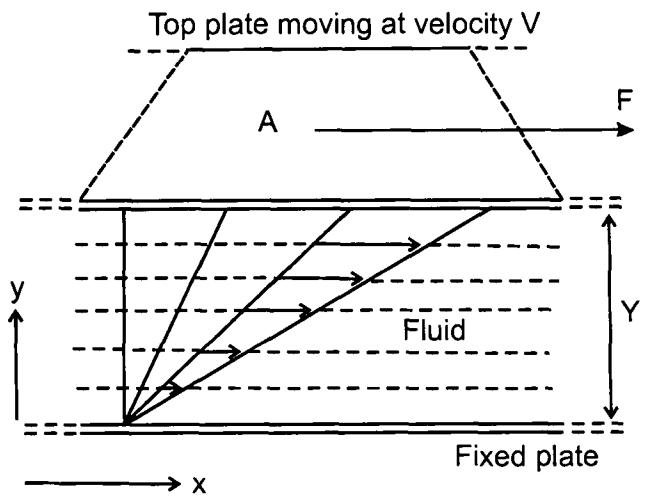

Figure 2.13: Viscous laminar flow

which in the case of a simple solid subjected to shear, is constant.

We will now consider one of the simplest models of fluid flow. Consider a fluid contained between two infinite parallel plates a distance Y apart, as shown in figure 2.13. The infinite plates allow us to ignore any edge effects.

The fluid is sheared by moving the top plate with a constant tangential force F per unit area A, giving the shear stress σ:

$$\sigma = \frac{F}{A} \tag{2.13}$$

The bottom plate is kept fixed. The top plate accelerates until it reaches a constant velocity V; the applied tangential forces balances out the resistance of the fluid. The fluid has reached a steady state. We assume that the fluid has "stick boundary conditions"; the fluid layer next to the plates are stuck to it and therefore move at the same velocity as the plate. This means that the fluid next to the top plate moves with velocity V and the fluid next to the bottom plate is stationary. What about the rest of the fluid? If we assume laminar flow then the simplest thing is to assume that the fluid moves with a constant velocity gradient throughout the bulk. This lets us define the shear rate

$$\dot{\gamma} = \frac{\delta \dot{x}}{\delta y} = \frac{V}{Y} \tag{2.14}$$

which is proportional to the shear stress:

$$\sigma = \eta \dot{\gamma} \tag{2.15}$$

where the constant, η is known as the viscosity and is a measure of the fluid's internal resistance to deformation. This model is known as a Newtonian fluid.

2.4.1.1 Peclet Number

When considering the flow of colloids it is useful to consider the Peclet number, which is a measure of the relative importance of convective motion of shear flow to diffusive Brownian motion. The characteristic time for the restoration of the equilibrium micro-structure of the colloidal suspension after a disturbance is typically taken as the time for a particle to diffuse a distance equal to its radius. This Brownian relaxation time is $t_{relax} \sim R^2/D$. The characteristic time for shear flow to have a significant effect on the suspension micro-structure is

$t_{shear} = 1/\dot{\gamma}$. Comparing these two characteristic times gives us the shear Peclet number

$$Pe = \frac{t_{relax}}{t_{shear}} = \frac{6\pi\eta_s R^3\dot{\gamma}}{k_B T} \tag{2.16}$$

For $Pe < 1$ the structure is thermally driven; the Brownian motion of the particle is not significantly affected by the shear. For $Pe > 1$ the structure is mechanically driven and can be radically altered by the flow.

2.4.2 Hard Sphere Colloids Under Shear

In this section we review what is known about pure hard sphere suspensions under shear. Experiments have been conducted for steady shear, where the strain is increased up to very high strains, and oscillatory shear, where a fixed strain amplitude is used at a certain frequency. I will consider both steady and oscillatory shear as there can be significant differences in the effects of these two kinds of shear. The oscillatory experiments are however more directly relevant to this work.

Lower volume fraction fluids remain amorphous under both types of shear. However, oscillatory shear, which imposes a strain $\gamma = \gamma_0 cos\omega t$ induces order in dense colloidal fluids that are just below the freezing transition. Light scattering experiments show sufficient strain amplitude, γ_0 induces low strain regime face-centred cubic (FCC) ordering [24],[25], see figure 2.14 (A), (B). A transition to the high strain amplitude regime (figure 2.14 (D)) is found for strain $\gamma_0 \sim 1$. Even higher strain disorders the structure returning it to an amorphous state. Optical microscopy oscillatory shear experiments [26] at lower Peclet number and frequency did not find any evidence of ordering suggesting that these parameters must be considered along with the strain. Steady shear, in contrast, leads to a distortion of the amorphous structure but not crystalline ordering as found in the oscillatory case [25] . High shear rates lead to strong shear thinning (reduced viscosity) of the sample as well as some evidence for string-like order as predicted by molecular dynamics simulations.

Light scattering measurements on coexisting fluid-crystal samples experiencing oscillatory shear show similar behaviour as found just below the freezing transition [25]. A lower strain amplitude is required to induce the low strain regime order and the high strain order persists to a higher strain amplitude before the structure becomes disordered. Steady shear leads to a transition to weak ordering of either liquid-like string ordering or of freely slipping layer ordering. Microscopy measurements of oscillatory shear [26] show evidence of order, but fully ordered

layers were only observed near the bottom of the shear cell in the high strain regime. Regions of crystal order surrounded by disordered fluid were observed higher up in the cell.

Oscillatory shear induces a sample that is fully crystalline in equilibrium to form the low shear FCC structure for $\gamma_0 < 0.5$ and the high shear ordering is observed for $\gamma_0 > 0.5$. Steady shear measurements find the same transition with increasing shear rate. Microscopy measurements [26] reveal more details about the differences in structure between the two strain regimes. Below a strain amplitude of $\gamma_0 < 0.5$ the orientation of the crystal structure was observed to be peaked in the direction of the low strain orientation but with a spread of up to 30° in orientation around this. The structure was poly-crystalline. For $\gamma_0 > 0.5$, the high shear orientation of crystal was observed within a few minutes of applied shear, much faster than the timescale for nucleation and growth of equilibrium crystals. A single crystal was observed filling the field of view, this is in contrast to the poly-crystalline nature of the equilibrium crystals.

Echo light scattering experiments show that a hard-sphere colloidal glass responds to low strain amplitudes elastically [27], [28]. The glass stops responding elastically at a critical strain amplitude that depends on volume fraction. Above this critical strain amplitude the particles start to undergo irreversible rearrangements. Light scattering oscillatory shear experiments [25] show that at low strain amplitudes the FCC structure is found coexisting with amorphous and layer ordering, see figure 2.14 (C). This is explained by the congestion that prevents equilibrium crystallisation. There is a transition to the pure high strain layer structure with increasing strain amplitude that is consistent with the model. Steady shear experiments show evidence for the layer ordering coexisting with the amorphous structure. Microscopy reveals defects present in the crystal structure with vacancies and dislocations [28].

A model that can explain the different crystal orientations at different strains and volume fractions is based on the idea that the observed ordering is governed by the packing geometry which allows the easiest flow in response to the applied oscillatory strain: this depends on the magnitude of the strain and the colloid volume fraction [25].

The FCC crystal layers can slip freely without collisions with neighbouring layers, but only up to a limited strain: we call this the low strain regime (figure 2.14 (A), (B)). The maximum strain that can be accommodated depends on the volume fraction of the shear-induced crystal. The maximum strain ranges from $\gamma_0 < 0.5$ for the most dense colloidal suspension ($\Phi = 0.64$) to $\gamma_0 < 1$ for $\Phi = 0.4$. For $\Phi < 0.4$ there is no limit on the strain as the crystal layers always have space to slide past each other. The close packed direction is perpendicular to the velocity axis (the direction the plate moves in as shown in figure 2.13). Above $\Phi = 0.64$ the particles

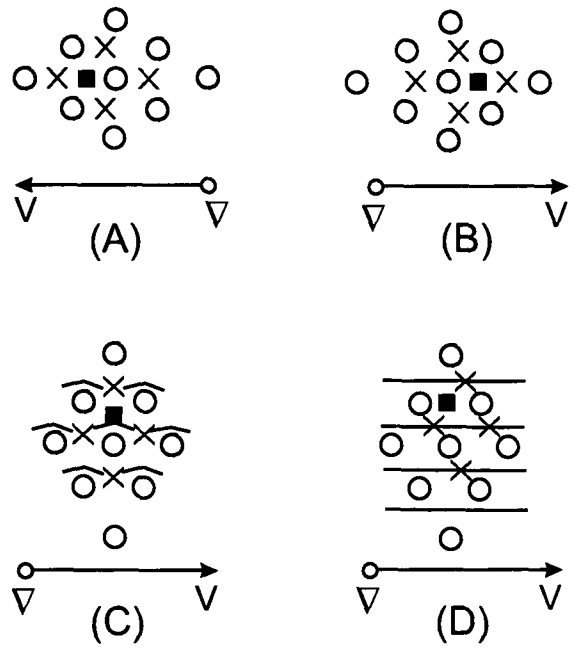

Figure 2.14: A schematic diagram of the different real space structures in the model proposed by Ackerson in [25]. (A), (B) Face centred cubic twin strucutures having characteristic ..ABCA.. stacking order. Note the relatively easy transition between the two twin structures for amplitudes oscillations near unity ($\gamma_0 < 1$). (C) Registered randomly stacked layers having no characteristic ..ACAB.. stacking order. The layers may slip past one another along the zig-zag path indicated (D) Freely slipping layers become centred over one another to move along the straight lines indicated. The position of layers along these lines is random. Symbols denote particles in neighbouring stacked layers e.g. ○ = layer A, X = layer B, ■ = layer C. V = velocity direction, ∇ = shear direction (into page)

are caged by their nearest neighbours and so cannot move past each other, limiting the strain. At $\Phi = 0.74$ no motion is possible, this is the closest packing volume fraction.

The crystal structure is different if a higher strain is applied. A different orientation of the close packed direction, parallel to the velocity axis allows the crystal layers to slip freely in the applied shear at all strains up to a volume fraction of $\Phi = 0.58$, providing the crystal layers line up with each other (figure 2.14 (D)). At higher volume fractions, (up to $\Phi = 0.64$) the layers must execute some zig-zag motion to slip in the applied shear flow (figure 2.14 (C)). This is the high strain regime.

2.4.3 Colloid-Polymer Gels Under Shear

Limited experiments on the rheology of colloid-polymer gels have been conducted by Meeker [14]. The resulting flow curves were interpreted as being consistent with a very low yield stress system. Computer simulations of the behaviour of dense attractive particles under shear have only been conducted for steady shear conditions [29]. It was found that the attraction between the particles enhances the viscosity of the system over the hard sphere case, although shear

thinning still occurs at high shear rates. Ordering is found at shear rates much higher than that found in hard sphere simulations. Interestingly, at lower shear rates liquid-like short range order is found along with intermediate range correlations between particle cluster within the bulk suspension that are very short lived. The attractive force is thought to effectively inhibit the disorder-order transition. The type of ordering found depends on the particle volume fraction, Φ. For $\Phi = 0.47$ string-like order is found co-existing with disordered regions. For $\Phi = 0.50$ string-like order is found co-existing with layer ordering. For $\Phi = 0.57$ only the ordered layer phase is found.

2.5 Observing Colloids

2.5.1 Techniques Used

Several different techniques have been used to study colloidal systems under shear with their own advantages and disadvantages. Light scattering is the main technique used as it can be used with a Couette geometry, as commonly used in rheometers, although not all $\underline{q}$ vectors are equally convenient to study. The structure of the sample is only indirectly measured from light scattering intensity patterns. The suspension micro-structure is determined in the same way as x-ray scattering patterns for atomic and molecular solids are used to determine crystal structure. For example shear induced ordering is detected by a redistribution of intensity within the diffraction ring e.g. Bragg spots. Light scattering averages over a large part of the sample so only the average structure can be studied.

Microscopy experiments have the advantage of studying the particles in real-space, allowing features and differences from the average structure (detected with light scattering) to be seen. A flat parallel-plate shear cell is required when using a standard microscope. It is not possible to obtain strains that are as high as those available in a Couette geometry.

The technique of light scattering-echo is described in more detail below but basically detects whether a structure is responding elastically to the imposed strain by correlating the scattered light every oscillation period. Its main advantage is that turbid samples can be used in contrast to the other techniques where any multiple scattering will degrade the quality of the results obtained.

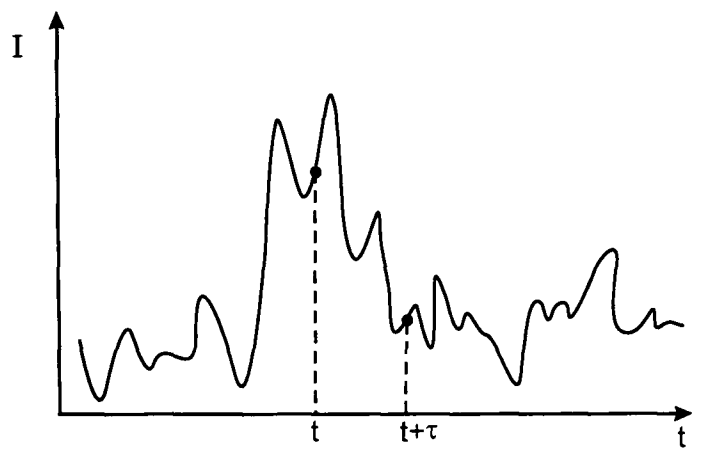

Figure 2.15: Schematic diagram of an intensity trace against time for a light scattering experiment. The dynamics of the system is followed by finding a time correlation function which compares the signal at time, t and a later time $t + \tau$, where τ is the delay time.

2.5.2 Light Scattering

The careful use of light scattering can give us useful information about the structure and dynamics of systems with comparable length-scales to the wavelength of visible light. When light is scattered from a material, the electric field of the incident light induces a dipole moment in the molecules of the material. The oscillating dipoles then re-radiates, giving rise to scattered light.

The ready availability of powerful visible light lasers has made light scattering a powerful tool in the study of colloidal systems. Static light scattering has been used to accurately determine the size of colloids [30]. Dynamic light scattering, as the name suggests, has been used to study the dynamics of colloidal systems [31]. We will now describe dynamic light scattering in more detail at both the single and multiple scattering limits. Each limit presents its own advantages and disadvantages.

2.5.2.1 Dynamic Light Scattering (DLS)

Photons from a laser are coherent i.e. all of the photons are in phase. When the photons are incident on colloidal particles the photons are scattered, leading to phase changes in the photons. These photons subsequently interfere with each other to produce a highly irregular intensity pattern on a screen placed on the opposite side of the colloid sample to the laser. This "speckle pattern" fluctuates in time. At a particular point the light intensity changes with time as the particles move with respect to each other. This fluctuating intensity gives information about the dynamics of the system. It is usual to measure the time auto-correlation function of

the scattered intensity $I(t)$ of a single speckle or diffraction spot. The time auto-correlation function compares the signal with a delayed version of the signal, as shown in figure 2.15. Usually, it is the normalised intensity correlation function that is determined.

$$g^{(2)}(\tau) = \frac{\langle I(t+\tau)I(t)\rangle}{\langle I(t)\rangle^2} \tag{2.17}$$

where τ is the delay time. However, it is $g^{(2)}(\tau) - 1$ that is of interest. At long times ($\tau \to \infty$) $I(t)$ and $I(t+\tau)$ fluctuate independently giving $g^{(2)}(\tau) = 1$. So if we use $g^{(2)}(\tau) - 1$ then $g^{(2)}(\tau) - 1 = 1$ corresponds to perfect correlation and $g^{(2)}(\tau) - 1 = 0$ corresponds to no correlation between $I(t)$ and $I(t+\tau)$.

In DLS a specific Fourier component of the density fluctuations is detected. Therefore, only the dynamics at a particular scattering wave-vector, q is determined and length-scale of order $\sim 1/q$ is probed. By detecting light from different scattering angles of the detector θ with respect to the incident light, different wave-vectors can be studied as $q = (4\pi/\lambda)\sin\theta/2$, with λ the light's wavelength in the medium.

The interpretation of standard dynamic light scattering experiments relies on the sample only scattering each photon once (or not at all). This requires the use of nearly transparent samples as this reduces multiply scattered light to a minimum. This can be achieved in practice by closely matching the refractive index of the colloid to that of the solvent. This limits experiments to systems where this is possible to achieve. Obtaining transparent samples is very hard, if not impossible for industrial or everyday colloidal systems such as paint or milk.

A clever technique has been developed to allow experiments with slightly turbid systems called two-colour dynamic light scattering. The correlation is made by cross-correlating the scattered intensity from two different laser beams of different wavelengths, but with the same q. This requires complex alignment of the lasers and optics. This cross correlation eliminates the influence of any multiply scattered light but it relies on there still being sufficient singly scattered light to form the correlation [32].

2.5.2.2 Diffusing Wave Spectroscopy (DWS)

A technique that uses multiply scattered light to its advantage is called diffuse wave spectroscopy (DWS) [33], [34]. The photons are scattered many times, N, in a turbid sample, before exiting the sample. For $N \gg 1$ the path of the photon can be modeled as a random walk of step length l^*, the transport mean free path. This is the length scale over which the photon

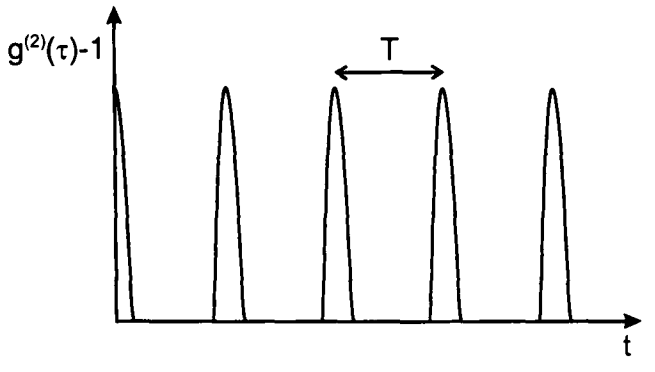

Figure 2.16: Schematic diagram of $g^{(2)}(\tau) - 1$ showing the "echos" at delay times equal to integral multiples of T

loses "memory" of its initial direction of propagation. This means that DWS is independent of the scattering wave-vector and thus there is no dependence on the scattering angle. A small particle scatters isotropically so $l^* \approx l$, where l is the mean distance between scattering events. Larger particles preferentially scatter in the forward direction so $l^* > l$.

As in dynamic light scattering the measured quantity is the time correlation function. This will depend on the geometry of the incident beam, the number of scattering events, whether the scattering geometry is transmission or back-scattering and of course on the intrinsic dynamics of the sample.

A characteristic of the DWS technique is the ability to probe smaller length scales than is possible with ordinary DLS. While DLS probes a length scale of order $1/q$, the length scale l_{DWS} probed by DWS, $l_{DWS} \simeq 1/\sqrt{N}k$, $(k = 2\pi/\lambda)$ is smaller by a factor equal to the square root of the number of scatterings. So the average number of scattering events is important in determining the length scale studied in an experiment.

2.5.2.3 Light Scattering Experiments on Sheared Samples

Light scattering can be extended to study the effect of oscillatory shear on a sample. In this recently-developed technique [35] the sample is subjected to an oscillatory shear strain during the light scattering measurement. The shear strain makes the scattering particles move with respect to each other causing the relative phases of the light scattered by the particles to change. This in turn causes the speckle pattern to change. A measurement of the time correlation function will show a decay as the scattered light become decorrelated as the sample is distorted by the induced flow. If, however, after one period, T, of oscillation (or an integral number of periods) the particles return exactly to their original positions then the speckle pattern also returns to its original configuration. The result is that $g^{(2)}(\tau)$-1 exhibits "echoes" of amplitude

1 at delay times equal to integral multiples of T, as shown in figure 2.16. On the other hand, if shear induces some irreversible rearrangements and some of the particles do not return to their original positions, the echoes will have amplitudes smaller than 1.

The DWS limit was the first used with the "echo" technique and the shape of the echos can be theoretically understood. It can be desirable or necessary to use less turbid samples. In this case the technique is called light scattering echo (LS-Echo) . The results are harder to interpret in this case as the random walk assumption for the scattered photons no longer holds.

Here I will summarise a simplified theory to aid understanding of this technique and interpretation of the results. For more details see [33]. For the simple case of a dilute suspension of particles undergoing Brownian motion and under zero shear, studied in the single scattering regime (i.e. by ordinary DLS) we have [31]:

$$\sqrt{g^{(2)}(\tau) - 1} = \exp\left(-\frac{1}{6}q^2\langle\Delta r^2(\tau)\rangle\right) \tag{2.18}$$

where $\langle\Delta r^2(\tau)\rangle$ is the mean-square displacement of a scatterer. In the strong multiple scattering limit (i.e. by DWS) it can be shown that the correlation function in the transmission geometry can be approximated by

$$\sqrt{g^{(2)}(\tau) - 1} \simeq \exp\left(-\frac{1}{6}Nk^2\langle\Delta r^2(\tau)\rangle\right) \tag{2.19}$$

where $k = 2\pi/\lambda$ (= $q/2$ at $\theta = 180^o$).

Subjecting a sample to an oscillatory shear strain induces displacements of the particles in addition to those caused by Brownian motion. The decay of the correlation function, $g^{(2)}(\tau = mT)$ (with m a positive integer), can be written as:

$$\sqrt{g^{(2)}(\tau) - 1} \simeq \exp\left\{-\frac{1}{6}Nk^2\left[\langle\Delta r^2(\tau)\rangle_B + \langle\Delta r^2(\tau)\rangle_S\right]\right\} \tag{2.20}$$

where $\langle\Delta r^2(\tau)\rangle_B$ is the mean-square displacement associated with Brownian motion and $\langle\Delta r^2(\tau)\rangle_S$ is that caused by the shear. Analysis of the actual shapes of the echoes, described by $g^{(2)}(\tau)$ at $\tau \approx mT$, is a complicated matter.

2.5.3 Microscopy

We will present a summary of the principles of microscopy relevant to this work from a very practical point of view. A more detailed and theoretical treatment, as well as extensive refer-

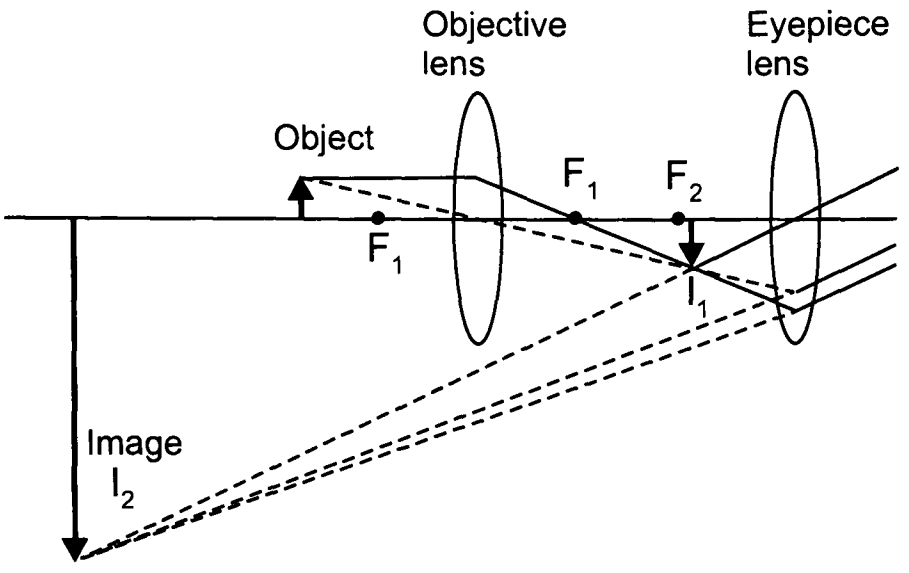

Figure 2.17: A schematic diagram showing the path of light rays through the two lenses in a compound microscope resulting in a greatly magnified image of the object

ences can be found in the excellent handbook thesis of Mark Elliot [36] or in the microscopy handbook series of the Royal Microscopical Society [37].

2.5.3.1 Principles of Microscopy

Components of a Microscope The development of microscopy was driven by the desire to magnify minute objects that could not be seen with the naked eye. A microscope in its simplest form uses a single lens in combination with the eye, this is a simple microscope e.g. reading glasses, magnifying glass. A compound microscope uses two magnifying components, the first is called the objective lens and the second the eye lens. A simple ray diagram (figure 2.17) shows how the two lenses are used to produce a greatly magnified image (I_2) of the object. The magnification is simply the image size divided by the object size. The object is illuminated on the opposite side to the objective by a lamp. For high magnification objectives a condenser lens is needed to focus all of the light from the lamp on the small area of the object being viewed. The lens acts like an objective in reverse with a similar magnification and aperture.

In practice, most modern research grade microscopes (see figure 2.18 for a schematic diagram) have "infinite tube-length" which refers to the fact that the intermediate image formed by the objective is at infinity, because the object is in the front focal plane of the objective. One can see in the figure that two rays from the one object point are parallel behind the objective. These microscopes use very sophisticated compound objective lenses that offer a range of magnifications.

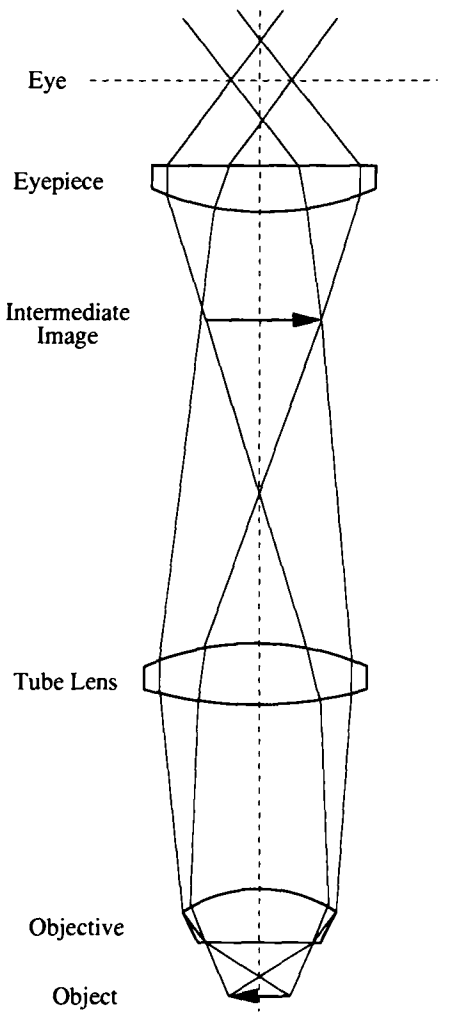

Figure 2.18: A schematic diagram of the infinite tube-length compound microscope.

Real Lenses - Aberrations In the real world lenses are not perfect, containing inherent defects called aberrations. There are two types: spherical and chromatic. The best objectives can almost perfectly correct for these aberrations and give vastly better images than the cheapest alternatives.

Spherical aberrations are caused by rays which pass through the margins of the lens being refracted more than those rays that pass near the centre. This effectively means that every part of the lens in the vertical direction has a different focal length. The combination of all the rays passing through the lens gives a fuzzy image as any sharp plane has superimposed upon it many out-of-focus planes. Correction for spherical aberration can be made by making compound lenses out of glass with different refractive indices. The overall effect of this correction is to bring the central and marginal rays to a focus at the same point giving a sharp image in a single plane.

Chromatic aberration occurs as the different wavelengths of light that pass through the lens are diffracted more the longer the wavelength (red more than blue). This means that there will be a spread in the point of focus for different colours. Correction for chromatic aberration can be made by using compound lens with different dispersion characteristics. This has the effect of bringing the different colours to a focus at the same place.

Important Objective Parameters The numerical aperture is a way to quantify the objective aperture while taking into account the effect of any immersion medium. It is defined as the sine of one half of the angular aperture, u, multiplied by the refractive index, n, of the medium between the object glass and the front lens of the objective.

$$N.A. = n \times sin(u) \tag{2.21}$$

So a dry lens has air as the medium with $n = 1.0$. $sin(u)$ is always less than 1 as the maximum half angle is 90°. In order to maximise the numerical aperture of the objective the gap between the objective and the object cover-glass can be filled with a medium. In this case the objective is called an immersion lens and will have $n > 1$, hence $N.A. > 1.0$ giving a greater $N.A.$ than a dry objective. The medium might also eliminate the refraction that occurs at the glass/air and air/glass boundaries. The refraction reduces the maximum angle that light can enter the objective. Oil is commonly used with the same refractive index as the glass. This allows an $N.A.$ as high as 1.4 compared to a maximum of $N.A. = 0.95$ for a dry objective. Little light is lost at the boundaries either.

Lenses are designed so that the numerical aperture increases with the magnification. Higher magnification makes objects look bigger but it is the ability to see more detail that is the crucial one i.e. resolving or separating parts of an object that are not evident at lower magnification. For every $N.A.$ there is a limit beyond which further magnification does not give additional detail. This is called empty magnification. So the ability to resolve detail is proportional to the numerical aperture not magnification as many naively assume. For an illuminating cone equal to that of the objective the distance, R between two points that can be separated sufficiently to determine that there are two separate points is given by:

$$R = \frac{0.61\lambda}{N.A.} \tag{2.22}$$

This is also known as the Rayleigh criterion. Note this only applies to coherent light.

The depth of focus which is the amount of the object that is in focus simultaneously is inversely proportional to the numerical aperture. Low N.A. gives an image that shows portions of a transparent object above and below the theoretical plane of focus that are in focus as well. High N.A. gives an image of only the plane of focus with no depth visible.

The working distance is the distance between the front of the objective and the focal plane (where the object being studied should be positioned). As the focal length of the objective is shortened the working distance decreases. Low magnification objectives can have a working distance of up to a few centimetres, whereas high magnification objectives almost touch the object. For high magnification lenses with equivalent focal length an increase in N.A. gives a decrease in the working distance.

The object is usually covered with cover-glass. This glass is effectively the first element of the objective. The optical effect of the glass must be taken into account when designing objectives. A small difference in thickness of the glass away from that which the lens was designed for can have a large effect on image quality.

2.5.3.2 Enhancing Contrast

For objects where the difference in absorption of light is very small compared to the background medium (such as colloidal particles or living cells) they are found to be invisible to the eye in bright field microscopy. The object does however cause small changes in the phase relationships between the rays of light as they emerge. This phase change is caused by differences in refractive index or thickness within the object. Contrast as seen by the eye is caused

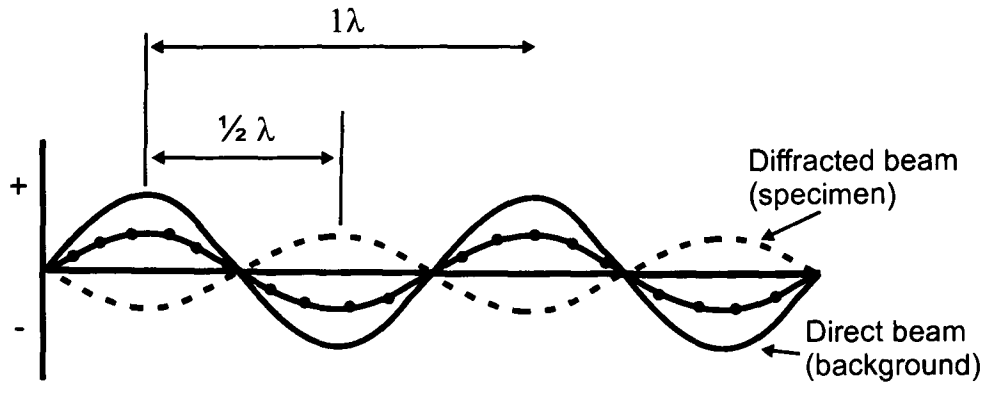

Figure 2.19: A diagram showing a light beam passing through an amplitude object. The diffracted beam (originating at the specimen) is shown by a dashed line and is half a wavelength out of phase with the direct beam. The resultant beam (shown as a continuous line with superimposed black dots) is the sum of the direct (background) beam and the diffracted (specimen) beam. Note that this resultant is in phase with the direct beam but of lower ampltitude. Figure reproduced from [37].

by amplitude changes in the light that passes through the object. So what is needed is a way to convert the phase changes into amplitude changes so that the eye sees some contrast. The simplest method of doing this is know as phase contrast.

A more sophisticated method that has superseded phase contrast is known as differential interference contrast and is the technique used for the bulk of this work involving light microscopy. A completely different way to enhance contrast is by making the object fluoresce in a different colour to the illuminating light source. By filtering out the illuminating light, only light from the object is used to form the image. Combining fluorescence with a confocal microscope eliminates the out-of-focus light giving an image with excellent contrast.

Phase Contrast The technique of phase contrast was invented by Frits Zernike in 1934 and is an efficient method of enhancing contrast without unacceptable loss of resolution. Phase contrast works by increasing the optical path of the light diffracted from the object. When this diffracted light interferes with attenuated direct light to produce the image the resulting amplitude of the light is changed sufficiently to produce contrast in the image.

According to Abbe's theory all specimens diffract light and it is this diffracted light that carries information about the structure of the specimen. In order to understand how phase contrast works we consider only simple light waves that capture the essential features of phase shifts and interference [37]. A fuller treatment involving vectors can be found in [36].

The image is made up of two beams of light. Direct, undiffracted light and light diffracted by the specimen. For a specimen that absorbs light, the diffracted light is half a wavelength

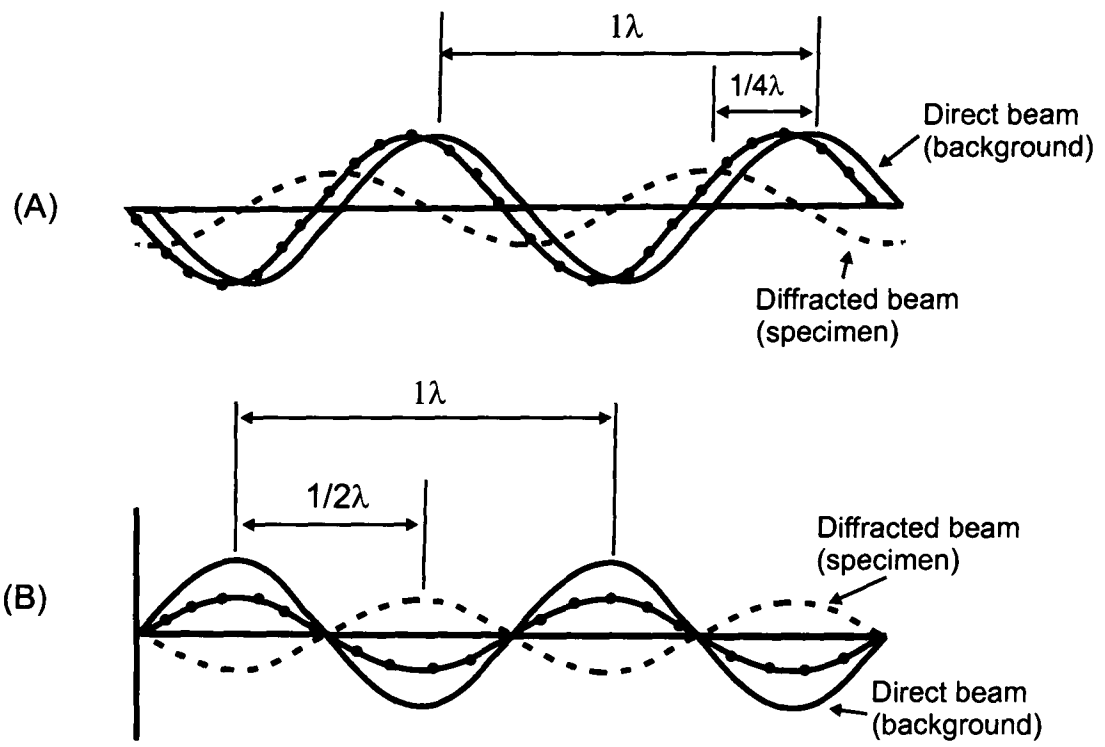

Figure 2.20: (A) The direct, diffracted and resultant beams for a transparent, phase object. When the direct beam passes through a thin, transparent object, the resultant beam will show a small phase retardation with respect to that part of the direct beam which does not encounter the object. As in figure 2.19 the resultant beam is the sum of the direct (background) beam and the diffracted (specimen) beam. The diffracted beam (dashed line) is one quarter out of phase with the direct beam. (B) If a further one quarter retardation is added in the microscope to the diffracted beam, so shifting the curve for that beam (dashed line) a further quarter of a wavelength to the left, a total retardation of one half of a wavelength with respect to the direct beam gives the situation illustrated. The image of the transparent phase object has been transformed in a simulated amplitude object with sufficient contrast for it to be clearly seen. Figure reproduced from [37].

out of phase with the direct light. The diffracted and direct light interfere with each other. The resulting image is of lower amplitude so the specimen can be seen (see figure 2.19). A non-absorbing specimen on the other hand does not give any contrast in the final image so it follows that the phase difference between the direct and diffracted beams cannot be as large as half a wavelength. The diffracted beam is scattered at interfaces between regions of rather small differences in refractive index. This can be shown to result in phase differences of only about a quarter of a wavelength. This difference cannot result in a significant change in the image through interference (see figure 2.20 (A)).

The phase contrast technique alters the phase difference between the direct and diffracted rays to maximise the interference between them, giving the maximum contrast. The diffracted beam is made to pass through a slightly longer optical path, an extra quarter wavelength. When the diffracted beam then interferes with the direct beam to form the primary image there is now a half wavelength phase difference between them and this gives considerable contrast. The non-absorbing, phase specimen effectively behaves as an absorbing, amplitude specimen (see figure 2.20 (B)).

In modern microscopes phase contrast is implemented by using a special objective and corresponding condenser. An annular diaphragm is fitted at the lower focal plane of the condenser, this produces a ring of light in the back focal plane of the objective. The objective is specially made with a phase plate which selectively alters the phase of the direct light with respect to the diffracted light. The area of the phase plate where the image of the illuminating annulus falls, called the phase ring, is designed to give a quarter of a wavelength less shift to the phase than the rest of the area of the plate. If no specimen is present then all the light will pass through the phase ring. A diffracting specimen will deviate light from this path and it will pass through the optically thicker part of the phase plate.

The transmission amplitude of the direct beam must be reduced to match the amplitude of the diffracted beam to maximise the contrast. This is achieved by adding a thin layer of an absorbing substance to the phase ring. This is why you can see the phase ring when you look through a phase contrast objective. It is the difference in transmission that you can see as any phase change is invisible.

There are a few disadvantages with phase contrast that should be noted. A halo surrounds all contrasted features partly caused by the way light passes through the phase ring. Also, phase contrast only works well with extremely thin objects. A typical phase contrast image of colloid particles forming a thin layer on a coverslip is shown in figure 2.21 (LHS).

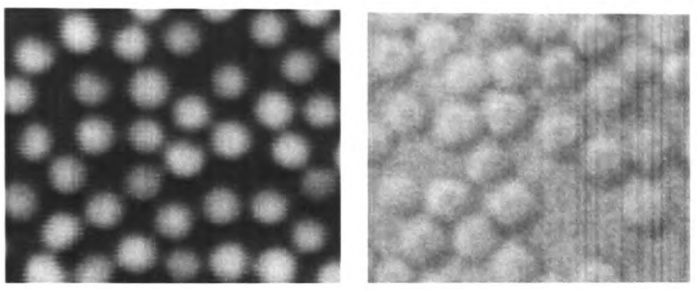

Figure 2.21: Two typical images of a thin layer of colloid particles ($R = 689nm$) on a coverslip using different methods of contrast enhancement. LHS = Phase contrast, RHS = DIC.

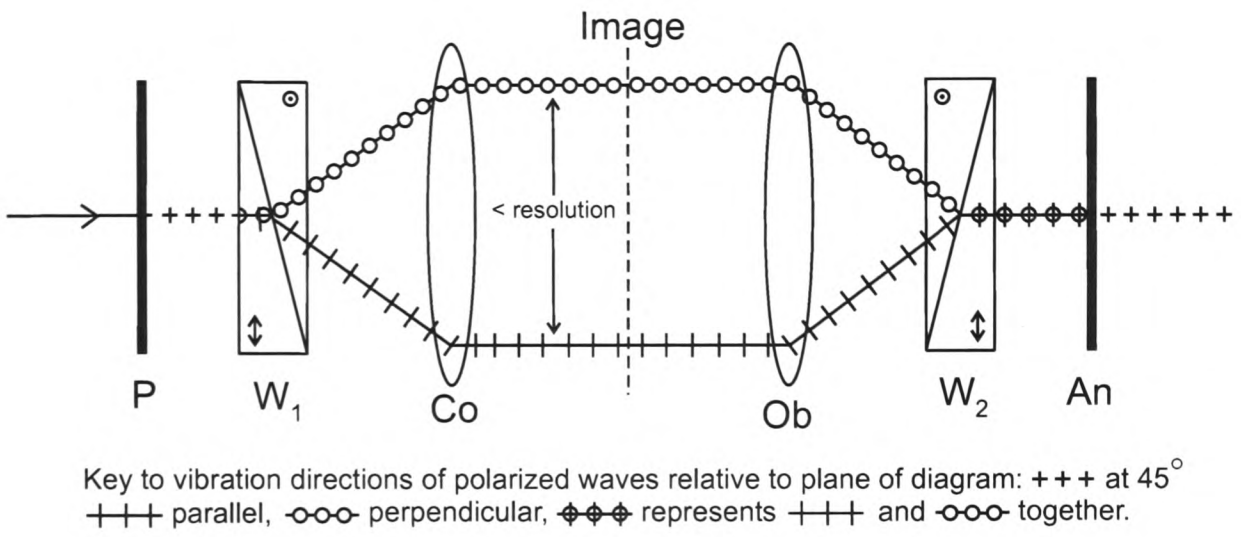

Figure 2.22: A schematic diagram of the special components of the DIC microscope: a polariser P, a Wollaston prism W_1 at the front focal plane of the condenser Co, another Wollaston prism W_2 at the front focal plane of the objective Ob and a second polarising filter, the analyser A. Figure reproduced from [36].

Differential Interference Contrast Differential interference contrast (DIC) is a technique that was patented by Nomarski in 1953. It produces contrast in an image from a transparent specimen by forming each point in the image by interference between two beams that pass through the specimen very narrowly separated. Any phase difference between the two beams is caused by the gradient in the refractive index or thickness of the specimen at that point in the specimen. Thus if the gradient or differential of the refractive index change that gives rise to the contrast in the final image. It can be helpful to remember that the contrast in DIC is due to "wedges" whereas in phase contrast it is due to "edges" [37].

In a DIC microscope the splitting and recombining of the beam is achieved with Wollaston prisms. A Wollaston prism is formed from two geometrically similar wedges of doubly refracting material. They are cut so that the optical axes are at right angles, one to the other. Figure 2.22 shows the special components of a DIC microscope. A beam of plane polarised light entering the prism at 45° to its axis will be split by the prism into two mutually perpen-

dicular beams. The first prism is placed after a polariser. The split light passes through the specimen. The separation between the beams is smaller than the length scale resolvable by the microscope. The two beams are recombined by the second prism and as they came from a common source they can interfere. The recombined beam then passes through the analyser. The practical problem with this setup was that the second prism had to be placed in the focal plane of the objective which is found within the composite objective housing. If the prism is placed within the objective this prevents the use of the objective for other kinds of imaging. Normarski solved this problem by modifying the second Wollaston prism to allow it to be placed outside the objective but to appear to the light beams as if it were still in the focal plane. The prism is commonly mounted on a slider that fits into the microscope tube toward the nose-piece.

Members of each pair of beams will encounter differing optical paths due to variations in refractive index and thickness of components of the specimen. When both paths through the area are equal then both paths remain in phase. The resulting point on the image is maximally dark, as you would expect for light passing through crossed polars. When the optical paths differences are present due to steps or gradients in the refractive index or thickness then one beam will be advanced or retarded in phase with respect to each other. As the two beams are only infinitesimally separated as they pass through the specimen they are not far enough apart to have their phases shifted by different features of the specimen with corresponding different refractive indices. Therefore, it is the local change of the refractive index, or gradient that produces the respective phase shift of the two beams. The relative path of all of the pairs of beams can be changed by shifting the position of the second Wollaston prism. This alters the relative thickness of the upper and lower components of the wedge through which the beams pass. This will advance one or other of the beams with respect to the other, changing the contrast of the whole image.

The advantages of DIC are a higher resolving power than phase contrast partly due to the absence of the halo that surrounds phase contrast features. When combined with a high numerical aperture objective DIC produces images with a very shallow depth of field, effectively giving optical sections. As a result, out-of-focus blur impairs image sharpness to a much lesser degree than with other techniques. Good images of relatively thick objects are possible compared to phase contrast where very thin objects are required. There is an important artifact found in DIC images that should be noted. Consider a spherical particle, it will appear to be lit from the diagonal edge giving a shadowing effect. This gives a misleading three dimensional appearance to the image which is of course purely two dimensional in nature. A typical DIC image of colloid particles forming a thin layer on a coverslip is shown in figure 2.21 (RHS).

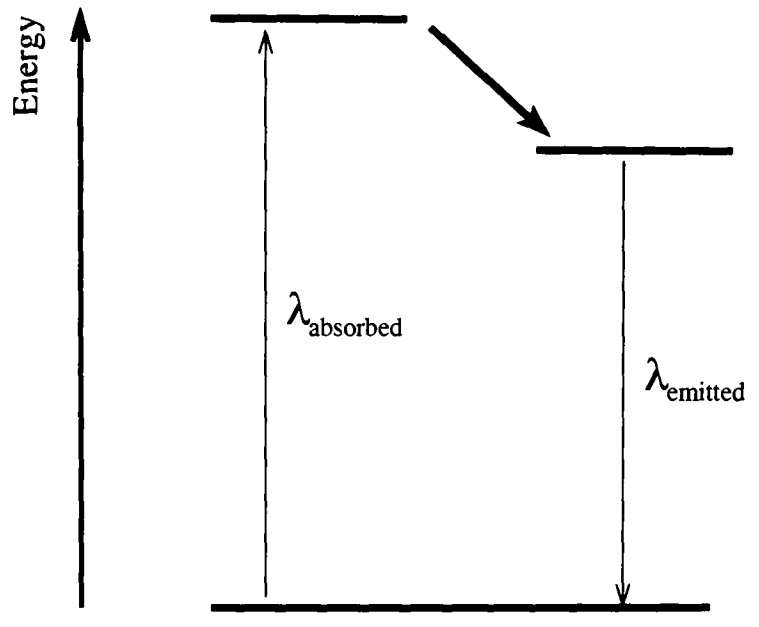

Figure 2.23: Energy diagram of fluorescence exitation.

Fluorescence Microscopy Many of the problems associated with contrast are due to the fact that the specimen is transparent i.e. does not absorb any light. A solution to this is to make the object emit light, so that it stand out against a dark background. This is the basic principle of fluorescence microscopy. Firstly, we will look at how fluorescence works and then how it is applied in a microscope.

When light is shone on some molecules they emit light of a different colour. This is called fluorescence. The molecules absorbs high energy light, exciting some of their electrons to a higher energy state (see figure 2.23). Some of the energy is lost internally as the electron returns to its original energy level. Most of the energy is emitted as a photon of lower energy. So we can discriminate between the emitted and incident light. The wavelength of the light emitted depends on the molecule as does the excitation light wavelength. These dye molecules can be attached to specific parts of a sample and only these parts of the sample are visible under the microscope as the excitation light is filtered out.

A few extra features are needed in a fluorescence microscope. A special dichroic (properly called dichromatic) mirror is used. This mirror reflects light shorter than a certain wavelength and passes light longer than that wavelength. A schematic fluorescence microscope is shown in figure 2.24. A special lamp produces the excitation wavelength. This light is blocked from entering the eyepiece or detector by the dichroic mirror. So only the light emitted from the sample enters the detector rather than the scattered incident light. When the same lens acts as both the objective and the condenser, illuminating the sample as well as detecting the emitted light from the sample, this is called epi-fluorescence. The setup more similar to a light microscope

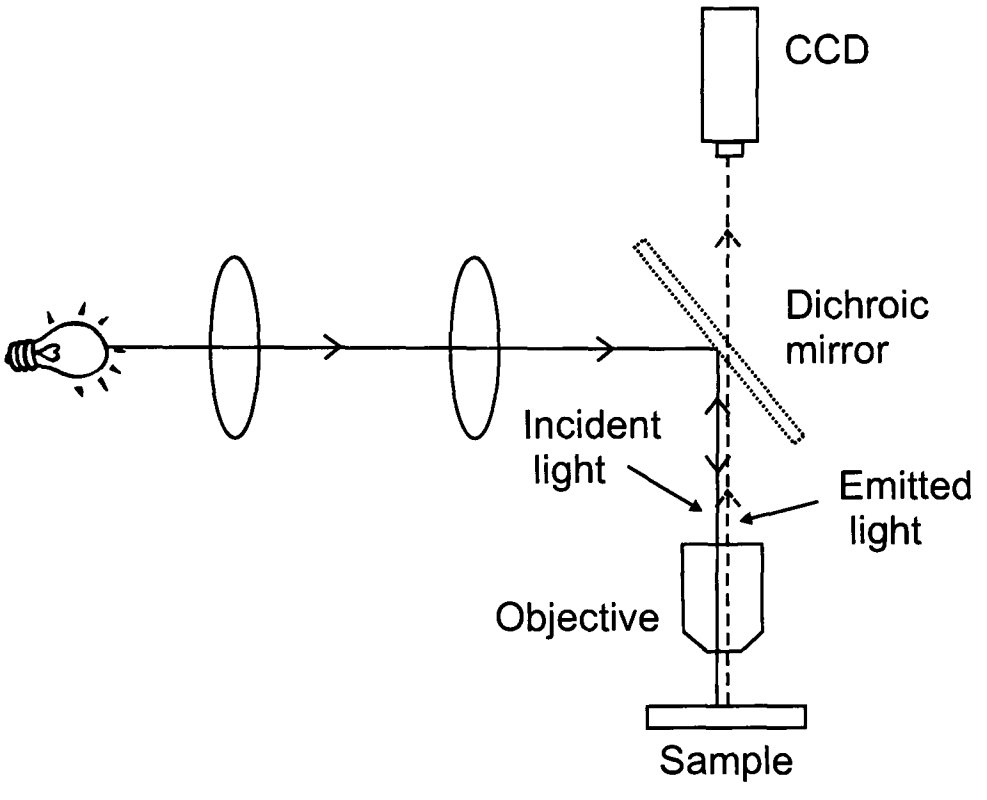

Figure 2.24: A schematic diagram showing the paths of the incident light from the bulb and the light emitted from the sample. Any scattered incident light is blocked by the dichroic mirror. Only the light emitted from the sample reaches the CCD.

is called trans-fluorescence.

This method works very well for thin samples. However, for thick samples there are serious problems. Usually the whole sample is illuminated by the excitation light. This causes the whole sample to fluoresce at the same time. The highest intensity in the sample will be at the focal point of the objective but other parts of the sample will get some light and will fluoresce as well. This background haze in the resulting image seriously degrades the quality, ruining the contrast. This can be thought of a case of there being too little signal to noise in the image. The solution to this problem involves using the confocal principle.

The Confocal Principle The confocal principle is a way to minimise the light that falls on the image from out of focus planes so that the image is formed only from light from the focal plane of the objective. This is achieved by placing a screen containing a pinhole in the plane **con**jugate to the **focal** point of the objective lens [38]. This plane is where the focal point of the objective forms an image. As seen in figure 2.25 the pinhole blocks light that comes from nearby planes that are out-of-focus. The advantage of this technique is that all light is discarded except light that originates from a thin region centred on the focal point. This gives excellent image quality and contrast. Another important feature is that the image only comes from a very

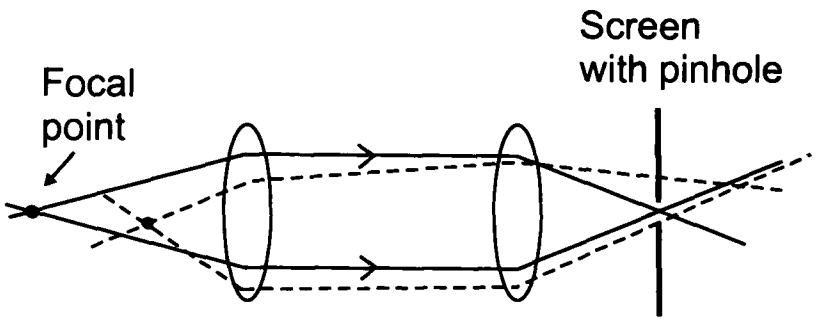

Figure 2.25: A schematic diagram of the confocal pinhole. Light emitted from the focal point of the objective lens (solid light rays) passes through the pinhole. Light emitted from nearby planes (dashed light rays) is blocked by the pinhole.

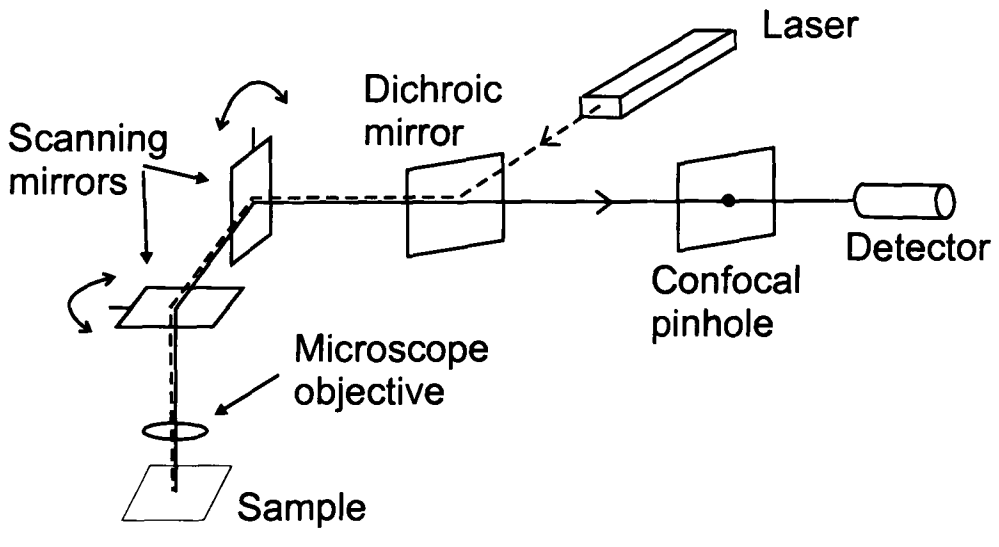

Figure 2.26: A schematic diagram of laser scanning confocal microscope. Note, dashed light ray is incident laser light and solid line is light emitted by sample.

thin layer of the thick sample. The image is an optical section. This has important applications in 3-D reconstruction of objects which will be covered later.

It is possible to use a confocal microscope with visible light but the technique works best when combined with fluorescence [38]. Typically, modern research microscopes use lasers to emit the light used to stimulate the fluorescent dye and scan the laser across the sample to form the image. Therefore, these microscopes are called Laser Scanning Confocal Microscopes (LSCM). (There is no single convention for the order of the letters so CLSM and CSLM are also commonly seen in the literature). I will now explain the main features of a LSCM as shown in figure 2.26.

A high intensity laser is used. A range of different wavelengths of light can be used from ultra-violet to infra-red depending on the dye wishing to be used. Solid state lasers which are much more compact are increasingly favoured over gas lasers. The most advanced pulsed lasers can be used over a large continuous range of wavelength in contrast to most lasers that only offer a

few specific emission lines.

The laser scans the sample to build up the image a line at a time in a similar way to the electron beam building up an image in a cathode ray tube television. Either the microscope stage or the laser beam have to move to conduct the scanning. For technical reasons it is most common to move the laser with tiny mirrors constraining the beam within the objective lens.

The detector is a photo-multiplier tube that detects the intensity of the emitted light at each point of the image in turn. Purpose-built computer software displays the image and allows the various parameters to be varied. These include the scan speed, the resolution in pixels of the image, the ability to zoom into a small area within the view available with the objective. The software can be used to take time series. A 2-D image is recorded sequentially in time allowing dynamic events to be studied. The objective focus control can be computer controlled using a piezo motor. This allow for z-scans, as each 2-D image is a thin optical slice through the 3-D object. A sequential series of 2-D images are recorded each separated by a small distance in the z-direction. This builds up 3-D information about the object. With suitable software it is possible to render 3-D projections and other forms of 3-D analysis.

Chapter 3

Experimental Methods and Materials

3.1 Introduction

In this chapter we first describe our model system and samples used in this work. Secondly, we describe our experimental setups and methods used in the light scattering, optical and confocal microscopy experiments.

3.2 The Model System

Any experimental model system can not perfectly match the theoretical hard sphere model. Real colloids do not have perfect hard sphere interaction and cannot ever be perfectly mono-disperse. Real polymer is not perfectly mono-disperse in molecular weight. In this section we describe our model system and the samples used in this work.

3.2.1 Colloids

The colloidal particles used in this work were spherical polymethylmethacrylate (PMMA) particles. All of the PMMA particles used in this work were made by A. Schofield. The particles were sterically-stabilized by grafting chains of (poly)hydroxystearic acid (PHSA) onto the surface. The particles were suspended in cis-decalin (decahydronapthalene) or a mixture

Colloid	Fluorescent	R^{cis} [nm]	$R^{density}$ [nm]
1	no	689 ± 68	-
2	yes	533 ± 53	544 ± 54
3	yes	1100 ± 110	1122 ± 112

Table 3.1: The different colloids used in this work, showing whether they are flourescent or not, and their radius, R in both cis-decalin and density-matched solvent (uncertainty in R from polydispersity of $\sim 10\%$).

of cis-decalin and cycloheptyl-bromide (CHB) when a density match with the PMMA was desired. (See section 3.2.2 for densities.) Fluorescent PMMA colloids were also prepared by A. Schofield for use with the laser scanning confocal microscope according to the methods of Jardine et al [39]. The fluorescent monomer 7-nitrobenzo-2-oxa-1,3-diazole-methyl methacrylate (NBD-MMA) is chemically incorporated into the PMMA during prepearation giving colloids with a yellow colour, in contrast to the usual grey/white colour. Table 3.1 shows the colloids used in this work and the radius, R of the colloid in both cis-decalin and density-matched solvent.

The radius of the particles was measured by crystallography (by A. Schofield). The radii of the colloid particles used in this work are given in table 3.1. This method measures the lattice spacing of colloidal crystals from a fluid-crystal coexisting sample. These crystals have a known volume fraction ($\Phi = 0.545$). This allows the particle radius to be calculated. For very large particles ($R > 1000nm$) there is very fast sedimentation so the volume fraction of the crystal phase is no longer reliably known. Instead, dynamic light scattering is used to measure the hydrodynamic radius [40]. These measurements were conducted in cis-decalin. For the mixture of cis-decalin and CHB it has been shown that the particles swell, giving an increase in the radius of $R \sim 2\%$ [41]. Pusey [42] developed a simple theory based on Lindemann's melting criterion and found that crystallisation is suppressed for a polydispersity $\gtrsim 10\%$. As the colloid particles used in this study were found to crystallise the polydispersity is estimated as 10%. A precise measure of polydispersity was not necessary for this work.

The size of the colloid particles is a very important factor to consider before commencing microscopy experiments. The resolution limit of the microscope is approximately 300nm. It is important to use particles with a diameter greater than this otherwise individual particles will not be visible. It makes sense to use large particles therefore, which are easier to see. However, if the particles are too large they cease to be colloidal. This means that the thermal motion of the particles will no longer balance the pull of gravity and the particles will quickly sediment.

This becomes less of a problem with dense suspensions or weak solids such as the gels used here. Particles of radius between 500nm and 1000nm were found to be suitable, being easily visible but not sedimenting in the timescale of an experiment. (See figure 5.1).

3.2.2 Solvent

The refractive index difference between the solvent and the colloidal particles is very important for optical experiments as this gives contrast between the particles and background solvent. If the difference is too large then multiple scattering unacceptably reduces the quality of the images in microscopy and only single particle layer samples can be imaged. If the refractive indices are identical then the particles are invisible (note, unless they are fluorescent). It was found experimentally that of the solvents used with PMMA ($n = 1.49$) cis-decalin ($n = 1.48$) gave the best image quality. Particles suspended in dodecane gave too much scattering and very poor images. Cis-decalin solvent is also the most commonly used solvent in past experiments as it is a good solvent for PHSA and PMMA is known to be very stable in this solvent. The close refractive indices also reduces the van der Waals attractions. CHB ($n = 1.50$) is also a good solvent for the PHSA and has the advantage of having a slightly higher density than PMMA ($\rho_{PMMA} = 1.19gcm^{-3}$ and $\rho_{CHB} = 1.29gcm^{-3}$, whereas $\rho_{decalin} = 0.89gcm^{-3}$). A mixture of solvent can be made that matches the density of the PMMA, thereby eliminating the effect of gravity at a fraction of the cost of a space shuttle. There is the added advantage (when using fluorescent particles) that this mixture also approximately refractive index matches at the same time.

Since the bulk of this work was completed, it has been shown that CHB induces a slight charge to the PMMA particles [43]. We do not know what effect this has on our findings. Our data collected using CHB should therefore be treated with some caution. The long term stability of PMMA in CHB has not been studied in detail but stock solutions kept for over a year show no change.

3.2.3 Polymer

The polymer is non-absorbing polystyrene (PS) obtained from Polymer Laboratories dissolved in the same solvent as the PMMA particles. The size of a polymer coil is characterized by the radius of gyration, r_g. The radius of gyration of a polymer coil depends on the particular polymer, solvent and the solvent temperature. According to Berry [44], the radius of gyration

$M_w[gmol^{-1}]$	$r_g^{cis}(\theta)[nm]$	$r_g^{cis}(295K)[nm]$	$r_g^{density}(295K)[nm]$	$C^*_{cis}[mgcm^{-3}]$
7,300,000	74.6 ± 5	108 ± 8	-	2.32
2,536,000	44 ± 3	56 ± 4	58.0 ± 4	5.65
7,500,000	76 ± 5	110 ± 8	113 ± 8	2.27

Table 3.2: The different polymers used in this work, showing their molecular weight M_w, radius of gyration when dissolved in cis-decalin at the theta temperature, $r_g^{cis}(\theta)$ at room temperature, $r_g^{cis}(295K)$ and in the density-matched solvent at room temperature, $r_g^{density}(295K)[nm]$. Also shown is the overlap concentration C^*, in cis-decalin (as defined in equation 3.5).

of a polystyrene coil suspended in cis-decalin at a temperature $T(K)$ in given by

$$r_g = r_g^\theta \sqrt{1 + \frac{134}{105} z(T)} \tag{3.1}$$

where $r_g^\theta = 0.0276\sqrt{M_w}$ is the radius of gyration at the theta temperature T_θ ($T_\theta = 285.5K$ for polystyrene in cis-decalin), M_w is the molecular weight ($gmol^{-1}$) and $z(T)$ is the Fixman parameter

$$z(T) = 0.00975\sqrt{M_w}\left(1 - \frac{T_\theta}{T}\right) \tag{3.2}$$

See table 3.2 for the M_w, $r_g(\theta)$ and $r_g(295K)$ for the polymer used in this work.

There is a small swelling effect on r_g for polymers dissolved in the density matching solvent mixture containing both cis-decalin and CHB. Measurements by Prasad [45] show that $r_g^{density}$ for polymer in the density matching solvent mixture is $\sim 3\%$ larger than for polymer in pure cis-decalin at room temperature, within experimental uncertainty. See table 3.2 for $r_g^{density}(295K)$.

The polydispersity in molecular mass of the polymer coils can be calculated from the ratio of the weight averaged molecular mass to the number averaged mass M_w/M_n. This quantity is quoted by the polymer manufacturer and is related to the polydispersity in M_w by

$$\sigma^2_{M_w} = \frac{M_w}{M_n} - 1 \tag{3.3}$$

which gives a polydispersity [46] in the ideal radius of gyration of:

$$\sigma_{r_g^\theta} = \frac{\sigma_{M_w}}{2} \tag{3.4}$$

Table 3.2 shows the resulting polydispersity in r_g as the error in r_g. Table 3.3 shows the resulting size ratios for the different colloids and polymers.

System	Solvent	Colloid, R [nm]	Polymer, r_g [nm]	Size ratio, ξ
A	cis-decalin	689 ± 69	108 ± 8	0.156 ± 0.019
B	cis-decalin	533 ± 53	56 ± 4	0.106 ± 0.013
C	cis-decalin	1100 ± 110	110 ± 8	0.100 ± 0.012
D	Density-match	1122 ± 112	113 ± 8	0.101 ± 0.012

Table 3.3: The resulting size ratio, ξ, for the different systems studied in this work.

3.2.4 Preparation of Colloid Stock

Colloid stock solutions were prepared with the desired solvent and known volume fraction. This involves two processes: "washing" the colloid stock and determining the volume fraction.

Washing Washing the colloids is a simple process where one solvent is replaced with another. The colloids after manufacture are dispersed in dodecane, whereas we wish to use cis-decalin. Density matching involves replacing most of the cis-decalin with CHB. This is achieved by "spinning down" the colloid stock in a centrifuge. The centrifuge greatly accelerates the sedimentation of the particles, giving a compact sediment at the bottom of the sample vial. The excess solvent is removed and replaced with the new solvent. This process is repeated until negligible original solvent remains. This can be checked using an Abbe refractometer to compare the refractive index of the solvent from the colloid stock with the original pure solvent, to check that they are the same. When density matching, CHB is added until the colloid stock no longer sediments in the centrifuge, checked for 24 hours. When the sediment eventually forms, the sediment is weighed and the appropriate amount of excess solvent is returned to the stock to give the desired volume fraction. The rest of the solvent is retained as the density matched solvent for preparing the samples and polymer stock. Note that adding CHB to fluorescent colloids causes some fluorescence to leak out from the particles. This quantity is negligible in comparison to that in the particles and has no discernible effect of image quality.

Volume Fraction The colloid stock volume fraction is calibrated by weighing the spun-down sediment. The sediment is assumed to have a volume fraction of $\Phi_{RCP} = 0.64$, the volume fraction for random close packed large, mono-disperse colloidal particles. A related method of measuring the colloid stock volume fraction is to directly measure the height of the sediment in the sample container compared to the excess solvent. This method uses the

same assumption that $\Phi_{RCP} = 0.64$ and also it is hard to measure accurately as the spun down sediment interface with the solvent is not level, due to the sample cell spinning at an angle to the vertical. A known volume of solvent is then added to produce a colloid stock solution with volume fraction $\Phi = 0.54$. Any higher volume fraction than this and the stock is too thick to transfer with a pipette.

A more accurate method of determining the volume fraction exists by measuring the proportion of the sample that is in the crystal phase in a colloid solution in the fluid-crystal co-existence region. It is known that 0% crystal phase corresponds to $\Phi = 0.494$ and 100% crystal phase corresponds to $\Phi = 0.545$, with the proportion of crystal varying with volume fraction in a linear way inbetween. However, this technique relies on the iridescent Bragg scattering of visible light from the colloidal crystals. The particles used in this study sediment too fast to crystallise so it was not possible to calibrate the volume fraction this way.

It is possible to measure the volume fraction of a region of a colloidal suspension if the particle coordinates have been calculated from a 3-D image volume recorded with a confocal microscope. This allows an independent check of the volume fraction but is very sensitive to any uncertainty in the radius of the particles.

3.2.5 Preparation of Polymer Stock

When making up a polymer stock solution, a known mass of dried polymer is added to solvent, giving a polymer stock of concentration, C_p.

The units of concentration are mass/volume. A magnetic stirrer is added which helps to dissolve the polymer. As the concentration of polymer in a solution increases the molecules start to overlap and begin to entangle with each other. Entangled polymers will interact strongly with each other. The critical concentration, C^*, known as the overlap concentration is the concentration, at which the polymer spheres fill the sample volume. This is found from

$$C^* = \frac{3M_w}{4\pi N_A r_g^3} \tag{3.5}$$

This allows us to define the polymer volume fraction, Φ_p:

$$\Phi_p = \frac{C_p}{C^*} \tag{3.6}$$

which is the polymer concentration relative to the overlap concentration.

When making up density matching polymer stock the excess solvent from the colloid stock is used. Typically, polymer stocks were prepared with $C_p \sim C^*$ ($\Phi_p \sim 1$) to allow samples with high polymer concentrations. Shown in table 3.2 is the estimated overlap concentration, C^*, in cis-decalin for the polymers used in this work. Such a polymer stock still has very low viscosity ($\eta \sim 10mPas$) as the overlap concentration occurs at a very low mass fraction of polymer due to the very large size of the polymers.

3.2.6 Sample Preparation

Measured amounts of each component (colloid and polymer stock and solvent mixtures) are added by weight to a small 2ml cylindrical glass cell to give a sample of the desired colloid volume fraction Φ_c and polymer concentration C_p. The samples were thoroughly mixed by tumbling overnight. Thread seal tape was wrapped around the join between the lid and cell to reduce solvent evaporation. Density matched samples were stored in a dark fridge as light destabilises the CHB solvent, and the reduced temperature further reduces evaporation.

3.2.7 Estimating the Depletion Potential

In section 2.3.1 we had an expression for the depletion potential, $U_{dep}(r)$. We now want to estimate this value for the case when the particles are in contact i.e. $r = 2R$. We want to take account of the effect on the size of the depletion zones due to the high concentrations of polymer as described in paragraph 2.3.1, so the depletion potential is calculated from two parts, the overlap volume and the osmotic pressure, giving:

$$U_{dep}(r = 2R) = -\Pi_p V_{overlap} \tag{3.7}$$

where the overlap volume at contact is:

$$V_{overlap}(r = 2R) = \left(1 - \frac{3}{2(1+\xi^*)} + \frac{1}{2}\left(\frac{1}{(1+\xi^*)}\right)^3\right) \times \frac{4}{3}\pi R^3(1+\xi^*)^3 \tag{3.8}$$

We calculate ξ^* according to the method described in section 2.3.1 and Appendix A.

To calculate the osmotic pressure [8], we first need the osmotic compressibility. This is found from renormalization group (RG) theory for polymers in the full excluded volume limit as $\Pi_p \neq nk_BT$ for polymers in a good solvent, as there are correlations between the polymers.

$$\left(\frac{\partial\tilde{\Pi}}{\partial\phi_p^r}\right) = \frac{1}{\xi^3}\left(1 + 2.629\phi_p^r\left(\frac{1 + 3.251\phi_p^r + 4.151(\phi_p^r)^2}{1 + 1.480\phi_p^r}\right)^{0.309}\right) \tag{3.9}$$

where ϕ_p^r is the free polymer volume fraction and $\tilde{\Pi}$ is the dimensionless osmotic pressure.

We can now calculate the osmotic pressure by integrating the osmotic compressibility over the free polymer volume fraction.

$$\frac{\Pi_p}{k_B T} = \frac{1}{\frac{4}{3}\pi R^3}\int_0^{\phi_p^r} \alpha\left(\frac{\partial\tilde{\Pi}}{\partial\phi_p^{r'}}\right)_T d\phi_p^{r'} \tag{3.10}$$

We can now calculate the depletion potential at contact for the samples used in this work which are shown in table 3.4 along with a summary of all of the other sample values. The large uncertainty in the calculated values of the depletion potential reflects the polydispersity of the colloid particles and polymer coils. These random errors convert into large uncertainties in the volumes of the colloid and polymer which are used to calculate the overlap volume, free volume and osmotic pressure. Note that the depletion potential value we have calculated here is an upper estimate as we have assumed that the solvent is a good solvent. The solvent is actually some way in-between a theta (ideal) solvent and a good solvent and thus the contribution to the depletion potential from the osmotic pressure is most likely to be smaller than we have assumed. This systematic error in the osmotic pressure is not known, so it is not included in the error bars of the depletion potential.

3.2.7.1 Phase Diagram

The experimental colloid-polymer phase diagram in figure 3.1 shows the calculated position of all of the gel samples in table 3.4. Note the large range of polymer volume fractions covered, penetrating deep into the non-equilibrium gel region.

3.2.8 Errors

The uncertainty in the final sample composition come from uncertainties in the concentration of solvent mixture, and colloid and polymer stock solutions and, once the sample has been made, any solvent evaporation.

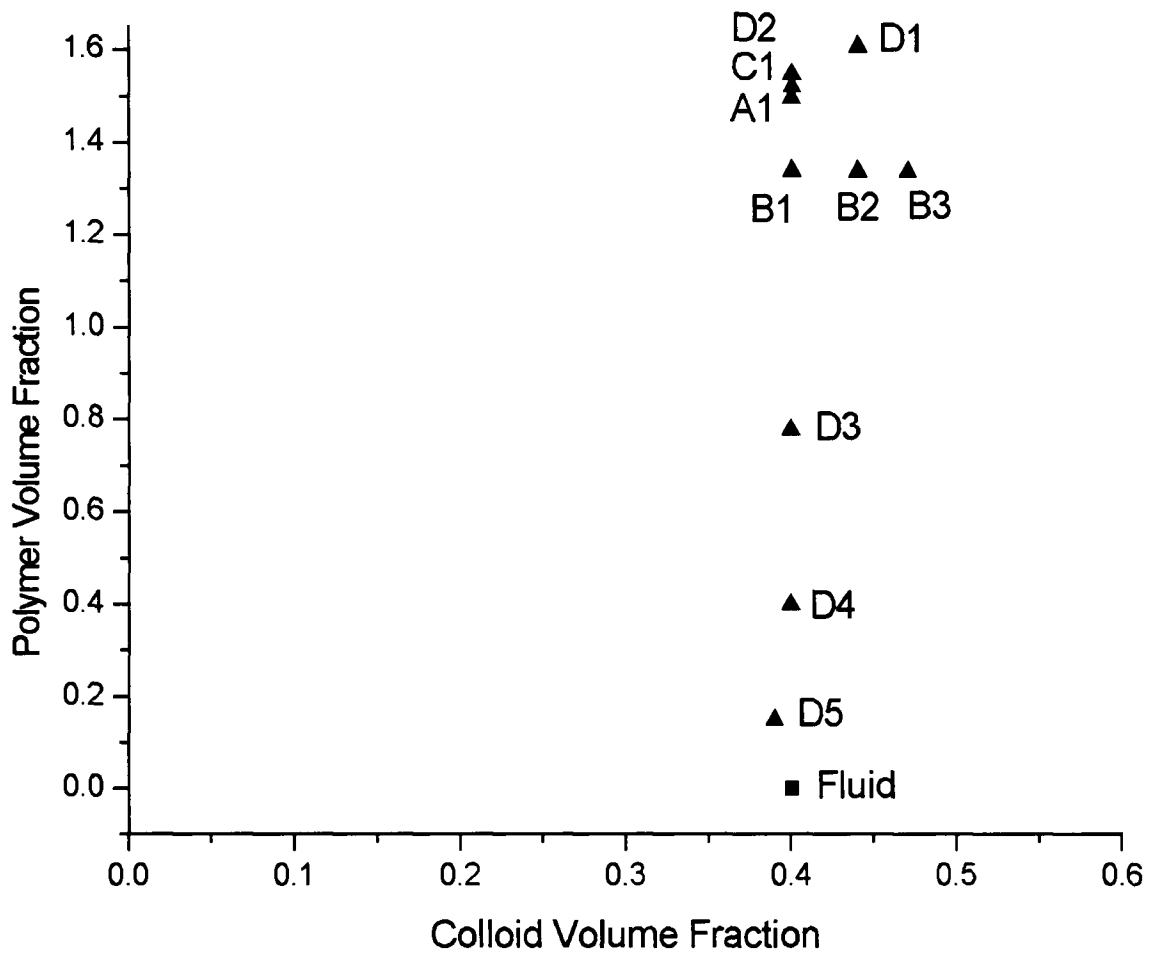

Figure 3.1: Colloid-polymer phase diagram showing the gel samples used in this work (see table 3.4, ▲ = gel, ■ = Fluid)

Sample	Solvent	R [nm]	Φ_c	r_g[nm]	Φ_p	ξ	ξ^*	$U_{dep}^{r=2R}[k_BT]$
A1	cis-dec	689	0.40	108	1.5 ± 0.11	0.156	0.052	22 ± 8
B1	cis-dec	533	0.40	56	1.34 ± 0.09	0.106	0.065	21 ± 7
B2	cis-dec	533	0.44	56	1.34 ± 0.09	0.106	0.065	21 ± 7
B3	cis-dec	533	0.47	56	1.34 ± 0.09	0.106	0.065	21 ± 7
C1	cis-dec	1100	0.40	110	1.54 ± 0.11	0.100	0.033	33 ± 12
D1	ρ-match	1122	0.44	113	1.61 ± 0.11	0.101	0.028	46 ± 16
D2	ρ-match	1122	0.40	113	1.55 ± 0.11	0.101	0.030	39 ± 14
D3	ρ-match	1122	0.40	113	0.78 ± 0.05	0.101	0.043	19 ± 7
D4	ρ-match	1122	0.40	113	0.40 ± 0.03	0.101	0.058	10 ± 4
D5	ρ-match	1122	0.39	113	0.15 ± 0.01	0.101	0.081	5 ± 2

Table 3.4: The different samples used in this work. The letter signifies which system the sample is from (see table 3.3). For each sample we show the the suspending solvent (ρ-match = density-matching mixture of cis-decalin and CHB) and values for the colloid radius, R, colloid volume fraction, Φ_c, radius of gyration, r_g (at room temperature, 295K), polymer volume fraction, Φ_p, size ratio, ξ, reduced size ratio due to the concentration effects, ξ^* and the estimate of the depletion potential at contact, $U_{dep}^{r=2R}$

Solvent Stock Uncertainty in the density matching stock comes from any uncertainty in determining its exact composition. The amount of added CHB gives an estimate of the final composition of the solvent stock, but this is not exact as the PMMA particles absorb an unknown amount of CHB in preference to cis-decalin. The solvent composition can also be calculated by measuring the refractive index of the stock and using this value to calculate the relative proportion of each solvent. This can be measured to an accuracy in $n \pm 0.002$ with an Abbe refractometer. This gives the uncertainty in the solvent mixture density of 0.15 %.

Colloid Stock The estimated uncertainty in Φ_{RCP} (± 0.01) gives a systematic error in the colloid stock volume fraction. Although samples with different colloid sizes come from different stock solutions this systematic error should be similar for all the samples as Φ_{RCP} should be very similar for the colloids used in this work. Also, there is uncertainty in the balance used to weigh RCP colloid stock and the mass of solvent added to it. It is estimated that the balance is accurate to $\pm 0.001g$ which leads to a further uncertainty on Φ_c of $\pm 0.01\%$. Volume fractions calculated from particle coordinates are correct within approximately 2.5% due to the uncertainty in the colloid radius and local volume fraction differences between different image volumes.

Polymer Stock The uncertainty in the polymer stock is mainly due to weighing errors. Most important, the very small amount of dried polymer (typically 0.1g) used gives quite a large uncertainty in C_p of $\sim 1\%$. This will only be a relative error for samples made with the same polymer stock.

Sample Composition Taking into account all the above, the accuracy in the relative concentrations of colloid and polymer in different samples is limited to weighing errors and is calculated to be $\Delta\Phi_c = \pm 1\%$ and $\Delta C_p = \pm 2\%$ ($\Delta\Phi_c = \pm 1.4\%$ including uncertainty in Φ_{RCP}).

Evaporation The seals on the stock bottles and sample cells are not perfect even with sealing tape so some solvent evaporation occurs. This was monitored by checking the weight of the bottles before they were used. Any solvent that was lost was replaced and the bottles shaken before use. Therefore, there is a negligible effect of evaporation on the sample composition.

3.3 Light Scattering Echo

In this section we describe the experimental setup and methods for our LS-echo experiments.

3.3.1 Experimental Setup

3.3.1.1 Setup

The experimental light scattering echo setup is shown in figure 3.2. The sample is illuminated from below by a helium-neon laser (Model 127 from Spectra Physics) that emits light with a wavelength of 633nm. The laser operated at a power of 20mW. The shear cell is clamped onto a horizontal table to ensure it remains in the same position throughout the experiment. The table has a cut out hole to allow the laser beam to pass through into the shear cell. The scattered light is detected in the transmission direction by a single mode fibre (from OZ Optics Ltd.), connected to an avalanche photo-diode (SPCM AQR 13-FC from EG&G) operating in the photon counting mode. One polariser (P_1) is placed between the laser and the shear cell. A second polariser P_2 orientated at right-angles to the first is placed in front of the fibre. Any residual (polarised) single scattered light is cut out, ensuring a minimum of two scattering events.

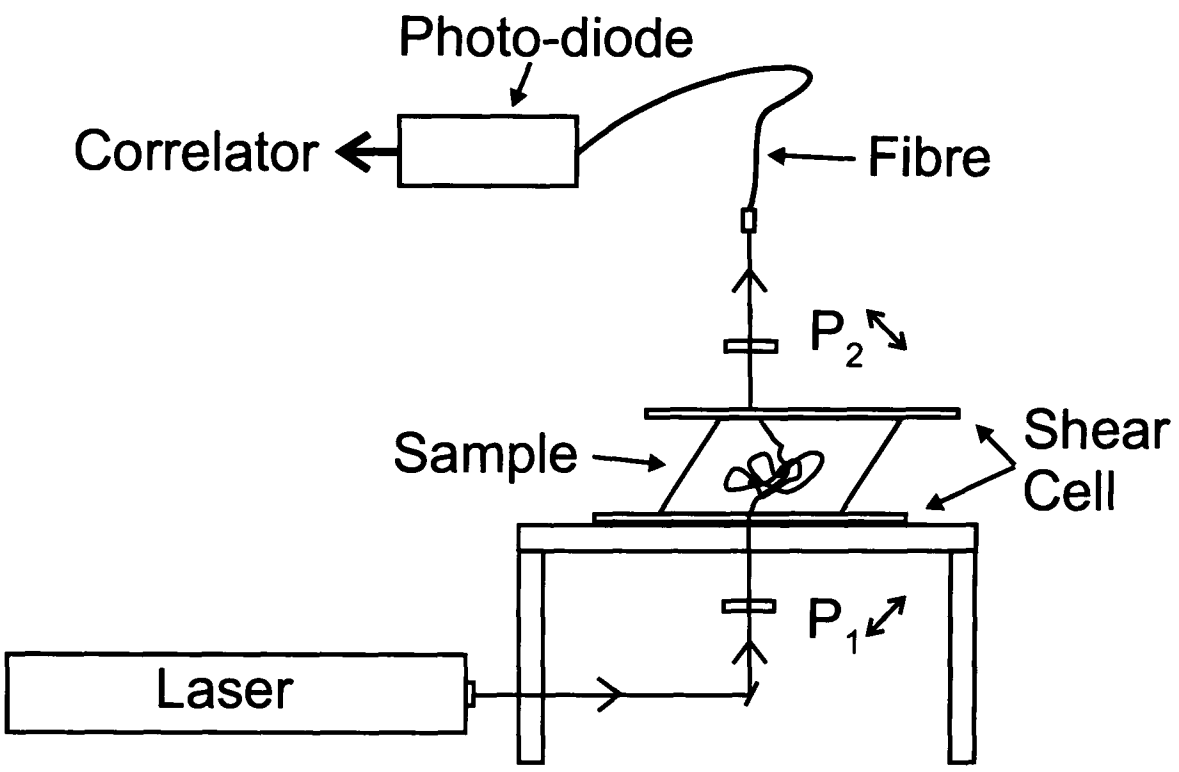

Figure 3.2: Schematic diagram of experimental light scattering echo setup showing the path of the laser beam.

3.3.1.2 Correlator

The intensity auto-correlation function is measured using a flexible correlator card, the Flex410R from Flexible Instruments, available from Correlator.com. This correlator has the essential features that a large number of channels (up to 512) can be arbitrarily distributed. A channel can be placed at any delay time, $\tau = nS$, where S is the "basic" sample time, and $n \leq 256K = 262144$ giving the maximum delay time. This means that the delay channels can be clustered around delay time $\tau = mT$. Such a customised channel layout allows accurate measurement of the narrow echos by placing a large number of channels in the small range of τ in which the echo appears.

There are a large but still limited number of channels available so a balance must be struck between the accuracy of each individual echo and the number of echos measured simultaneously. A large number of channels are also required to capture the initial decay of the correlation function of the 0th echo accurately. The width of the echos decrease with increasing strain so the channel layout must be altered to maintain sufficient points to determine the shape and maximum height of the echo. A maximum of 20 echos was found to be the practical upper limit, resulting in about 25 data points per echo. It is possible to choose which echos are measured. For example the first 20 echos could be measured or a larger range such as the first 10 echos, then the 20th, 30th, 40th, 50th, 60th, 70th, 80th, 90th ,100th and 110th echo. This allows the

echos to be studied to quite long delay times.

3.3.1.3 Scattering Conditions

If we are interested in measuring particle displacements of order 100 nm or more, we cannot allow the number of scatterings N to be too large or $\sqrt{g^{(2)}(\tau)-1}$ will decay to zero (or at least to the noise level) for displacements smaller than this. This is due to the fact that the DWS length scale (see section 2.5.2.2) is $l_{DWS} \simeq 1/\sqrt{N}k$ so if N is too large the length scale probed will be too small to be of interest. So we are forced to work with a relatively small number of scatterings where equation 2.20, derived for the full DWS (strong scattering) limit, may not be valid.

The experiments were conducted with cis-decalin as solvent. Different plate gap sizes were used to vary the scattering conditions. The transmission coefficient, T is calculated from.

$$T = \frac{\mathrm{TransmittedPower}}{\mathrm{IncidentPower}} \tag{3.11}$$

The incident power is measured with a light meter for the laser without the shear cell present. The transitted power is measured above the shear cell, at the position with the maximum intensity.

The transmission coefficient, T can be related to the light mean free path,l and compared to L, the distance the light travels, which is estimated as the plate gap size, d. The number of scattering events, N is estimated from $N = L/l$ where

$$T = exp - (L/l) \tag{3.12}$$

So for d = 0.8mm, average $T \sim 0.23$, gives $L/l \sim 1.5$. For d = 1.3mm, average $T \sim 0.08$, gives $L/l \sim 2.5$. For d = 1.8mm, $T \sim 0.04$, gives $L/l \sim 3.1$.

3.3.2 Experimental Procedures

In this part we will describe how we conducted the LS-Echo experiments. Note, these experiments were conducted with shear cell 1 (see section 4.6).

Experiments were conducted at two different frequencies, 10Hz and 70Hz. These experiments were repeated at three plate separations, 0.8mm, 1.3mm and 1.8mm. The laser was turned on about an hour in advance to allow the laser power to stabilise. The solvent bath (see section

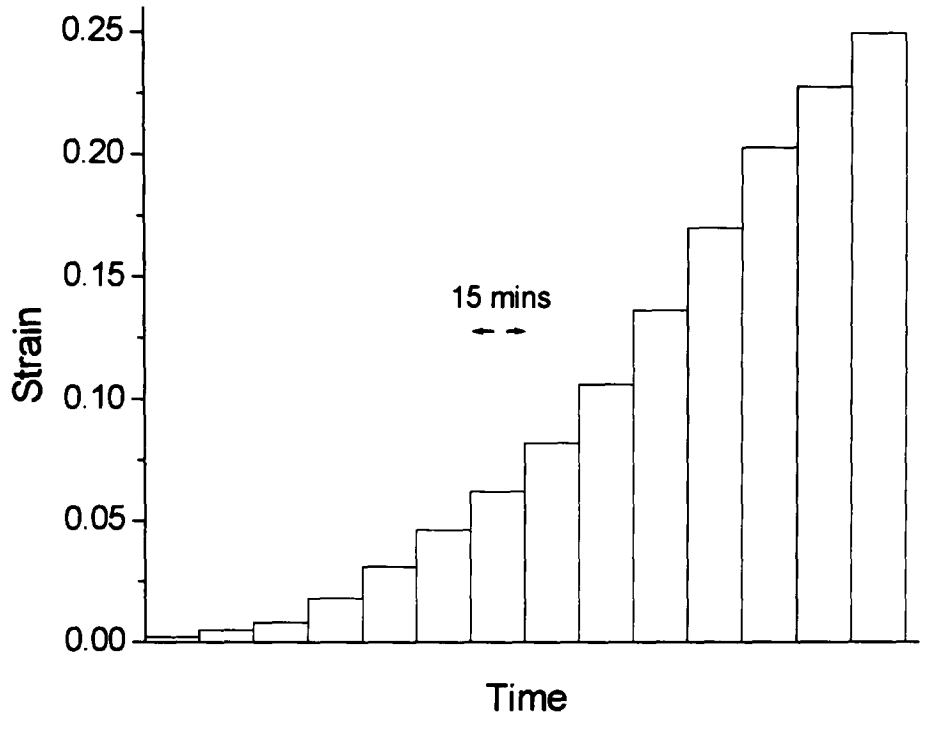

Figure 3.3: Schematic graph of typical step strain light scattering-echo experiment. Typical time at each strain was 15 minutes.

4.6.1) was filled with decalin to reduce evaporation of the sample. The sample bottle was shaken to rejuvenate the sample. The sample was then loaded with a pipette onto the bottom plate of the shear cell. The top plate was placed on top of the sample, causing it to spread out. The sample typically covered the glass window in the top plate, an area of approximately $2cm^2$. Typically experiments were started after a delay of approximately 30 minutes following loading. The strain was then increased and another set of results was obtained, see figure 3.3. Up to three sets of results were obtained at each strain. Each set of results took 5 minutes and provided data for different ranges of echos. This was repeated up to the maximum strain available. So in contrast to the microscopy measurements the sample was sheared continuously for the whole experiment and sheared for longer at each strain. (15 minutes compared to 2 minutes for a typical microscopy experiment). At the end of the experiment a light meter was used to measure the maximum transmission of light passing through the sample.

3.4 Microscopy

In this section the methods used for the light microscopy and confocal experiments are described as well as the analysis programs used for quantitative analysis of the gel structure.

3.4.1 Light Microscope

The upright light microscope used in this work was a Zeiss Axioscope FS. We use a 100× oil immersion Differential Interference Contrast (DIC) objective (Zeiss, Plan Apochromat) with a working distance of 0.17mm, and numerical aperture of 1.4. Further magnification was provided by additional 1.25× and 1.6× lens after the objective. Early images were recorded with a 40× phase contrast objective but the image contrast was found to be much poorer than with DIC. Typical phase contrast images are not shown in this work as the contrast (especially on paper) is so poor that all useful information is lost. DIC imaging has the advantage of allowing the whole field to be viewed on a monitor at video rate, in contrast to the confocal that needs scanning to produce the image. The images were obtained by digitising frames from a CCD camera (Hitachi Denshi Ltd.) with a image capture board (MuTech MV-1000) which were then displayed using the program Metamorph (Version 3.0, Universal Imaging Corporation). The digitisation process was too slow to allow video rate digitisation. The images were enhanced to increase the contrast by grey level stretching. This process involves spreading the limited range of grey levels that are present in the image histogram over the whole grey level range.

3.4.2 Confocal Microscope

The laser scanning confocal microscope (LSCM) used in this work was a Nikon Eclipse TE300 inverted microscope fitted with the Radiance 2100 laser scanning system from Biorad. This confocal microscope only became available one year after this work began. For the first year of this work only the Zeiss light microscope was available. The software used to control the microscope was Lasersharp 2000 also supplied by Biorad. The laser was a 4 line Argon ion laser emitting at 457nm, 476nm, 488nm and 514nm. The laser line we used was 488nm and from a maximum power of 5mW we typically used a power of between 1% and 5 % of the maximum available. The fluorescent colloid particles absorb strongly at this wavelength and emit over a range of frequencies above 500nm. A 500nm long-pass filter was used to separate the incident and emitted light. The 488nm light was blocked by a filter. A photomultipler

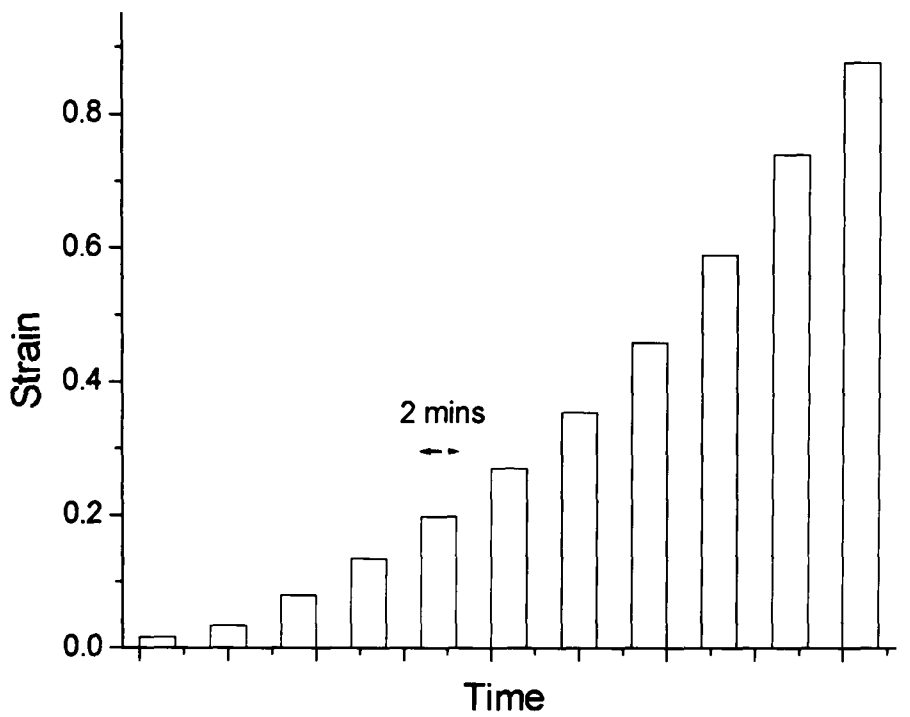

Figure 3.4: Schematic graph of typical step strain microscopy experiment. Typical time at each strain was 2 minutes

tube detects the light pixel by pixel scanning across the objective window giving an image on the computer screen that can then be digitally recorded. Both 100× and 60× Nikon oil immersion objectives were used, both with NA =1.4 and working distances of 0.13mm and 0.21mm respectively.

3.4.3 Experimental Procedures

Experiments were conducted at oscillatory frequencies of 70Hz, 10Hz and 1Hz. Figure 3.4 shows how different strains are applied to a sample in a typical experiment. The strain is steadily increased in steps but stopped each time to allow for the sample to be explored with the microscope and for images to be recorded (typical time taken $\sim$ 5 minutes). The gel structure appears frozen as soon as the shear is stopped so the structure at the end of the shear period is retained. Typically, the strain is applied for a duration of 2 minutes at each strain, although other durations were also studied. In some experiments a certain strain was immediately applied to a fresh sample. The shear direction is left to right as seen in the microscopy image figures. There is often a small amount of drift of the whole sample during shear (of order $100\mu m$). Therefore, it is not always possible to observe the same region of the sample before and after shear.

Here I will report what I found to be the best parameter settings for use with different kinds of image recording with the confocal microscope. For a frozen or stationary sample an excellent quality image may be recorded. A slow scan speed (e.g. 166 lines per second (lps)) combined with a high pixel resolution (e.g. 1024×1024 pixels) results in a typical frame aquisition time of 5 seconds. With a $100\times$ lens at the lowest computer zoom single particle resolution of colloid particles of radius $R > 500nm$ is easily possible. Use of the computer zoom allows objects of interest to be seen more easily. (Note that the computer zoom does not affect the resolution of the image.) For a sample that is not motionless then a higher scan speed or lower pixel resolution can be used to reduce the scan time sufficiently for the motion to be negligible in the image.

A z-series is a set of scans in the same horizontal location but with the height or depth within the sample changed by a small amount between each scan. Two types of z-series or stacks can be obtained in a realistic time. A small number (e.g. 30) of large, high quality images can be recorded over a wide z-range (e.g. $100\mu m$) giving an indication of how the sample typically appears at different heights. Alternatively, a large number of images (e.g. 100) can be recorded over a small z-range (e.g. $20\mu m$) which gives a digitised part of the sample volume from which 3-D information can be extracted. A good technique is to start the z-scan at the deepest point in the sample (rather than the surface) because the photo-bleaching will be largely cancelled out by the increase in brightness gained by virtue of moving closer to the surface.

Now we look at the important considerations to take into account when recording a 3-D image volume. As mentioned above, a large number of images are required compared to a z-series that gives only a snapshot of the structure. This is necessary to give sufficient number of slices per particle in the z-direction to allow the particle centres to be determined accurately. This imposes constraints on the minimum scan time for the whole stack if the individual image quality is to remain high. Experimentation has found that at least 10 pixels per particle are needed in each dimension to locate the particle centre accurately. Larger particles (e.g $R = 1\mu m$ rather than $R = 0.5\mu m$) give better quality images as less zoom is required to give the same number of pixels per particle. The particles must remain stationary during the time taken for all of the slices for that particle to be recorded otherwise the position of the sphere can not be found accurately. The larger the area imaged the larger the number of pixels that must be used to retain sufficient pixels per particle. This increases the time taken for a stack to be recorded. Typically, images are recorded with 256×256 pixels for 100 slices. This gives a volume of $\sim 50\mu m \times 50\mu m \times 20\mu m$ containing about 3000 particles ($\Phi_c = 0.4, R = 1\mu m$). Such a stack of images takes about 3 minutes to record, using the slow scan speed (166 lps)

needed to give sufficiently good images.

For a time series, a number of images are recorded in the same place with a preset time delay between each image. The main choices to be made are the same as for the individual images: a fast enough scan is needed to capture the sample accurately, but the faster the scan speed then the more noisy the image becomes. Taking quality into account, the fastest possible image aquisition time is 0.5 seconds. The only limit on the number of scans is available disk space (200 is about the current practical limit).

3.4.4 Image Analysis

The determination of three-dimensional particle coordinates from real space microscopy images is a great step forward as it enables quantitative analysis of the particle structure. The program we used to determine the 3-D particle coordinates was written by Crocker, Grier and Weeks [47],[48] and kindly given to us by Weeks. We wrote the programs for subsequent quantitative analysis of the particle structure unless otherwise stated.

Image analysis consisted of several steps which will be described in detail below. The first step was using the confocal microscope to acquire a set of image sections from a sample to give an effective three-dimensional image of the sample volume. The 2-D images were stored as a 3-D array containing the brightness of each pixel in the image volume. All further processing was conducted in the IDL programming environment which is particularly suited to image processing.

3.4.4.1 Locating Particles

The analysis described below is used to find the (x,y,z) coordinates of each particle centre in the sample volume. The IDL routine used was written by Crocker, Grier and Weeks [47], [48]. Before locating the particles from the set of 2-D image sections it is necessary to clean up the images as inevitably there will be some instrument-derived noise present. A simple noise model is used to eliminate single pixel (random) noise by convolving the image with a kernel that attenuates the high frequencies as desired while preserving the edges. The alternative approach of low-pass filtering has the disadvantage of introducing blurring of edges. Other filtering operations could be applied at this stage if desired.

The filtered set of images can now be processed to find features, which are in our case spherical particles. It is worth noting at this point that the image of a spherical particle is usually distorted

in shape by the imaging system. In this case, the main distortion is that a spherical particle is distorted into a ellipsoid (egg shape). Also, non-cubic pixels are sometimes used. This is caused by there being fewer pixels per particle in the z-direction than in the x-y-direction leading to a squashed sphere. It is important that the algorithm takes these effect into account when finding the location of the particles.

The algorithm developed by Crocker, Grier and Weeks used to determine the particle centres can be divided into two parts which are only briefly described here. Further details can be found in [47]. Firstly, the (3-D) image is searched for local brightness maxima, where the "local" scale is defined by the first parameter *separation*. The separation, which specifies the minimum permissible separation of particle centres. Each maximum is assumed to correspond to a particle. The second parameter, *diameter*, describes the extent, in three dimensions, of the image of a particle, which may be larger but usually similar to $2R$. This parameter is used in the second part of the algorithm where for each local maximum in turn, a three-dimensional region of extent diameter around that point is considered. The particle centre for that maxima is identified as the centroid position of the bright points in the region.

Before image analysis can be conducted any particle with their centre within a layer of thickness R of the outer edges of the image volume are discarded. Any particles detected within this layer are likely to have inaccurate coordinates of the centre. It is likely that part of the image of the particle will be missing of the edge of the recorded volume. The algorithm will find the centre of the bright region assuming it is the whole particle, whereas the real centre of the particle is further out toward the edge of the image. This results in a shift in the position of the particle centre toward the centre of the image volume. Such particles are inaccurate and are removed with this routine.

A whole host of quantitative structural analysis techniques become available once the particle coordinates have been obtained from the real space image. However, it is also very useful to reconstruct a 3-D picture of the sample. Ray-tracing software (e.g. POV-ray, www.povray.com) can be used to produce a high quality picture of the sample. A sphere is placed at each of the determined particle locations. A position for a virtual camera is specified along with the position in the sample volume at which the camera is pointing. The desired lighting of reconstructions is also specified. This allows the sample to be viewed from any angle, a useful feature allowing the study of planes that can't be imaged directly. Also, the spheres can be colour-coded or excluded altogether depending on the value of some calculated parameter. For example, different colours could correspond to the particle having different numbers of neighbours.

Quality checking procedures In practice, especially for dense systems of particles, high quality images are required along with a process of experimentation to find the parameters that give the most accurate results. It is therefore important to have methods to check the accuracy of the particle coordinates, as well as to ensure that significant numbers of particles are not missed or false postives included. These procedures aided the determination of the best parameters and a qualitative idea of what defines a sufficiently high quality set of images.

Once the particle features have been located in an image volume two types of checks are possible to ensure the accuracy of the results. Firstly, it is important to check if any particles in the image volume have been missed entirely or if any false positives have been introduced. Overlaying a black dot at the nearest pixel to the particle centre on the original set of 2-D images gives an easy way to check this "visibly". This procedure was written by Weeks [48]. This is sensible when finding the best parameters for a particular system. However, this is too time-consuming for use with every image volume. Measuring the volume fraction and comparing it with the value calculated for the sample gives a quick method of routing out sets where the image analysis has gone badly wrong. This is usually due to a problem with the quality of the original image stack.

The particle coordinates of the features located can be checked by seeing if any of the particles would overlap with each other. This situation is not physically possible so finding overlapping particle indicates that a particle position is inaccurate.

Errors in particle coordinates The particle centroids are resolved with an error of $\pm 40nm$ in the lateral (xy) axes and $\pm 50nm$ (corresponds to $\pm 1/2$pixel). Higher accuracy is possible for well separated particles [20] but in this work the particles are in a dense suspension and often in contact with other particles. Accuracy is found to be reduced for particles in close contact.

3.4.4.2 Quantitative Analysis

Determination of the particle coordinates allows the kind of quantitative analysis of an actual real space sample normally restricted to computer simulations.

Radial Distribution Function (RDF) A very common measure of the structure of a sample is the pair distribution function (or radial distribution function). This is a measure of the

average density of particles as a function of distance from some arbitrary particle. For a given particle centre, g(r) describes the number of particles at a distance r away compared to the number at the same distance in an ideal gas at the same density. As the image volume is not spherical in shape the normalisation is increasingly inaccurate when the parts of the shell volume fall outwith the image volume. This leads to g(r) < 1 for high r. This error is complicated to correct and therefore not attempted here. The 3-D RDF can be calculated quite easily with IDL using a procedure written by Matthew Jenkins.

Important parameters include the number of bins used. A larger number of particles in the input file allow a larger number of bins to use, increasing the accuracy of g(r) while retaining a smooth curve. Due to the finite extent of the sample volume, half of the smallest dimension (typically the z-direction) gives the upper limit on r.

The two extreme cases of a disordered liquid and an ordered crystal illustrate the main features of g(r). In a crystal, there are certain separations at which a particle is more likely to be found (the so-called "nearest neighbour shells") which show up as peaks in g(r). In between the shells particles are less likely to be found there on average, which is reflected as minima in g(r). In a liquid, there is short range order. Any small group of particles will be in a fairly regular array and will resemble the local packing found in a crystal lattice. This leads to a strong first peak in g(r) and deep first minimum. But if more than a little distance from a group in a random direction then the neighbouring particles no longer possess long-range order characteristic of a crystal. Within a couple of radii, R, g(r) flattens out to the average density of 1.

2-D pair distribution functions can also be calculated with code very similar to the 3-D RDF. We adapted the 3-D RDF procedure written by Jenkins. This can be used to look at the local structure of 2-D planes. To make a 2-D plane from a list of 3-D particle coordinates a plane is specified (x-y, y-z or x-z) with a specified thickness. A thickness of $4R/3$ was found to achieve the best accuracy in including genuine in-plane particles. All particles within this thin slice are taken to be in the same plane, leaving for example just the (x,y) coordinates for a x-y plane.

A 1-D distribution can be calculated aswell in a similar way to the 2-D and 3-D cases. For this a line of particles is needed with only a 1-D coordinate. Again, this code was adapted from the 3-D RDF procedure written by Jenkins. The code allows a line to be selected from a 2-D plane at an arbitrary orientation angle, ϕ.

Number of Neighbours The "neighbours" of a particle are identified by their separation. g(r) shows a well defined minimum at $r = r_c$, where r_c is slightly larger than $2R + 2\Delta$ (the

range of the depletion potential). Particles with separation less than r_c are defined as being neighbours. An alternative approach would be to use the depletion potential range as the cutoff distance of a particle "bond". However, the range of the potential depends on Δ (see section 2.3.1 and Appendix A), which is not precisely known. Also, the range varies between different polymer concentration gels making direct comparisons problematic. The distribution of the number of neighbours and the mean neighbour number are important structural characteristics of a gel. A simple IDL procedure was written to calculate the number of neighbours for each particle in the sample volume. This code was adapted for use with 2-D planes.

It is possible to calculate the orientation angle in polar coordinates (ϕ, θ) of each neighbour for every particle. This gives the probability of finding neighbours at varying orientation angles averaged over the whole volume (plane). For a 2-D plane only a single orientation angle, ϕ is needed.

Remoteness In colloidal gels, voids of various sizes are present within the particle structure. The distribution of void sizes is an interesting quantity to measure. However, it is not just a simple case of measurement as the voids inter-penetrate and are complex shapes. Arbitrary choices would have to be made as to what constituted the extent of a void. This problem can be by-passed by instead measuring the "remoteness" [49]. The remoteness is the distance to the nearest particle from all points on a grid superimposed on the sample volume. If the remoteness is large this means that the nearest particle is a large distance away and therefore the existence of a large void can be inferred. The distribution of remoteness is only an indirect measure of the distribution of void sizes.

Chapter 4

Shear Cell

4.1 Introduction

In this chapter we discuss the design, development and testing of the shear cells used in the oscillatory shear experiments in this work.

4.2 An Ideal Shear Cell

4.2.1 Geometry

A parallel plate geometry was chosen as it would be possible to use it with a standard microscope in contrast to a Couette geometry. A linear geometry was chosen as a simple shear profile is the most elementary to understand theoretically. For LS-Echo and microscopy the linear geometry imposes a constant strain through out the whole sample. In contrast, a rotating geometry would give a varying strain in the radial direction of the cell.

The ideal linear geometry oscillatory shear cell is made up of two flat, parallel plates that move with a fixed oscillation frequency in opposite directions in a precise reproducable way inducing a simple shear profile on the sample. The strain is varied by either changing the amplitude of the movement of the plates in the horizontal direction or by changing the gap between the plates. The frequency should be variable. The two plates should be separately controllable as this allows for a larger total plate amplitude and allows the position of the zero movement plane to be adjusted.

The shear rate as defined in equation 2.15 is not constant in an oscillatory shear experiment unlike in a typical rheometer. We define the maximum strain amplitude γ_0 as:

$$\gamma_0 = \frac{A_1 + A_2}{2d} \tag{4.1}$$

where A_1 and A_2 are the amplitudes of the upper and lower plates respectively and d is the plate separation.

The average shear rate $< \dot{\gamma} >$ can be estimated from the oscillation frequency, ν and the strain amplitude , γ_0 imposed on the system, where $\gamma(t) = \gamma_0 sin(2\pi\nu t)$. The strain varies during one period from 0 to γ_0 as the plates are driven with a sinusoidal function. We use the root-mean-square (rms) value of the strain to estimate the average shear rate:

$$< \dot{\gamma} >= \sqrt{2}\pi\gamma_0\nu \tag{4.2}$$

4.3 Constraints

The main design criterion is for the shear cell to be suitable for experiments with both the LS-Echo setup and microscope. There are some general constraints that will be covered first then the specific constraints associated with the different microscopes and the LS-Echo setup will be considered.

4.3.1 Piezo Motor Constraints

The piezo motor gives precision oscillatory movement over a large frequency range 0 to 100Hz. The limited maximum amplitude of $100\mu m$ is the main restriction on the rest of the shear cell. The addition of a lever can increase this amplitude substantially. This restricts the strain range to $\gamma_0 < 1$. This fixes the gap size of the plates to be about between 0.1 and 1.0mm. The piezo can only push with a limited force so any restoring force used to move the plate in the opposite direction cannot be larger than this in magnitude.

4.3.2 Parallel Plates

The plates are constructed out of microscope slides or coverslips. The plate next to the microscope objective must be a coverslip. These are flat and, most importantly, transparent. These

slides come in a limited range of sizes the largest being approximately 6cm by 2cm. This must be surrounded by a strong supporting structure to keep the plates in a fixed position and to prevent cracking and bending of the glass. There must be some way of ensuring the two plates remain parallel or can be adjusted in such a way as to make them parallel. This is to ensure a constant gap (and strain) between the plates throughout the shear cell.

4.3.3 Variable Gap Size

Different gap sizes are desirable as the requirements for LS-Echo (multiple scattering by the sample) are the opposite to that needed for microscopy (as little multiple scattering as possible). The gap between the plates must be precisely set.

4.3.4 Solvent Bath

The shear cell is open at the sides so to reduce solvent loss it is desirable to have some form of solvent bath surrounding but not in contact with the sample. This solvent bath saturates the local atmosphere preventing solvent evaporation from the sample and any resulting change in composition.

4.4 Microscope Specific Constraints

We will first consider the constraints associated with the upright light microscope as this geometry and type of microscope impose the strictest conditions. We will then consider any differences in the constraints encountered with the inverted geometry and confocal type of microscope.

4.4.1 Upright Light Microscope

4.4.1.1 Microscope Geometry

The microscope geometry is very important with an upright microscope. The vertical space available to the shear cell is very limited with this type of microscope. The extra magnification lens and the objective housing all reduce the space. When the objective is focused on the sample, the image quality is heavily dependent on the position of the condenser. The condenser

is optimally set up with a method called Kohler illumination. This ensures that as much of the light passing through the condenser illuminates the sample in a uniform way. For high magnification objective lenses the condenser must be placed within a few millimetres of the glass below the sample to achieve Koehler illumination. Therefore, the bottom plate must be constructed to allow the condenser to approach closely to the glass on the bottom plate. The condenser can only rise a few millimetres above the height of the microscope stage so the glass part of the bottom plate must be very close to the stage. This means that the bottom plate must be quite thin and only just clear the stage.

The microscope stage is only a limited size and imposes a constraint on the size of the shear cell. The shear cell can overhang the sides of the stage but the cell must be balanced so as to be stable during the experiments. An alternative is to use a purpose built table to replace the stage. Such a table was constructed but was found to be very susceptible to vibrations from the surrounding environment. The microscope stage in contrast is very well damped and does not suffer from this problem.

4.4.1.2 Shear Cell Plates

There are two plates that must be transparent. High quality glass slides and coverslips are readily available but only in certain fixed sizes. Although microscope slides can be cut to a smalller size, coverslips are too fragile. It is necessary to use a coverslip (typical thickness $\sim$ 0.1mm) between the sample and the objective. The objective is corrected for use with a coverslip. The objective would be unable to focus through thicker glass due to the small working distances of about 0.2mm for high magnification lenses. The choice of glass between the condenser and the sample is less critical but a microscope slide (typical thickness $\sim$ 1mm) is very strong compared to the thin and fragile coverslip. Also, two coverslips could be distorted by the sample, bending them and altering the gap between the plates. Such an arrangement of two coverslips would have been desirable as it would allow the sample to be viewed from both sides. It is important that the plates are sufficiently parallel that the sample stays within the view of the microscope. The action of compressing the sample between the two plates induces a flow if the plates are not parallel.

If the gap is too large then there is so much scattering of the illuminating light from the condenser that the image quality is drastically reduced. It was found experimentally that a gap less than $500\mu m$ was needed to give sufficient image quality. A sufficient gap is needed to allow one to image bulk behaviour away from the plate surfaces.

4.4.2 Inverted Confocal Microscope

The inverted microscope presents fewer constraints on the design of the shear cell. The major difference is that the objective is mounted below the shear cell so the coverslip must be mounted on the bottom plate. This also means that the shear cell must be designed to allow the objective to touch the coverslip on the bottom plate, which is necessary for oil immersion. The microscope stage is much larger so there is more space available for the shear cell. The condenser has a long working distance so there are no significant restrictions on the height of the shear cell. When using the confocal microscope the image is formed from reflected light so the thickness of the sample is no longer an issue.

4.5 Light Scattering Echo Shear Cell Constraints

Use with the light scattering setup imposes some constraints on the design of the shear cell. These constraints are not as severe as those for microscopy but they are still important considerations to take into account when making a shear cell.

The laser beam must be able to pass through the sample in the vertical direction. Therefore, the shear cell plates that enclose the sample must be made of high quality optically transparent glass.

A compromise must be struck between maximising the available strain (the smaller gap the better) and having sufficient multiple scattering to get a good signal to noise ratio for the detector (large gap needed).

The plates undergoing oscillatory shear must return to precisely the same position after each period of oscillation. The LS-Echo method relies on the assumption that any variation in the scattering intensity from one period to the next is due solely to particle rearrangements. So there must not be any wobbling of the plates during the oscillations as this would lead to a false detection of particle rearrangements. So, this ensures that any drop in the height of the echos is due to the sample rather than the shear cell.

The timescale studied in the experiment is limited to shorter than the timescale associated with the Brownian motion of the particles. Brownian motion will lead to a decay in the height of the echos to zero without any shear induced rearrangement being involved. Therefore, to study the effects of shear as many echos as possible must be fitted into the short space of time before the

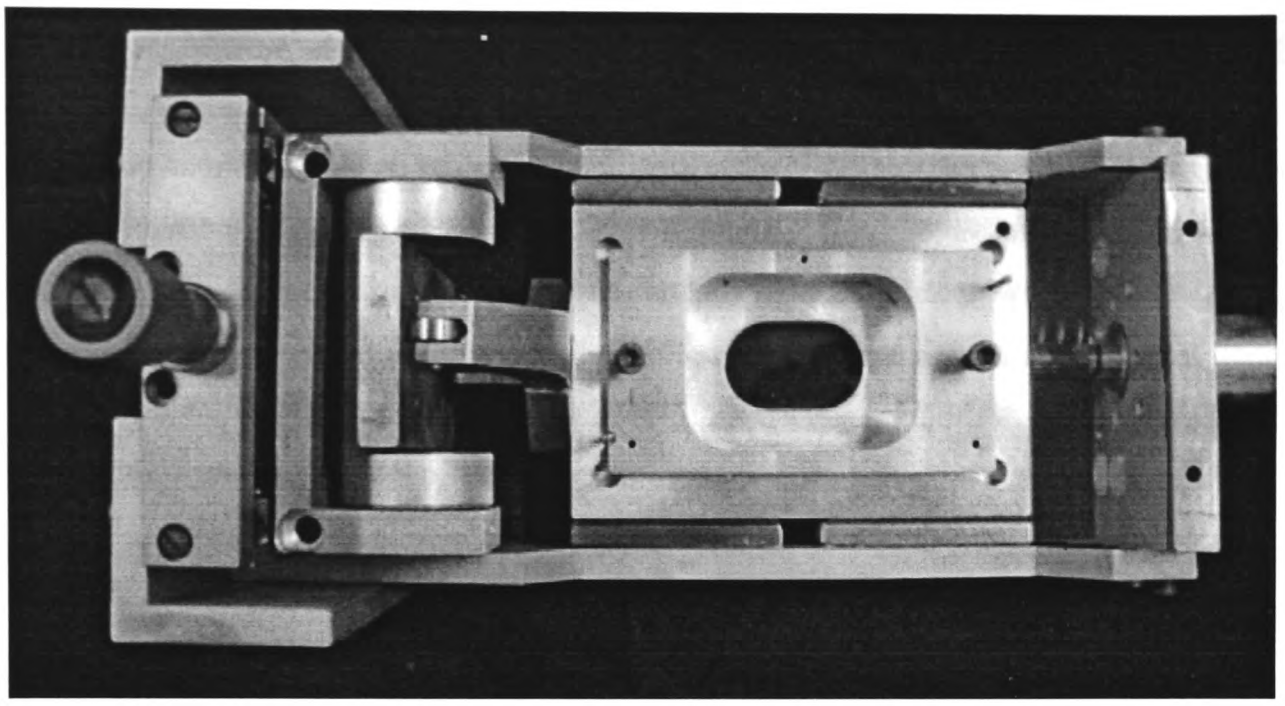

Figure 4.1: Photos of Shear Cell 1: Top: shear cell with top plate in place, top plate shaped to allow microscope objective to touch the coverslip. Bottom left: lower plate with ball bearings placed in holes cut in microscope slide, surrounded by solvent bath. Bottom right: Top plate can be removed for loading of the sample, note coverslip is glued on underside.

effects of Brownian motion become apparent. So as high a frequency of oscillation (minimum period between echos) as possible is desirable.

4.6 Shear Cell 1:- Optical Microscope Model

4.6.1 Design

Figure 4.1 show photos of the shear cell designed for optical microscopy (upright) and LS-Echo experiments. I will describe the main features with reference to the constraints discussed above. The shear cell was purpose built in the School of Physics Workshop. This shear cell

was based on an earlier bulkier version developed by G. Petekidis that was only used for light scattering experiments. Shear cell 1 was the first to be able to be used with a microscope.

The shear cell consists of two plates that are connected to an aluminium frame by precision ball slides (two per side for each plate). They ensure smooth, low friction movement of the two plates. The size of the ball slides limits how close the plates can get together and the horizontal size of the plates.

The frame is slightly longer than the microscope stage so overhangs slightly. The lower plate is a single piece of aluminium with a rectangular hole in the centre covered with a microscope slide. A thin channel surrounds the glass slide serves as a solvent bath. The top plate comes in two pieces: an outer part connected to the ball slides, and an inner removable part slightly larger than the coverslip attached to it. Four holes cut near the outer edges of the microscope slide contain size-graded ball bearings upon which the top plate coverslip sits. Two pins fix the inner top plate firmly in position.

A lever connects the two plates. The lever is added to increase the total amplitude of the plates and thus increase the total strain available. The lever ratio is adjustable with a micrometer. The lever is connected to the top plate by a steel rod topped with a roller on one end and bolted to the plate at the other. The expected lever ratio amplitude is not necessarily obtained as extra resonances are created. For certain settings of the lever, the bottom of the lever can be below the frame of the cell. So when used with the microscope this part of the cell must be hanging off the stage, restricting how much the cell can be moved about under the microscope.

There is a hole in the frame to allow the piezo motor to push against the bottom plate. A spring is placed between the frame and the top plate, above the piezo to return the top plate (not driven by the piezo) to its original position. The spring constant of the spring has to be sufficiently high to ensure this.

The four ball bearings used come in four sizes: 1.5mm, 2.0mm, 2.5mm and 3mm. As they are placed in holes made in the microscope slide attached to the bottom plate, the actual gap between the plates is the ball size with the microscope thickness (1.2mm) subtracted, as the inner top plate rests on top of the four ball bearings. So the available plate gaps are 0.3mm, 0.8mm, 1.3mm and 1.8mm. The balls roll between the plates during the shear. Providing the microscope slide is parallel to the metal bottom plate it is attached to then the balls keep the two plates parallel. The inner top plate is set into the bottom plate. There is sufficient space for the top plate to move in the horizontal direction during shear for it to avoid hitting the edges of the bottom plate. The glass slides are attached to the plates using ultra-violet (UV) cured glue.

This glue remains liquid until cured with UV light. Heating with a hot air gun thins the glue giving a less viscous glue. It is important to have an even distribution of glue to keep the glass parallel to the metal plates. This is especially important for the slide attached to the bottom plate. The parallelicity of the plates (even-gluing test) is tested by placing solvent between the glued plates. As the solvent has a much lower viscosity than typically colloid samples if the plates are not sufficiently parallel then the drop of solvent will move to the edge of the plate. If the solvent drop remains in position then the plates are sufficiently parallel.

4.6.2 Vibrations

The oscillation of the piezo motor causes the whole shear cell to vibrate when high frequencies are used. This becomes quite severe at high plate amplitudes which can impose a limit on the available voltage of the piezo that can be used. This limits the maximum amplitude and therefore strain that can be achieved with the shear cell.

4.6.3 Fitting the Microscope

The inner top plate has a bath like shape with a hole in the centre and the coverslip glued below. There is enough space for the objective to touch the upper surface of the coverslip. The only problem with this is that the end of the objective can not be seen as it is lowered toward the coverslip. Therefore, considerable care must be taken with high magnification lens that must almost touch the coverslip to avoid bending or breaking of the coverslip. The condenser is accommodated by a large enough hole in the bottom plate to allow it to almost touch the bottom side of the microscope slide on the bottom plate.

4.6.4 Driving the Shear Cell

The motor that makes the plates move in all the shear cells discussed in this chapter is a piezo-electric actuator (close-loop LVPZT translator P841.60, Physik Instruments). It has a linear response to an input voltage giving a maximum amplitude of $100\mu m$ at 12V. The position of the piezo can be altered with a DC offset and oscillated with a sinusoidal voltage input.

The piezo controller (LVPZT amplifier module E-505 and PZT servo-control module controller, from Physik Instruments) takes in the signal from the function generator and uses it to control the piezo. There is a feedback signal from the piezo to ensure a precise motion is obtained.

A precision function generator capable of locking the frequency precisely is needed for the LS-Echo experiments. The function generator was the TG1010 manufactured by TTi. The frequency, sinusoidal controlling voltage and DC offset were set on the frequency generator and fed into the piezo controller.

4.7 Shear Cell 2 :- Confocal Microscope Model

The confocal microscope provides superior image quality and optical slices of the sample. However, Shear Cell 1 was not designed for use with the inverted confocal microscope in our lab that became available at the end of the first year of this work. Shear Cell 1 was designed around the Zeiss upright microscope whereas the Nikon confocal was an inverted microscope. In contrast to the upright microscope, the objective lens is positioned below the bottom plate in an inverted microscope. For high magnification objectives only a thin coverslip can be used on the bottom plate, between the objective and the sample. For Shear Cell 1 to work with the inverted confocal microscope the microscope slide would have to be replaced by a coverslip. The problem with this was that for Shear Cell 1 the replacement of the microscope slide on the bottom plate with a coverslip removed the means of calibrating the plate gap. We would be prevented from the use of the ball bearings to set the gap between the plates and maintain the plates in a parallel position. This is due to the fact that the balls must be placed in holes in the microscope slide bottom plate, but a coverslip is too thin and fragile to allow suitable holes to be made. As Shear Cell 1 was unsuitable a new shear cell was needed before shear experiments could be conducted with the new confocal microscope. Given this opportunity a more versatile shear cell was constructed by the School of Physics Workshop. Photos of Shear Cell 2 are shown in figure 4.2. Both the top and bottom plates contained removable centre parts containing the glass plates. The idea behind this was to have more than one set of inner plates. This would give a backup set of plates if the glass on one set was damaged. Also, different sets of plates could be set with different gaps. The shear cell could be used either with an inverted or upright microscope depending on which plate set was used.

The basic shape of the shear cell frame was the same. Although the cell was slightly wider as the inverting microscope stage was bigger. The plates were mounted on thin metal rods in addition to the precision ball slides. The rods were initially used as a simpler alternative to the ball slides, but they did not offer the smooth motion required so ball slides were added. The spring in this case were placed on the metal rod. A lever was again used but it only had three fixed positions rather than a continuously variable range with a micrometer. The piezo pushed

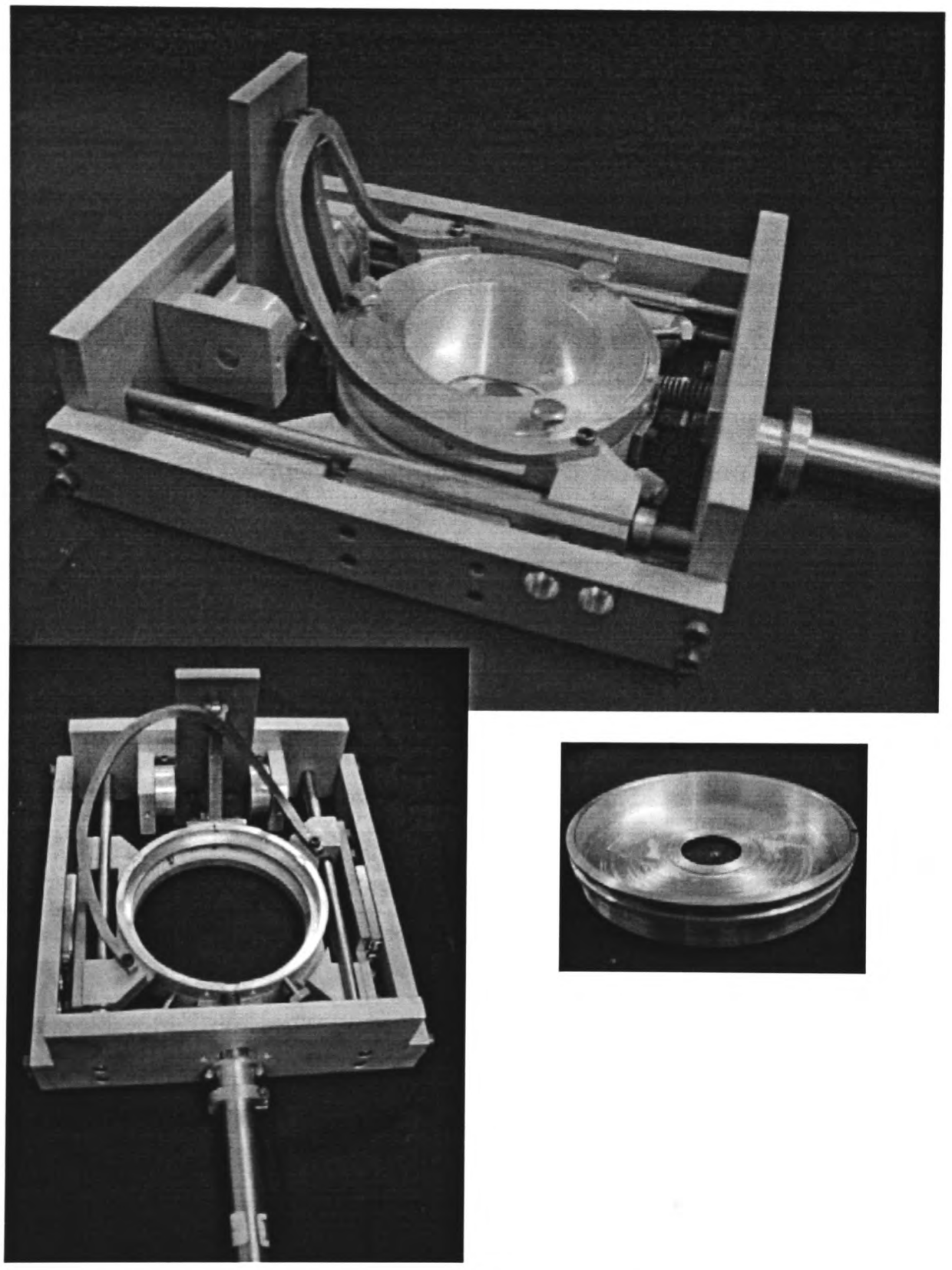

Figure 4.2: Photos of Shear Cell 2. Top: Shear cell with both plates in place. Bottom left: Both inner plates removed from cell. Bottom right: lower inner plate with coverslip.

the top plate rather than the bottom plate.

Each plate had a removable circular inner section. The inner part of the top plate resembled an inverted top hat with a hole and had attached to it a microscope slide. The bottom plate resembled a flat plate with a raised edge and a hole in the centre covered with the coverslip. The inner bottom plate was securely attached in a precise manner to the outer plate with three pins. The inner plate had a V-shaped groove on its outer edge, into which two pins fitted. The third pin was adjustable and used to lock the inner plate in place. The top plate had three vertical screws which rested on the edged of the outer top plate. A screw came from the side of the outer top plate holding the top plate in place.

The height of the screws was finely adjustable and were used to fix a desired gap between the two glass plates. As the three screws could be adjusted independently the plates could be made parallel by ensuring that the three screws all gave the same gap between the plates.

4.8 Shear Cell 3 :- Alternative Confocal Microscope Model

A third new shear cell was designed from scratch to give the simplest design possible with the smallest number of moving parts, see figure 4.3. Ease of construction was also an important consideration as, for example, the correct fitting of the linear ball slides to the frame and the plates was very complex. This shear cell was designed only for use in an inverted microscope. This simpler design gives a shear cell that is relatively free from resonances. Shear Cell 3 was constructed by the School of Physics Workshop.

4.8.1 Design

This shear cell retained the aluminium frame of the other shear cells but the plates and how they are attached to the frame is different. The bottom plate is made from copper clad glass epoxy printed circuit board. It is extremely flat and therefore suitable for mounting the coverslip on. This is screwed to a plastic frame forming the whole bottom plate. The inner part of the top plate is the same backing board with a microscope slide attached, this is screwed onto a smaller plastic frame that sits inside the rest of the top plate. The inner part also contains three screws used to alter the gap and keep the plates parallel. The two plates are attached to the outer frame by two thin metal rules on each side of each plate. These act as supports and restoring springs in one. A lever connects the two plates. When the piezo is pushed against the bottom plate the

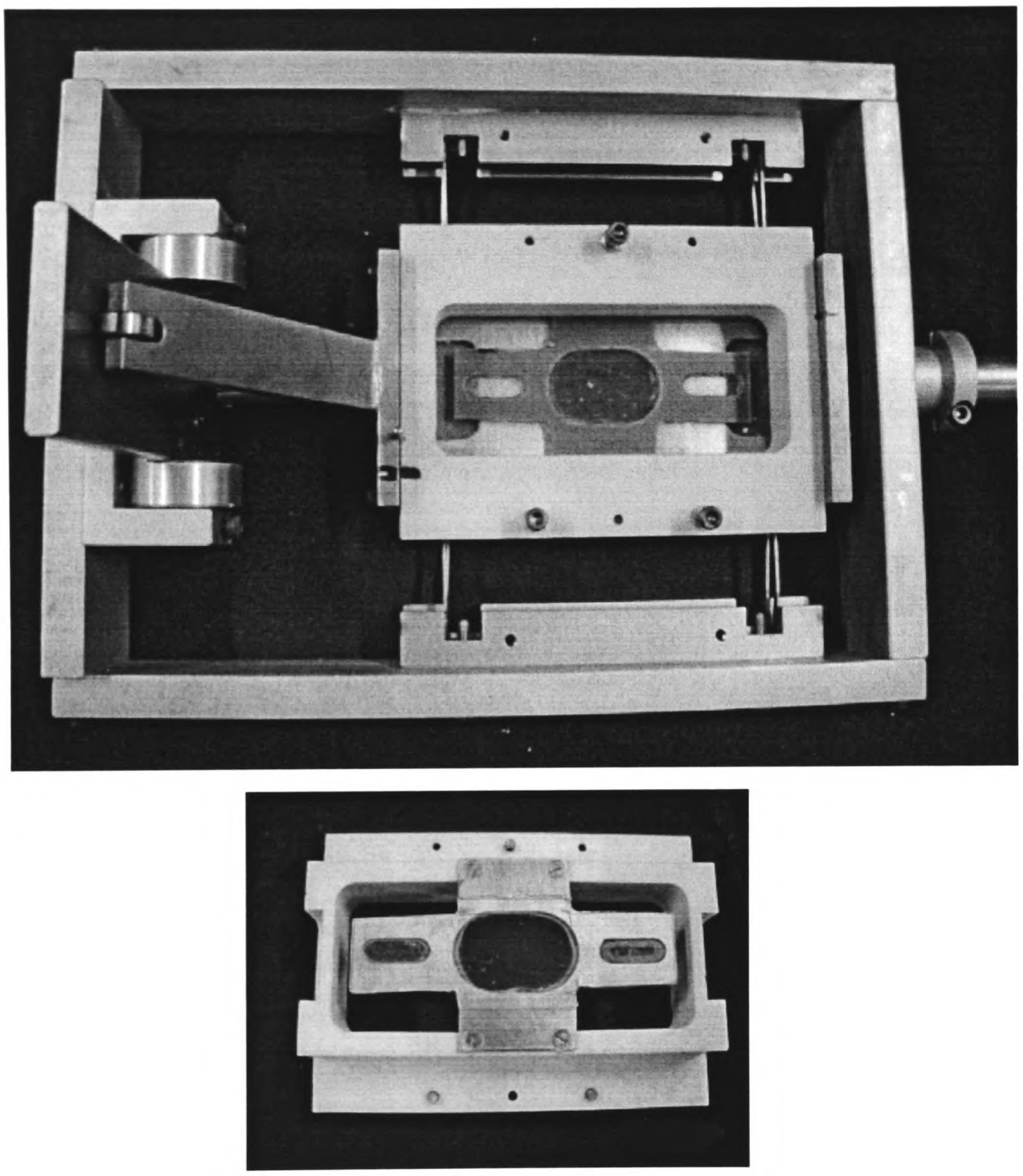

Figure 4.3: Photos of Shear Cell 3. Top: Shear cell with top plate in place. Bottom: Top plate with microscope slide attached.

rules are pushed slightly to the side giving a restoring force. The rules are spark welded to the plates and frame.

4.9 Equipment Testing Methods and Results

The shear cell was calibrated and tested before any experiments were conducted. The calibrations were tested at regular intervals as the amplitude of the plates could not be monitored during the experiment. Tests were conducted on the amplitude of the two plates with changing voltage and frequency of the piezo motor. For shear cells 2 and 3 the plate gap was calibrated.

4.9.1 Plate Amplitude Calibration

4.9.1.1 Testing Method

A microscope is used to view the shear cell plates. A ruler slide etched with a scale from 0 to $100\mu m$, in intervals of $10\mu m$ was attached to the plate being calibrated. The ruler was magnified with a $10\times$ objective and viewed on a monitor ($10\mu m$ corresponded to 5mm on the monitor). The piezo was set at a particular frequency and voltage and the resulting plate amplitude was measured. At low frequency the actual movement of a particular point on the ruler could be measured. For higher frequencies (greater than $\sim$ 10Hz) the ruler moves so fast this is not possible. Instead, the two extreme positions of the ruler can be seen overlapping but flickering. When the monitor refresh rate is synchronized with the oscillation frequency a frozen image is seen of the two extreme positions and the difference between them gives the amplitude of the plates. For example if the $20\mu m$ bar is overlapping with the $40\mu m$ bar, then the plate has an amplitude of $20\mu m$. This is repeated for each plate giving a total amplitude of the two plates for varying voltage at a particular frequency. The amplitude is converted to a strain giving a strain versus voltage plot that can be referred to during the experiment. We assume that the absence of a sample between the plates gives the same results as when the sample is present.

4.9.1.2 Typical Results

Here I show typical results for the calibration of the 1st and 3rd shear cells.

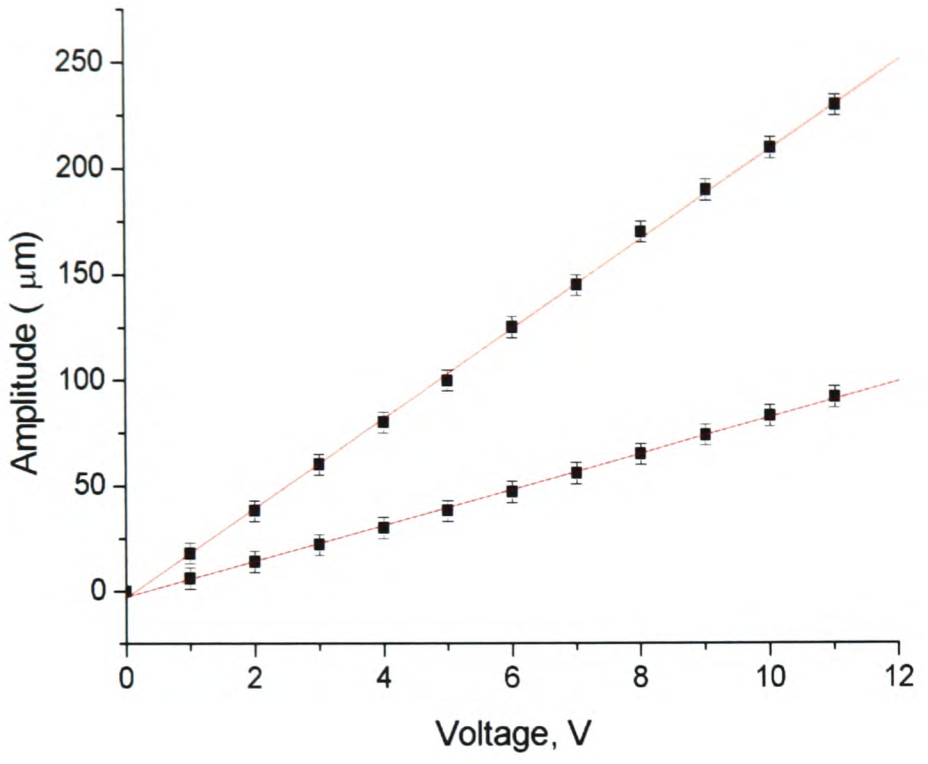

Figure 4.4: Amplitude vs Voltage top and bottom plate for 70Hz, Shear Cell 3, • = Bottom Plate (piezo driven), ■ = Top plate (lever driven). Solid lines = linear fits

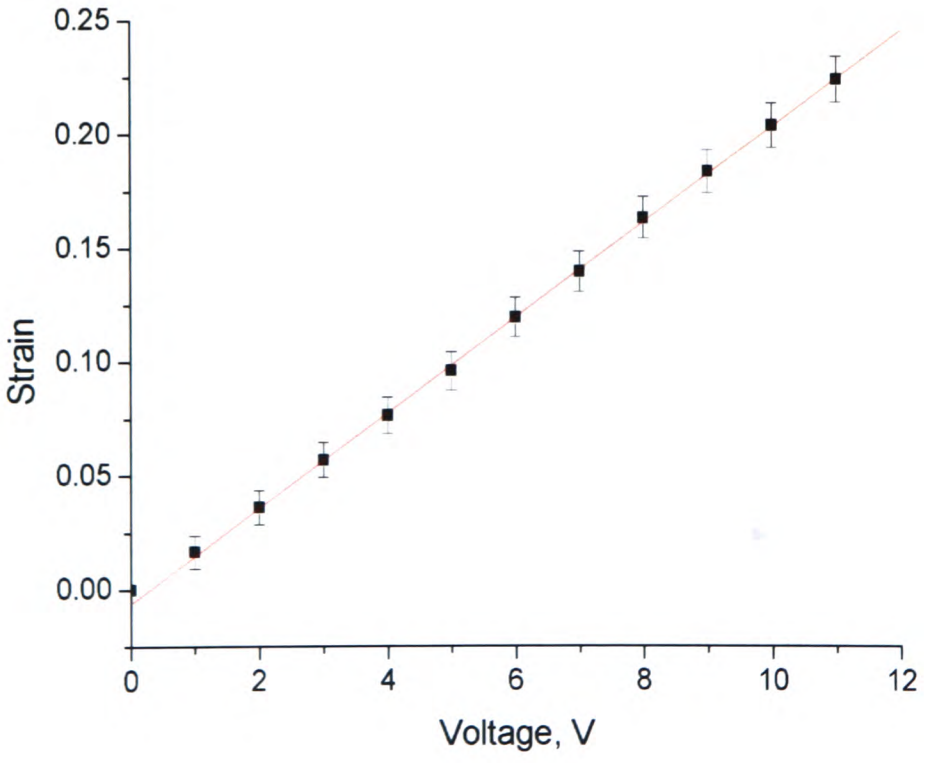

Figure 4.5: Strain vs Voltage for 70Hz, Shear cell 3, Gap = 710 μm. Solid lines = linear fit.

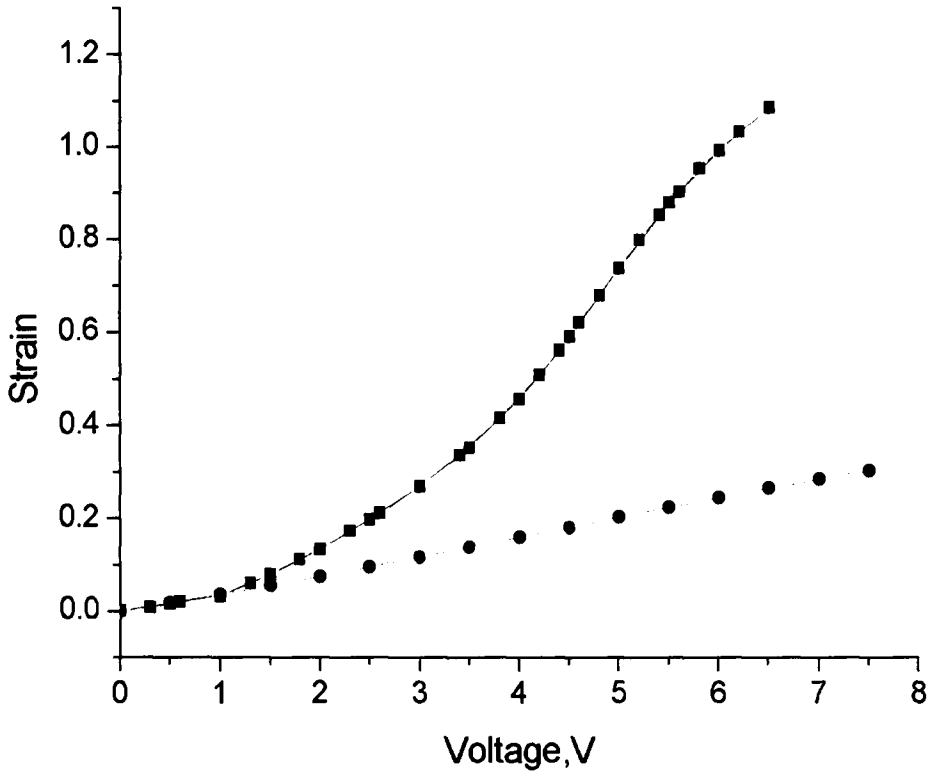

Figure 4.6: Voltage vs strain at 70Hz,10Hz and 1Hz for shear cell 1, ■ = 70Hz, • = 10Hz and 1Hz

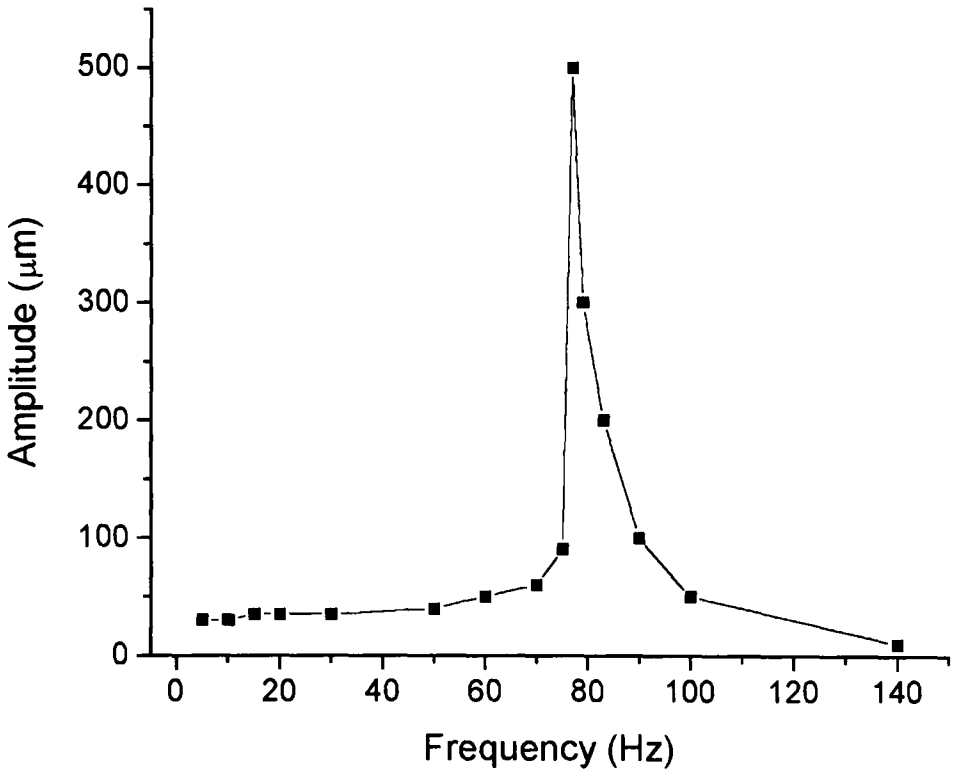

Figure 4.7: Amplitude vs frequency graph, showing resonance at $\sim$ 80Hz, for Shear Cell 1

Firstly, we look at the Shear Cell 3. Shown in figure 4.4 is the amplitude versus voltage at 70Hz for both the bottom plate that is attached directly to the piezo and the top plate which is attached to the lever. As expected for the bottom plate, the amplitude is linear with applied voltage and the total amplitude is the maximum amplitude the piezo is capable of providing. The top plate amplitude is also linear and several times larger than the bottom plate amplitude due to the effect of the lever, where the lever ratio is ~ 2. Similar results are found at 10Hz. No significant variation in the amplitude with frequency was found for this shear cell.

The figure 4.5 shows the results in figure 4.4 in the more useful form of strain against voltage. A linear strain response is found for increasing voltage. Similar plots were found for the second shear cell.

Now we look at the Shear Cell 1. In contrast to Shear Cell 3, figure 4.6 shows that the first shear cell did not produce a linear strain response to applied voltage for high frequencies. The shear cell is more stable where a linear amplitude response to voltage is found but the total amplitude and therefore strain is lower. There is a balance to be struck between getting the maximum strain possible but maintaining a reliable calibration.

In shear cell 1 there is a dependence on the frequency of the plate amplitude for the plate linked to the directly driven plate by the lever. Figure 4.7 shows the amplitude of the bottom plate of the first shear cell plotted for changing frequency. There is a resonance about 80Hz. Around this resonant frequency the top plate amplitude is much greater than at frequencies far from resonance. The resonant frequency of the top plate depends on several factors namely: the stiffness and compression of the spring used to return the plate, and the position of the lever. The combination of spring and lever chosen was that which gave the maximum stable amplitude of the plate at 70Hz. This resonance was eliminated in Shear Cell 2 and 3 but resulted in a lower maximum strain being available.

A stable amplitude calibration is one that remains at the same amplitude within reading errors for a continuous period of several hours and remains the same, within errors, at a later date. A change in the calibration, always giving a reduction in the amplitude for a given voltage, was a good indication that some part of the shear cell had slackened off, or become loose. This could be checked and corrected and a new calibration taken.

4.9.2 Plate Gap Calibration

For shear cells 2 and 3, the gap between the plates can be changed with screws on the top plate. It is important to calibrate the gap between the plates as accurately as possible as the gap

between the plates determines the strain and is assumed to be the same at all places in the shear cell. Also, if the plates are not parallel then the sample will drift in the shear cell.

4.9.2.1 Method for Measuring the Plate Gap

Both plates of the shear cell were covered with a drop of dilute colloidal particles. The solvent evaporated leaving a single layer thickness of dry particles partially covering each plate. A microscope was used to image each layer of particles in turn with a $10\times$ dry objective. The fine focus control knob has a micron scale marked round it which can be read to an accuracy of $\pm 2\mu m$. One turn of the Nikon microscope knob corresponds to 100 μm. Therefore, the gap between the two layers of particles and thus plates can be measured.

4.9.2.2 Method for Calibration of the Plate Gap

There are three screws in the top plate that control the gap with the bottom plate. The bottom plate remains fixed in place. Turning the screw further into the plate makes more of it stick out below the top plate, increasing the gap between the plates. Turning the screw further out of the plate reduces the gap. One full turn of a screw corresponds to a change in height of $\sim 400\mu m$. The gap is measured as described above in the three places on the glass part of the plate closest to the screws. When all three positions give the same gap then the plate is calibrated.

An initial rough calibration is obtained by placing a number of coverslips (each $\sim 100\mu m$ thick) between the two plates. The top plate particle layer is imaged at each of the three points in turn. The screw is turned increasing the gap until the top plate is seen to move. This is the point where the gap is greater than the combined coverslip thickness and the plate is lifted off the coverslips. This is repeated for the other two screws giving an approximate calibration. This calibration is refined by repeating the following process for each screw in turn. Firstly, image the particles at the top plate, then move the focus control knob by the amount the plate needs to be adjusted by to give the desired gap. The particles will go out of focus. Now, move the screw in the appropriate direction while watching for the particle to come back into focus. When the particles comes back in focus then the top plate will have the desired gap. The one problem with this method is that changing one screw alters the gap at the other two points that are viewed. This is due to the fact that the nearest point to the screw is a small distance away from the screw defining the gap so when one screw is changed there will be a lesser change in the gap at the other positions. So the new positions of the other two points is checked.

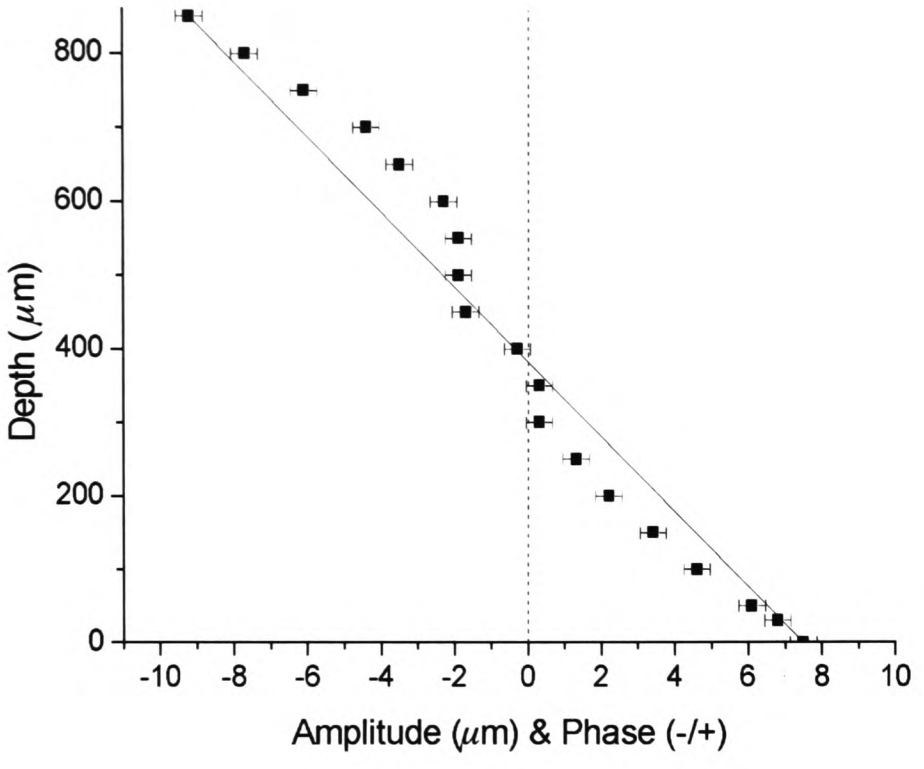

Figure 4.8: Measured shear profile for Shear Cell 2 for fluorescent tracker particles in a dense suspension. Total amplitude of the particles at a given depth (where $0\mu m$ = bottom plate) with the sign signifying whether the particles are most closely in phase with the bottom plate (+ phase) or the top plate (- phase). Solid line = linear shear profile.

This process is then repeated for each screw in turn, needing smaller changes in the gap each time until the three points give the same plate gap within reading errors. The plate gap is now calibrated.

4.9.3 Shear Profile

The shear profile of the amplitude of movement of particles within the sample expected from two plates moving in opposite directions is a linear amplitude profile as was shown in figure 2.13. There is a stationary plane at a certain height depending on the ratio of the amplitudes of the two plates. It is important to check whether this is in fact the case. Of particular importance is if the particles are slipping at the plate surfaces.

4.9.3.1 Method

This can be checked with particle velocimetry. The amplitude of particles at different distances between the plates is measured. This was achieved using a small number of tracer fluorescent PMMA particles in an index matched suspension of standard PMMA particles. In this way dense colloidal suspensions and colloidal gels could be checked. The confocal microscope was used with the shear cell oscillating at low frequencies. Due to the image quality dropping rapidly with distance into the sample measurements could only be made all the way through the sample in some cases. A good indication of a simple shear profile is a change in the direction of the particles when the stationary layer is passed through. Below the stationary plane the particles move in step with the bottom plate. Above the stationary plane at the same time the particles will be moving in the opposite direction, in phase with the top plate.

4.9.3.2 Results

The results shown here in figure 4.8 were conducted on shear cell 2. They show a shear profile that is close to but not in perfect agreement with the expected linear profile. As there is no difference in the plates with the other shear cells the results are assumed to apply to the other shear cells.

It has been found that if the plate gap is too small ($< 300\mu m$) then deviations from a simple shear profile are found. Therefore, the plate gap was always chosen to be $\geq 300\mu m$ in all experiments.

4.9.4 Errors

The reading error associated with calibration of the plate amplitude at a fixed frequency and voltage is estimated to be $\pm 5\mu m$.

The corresponding error in the total plate amplitude is therefore $\pm 10\mu m$. Note, this assumes a "stable" voltage to amplitude response (see section on stability). In Shear Cell 1, the plate gap, d, is set by the precision ball bearings (diameter $\pm 5\mu m$) but any unevenness in the glue between the bottom (metal) plate and glass microscope slide will also vary the plate gap. The glue is estimated to vary by $\pm 10\mu m$. This gives a total error in the plate gap of $\pm 15\mu m$ for Shear Cell 1.

In Shear Cell 2 and 3 the plate gap is directly measured. Typically, the plates are parallel to within $\pm 20\mu m$.

Typical values for a strain $\gamma_0 = 0.15$ are given below:

In shear cell 1 with an amplitude of $90 \pm 10\mu m$ and plate gap $d = 300 \pm 15\mu m$, $\gamma_0 = 0.15 \pm 0.025$.

In shear cell 2 with an amplitude of $225 \pm 10\mu m$ and plate gap $d = 750 \pm 15\mu m$, $\gamma_0 = 0.15 \pm 0.01$.

The strain experienced by a particle at different heights in the shear cell will vary as the shear profile is not perfectly linear (see figure 4.8). For a typical viewing depth of 50 μm the strain is found at low plate amplitudes to be up to 30% higher than expected from the imposed strain. This increases the uncertainty in the strain more for shear cell 1 than cell 2. It is worth bearing in mind this uncertainty in the strain when trying to link a shear induced structure to a particular strain.

Chapter 5

Quiescent Structure of Dense Gels

5.1 Introduction

We present here a detailed study of the microscopic structure of dense colloid-polymer gels of varying polymer volume fraction, Φ_p and colloid volume fraction, Φ_c. This includes direct optical and confocal microscopy observations of the gel structure and the quantitative analysis of the positions of the particle centres extracted from 3-D image volumes.

5.2 Qualitative Observations of the Gel Structure

We first present a qualitative set of results for the full range of studied colloid-polymer mixtures found for varying polymer volume fraction, Φ_p, with constant Φ_c. The appearance of a high Φ_p gel sample is described and the sedimentation profile is studied to determine whether the sample is a transient gel. The microscopic structure of three different Φ_p samples is described and contrasted with the structure of a pure colloidal fluid.

5.2.1 High Φ_p Gel

In this experiment we study the macroscopic appearance of sample A1 (see table 3.4). In the sample bottle the gel appears uniform, cloudy grey. No phase separation is observed. Figure 5.1 shows the sedimentation height profile for the gel and a pure colloidal fluid of the same volume fraction ($\Phi_c = 0.4$) over a period of several days. No change is observed for the gel within the

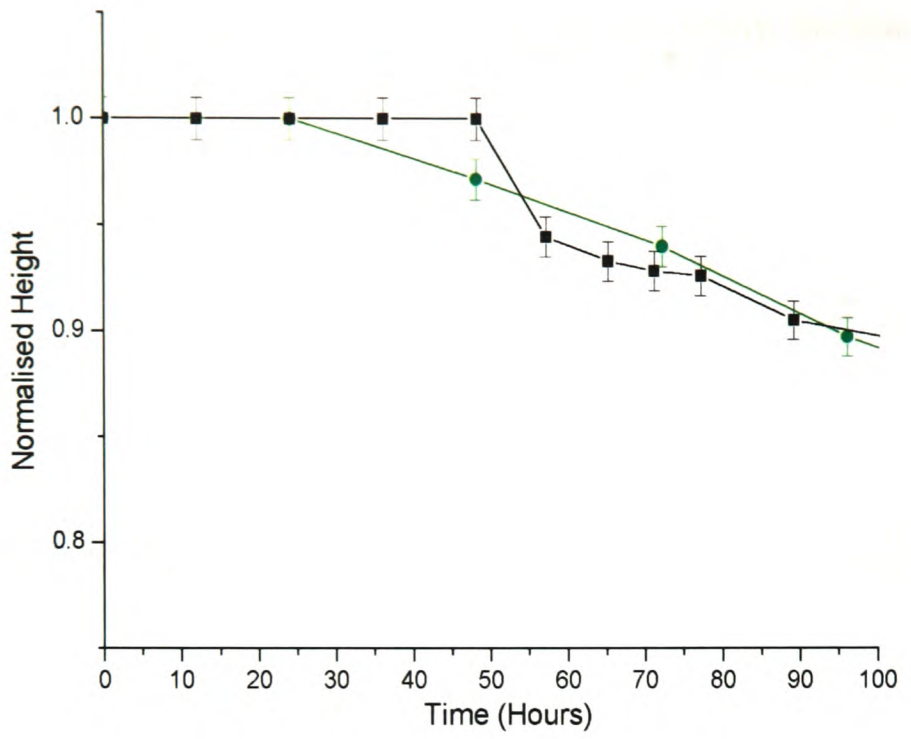

Figure 5.1: This figure shows the sedimentation profile of gel A1 (■, black) versus a Φ_c = 0.4 colloidal fluid (●, green). The sample was placed in a 2ml sample cell (1cm diameter × 2cm height). Measurements made from recorded image in which the cell has been magnified by 10 × (uncertainty in height is $\sim 1\%$). The gel sample does not sediment significantly over 50 hours whereas the fluid starts to sediment earlier.

shear cell experimental timescale of up to eight hours. A clear supernatant is observed after approximately 50 hours. This sedimentation is slightly slower than for a fluid sample of the same volume fraction. The lack of phase separation and the high polymer volume fraction are consistent with the sample forming a colloidal gel. The latency time is extremely long.

Now we describe the microscopic structure of the high Φ_p gel (sample A1, see table 3.4). Two-dimensional optical sections of the gel structure were obtained for a sample loaded into Shear Cell 1. In this experiment the shear cell is only used as a sample holder to study the quiescent state, no shear of the sample takes place. A plate separation of d = 0.3mm was used for these microscopy experiments. Figures 5.2 and 5.3 show images of the gel at two different depths below the top plate, approximately $20\mu m$ and $60\mu m$ respectively. The gel is imaged with an optical microscope (contrast enhanced with DIC). The image quality does degrade with depth into the sample. The colloidal gel structure fills space. All of the particles are frozen on observable length scales. This occurs within a few seconds of loading the sample and is complete by the time the first images are recorded ($\sim$ 1 minute). No free particles or moving clusters are observed. There are void regions from which particles are absent, ranging in size from a few to many particle diameters (uniform grey regions in the images). These voids are difficult to observe in the bulk of the sample as light from out of focus particles obscures

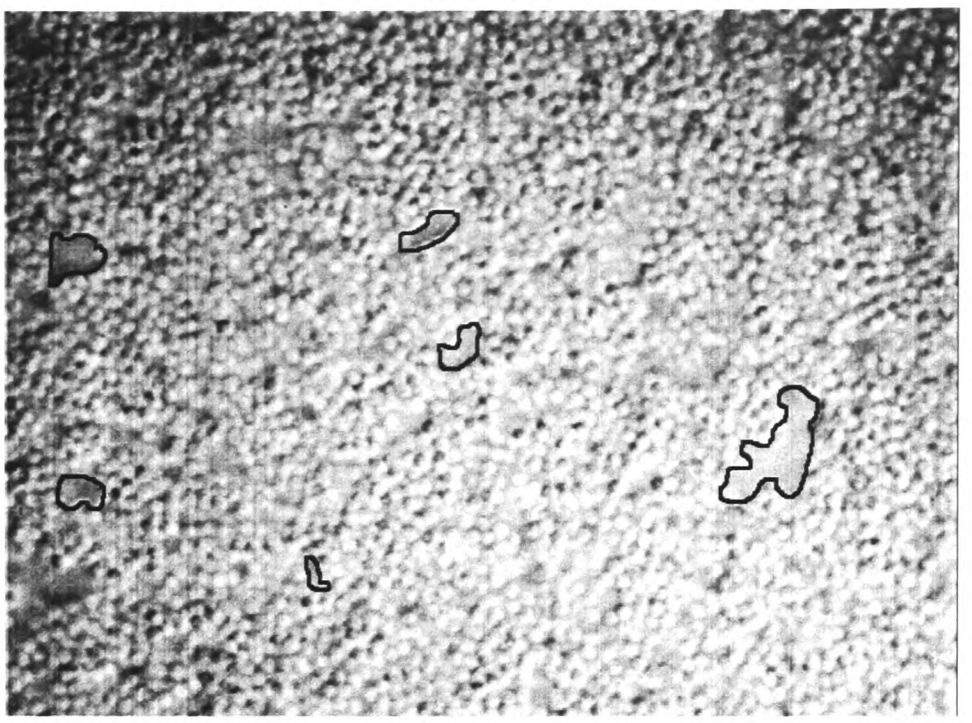

Figure 5.2: Optical Microscopy image using a DIC x100 objective of Sample A1 (see table 3.4). This image shows the quiescent gel structure at the particle length scale. Note the void areas (for example those outlined by a black line), the uniform grey empty areas that are free from particles. Depth = near top $\approx 20\mu$m.[Image size $\sim 100\mu m \times 80\mu m$]

the empty regions. No crystalline order is observed. The presence of the plates can lead to structural differences, but only up to $10\mu m$ from the surface. A continuous, dense layer with few empty spaces is often observed in this surface region. All images shown in this work are recorded from outwith this surface layer i.e. in bulk conditions.

The study of two-dimensional time series of a high Φ_p gel over time scales of up to an hour show no observable changes to the structure such as rearrangement of particles. Figure 5.4 shows such a time-series for sample D1. The 2-D position of the particles is constant over time, no motion of the particles is observed at all. Aging over longer timescales can not be ruled out as timescales longer than a few hours were not experimentally observed.

5.2.2 Medium Φ_p Gel

In this section we look at the microscopic structure of the medium Φ_p gel samples B1 and B3 (see table 3.4, using Shear Cell 2). Figure 5.5 (A) is a typical confocal image of the medium polymer volume fraction gel (B1) studied. Note the colloid particle radius is about half the size of that used in the majority of the confocal experiments. The particles form a dense network of clusters separated by voids that can be many particle diameters in size. The largest voids in this image are of order 10 particle diameters. The range of sizes of the voids can vary between

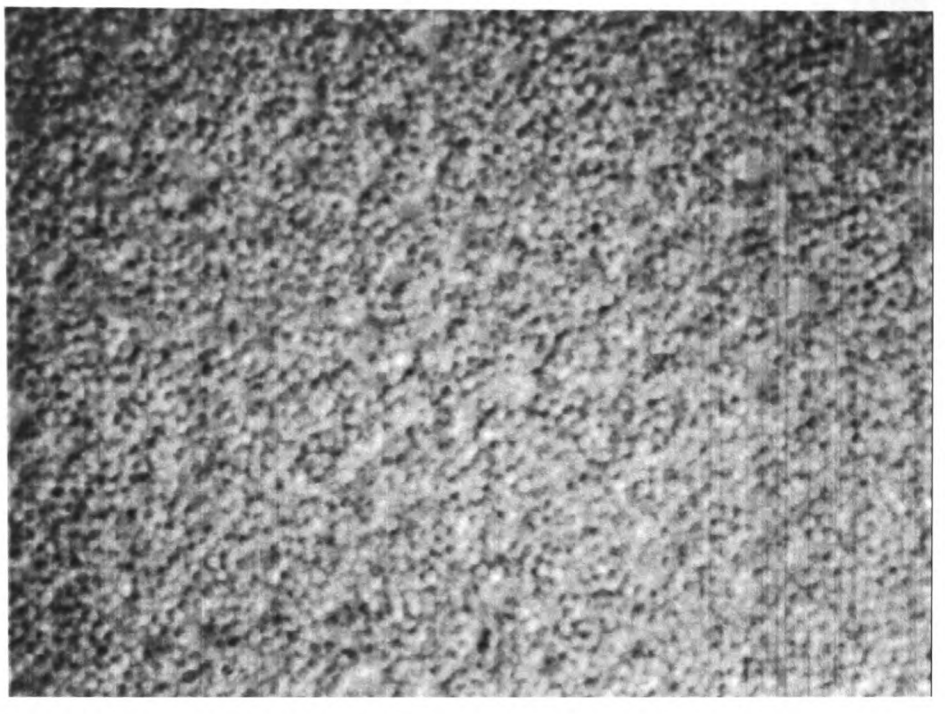

Figure 5.3: Optical Microscopy image using a DIC x100 objective of Sample A1 (see table 3.4). This image shows the same sample as figure 5.2, but deeper into the sample $\approx 60\mu$m in. The image quality degrades with depth into the sample. The particles can still be seen clearly, however the voids are not easily visible.[Image size $\sim 100\mu m \times 80\mu m$]

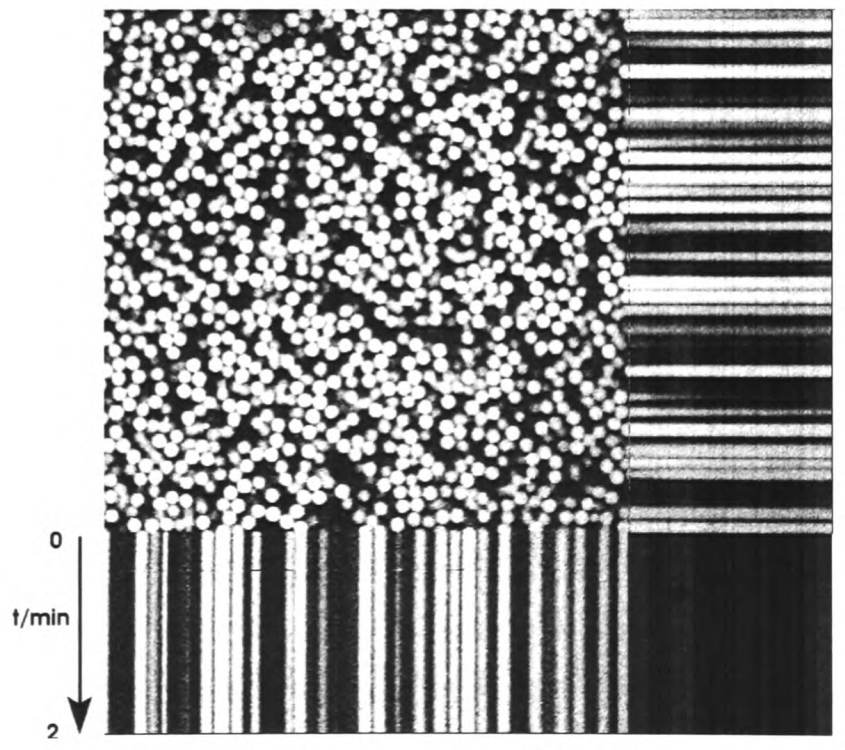

Figure 5.4: A 2-D x-y plane with two projections showing a time series of the two single pixel thickness lines at the bottom and right edges of the image for sample D1. The constant pixel values over time (2 minutes) show that the sample is frozen.[image size = $\sim 77\mu m \times 77\mu m$]

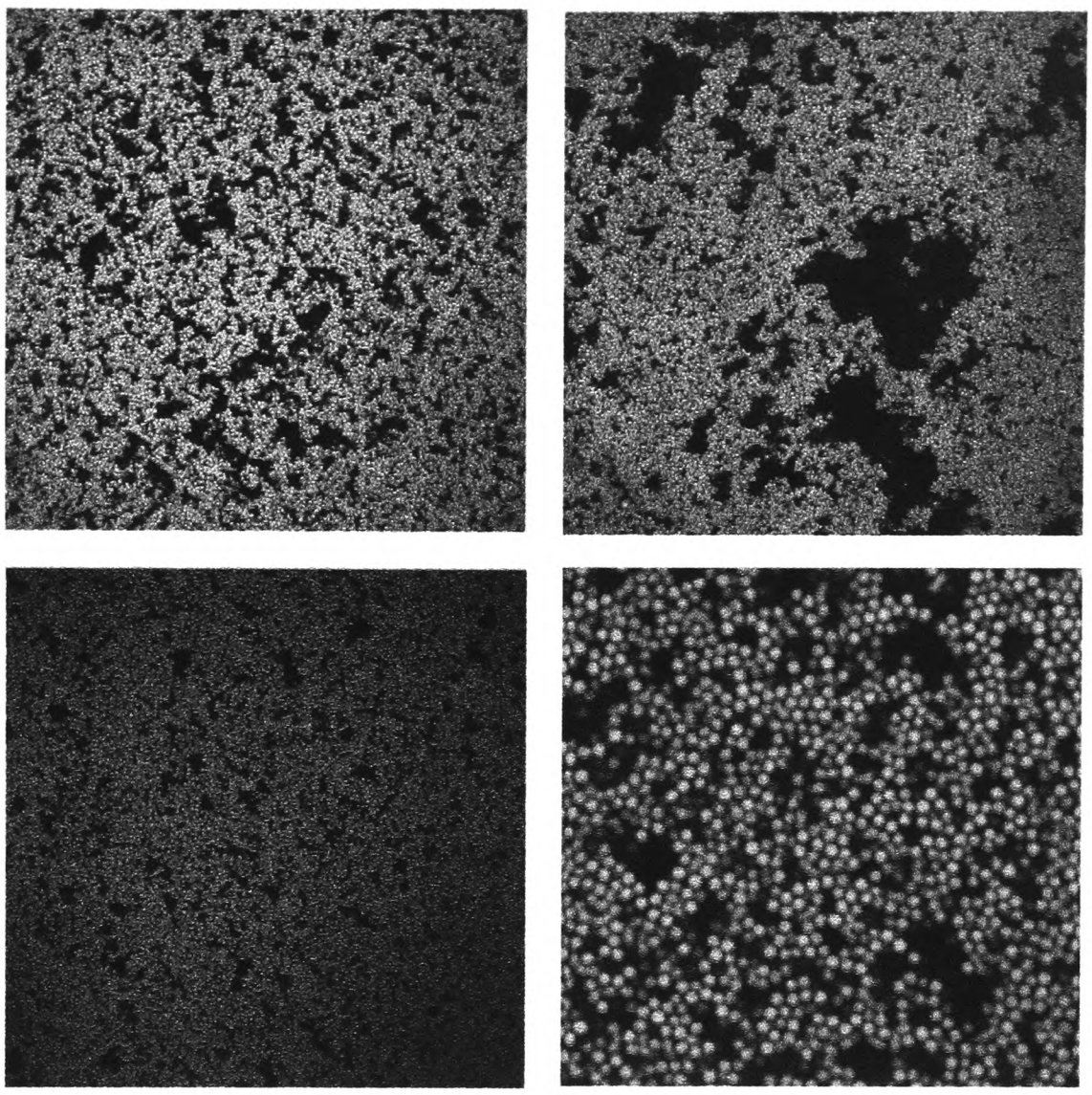

Figure 5.5: Top left to bottom right (A) - Gel B1: typical image, (B) Gel B1: larger void regions (C) Gel B3: higher colloid volume fraction , (D) Gel B1: zoomed in to show individual particles [Image size (A, B, C) $\sim 123\mu m \times 123\mu m$, (D) $\sim 36\mu m \times 36\mu m$]

samples. In figure 5.5 (B) a different experiment with the same sample B1 is shown. We find much larger voids in this case than are seen than in (A). The largest voids in this image are of order 20 particle diameters. Figure 5.5 (D) shows the local structure formed by the individual particles for B1. The particles form a very inhomogeneous structure of small dense clusters, separated by small voids and gaps. Figure 5.5 (C) shows the gel structure for a higher colloid volume fraction, $\Phi_c = 0.467$ gel (Sample B3). A similar structure is seen despite the higher particle density.

5.2.3 Microscopic Structure of Very Low Φ_p Gel

The polymer volume fraction for this gel (sample D5, see table 3.4), using Shear Cell 3) is a tenth as large as for the highest Φ_p gels studied (samples D1, D2). An image of the structure

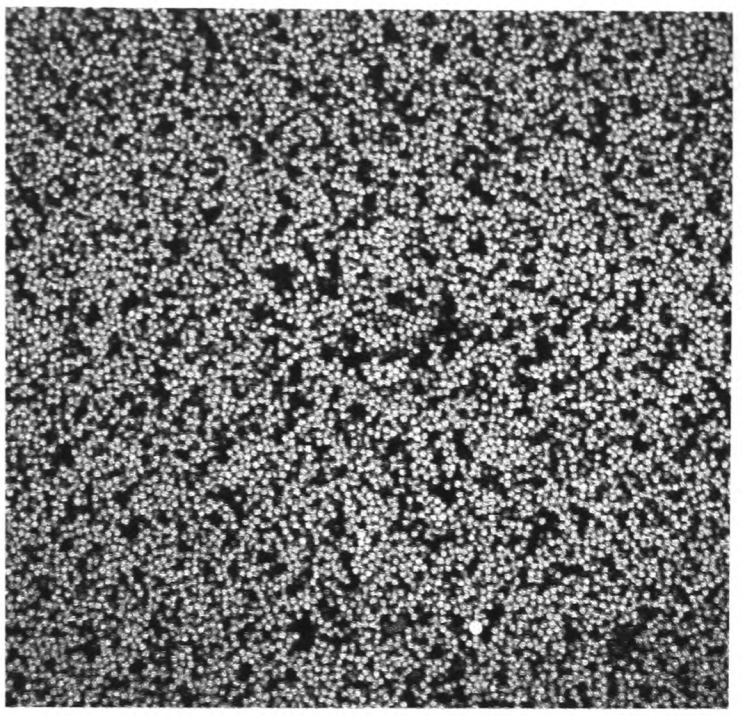

Figure 5.6: Typical confocal gel image of quiescent structure for very low Φ_p gel (Sample D5). Structure is not completely frozen. Lots of localised motion is evident. [box size is 210 μm × 210μm]

of the gel is shown in figure 5.6. The structure is similar to that of gel B1 (see figure 5.5 (B)). However, the particles are all jiggling about a lot more while still joined up in space-filling clusters, with even occasional particle rearrangement being observed. The voids are typically small in size.

5.2.4 Microscopic Structure of Pure Colloidal Fluid ($\Phi_p = 0$)

The pure colloidal fluid ($\Phi_p = 0$) is shown in figure 5.7. In total contrast to the gel samples the particles are all moving in Brownian motion, and homogeneously distributed. Only 2-D images are possible as the particle motion prevents the capture of sufficient images per particle to allow particle coordinates to be determined.

5.3 Quantitative Study of Gels with Varying Φ_p

In figure 5.8 are the four different gels we have quantitatively analysed along with a reconstruction of the same 2-D plane of the original 3-D volume. Preliminary experiments with a high Φ_p gel sample, in which the large particles were suspended in cis-decalin (Sample C1) showed that sedimentation of the particles was significant in experimental timescales (this was not found to be the case for the other two sizes of particles (A and B samples). Therefore,

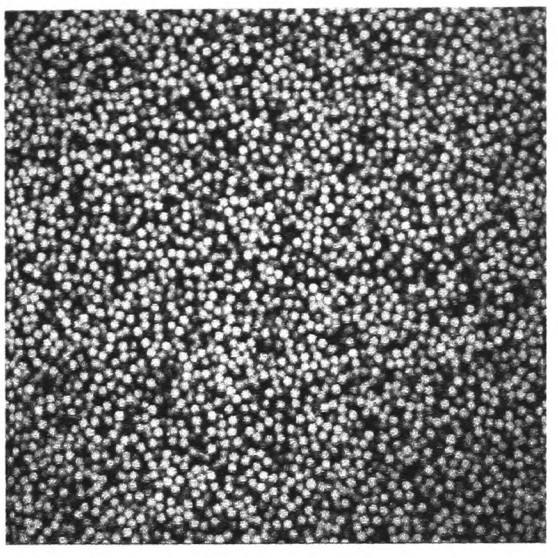

Figure 5.7: Typical confocal image of colloidal fluid. $\Phi = 0.40$ [box size is 123 $\mu m \times 123 \mu m$]

all further experiments with the large particles were conducted with density matched samples (D samples). Sample D4 is a low Φ_p gel, D3 has medium Φ_p, D2 has high Φ_p and D1 is also a high Φ_p gel but with higher Φ_c than D2 ($\Phi_c = 0.44$ versus $\Phi_c = 0.40$). Shear Cell 3 was used as a sample holder. In the high Φ_p gels (Images (D1) and (D2)) the particles form a frozen network containing empty regions, or voids and small interconnected clusters. Only small voids are observed with a maximum length scale of order 5 particle diameters. On a local scale the particles are clustered giving the inhomogeneous appearance of the gel. In the medium Φ_p gel (Image (D3)) a similar local structure of the particles is observed. However, the voids appear larger and the particles more clustered. The gel is again frozen on observable length-scales. In the low Φ_p gel (image (D4)) the structure is similar to that seen in (D3) but the particles appear to form more dense clusters. The voids seem almost to be interconnected, at least in 2-D. The gel structure in this case is not completely frozen. A few particles in a 2-D slice have detectable motion but on a length-scale much smaller than a particle diameter. No particles rearrangements were observed though. The motion of the particles is even greater for the very low Φ_p gel, preventing the acquisition of accurate particle coordinates. Bearing these qualitative observations in mind we can now look at the quantitative analysis of the structure of these gels.

5.3.1 Radial Distribution Function

The radial distribution function, $g(r)$ for the four different polymer volume fractions is shown in figure 5.9. There is a strong first peak centred at one particle diameter. There is a weak second peak slightly before two particle diameters. The first minimum is asymmetric with respect

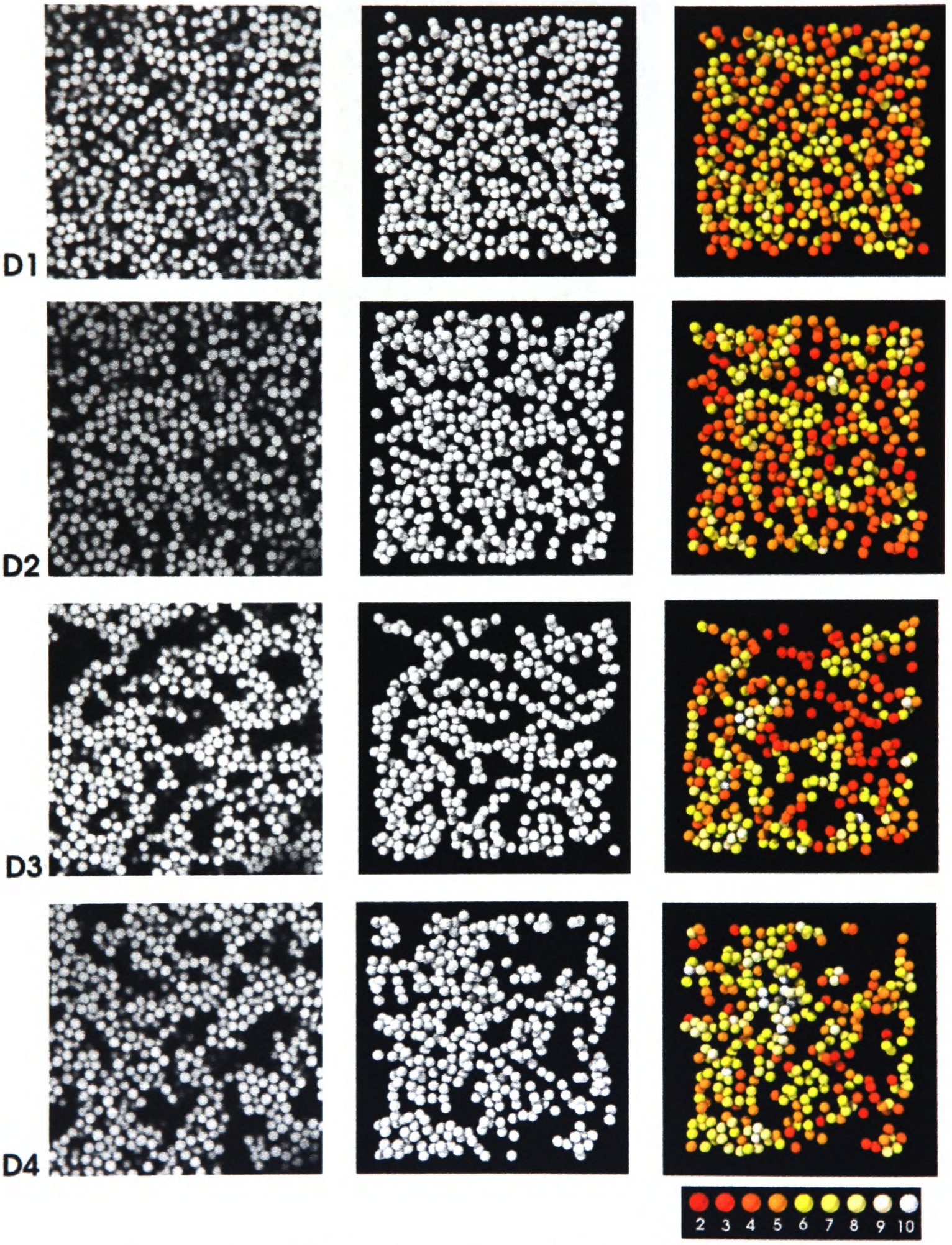

Figure 5.8: Column 1: Typical 2-D confocal images $[51\mu m \times 51\mu m]$ obtained from 3-D image volume $[51\mu m \times 51\mu m \times 20\mu m]$. Column 2: Same plane as in column 1 formed from a 3-D projection of particles positions from a limited depth range $[51\mu m \times 51\mu m \times 1.5\mu m]$. Column 3: as column 2 but colour signifies the number of neighbours (red = low number $->$ white = high number). From top to bottom are samples D1, D2, D3 and D4. (Note: particles within radius R of original image edge have been removed in column 2, particles within 2R of original image edge have been removed in column 3).

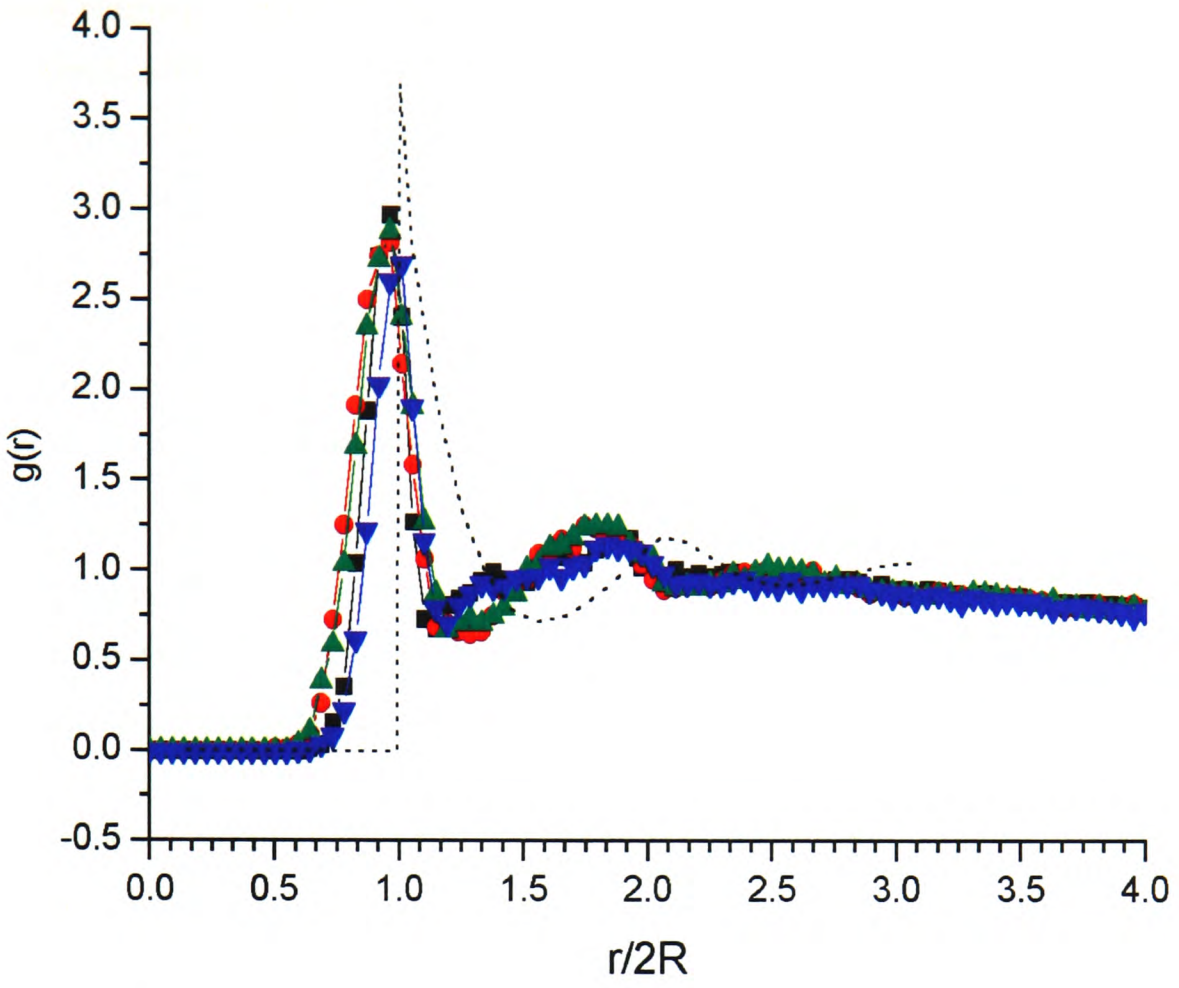

Figure 5.9: Radial distribution function, $g(r)$ for gels with varying polymer volume fraction, Φ_p. $g(r)$ calculated for the image volumes shown in figure 5.8. with about 3000 particles per curve and 200bins. Also shown is the calculated hard sphere fluid rdf for $\Phi_c = 0.4$ (dotted line) ▼ $= D1$, ■ $= D2$, ● $= D3$, ▲ $= D4$

to the first and second peaks. There is no long range order, $g(r)$ falls to the average value of 1 within 3 particle diameters. There does not appear to be any significant difference observed between the different gel structures, in contrast to the qualitative differences observed. The short range average structure appears to be very similar. There is possibly a small difference between the high Φ_p and the lower Φ_p gels in the shape of $g(r)$ between the first and second maximum.

5.3.2 Coordination Number

Shown in figure 5.10 (Top) is the normalised distribution of the coordination number or number of neighbours per particle for each polymer volume fraction. A particle is considered a neighbour if another particle is within r_c, where r_c is defined as the 1st minimum of g(r). The distribution is formed from an average over several image stacks for each polymer volume fraction, typically 70,000 particles. For comparison the bond distribution is shown in figure

5.10 (Bottom) where a bond is defined using $r_c = 2R + 2\Delta$. A typical particle has 3-4 bonds compared to 5-6 neighbours. From this point onwards we will focus on the number of neighbours as this allows us to directly compare the different gels (that have different bond lengths). In general, a typical particle has about 5-6 neighbours. Very few particle chains exist (defined as particles in the neighbour distribution with 2 neighbours). There are no free particles and no particles were found to have more than 10 neighbours. Higher Φ_c leads to a shift in the distribution to higher number of neighbours. Lower Φ_p also leads to an increase in particles with many neighbours and a reduction in particles with few neighbours.

Figure 5.8 (column 3) shows a 3-D reconstruction for each gel with the colour of the particle corresponding to the number of neighbours it has. Most particles have neighbours that are outwith the thin 3-D volume shown. The higher average number of neighbours in the lower Φ_p gels can be seen by the overall brighter appearance of the reconstructed image when compared to the high Φ_p gels. Also, it is interesting to note that in the high Φ_p gels the high neighbour number particles (whiter) appear evenly distributed. In contrast, in the medium and low Φ_p gel the high neighbour number particles appear clustered together. The low neighbour number particles in all the gels appear mostly to sit on the edge of empty void regions.

5.3.3 Remoteness

Figure 5.11 shows the remoteness for varying Φ_p and Φ_c for the image volumes shown in figure 5.8. The remoteness is an indirect measure of the distribution of the voids. The remoteness is larger for decreasing Φ_p and smaller for increased Φ_c.

5.4 Discussion

5.4.1 Comparion of Experiments

We now want to look at what these results can tell us about the structure of the gel and its properties. We first consider the common features of the different gels we have studied then look at the differences.

We can estimate the position of the non-ergodicity boundary on the phase diagram with Mode Coupling Theory (MCT) using equation 8 from [50]. This gives the transition from fluid to gel occurring at $\Phi_p = 0.1$. This is just below the position of the lowest Φ_p gel studied. According to Sedgwick [16] if a sample is below the MCT line but above the gas-liquid binodal then phase

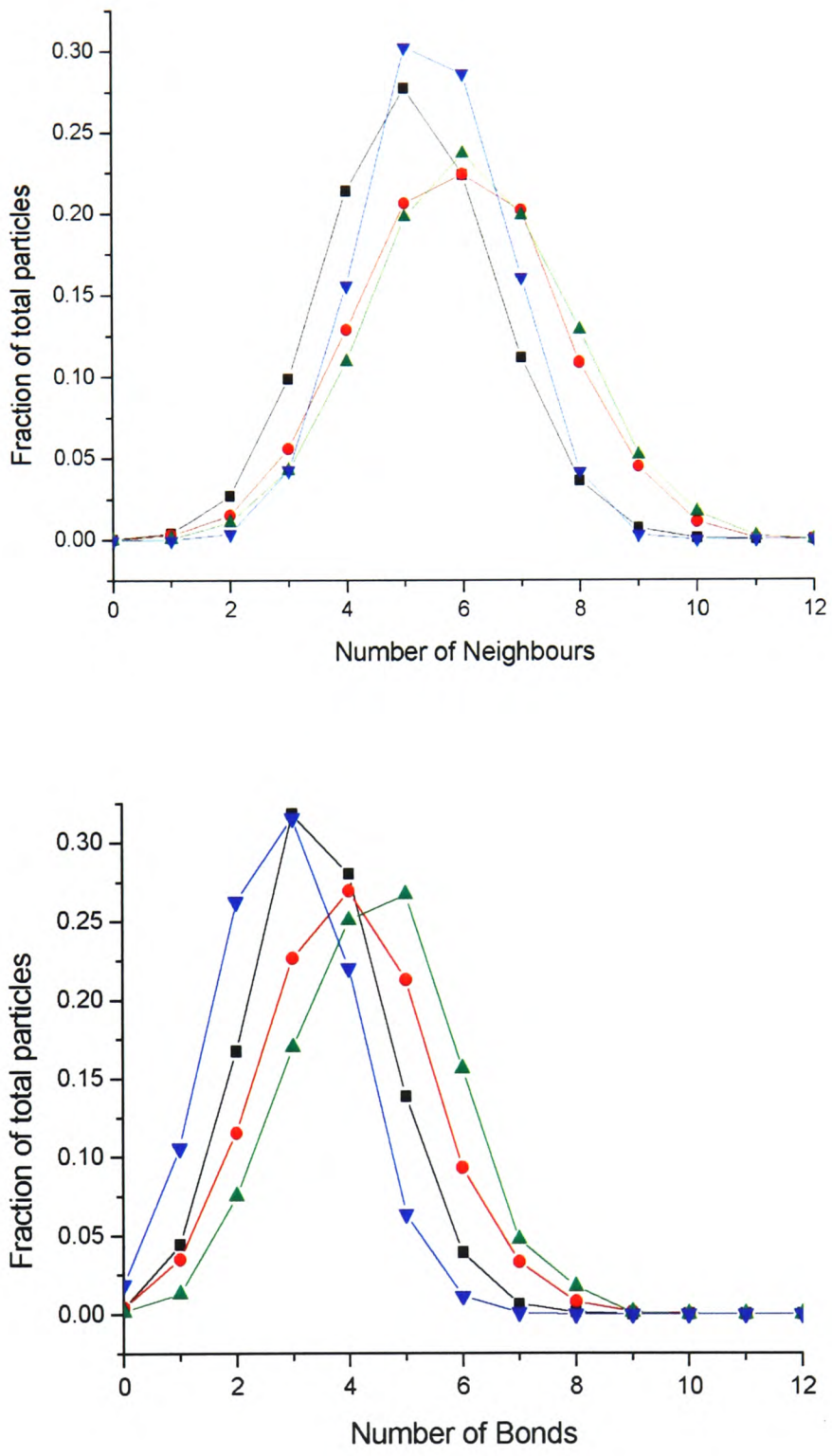

Figure 5.10: **Top:** Normalised neighbour distribution for varying Φ_p and Φ_c. A particle is considered a neighbour if another particle is within r_c, where r_c is defined as the 1st minimum of $g(r)$. The distribution is formed from an average over several image stacks for each polymer concentration, typically 70,000 particles. **Bottom:** Normalised bond distribution for varying Φ_p and Φ_c, where a bond is defined using $r_c = 2R + 2\Delta$. ($\blacktriangledown = D1$, $\blacksquare = D2$, $\bullet = D3$, $\blacktriangle = D4$)

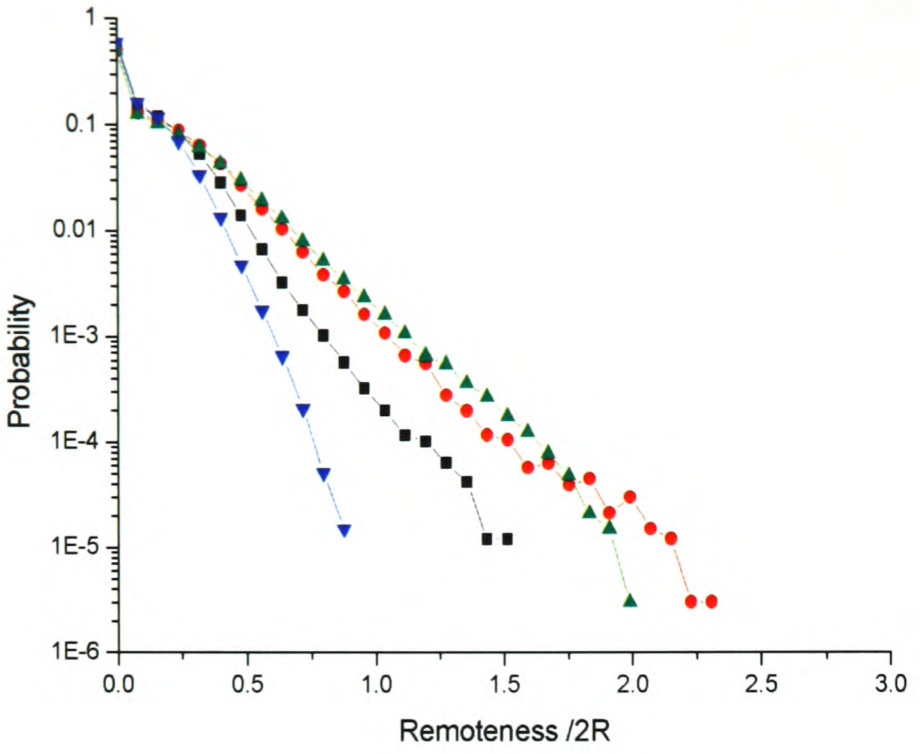

Figure 5.11: Remoteness for varying Φ_p and Φ_c. Quiescent Gels The remoteness is larger for decreasing Φ_p and smaller for increased Φ_c ($\blacktriangledown = D1, \blacksquare = D2, \bullet = D3, \blacktriangle = D4$).

separation would begin but as the dense phase crosses the MCT line, the sample arrests and forms a transient gel. As our samples are above the MCT line the arrest occurs throughout the sample and no phase separation can occur. We therefore do not believe that any of the gels studied here form through arrested phase separation - in contrast to transient gels at lower colloid volume fractions.

The local structure of a high colloid volume fraction gel as measured with $g(r)$ corresponds to a liquid. A typical particle will see a similar local environment in each of the gels. We can quantitatively compare the local structure of the gel with a pure hard sphere fluid at $\Phi_c = 0.4$. by calculating g(r) for the fluid (using methods in [51]). The RDF for the fluid is qualitatively a similar shape. However, we find that the first peak in $g(r)$ = 3.7 is higher in the HS fluid than in the gels $g(r) \sim 3$. The gel is therefore not as locally dense as a fluid at the same volume fraction. Note, that we find $g(r < 2R) > 0$, which is forbidden for particles of hard-core diameter of $2R$ (compare with $g(r)$ for the hard-sphere fluid).The polydispersity of the particles (standard deviation $\pm 110nm$) and the limited accuracy of locating particle centres (error of $\pm 40nm$ in x-y plane and $\pm 50nm$ in z-axis) contribute to $g(r)$ for $r < 2R$. This result illustrates the effect of experimental limitations on characterising the gel microstructure.

Varadan [20] also found $g(r < 2R) > 0$ when studying a different kind of colloidal gel.

The inhomogeneous long range structure of the gel can not be detected by measuring $g(r)$. The spread in the distribution of the number of neighbours per particle demonstrates some inhomogeneity at the local level. The amplitude of the first peak, $g(r) \sim 3$, tells us that although the particles are locally denser than would be expected for an ideal gas, the local clusters are not as dense as would be expected for a colloidal glass or crystal (typically the amplitude of the first peak, $g(r) \sim 6$ [52]). We find that the average number of neighbouring particles for the gels is 5 to 6. There are insufficient particles surrounding each particle for a cage to form that would trap the particle in a fixed position. Therefore, the gel can not be thought of as a repulsive colloidal glass (with local density $\Phi_c \geq 0.64$) full of holes. The calculated remoteness probability distribution provides a measure of the distribution of the voids that are responsible for the inhomogeneous appearance of the gels

The dense gel can be thought of as a low density strongly attractive glass; the attraction between the particles leads to all the particles being stuck to each other, leading to structural arrest despite the empty space available. This is supported by estimates of the timescale of Brownian motion of a free polymer coil compared to the timescale of Brownian motion of a free colloid particle. We assume that the polymer acts as a sphere diffusing in pure cis-decalin solvent. This gives $\tau_{relax} \sim 0.02s$ for the polymer coil, compared to $\tau_{relax} \sim 4.5s$ for the colloid particle (Sample A1). This shows that the polymer rearranges in a much shorter time. Therefore, a free colloid particle could move through the polymer solution without any difficulty. The polymer is not preventing the colloids from entering the void regions. This fits with the idea that it is the attraction between the colloid particles, albeit induced by the presence of the polymer, that prevents colloids from breaking off from the gel clusters and being observed as free particles.

We now look at the formation of the gel structure. The highest Φ_p gel structure and the structure of a pure hard-sphere fluid structure at the same volume fraction appear visually similar, except for the particles being frozen in the gel. This implies that the very high attraction associated with the high Φ_p gel leads to an immediate and irreversible formation of particle bonds in the gel, as predicted by DLCA. The high colloid volume fraction in the dense gel leads to the formation of multiple bonds per particle. This leads to the formation of clusters that almost instantly join up, spanning the sample volume giving a similar appearance to that of a pure colloidal fluid. There is not sufficient time or empty space for a fractal network to develop.

We now consider what rearrangement of particles, if any, occurs within the gel structure. We have found an increase in the average number of neighbours per particle and a higher probability of finding a high remoteness for decreasing Φ_p. We suggest that these two trends are

linked and can be related to compactification of the gel structure in the lower Φ_p gels not occuring in the high Φ_p gels. We have said that the dynamics of the particles within the gel vary with changing Φ_p (corresponding to varying U_0). The lack of any observable motion of the individual particles or clusters at high Φ_p is in contrast to significant jiggling and occasional particle rearrangement observed at low Φ_p. This suggests a large difference in the ability of the particles to rearrange and thus become more compact once particles have started to form bonds after loading of the sample and also in the time before any images are recorded. The rearrangement of particles will tend to lead to a small compactification of the clusters. This is what we believe is observed in the increase in the average neighbour number. In turn this will lead to more empty space for voids leading to a higher remoteness than found at high Φ_p. (In effect reversible DLCA).

It is not clear why such large voids are observed in some of the experiments conducted with the medium Φ_p gel, made with the smaller colloid particles (figure 5.5 (B)) and not in the medium Φ_p gel made with the larger particles(figure 5.8 (C)) . Possibly there is some particle size effect, relating to how the particles in the gel form into the gel or respond to loading. We have found that if the top plate of the shear cell is moved up and down, which disrupts the gel, then the very large voids disappear and a more typical structure is seen (such as figure 5.5 (A)). Doing the same thing for a gel made from the large particles has no noticeable effect.

The very long latency time $\tau_L \sim 50$ hours of Sample A1 (high Φ_p) can be explained by the very frozen structure of the gel as viewed under the microscope. The collapse of a gel requires significant rearrangement of the gel structure - this can only occur very slowly in this gel. This eventual small amount of sedimentation of the gel may be only particle sedimentation (due to the large particles used) with the gel slowing this gravitational effect when compared to the pure colloidal fluid which sediments more quickly.

We predict a qualitatively similar structure to be found at increased colloid volume fraction up to the high density attractive glass limit as we believe that our gels represent a low density example of an attractive glass as discussed above. Based on our observations of the change in the structure of the dense gel over a small range of colloid volume fraction ($\Phi_c = 0.4$ to $\Phi_c = 0.44$), we expect the structure to be more frozen for the same Φ_p with increasing Φ_c, due to an increase in the average number of neighbours with increasing volume fraction. Also we predict a decrease in the average remoteness with increasing volume fraction as there is less free space available for making voids.

5.4.2 Comparison with Other Work

We have presented here the first known study of the structure of high volume fraction colloid-polymer gels. We will now compare these results with other related colloidal gels. These can be split into two types. Firstly, low volume fraction PMMA-polystyrene gels as studied by Dinsmore *et al* [19] and secondly, high volume fraction silica colloidal gels as studied by Varadan *et al* [20] and Shah *et al* [17].

Our findings agree with those of Dinsmore (see section 2.3.3.1) regarding the decrease in average neighbour number for higher Φ_p in low volume fraction colloidal gels. Therefore, the behaviour appears to be a general phenomenon that does not depend on colloid volume fraction. Dinsmore finds that this leads to chain-like structures (defined at particles with 2 neighbours) whereas at the high volume fractions we consider we find a more fluid-like structure with few chains, $\sim 85\%$ of particles have more than 3 neighbours. This difference is most likely due to the much higher volume fraction. Interestingly, there is only a small difference in the number of neighbours between an average particle in a cluster present in the "fluid-cluster phase" (fluid of aggregates of finite and stable size) with $\Phi_c = 0.03$ and a particle in a dense gel at $\Phi_c = 0.40$. It is worth noting that Dinsmore analysed the structure of small clusters only of size 20-22 particles. The decrease in the number of neighbours found with increasing volume fraction ($\Phi_c = 0.03$ changing to $\Phi_c = 0.10$) may alternatively be explained by the increase in the free polymer volume fraction due to the higher volume fraction giving an increased attraction strength. The increased colloid volume fraction reduces the free volume available to the polymer increasing Φ_p^{free} used to calculate the attraction strength. This increased attraction strength may at least partly account for the decreased average neighbour number, as Dinsmore found such a decrease in average neighbour number associated with increasing the attraction strength. In contrast to Dinsmore, our results show that an increase in volume fraction of the gel leads to an increase in the average neighbour number as would intuitively be expected due to the higher number of particles present. Also, they find an increase in the average number of neighbours over time. Our gels form too quickly to allow a study of the aggregation kinetics, due to the high volume fraction leading to almost immediate contact between multiple particles. Such a study was possible at the very low volume fraction considered by Dinsmore. They found gels aggregated in intermediate regime between Diffusion limited CLA and Reaction limited CLA.

We compare our results to those of Varadan & Solomon (see section 2.3.3.1). We note that their experiments were conducted with silica colloidal particles, suspended in hexadecane rather

than PMMA suspended in cis-decalin (or cis-decalin and CHB). The attraction between the particles is determined by the temperature dependent conformation of short polymer chains grafted onto the silica surface. The equivalent size ratio/range of the attraction for this system is $\xi = 0.005$. The strength of the attraction increases with decreasing temperature with $U_0 < 10k_BT$ once the thermo-reversible gels have formed. We first look at the RDF. We confirm the findings of Varadan that a colloidal gel has a similar local structure as measured by the RDF as a dense fluid. Varadan found that varying the volume fraction of dense gels has no significant effect on g(r) and we find the same over the small range of volume fraction studied. However, some systematic differences are observed between the different types of gels in the local structure. We find a much higher first peak [g(r) $\sim$ 3 (at $r = D = 2R$)] than found by Varadan g(r) $\sim$ 2. Our first minimum is found very close to the 1st peak at g(r) $= 1.15D$ compared to g(r) $= 1.5D$ for the silica gels. This suggests that PMMA colloid-polymer gels are locally more dense that thermo-reversible gels. We now look at the neighbour distribution found by Varadan. The quantitative results can not be directly compared as the neighbour range, r_c, in their case is much larger than we have used. Qualitatively, they find a shift in the neighbour distribution to higher average neighbour number with increasing volume fraction. We find the same trend over the small range of studied colloid volume fractions. They find that the voids have a wide volume distribution.

We look at the microscopic picture proposed by Shah *et al* for colloid-polymer (silica-polystyrene) gels studied with ultra-small angle x-ray scattering. The polymer volume fractions they consider correspond to the lowest Φ_p we studied. They claim that their results correspond to a micro-structure of small clusters of particles (average $\sim 3-4$ particle diameters in size) and voids have a characteristic length scale of $5-8$ particle diameters. Comparison with 2-D confocal images presented here suggests that these claims are reasonable. We have not found any large dense clusters say of size ($\sim$ 10 particle diameters). The size of the void regions do seem comparable in size to the dense regions of particles. Looking at the 2-D reconstructions of the low Φ_p gel showing the number of neighbours per particle (figure 5.8 column 3 (D)) we see small bright regions (dense clusters) and small dark regions (voids) that are of a similar length-scale to that suggested by Shah. However, the difficulties in defining what is a cluster or single void (if such things make any sense in a space-filling continuous structure) prevent any more detailed comparison.

We consider how the dense gels change over time (age). The highly frozen structure implies that any aging of the gel will be very slow, especially for high Φ_p. These gels are strong gels as described by Meeker [14]. Measurements of the h(t) profile (figure 5.1) fit in with this. No

change in the gel was observed for two days, after which time a slow sedimentation occurred. This gel is incredibly long lasting compared to the transient gels studied by Starrs [15].

We look at our plot of remoteness and compare it to the simulations of Haw *et al* [49]. Our plot shows that the probability of finding a particular remoteness in the gel can be successfully measured. We found an exponential dependence on remoteness, the significance of which is not currently understood. It is interesting that at high volume fractions we find that the void structure does depend on volume fraction. This is in contrast to the volume fraction independent void structure found in the simulations (conducted at lower volume fractions). No experiments have measured the remoteness of low volume fraction gels so this difference could be a volume fraction effect or be due to differences between simulation and experiment.

Chapter 6

Dense Gels Under Oscillatory Shear

6.1 Introduction

In this chapter we present our experimental results on the oscillatory shear of dense colloid-polymer gels. In Part A we present results of an optical microscopy study of the shear of a high Φ_p gel at varying strain and frequency. In Part B we present the results of a comparison between 10Hz and 70Hz oscillatory shear using light scattering-echo, again on a high Φ_p gel. In Part C, we present a wide range of results on the oscillatory shear of dense gels with varying Φ_p and Φ_c conducted with confocal microscopy. This includes quantative analysis of the post-shear gel structure. Finally, we discuss these results in terms of a simple theoretical model and compare our experiments with other relevant work.

6.2 Part A: Optical Study of High Φ_p Gel at Varying Frequency

The experiments on a high Φ_p gel (Sample A1) at varying strain and frequency were conducted with Shear Cell 1, with a plate gap of 0.3mm and studied with an upright optical microscope fitted with a high magnification contrast enhancing DIC objective (see section 2.5.3.2).

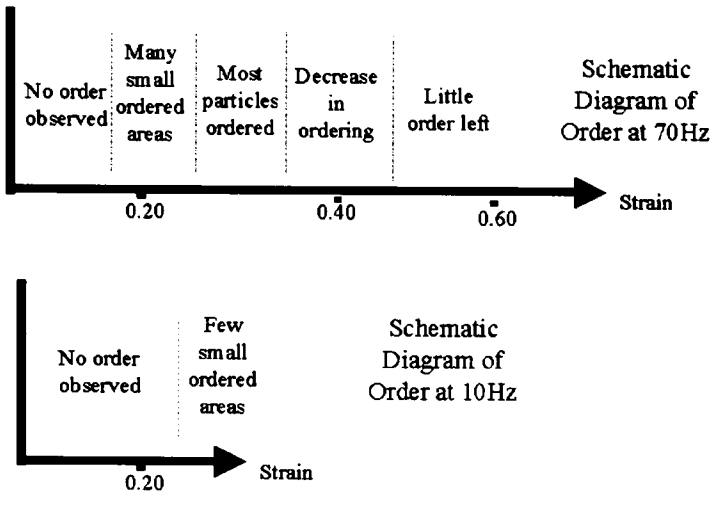

Figure 6.1: The two diagrams compare how much particle ordering is observed at different strains for step shear ramp experiment with Sample A1. Top = 70Hz, Bottom = 10Hz.

6.2.1 70Hz Step Shear Ramp

We first discuss experiments at 70Hz using the step shear ramp method (see section 3.4.3) with sample A1 (see table 3.4). The strain is steadily increased in steps but stopped each time to allow for the sample to be explored with the microscope and for images to be recorded. The structure appears frozen as soon as the shear is stopped. Typically the strain is applied for a duration of 2 minutes at each strain. The strain is increased in steps as shown in figure 3.4. The shear direction is left to right as seen in the microscopy image figures. There is often a small amount of drift of the whole sample during shear. Therefore, it is not always possible to observe the same region of the sample before and after shear

The schematic diagram shown in figure 6.1 (top) summarises the changing structures observed with increasing strain. Structures are seen that are not observed in quiescent colloidal gels. At strains below approximately $\gamma_0 \sim 0.1$, no change to the structure is observed. Images of the sample look similar to those of the quiescent structure shown in figure 5.2. However, increasing the strain further leads to a surprising effect on the structure of the gel. Figure 6.2 (top) shows a typical image of the gel having been sheared at $\gamma_0 = 0.13$. Small regions of ordered particles are observed, clearly visible against the background of the majority of particles that still form a disordered structure. Typically these ordered regions are small in size. Void regions are still present. However, as seen in figure 6.2 (bottom), in some places in the sample larger regions of order are observed coexisting with large voids. The orientation of the ordered regions of

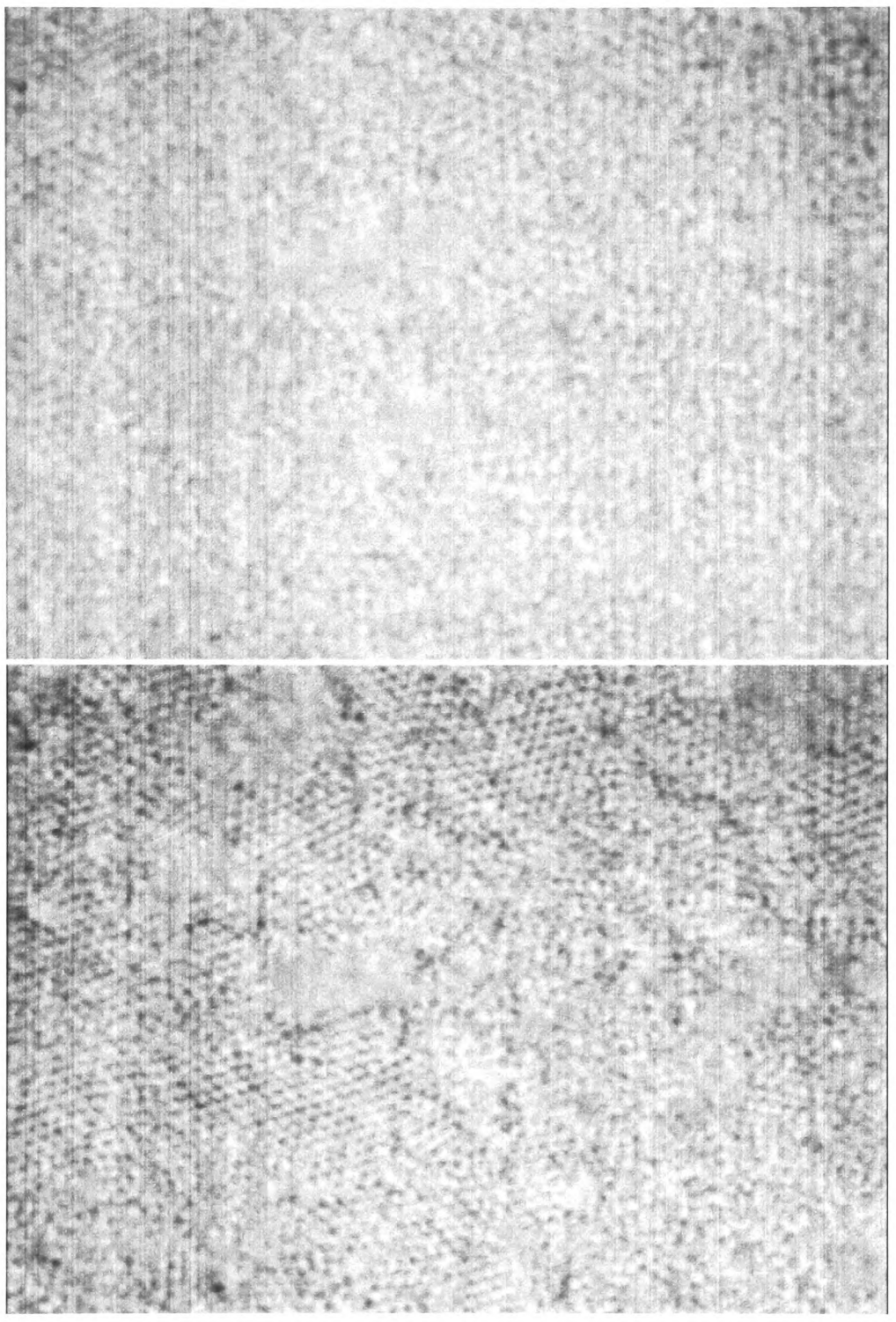

Figure 6.2: Optical Microscopy images from different parts of the sample enhanced with use of DIC. Sample A1 sheared at 70Hz for 2 minutes at γ_0 = 0.13 as part of shear ramp experiment. Depth $\approx$ 50μm. [Top image size $\sim 95\mu m \times 70\mu m$, Bottom image size $\sim 110\mu m \times 85\mu m$]

particles appears to be random. The ordered regions persist on experimental timescales, they appear to be frozen into the gel structure. This corresponds to the "Many small ordered areas" part of the schematic diagram (figure 6.1 (top)).

Increasing the strain leads to an increase in the amount of ordering typically seen. Figure 6.3 (top) shows the gel after experiencing a strain of $\gamma_0 = 0.27$. We observe that some parts of the sample are very ordered consisting of small and medium ordered domains separated by small voids or disordered regions. There appears to be a common orientation to some domains that are not in contact. Also, we observe that some parts of the sample are still disordered (see figure 6.3 (bottom), bottom left hand side). The large voids shown in this figure are quite uncommon and may only be visible when they are sufficiently deep in size to not be obscured by out of focus light from particles in nearby layes. This corresponds to the "Most particles ordered" part of the schematic diagram (figure 6.1 (top)).

Upon increasing the strain further we observe a decrease in the size and number of ordered areas observed. Figure 6.4 shows a typical image for the bulk of the gel after experiencing a strain of $\gamma_0 = 0.46$. The particles are mostly disordered with some small areas of ordered particles. Near the surface of the sample, next to the top plate, some very large voids are observed. Such voids are not observed at lower strains. Also, some less typical places in the sample contain larger regions of order than found here.

At yet higher strains, we observe a further reduction in ordering. In most parts of the sample bulk we observe a completely disordered structure as seen in figure 6.5 (Top) where $\gamma_0 = 0.88$. A few small ordered regions are observed as shown in figure 6.5 (Bottom) but this is atypical. The maximum strain available in this experiment with shear cell 1 for 70Hz was $\gamma_0 = 0.88$.

6.2.2 10Hz Step Shear Ramp

We now discuss the results for the shear ramp experiments conducted at a frequency of 10Hz, also conducted with sample A1 (high Φ_p gel). Again the strain is steadily increased in steps but stopped each time to allow for the sample to be explored with the microscope and for images to be recorded. Typically the strain is applied for a duration of 2 minutes at each strain. The second part of the schematic diagram shown in figure 6.1 (bottom) summarises the changing structures observed with increasing strain. We observed no changes to the structure of the gel for strains around that at which order appears for 70Hz ($\gamma_0 = 0.13$). On increasing the strain further, a few ordered regions are observed as in figure 6.6, which experienced a strain of $\gamma_0 = 0.24$. The majority of the sample remains disordered. Much less order is seen in comparison to

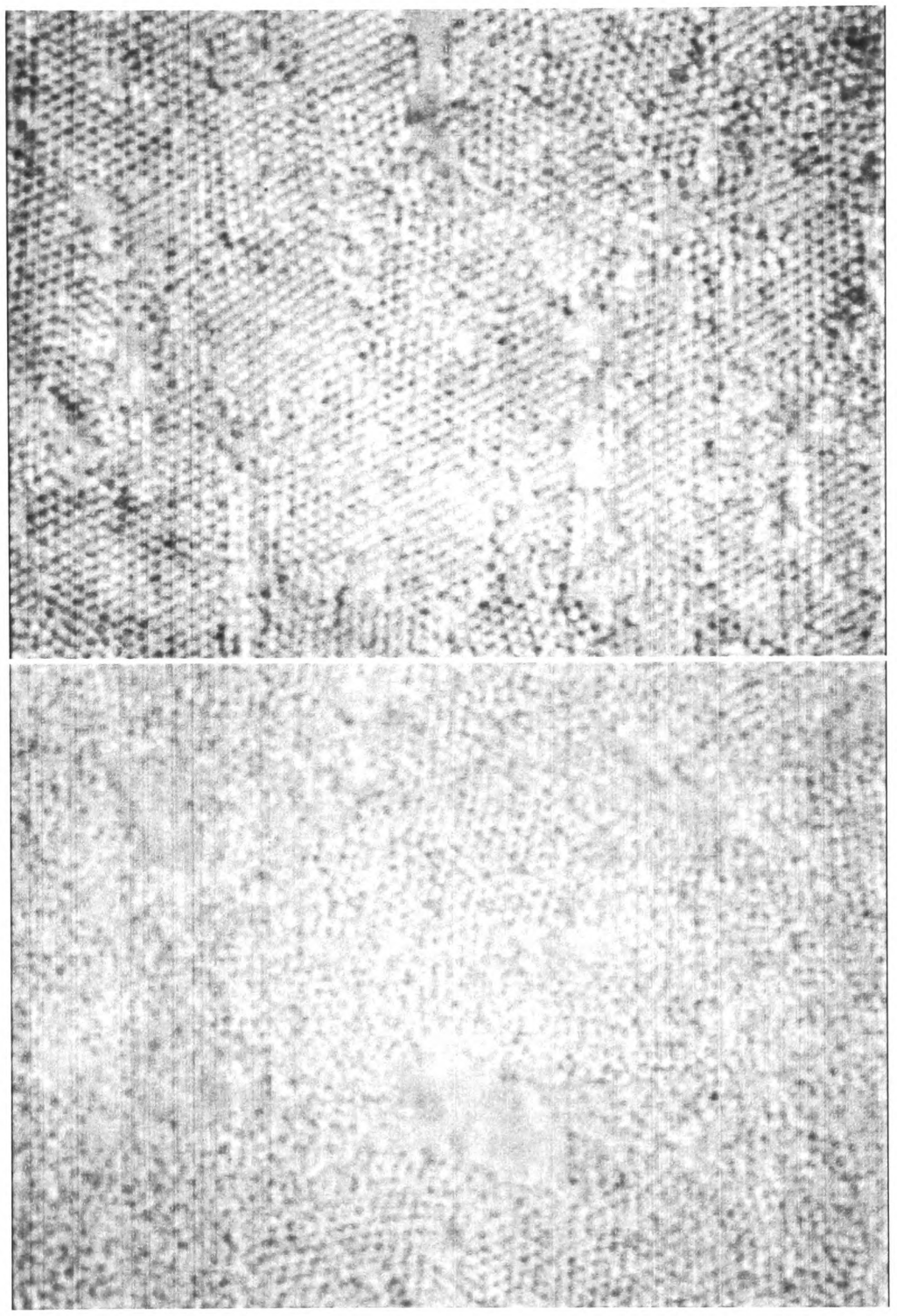

Figure 6.3: Optical Microscopy images from different parts of the sample enhanced with use of DIC. Sample A1 sheared at 70Hz for 2 minutes at γ_0 = 0.27 as part of shear ramp experiment. Depth $\approx$ 60μm. [Top image size $\sim 110\mu m \times 85\mu m$, Bottom image size $\sim 125\mu m \times 100\mu m$]

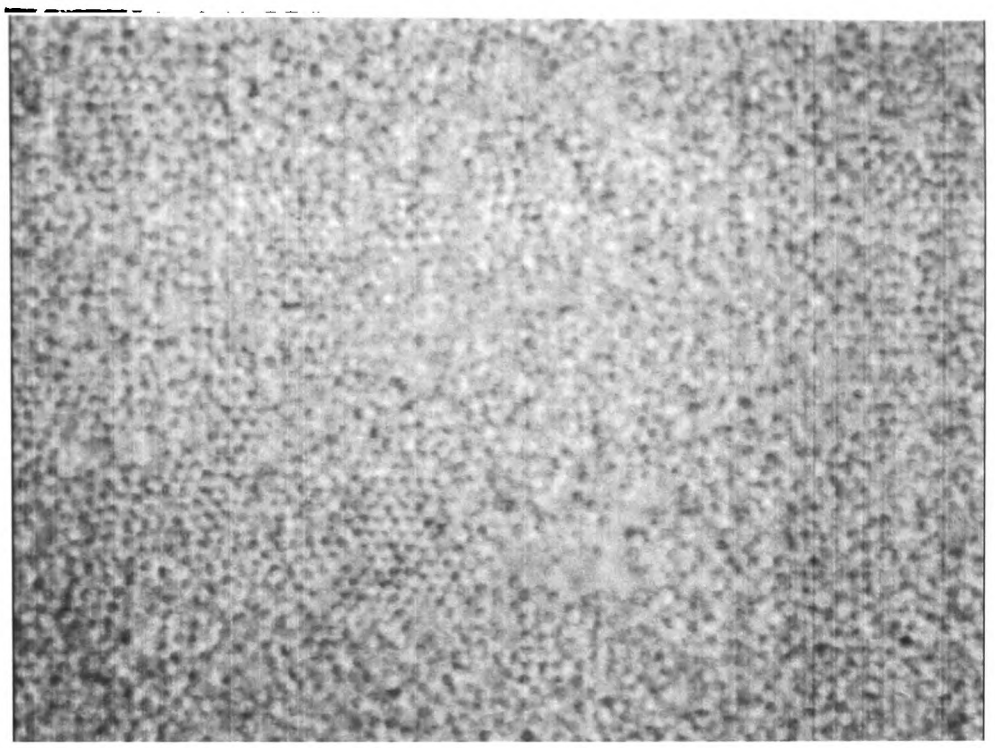

Figure 6.4: Optical Microscopy image enhanced with use of DIC. Sample A1 sheared at 70Hz for 2 minutes at γ_0 = 0.46 as part of shear ramp experiment. Depth $\approx 40\mu m$. [Image size $\sim 125\mu m \times 100\mu m$]

the same strains at 70Hz. Higher strains were unobtainable due to the lack of any resonance at this frequency (see figure 4.7) giving a maximum strain with shear cell 1 at 10Hz of $\gamma_0 = 0.3$. We also conducted an experiment in which a new sample was immediately sheared at 10Hz at a strain of $\gamma_0 = 0.3$. Some parts of the sample become very ordered figure 6.7 (Top) while other parts remain completely disordered figure 6.7 (Bottom). This is in contrast to the experiments conducted by increasing the strain in steps.

6.2.3 1Hz Step Shear Ramp

At 1Hz the same shear ramp experiment was repeated, again using sample A1 (high Φ_p gel). No change in the structure was observed up to the maximum available strain studied ($\gamma_0 = 0.3$). The images recorded looked the same as the quiescent gel structure shown in figure 5.2.

6.2.4 Frequency vs Strain Graph

We summarise the findings for the three experiments in figure 6.8 which plots the structure observed after shear for a given strain and frequency. We can picture a shear "phase" boundary between the cases where order is observed and those where no change in the structure is observed. The observed ordering implies that the particles in the gel structure have rearranged.

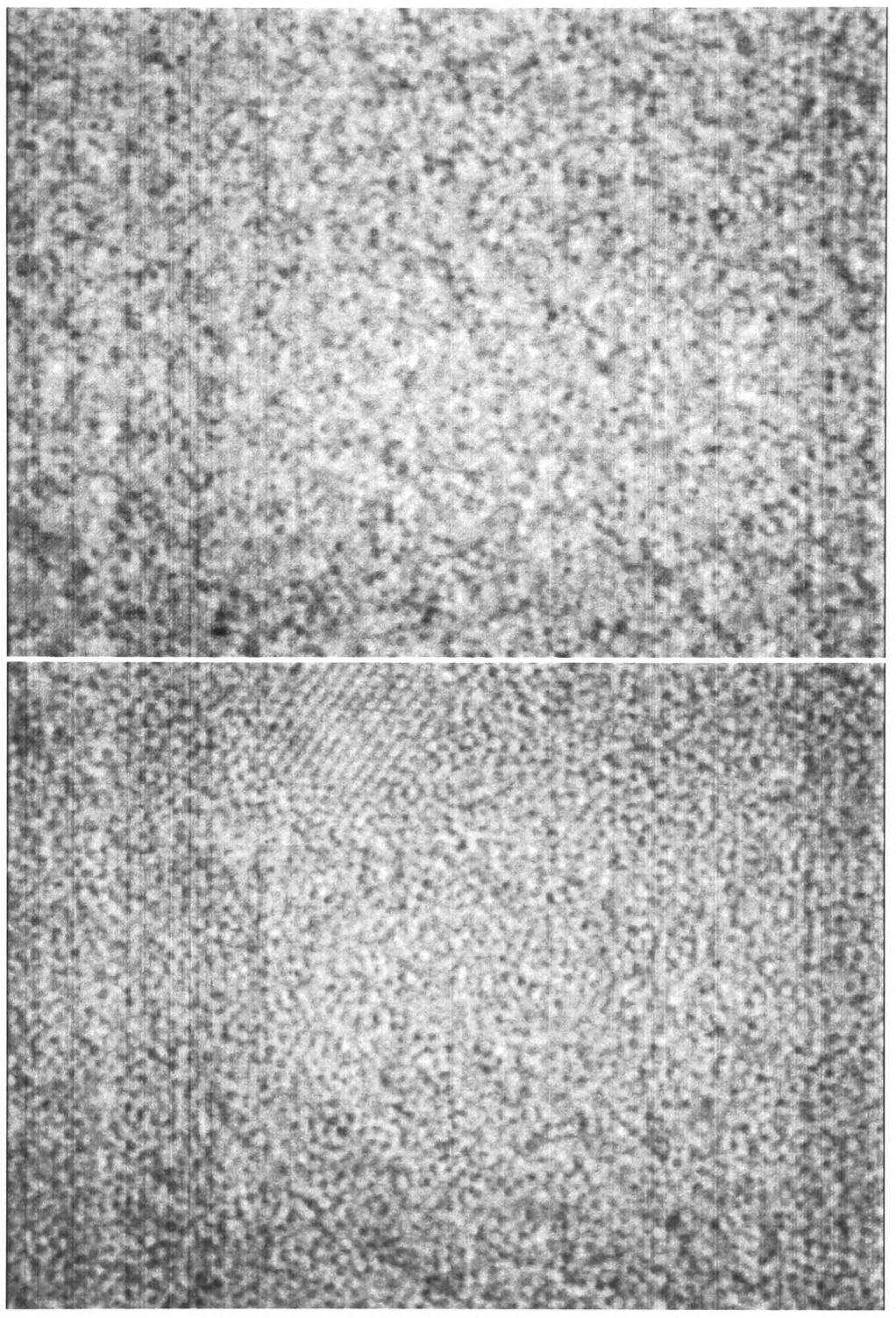

Figure 6.5: Optical Microscopy image from different parts of the sample enhanced with use of DIC. Sample A1 sheared at 70Hz for 2 minutes at γ_0 = 0.88 as part of shear ramp experiment. Depth $\approx$ 20μm. [Image sizes $\sim 110\mu m \times 85\mu m$]

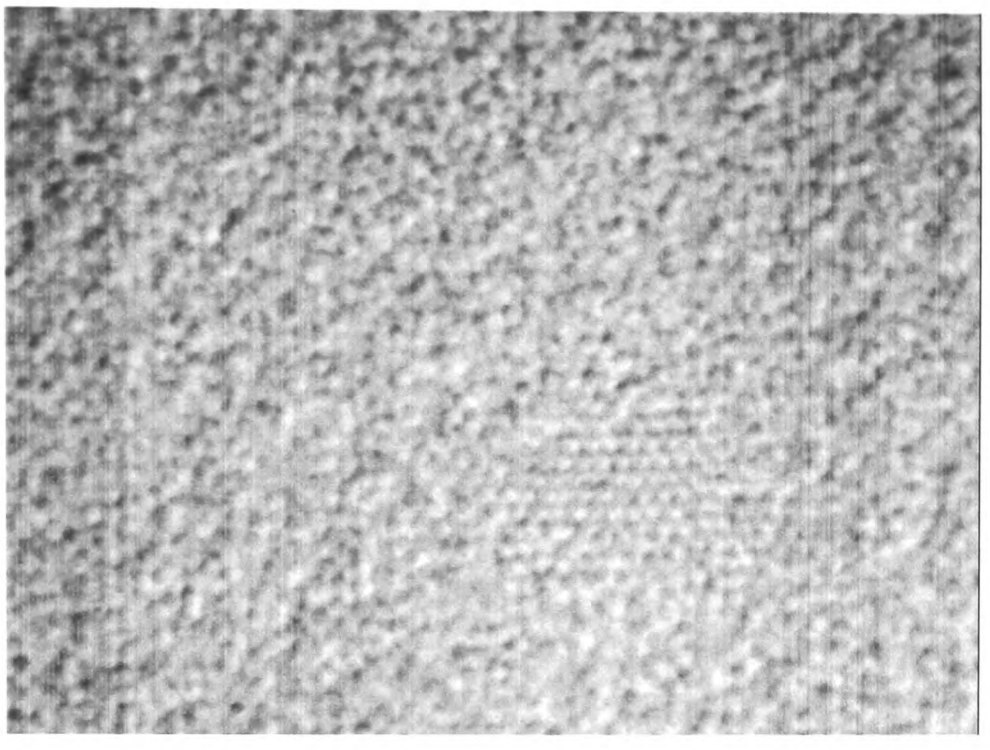

Figure 6.6: Optical Microscopy image enhanced with use of DIC. Sample A1 sheared at 10Hz for 2 minutes at γ_0 = 0.24 as part of shear ramp experiment. [Image size $\sim 90\mu m \times 70\mu m$]

We have found that a higher strain is needed to find ordering/rearrangement at lower oscillation frequencies.

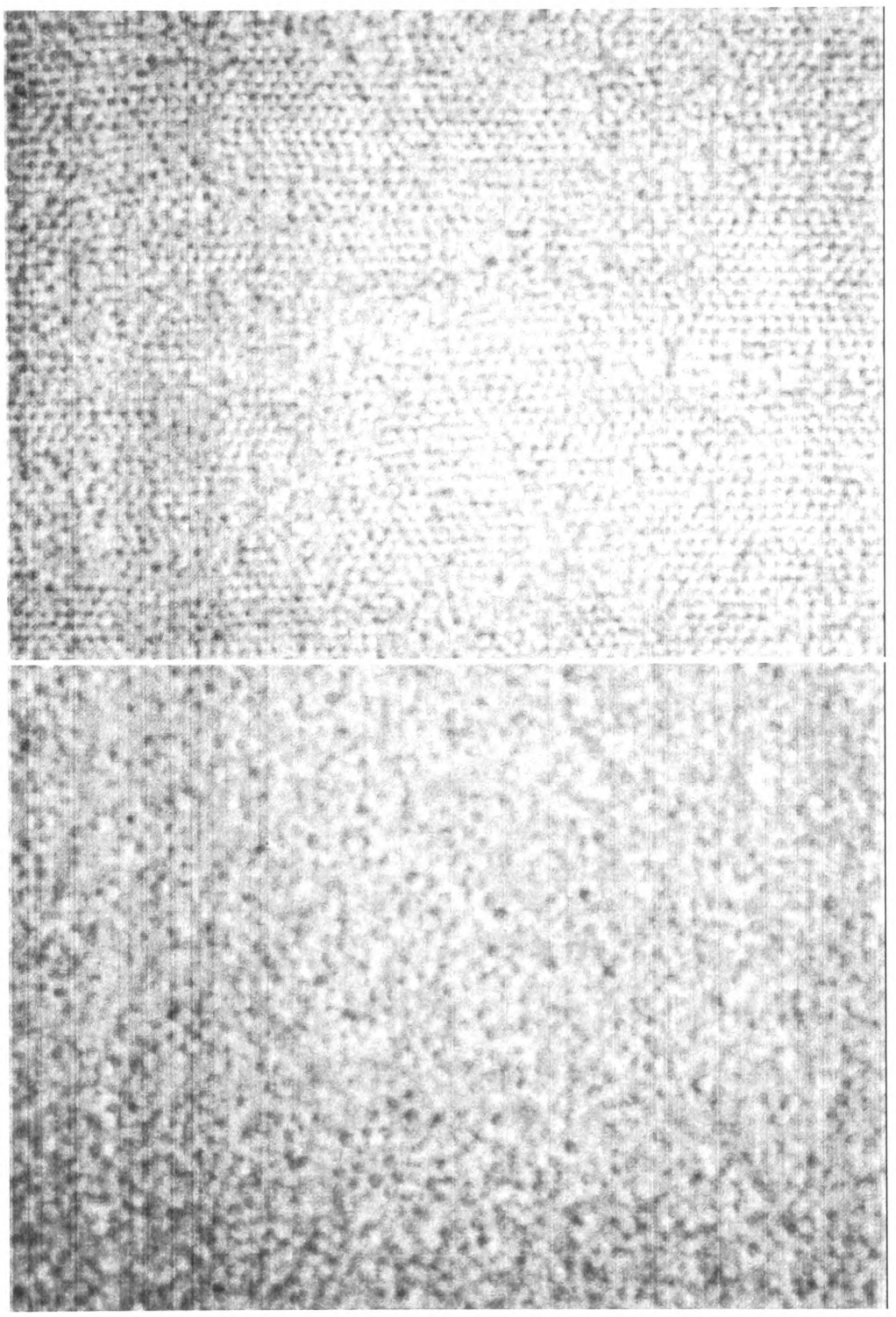

Figure 6.7: Optical Microscopy image enhanced with use of DIC. Sample A1 sheared at 10Hz for 2 minutes at γ_0 = 0.3. This strain was imposed immediately after a fresh sample was loaded. Depth $\approx$ 30μm . [Top image size $\sim 110\mu m \times 85\mu m$, Bottom image size $\sim 90\mu m \times 70\mu m$]

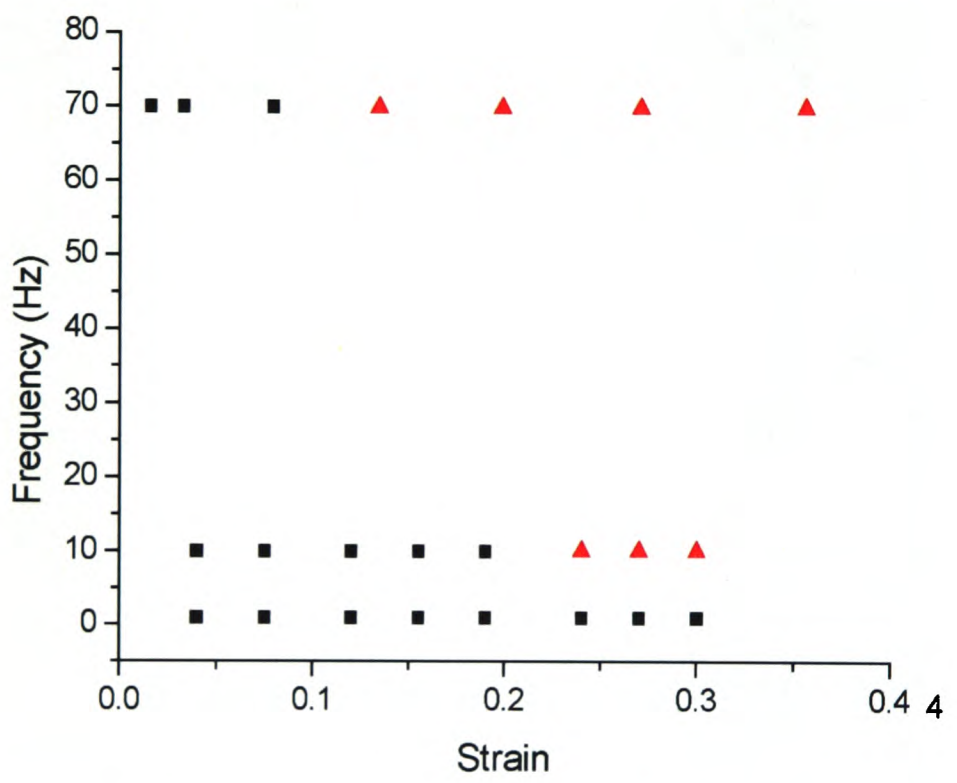

Figure 6.8: Frequency versus strain plots for the experimental optical microscopy data. (■ = no order, ▲ = order), (Sample A1)

6.3 Part B: LS-Echo Study of High Φ_p Gel at Varying Frequency

Experiments were conducted at two different frequencies, 10Hz and 70Hz. These experiments were repeated at three plate separations, 0.8mm, 1.3mm and 1.8mm. Typically experiments were started after a delay after loading of approximately 30 minutes. Up to three sets of results were obtained at each strain. Each set of results took 5 minutes and provided data for different ranges of echos. The strain was then increased and another set of results was obtained. This was repeated up to the maximum strain available. All experiments were conducted with shear cell 1.

6.3.1 Technique Results

Figure 6.9 (Top) shows a typical plot of raw echo data, showing results for several strains at a frequency of 70Hz. Each set of data takes typically 5 minutes in order to obtain good statistics. The strain is then increased and the next set of data obtained. The correlator delay channels in this case are grouped around the initial decay, echos 1 to 5 and 11 to 15. Figure 6.9 (Bottom) shows the initial echo decay and the shape of the 1st echo. The width of the echos decreases as the strain is increased. The channel layout is changed when necessary to accurately determine the echo peak and shape as it changes with increasing strain.

With increasing strain γ_0, the initial decay of the correlation function, arising from the deterministic motion due to the shear flow, speeds up while the echo becomes narrower. The width of the echo (at half height) is twice the initial decay time, τ_{ini}, and directly proportional to the inverse strain rate times the gap, d $(1/\ \dot{\gamma}_0\ d)$ [35]. The linear dependence of the initial decay rate (calculated in our case from the first echo), Γ_0/d (where $\Gamma_0(=1/\tau_{ini})$) on strain amplitude shown in figure 6.10 verifies the absence of wall slip in our measurements. Wall slip would lead to a drop in the observed curve with increasing strain. The increase in strain would not be felt by the sample and therefore there would not be a corresponding decrease in the width of the echo.

There is no significant time dependence (between sequentially obtained data sets) of the echo height for a sample experiencing a constant low strain. This was checked by loading a sample, leaving it for 4.5 hours, then it was sheared it at constant strain ($\gamma_0 \sim 0.001$) at 10Hz (see figure 6.11). Six separate data sets were obtained, one after another from the same part of the sample. The echo height is constant for a given delay time to within $\sim$ 10% over the time

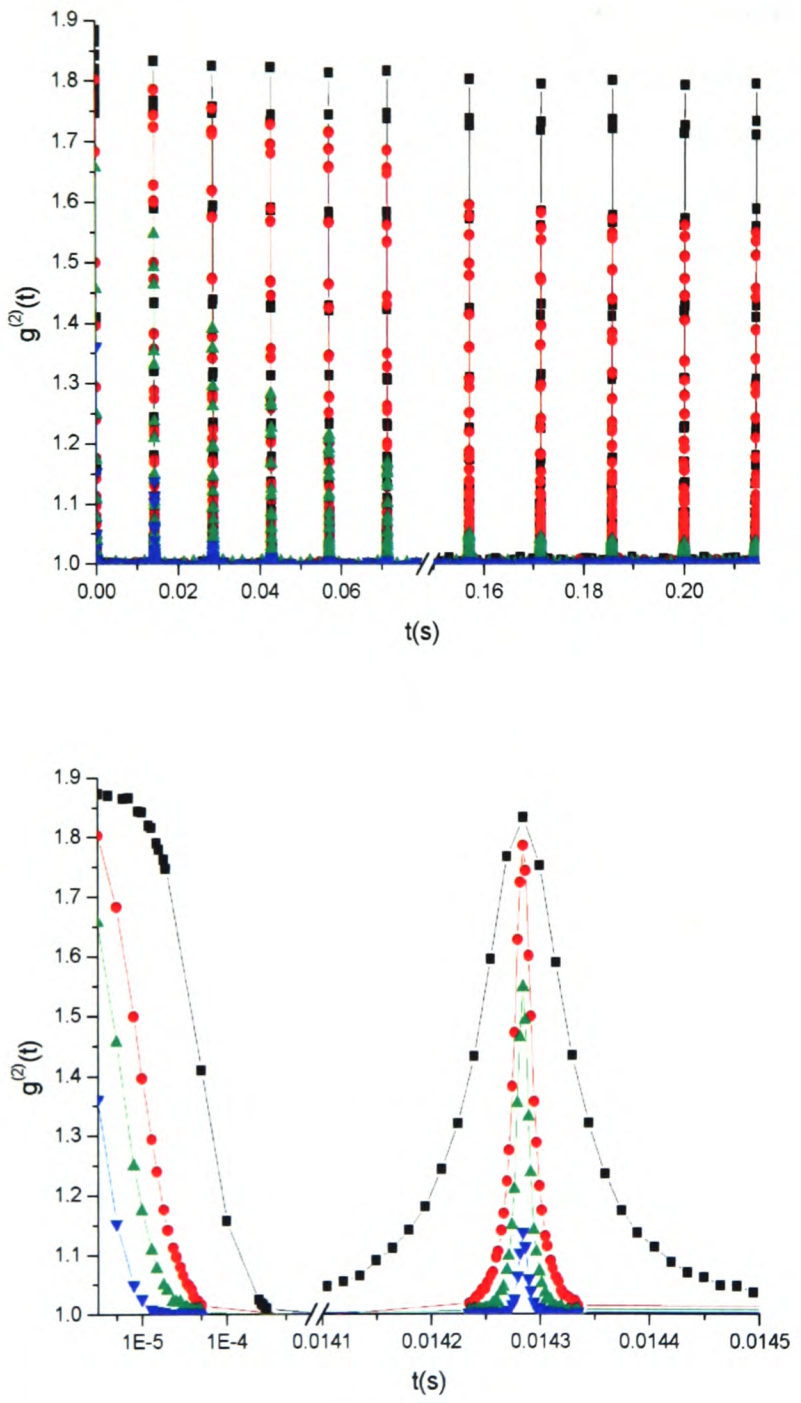

Figure 6.9: Typical LS-Echo plots for a frequency of 70Hz. The top plot shows typical raw data produced by each experiment. In this case, ten echos, 1 to 5 and 11 to 15 are shown. The bottom plot shows the change in the shape of the initial decay and 1st echo with increasing strain. The width of the echo decreases with increasing strain (■, γ_0 = 0.02, •, γ_0 = 0.14, ▲, γ_0 = 0.17, ▼, γ_0 = 0.23). (Plate gap = 1.3mm, Sample A1).

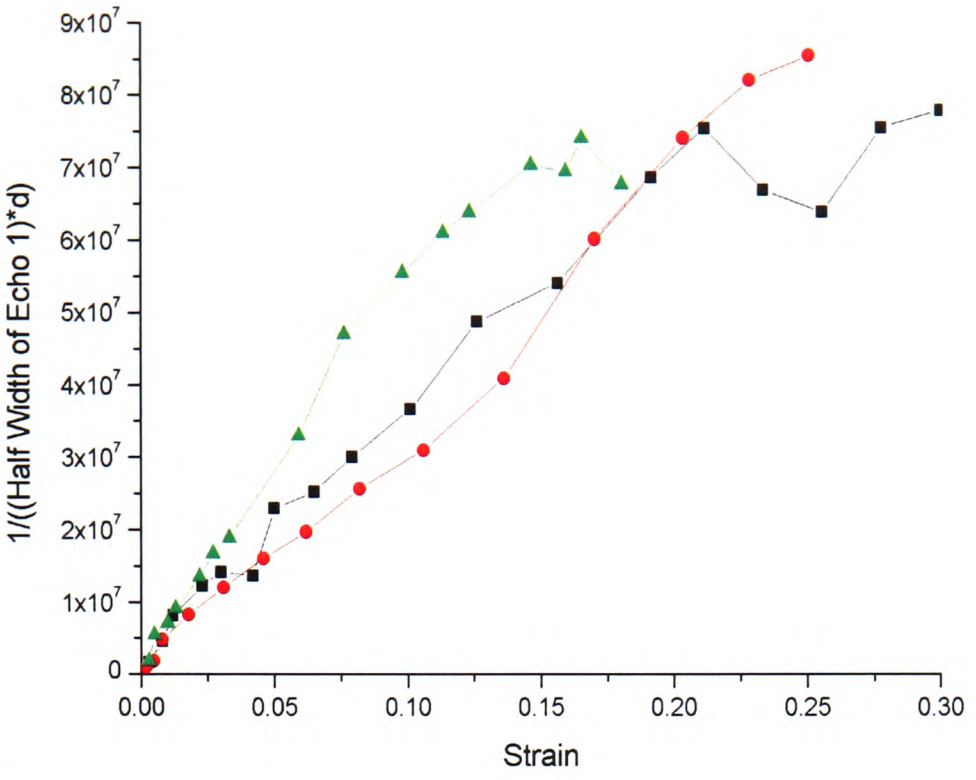

Figure 6.10: The inverse half-width of Echo 1 is plotted against strain for the three plate gaps. A straight line corresponds to no slip of the sample at the plates (Plate gap = 0.8mm (■), 1.3mm (●), 1.8mm (▲), Sample A1).

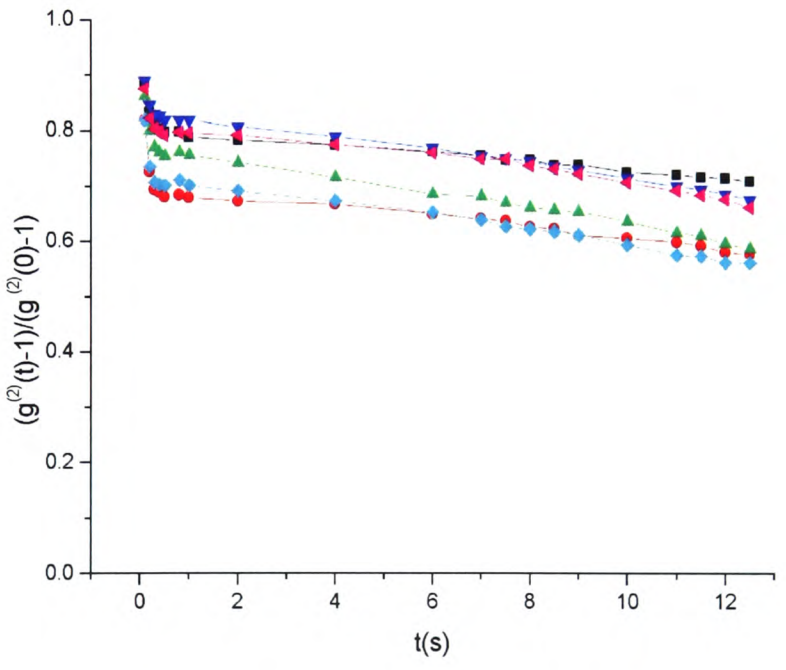

Figure 6.11: 10Hz six repeated measurements in the same place at very low strain, γ_0 = 0.001 with a delay of 4.5 hours after loading before the first set of measurements was taken. (Plate gap = 1.3mm, Sample A1).[Set 1 =■, Set 2 = ●, Set 3 =▲, Set 4 = ▼, Set 5 = ♦ and Set 6 = ◄]

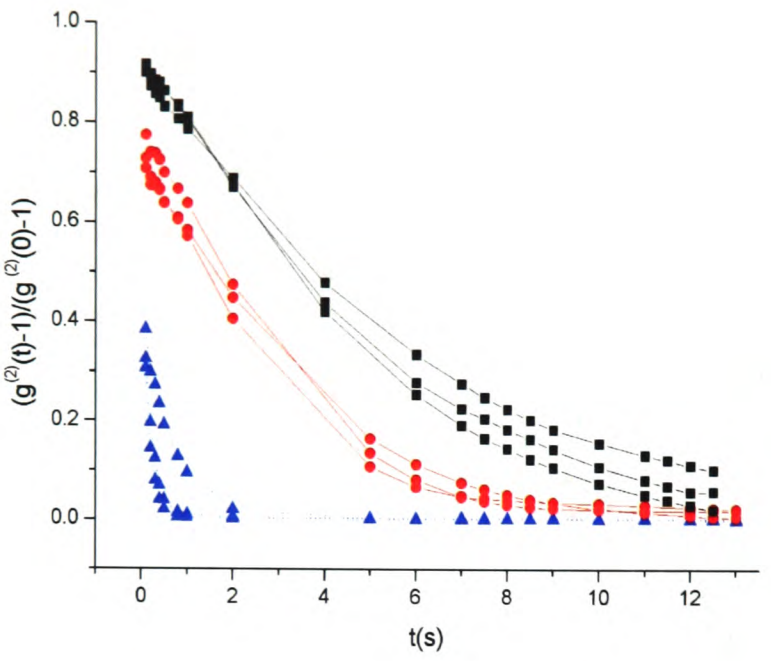

Figure 6.12: 10Hz, Experiment measuring echoes at each strain in turn. This is repeated 3 times to give a set of data for each γ_0 = 0.001 (■), 0.019 (•), 0.063 (▲)(Plate gap = 1.3mm, Sample A1).

taken to record the six data sets ($\sim$ 1hour). There is no apparent dependence on the sequence in which the data sets were obtained. Any greater decrease in the echo heights are due to the effect of the strain imposed on the sample.

If a sample is ergodic then an ensemble average (over all parts of the sample) which is required to calculate the correlation function is the same as a time average at a particular place in the sample. However, a colloid-polymer gel is non-ergodic, due to its inhomogeneous structure. Therefore a time average in different places may give different results, not always the same result as an ensemble average. The oscillatory shear of the sample during the light scattering measurement partly solves this problem. Different speckles are detected during the shearing motion so there is a partial ensemble average as well as a time average conducted during each measurement. We checked that the individual echo plots were reproducible, a test to see if a good enough ensemble average was being conducted. Figure 6.12 shows three repeated experiments at increasing strain for a frequency of 10Hz. There are only small differences between each set of data for each strain. The qualitative behaviour is the same and the spread between the data sets gives an estimate of the error in echo height for each set of data in the other echo plots.

6.3.2 Experimental Results

6.3.2.1 70Hz Step Shear Ramp

Figure 6.13 show a typical complete set of results for changing strain, at a frequency of 70Hz for a gap of 1.8mm. The data has been normalised by the initial decay height and only the envelope joining the echo peak heights is shown. For low strain (up to γ_0 = 0.06) the echo height is unchanged, remaining flat around 1 with increasing delay time. The height of the echoes decrease with increasing strain. The higher order echos drop in height more than lower order echoes. Figure 6.14 shows a wider range of echos at 70Hz ($d = 1.3mm$) than figure 6.13. Only selected strains are shown for clarity in the top part of the figure. For a given strain the echo height drops to zero within a delay timescale which we define as τ_{decay}. For strain, $\gamma_0 = 0.17$, $\tau_{decay} \sim 0.7s$ as shown as a dotted line in figure 6.14.

6.3.2.2 10Hz Step Shear Ramp

Figure 6.15 shows a typical complete set of results for changing strain, at a frequency of 10Hz for a gap of 0.8mm. In contrast to 70Hz, at low strain there is a drop in the echo height with increasing echo number. The frequencies of 70Hz and 10Hz imply another relevant time scale. This time scale has to be compared with the other important time scale of Brownian motion. Localised Brownian motion of the colloidal particles is found to be significant at the time scale probed by the 10Hz experiments (see section 6.3.3.1). The 100th echo corresponds to 10 seconds for 10Hz but only 1.4 seconds for 70Hz. Similarly to 70Hz the echo height drops with increasing strain, with the higher order echos dropping by a larger amount and at lower strains. In figure 6.16 we show selected echoes for the experiment at 10Hz (gap, $d = 0.8mm$) as well as for comparison the position of the timescale, $\tau_{decay} = 0.7s$ (for $\gamma_0 = 0.17$ at 70Hz). In contrast to the 70Hz experiment (figure 6.14) the echo height in the 10Hz experiment has not dropped to zero for strains $\gamma_0 > 0.17$ within this delay time of 0.7s. For $\gamma_0 = 0.22$ in the 10Hz experiment, $\tau_{decay} \gg$ 1s.

6.3.2.3 Strain vs Echo Height

In order to concentrate just on shear-induced rearrangement, we define

$$P \equiv \sqrt{g^{(2)}(\tau) - 1} \qquad \text{for} \qquad \tau = \mathrm{mT} \tag{6.1}$$

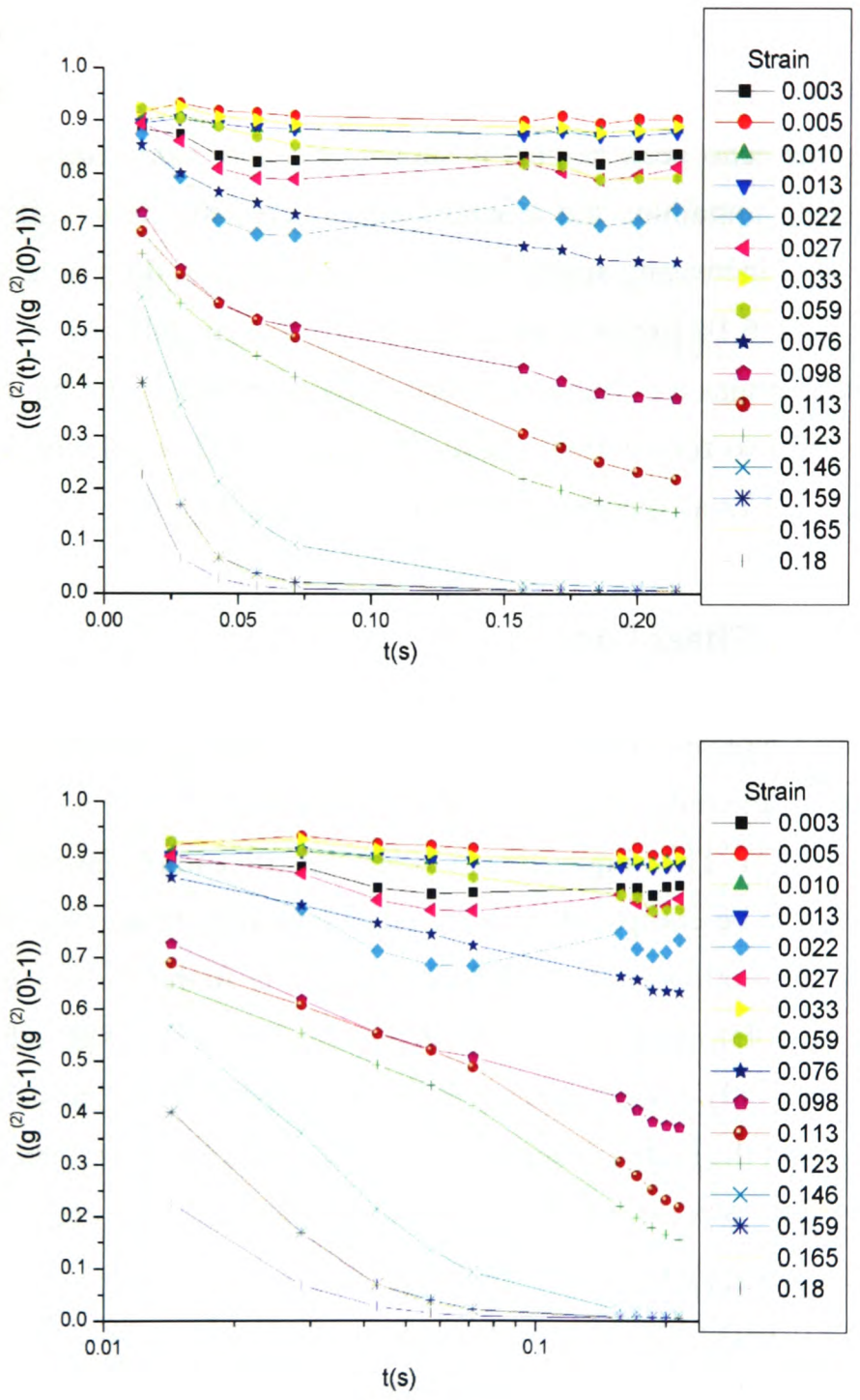

Figure 6.13: Top: Typical LS-Echo plot for a frequency of 70Hz. It shows the height of ten echoes, 1 to 5 and 11 to 15, for a range of different strains. Bottom: Same plot but with log scale on x-axis (Plate gap = 1.8mm, Sample A1).

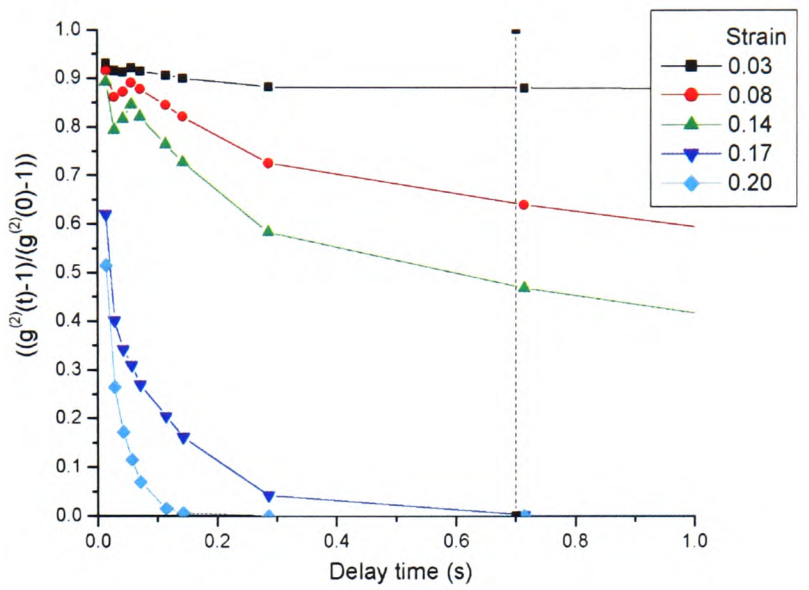

Figure 6.14: Typical Light Scattering Echo plot for a frequency of 70Hz (d=1.3mm). The top plot shows the height of ten echos at five selected strains. The bottom plot is the same data set but showing the full range of strains for comparison. shear experiment, . Vertical dashed line is the decay time, $\tau_{decay} = 0.7$s for $\gamma_0 = 0.17$.

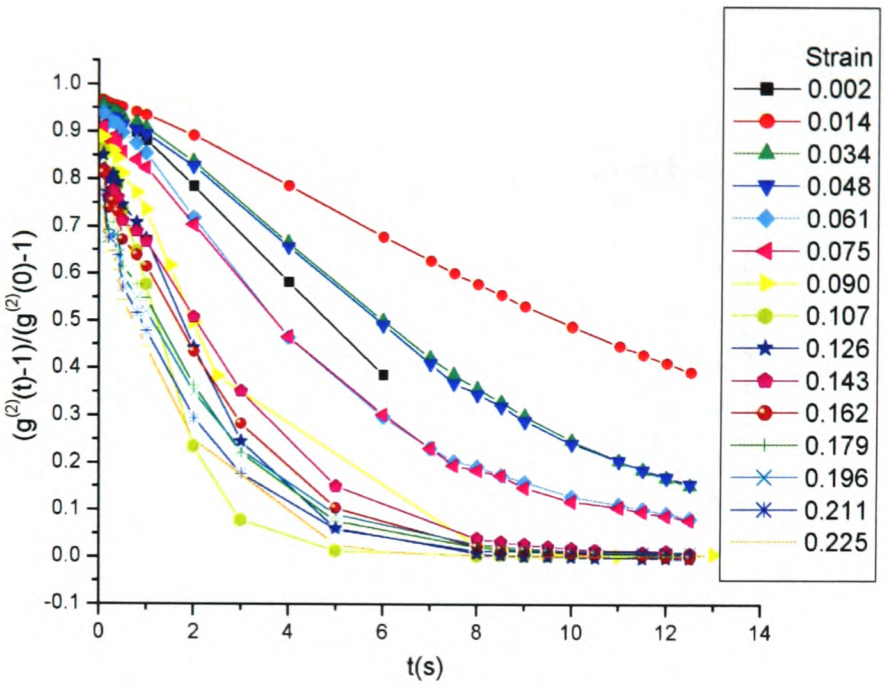

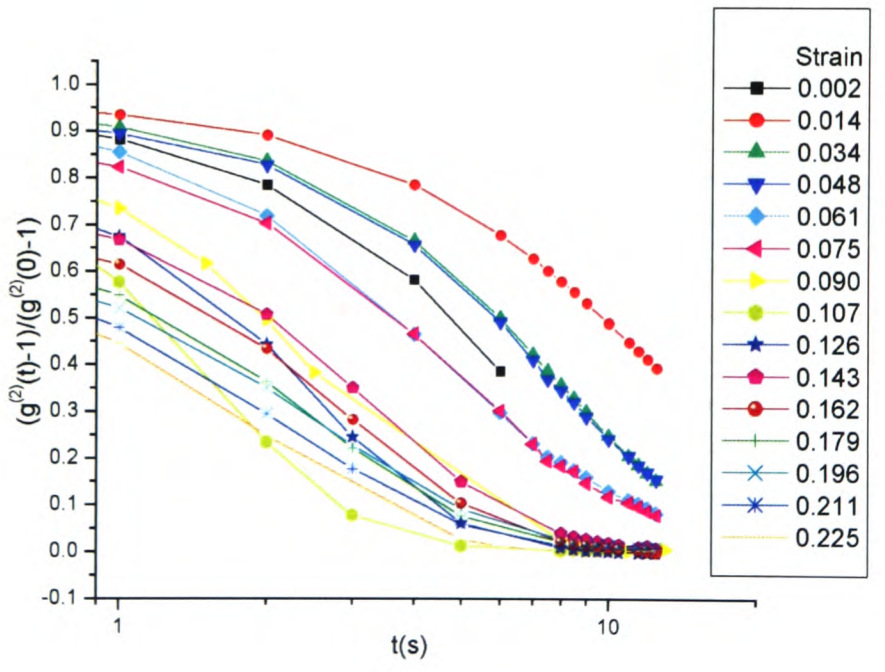

Figure 6.15: Top: Typical LS-Echo plot for a frequency of 10Hz. It shows the height of 20 echoes ranging from the 1st to the 125th echo. for several different strains. Bottom: Same plot but with log scale on x-axis (Plate gap = 0.8mm, Sample A1).

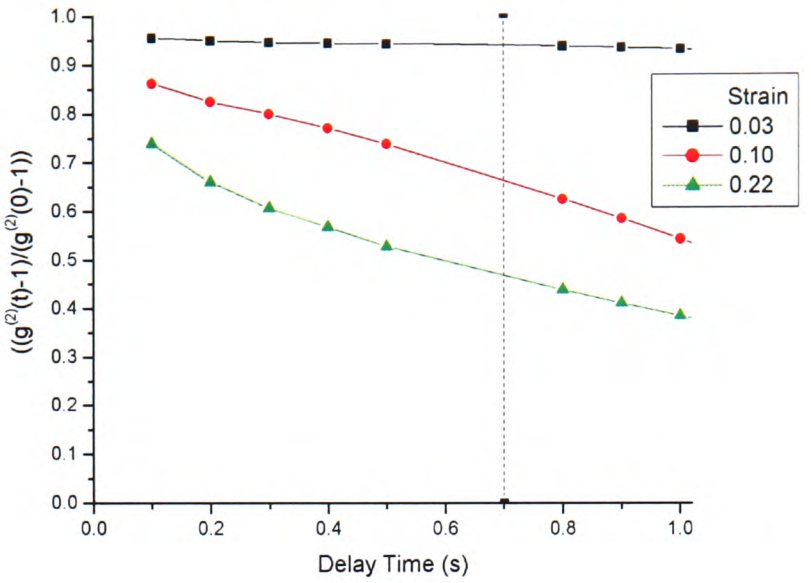

Figure 6.16: Typical Light Scattering Echo plot for a frequency of 10Hz (d=0.8mm). The plot shows the height of ten echos at three selected strains. Vertical dashed line is the decay time, $\tau_{decay} = 0.7$s for $\gamma_0 = 0.17$ at 70Hz, as shown in figure 6.14.

and consider the quantity P/P_0 where $P_0 = lim_{\gamma_0 \to 0} P$ [27], which measures the height of the echo at a certain strain relative to its height at low strain. At low strain amplitudes this quantity has a value 1, and any reduction from 1 reflects only reversible rearrangements. From equations 2.20 and 6.1 we get

$$P/P_0 \simeq \exp\left\{-\frac{1}{6}Nk^2\langle\Delta r^2(mT)\rangle_S\right\} \tag{6.2}$$

In figure 6.17 the effect of oscillatory shear, measured by the quantity P/P_0 is shown for 70Hz and 10Hz experiments conducted with three different gap thicknesses, 0.8mm, 1.3mm and 1.8mm. Figure 6.17 (Top) shows P/P_0 against strain for three different echos, for both 70Hz and 10Hz at a gap of 0.8mm. For 70Hz, the height of the first echo remains constant until $\gamma_0 \sim 0.25$ is reached. For $\gamma_0 \gtrsim 0.25$ the 1st echo decays sharply toward zero. By $\gamma_0 \sim 0.4$ the first echo has decayed to $P/P_0 \sim 0.4$. The 20th echo drops much earlier at $\gamma_0 \sim 0.12$ steeply toward zero. By $\gamma_0 \sim 0.2$, the 20th echo has decayed to $P/P_0 \sim 0.3$. No data for the 120th echo was obtained for 70Hz at this gap thickness.

For 10Hz, similar behaviour is seen. Unfortunately, only strains up to $\gamma_0 = 0.23$ were accessible due to technical reasons. The first echo decays slightly from $P/P_0 = 1.0$ to 0.9 by $\gamma_0 = 0.23$. The 20th echo at low strain is quite flat but at a lower value of $P/P_0 \sim 0.8$ due to the effect of Brownian motion already discussed. By $\gamma_0 \sim 0.2$ the 20th echo has sharply decayed to

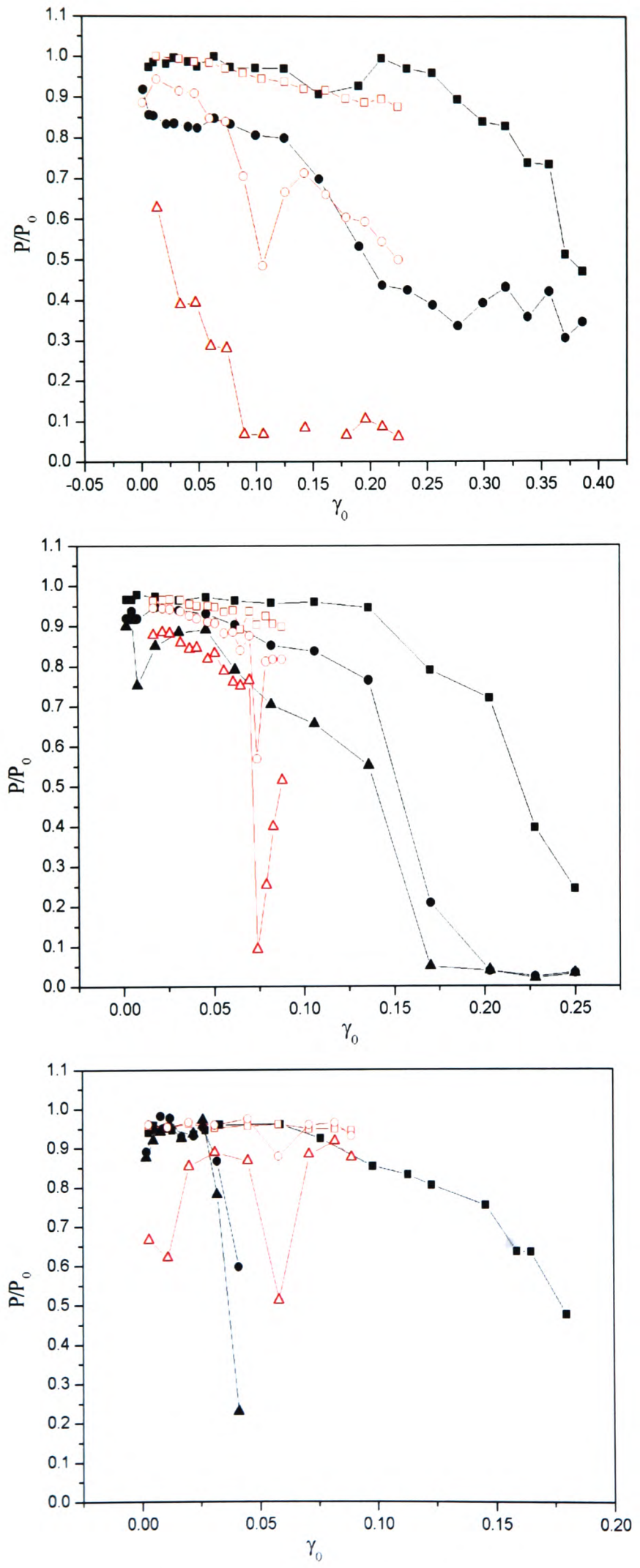

Figure 6.17: Strain dependence of the relative echo height (P/P_0) limit at γ_0=0 [P] for plate gap thicknesses of 0.8mm (Top), 1.3mm (Middle) and 1.8mm (Bottom). Shown are plots of the 1st echo (■), 20th echo (•) and 120th echo (▲) for 70Hz and the 1st echo (□), 20th echo (∘), and 120th echo (△) for 10Hz (Sample A1).

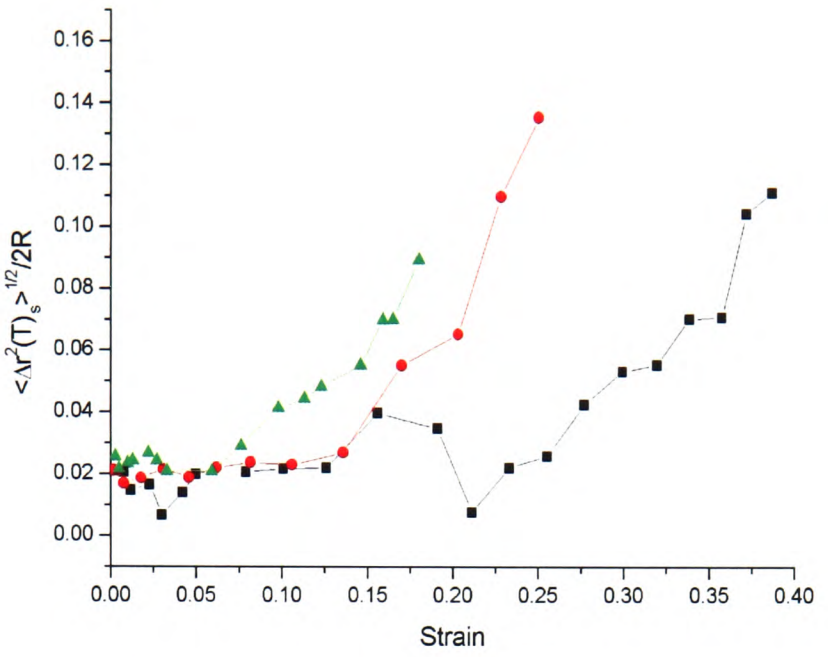

Figure 6.18: Square root of the shear-induced mean square displacement normalized to the particle diameter, $\sqrt{\langle \Delta r^2(\tau) \rangle_s}/2R$, as a function of strain amplitude for the three plate gap sizes [0.8mm (■) $N = 2$ as $N \geq 2$, 1.3mm (•) $N = 2.5$ and 1.8mm (▲) $N = 3.1$] (Sample A1).

$P/P_0 \sim 0.5$. The 120th echo decays at very low strain. By γ_0 = 0.1 the 120th echo has decayed away completely.

Figure 6.17 (Middle) shows the same echo height plots against strain for 70Hz and 10Hz for a plate gap of 1.3mm. The same trends are seen this larger gap, but the echos decay at lower strains than for a gap of 0.8mm. For 70Hz, the 1st echo starts to decay at $\gamma_0 \sim 0.15$ and by $\gamma_0 \sim 0.25$ has decayed almost to zero. The 20th and 120th echos have decayed to zero by $\gamma_0 \sim 0.1$. Figure 6.17 (Bottom) shows the same echo height plots against strain for 70Hz and 10Hz for a plate gap of 1.8mm. Again, similar trends are seen as in the smaller gaps. For 70Hz the 1st echo decays at a lower strain, decaying to $P/P_0 \sim 0.5$ by $\gamma_0 \sim 0.18$.

From the dependence of the height of the first echo with strain we can calculate the shear-induced mean square displacement of the scatterers, found by rearranging equation 6.2. Figure 6.18 shows the square root of the shear-induced mean square displacement normalised to the particle diameter, $\sqrt{\langle \Delta r^2(\tau) \rangle_s}/2R$, as a function of strain amplitude for the three plate gap sizes. The values for N are taken from section 3.3.1.3. The increase in mean square shear-induced displacement with increasing strain is found to be different for the three different plate gap sizes. This is not what we expect as $\sqrt{\langle \Delta r^2(\tau) \rangle_s}/2R$ is independent of the measurement geometry. This is discussed further below.

6.3.3 Light Scattering Echo Specific Discussion

Later on (section 6.5.1) we propose a model for the global response of dense colloidal gels to oscillatory shear that can make sense of many aspects of our experimental observations. Here we first discuss certain aspects of our echo light scattering data that will not be picked up again when we introduce our shear model.

6.3.3.1 Drop of low γ_0 high order echos at 10Hz

In the 10Hz LS-echo experiments (see figure 6.15) a decrease in the echo height at high echo number ($\tau \sim 10s$) is observed for all strains. No decrease in high order echos ($\tau \sim 1s$) is observed in the 70Hz experiments at low strains (see figure 6.14). We can make some progress in understand this behaviour by considering the relative timescales of Brownian motion and shear flow as expressed by the Peclet number (see equation 2.16). We can estimate the Peclet number for the particles used in the light scattering experiments at the two different frequencies. We use our known values for the particle radius, R = 690 nm (Sample A1) and the temperature, T = 295K. We must calculate the shear rate for each of the two frequencies. We can only estimate the shear rate using equation 4.2. We also need a value for the viscosity experienced by a colloidal particle in the colloid-polymer gel, but this is not known. So instead we estimate it using the solvent viscosity, η_s, which is the lower bound on the viscosity. This gives us for 70Hz, $Pe \gg 1$ for all measured strains (e.g. for $\gamma_0 = 0.05, Pe \sim 20$). For 10Hz, $Pe > 1$ for all but the lowest measured strains (e.g. for $\gamma_0 = 0.05, Pe \sim 2$). However, it is an order of magnitude lower than that found for 70Hz. For 1Hz, $Pe < 1$, for strains up to $\gamma_0 \sim 0.2$ and Pe ~ 1 for higher strain (e.g. for $\gamma_0 = 0.05, Pe \sim 0.2$). Note a more realistic viscosity would be larger than the cis-decalin viscosity which corresponds to higher Peclet numbers as the particle would feel a greater resistance to its motion, giving a larger τ_{relax}. The calculated Peclet number is consistent with the interpretation that Brownian motion is responsible for the echo drop. The Brownian motion timescale is smaller than the shear timescale but still large enough to be detected at long times/ high echo number. The 70Hz peclet number is much larger so the Brownian timescale is much too long in comparison with the shear timescale to be detected even at high echo number.

6.3.3.2 Linking LS-echo results with ordering

In the LS-echo experiments the Bragg scattering of the laser beam by the sample was regularly checked for evidence of Bragg spots which would indicate particle ordering in the sample. No Bragg spots were observed even in experiments where the strains lead to clear ordering in the corresponding optical experiments. This prevents us from making a link between particle ordering and the drop in the height of the echos observed in the LS-echo experiments; such as the drop in the echo height corresponding to ordering of the particles. We can explain the lack of Bragg spots by looking at the 2-D FFT (equivalent to Bragg spots as both in Fourier space) shown in figure 6.20. For a perfect crystal structure we expect a diffraction pattern (equivalent to FFT) with intensity maxima at a spacing that corresponds to the unit cell size of the crystal at a given angle, as the crystal acts as a diffraction grating for the laser light. However, we find that even the most ordered gel samples produced only weak bright regions in the resulting FFT. Therefore, we draw the conclusion that any ordering of the gel that did occur during the LS-echo experiments would have lead to a diffraction pattern (where the Bragg spots would be seen) which would have only very faint bright regions at best i.e. similar to the average of the FFT's of both ordered and disordered gel regions i.e. This is consistent with the observation of no bright Bragg spots during the LS-echo experiments.

6.3.3.3 Echo drop at lower strains for thicker plate gaps

The basic idea is that the differing number of scattering events for the different plate gap thicknesses should correspond to different length scales being probed and therefore account for the differences in the echo plots we observe (see figure 6.17). The plot of $\sqrt{\langle \Delta r^2(\tau) \rangle_s}/2R$ (see figure 6.18) should show all the curves on top of each other as the different length scale (from different N) is taken into account. We do not find this. When we use a thin gap (low N) we find the height of the echos drop at a higher strain than for the large gap (higher N), which seems to make sense. As we probe a smaller length-scale with the large gap so we find that the gel rearranges at this length-scale at lower strains than when we consider a longer length-scale (thin gap). Rearrangement on the smaller length scale cannot be detected using the thin gap so there will be no drop in the echo heights. It is possible that the theory breaks down at low numbers of scattering events as the theory is based on the many scattering events (DWS) limit.

6.3.3.4 Slip check

By measuring the decrease in half width of the echoes with increasing strain we have shown that no significant slip of the sample at the plates is found (see figure 6.10. However, we did not expect to find a different dependence of the half width on strain for the different plate gaps. We do not currently have an explanation for this.

6.4 Part C: Confocal Study of Dense Gels with Varying Φ_p

6.4.1 31 Minutes Shear at 70Hz, $\gamma_0 = 0.15$

We first present an experiment with a long shear time (31 minutes) at a single strain, $\gamma_0 = 0.15$ at 70Hz for a high Φ_p gel, sample D1 (see table 3.4). This experiment was conducted with Shear Cell 3 and studied with the Nikon inverted LSCM fitted with a high magnification objective lens. The quiescent structure before shear (Stack 1) is shown in figure 6.19 (Top left) and is the same stack as used in figure 5.8 (A) in chapter 5. After the shear was stopped, three 3-D image volumes were recorded. These are also shown in figure 6.19. The randomly chosen location in the sample (Stack 2) is clearly different from the quiescent structure. Small ordered groups of particles coexist with disordered regions and small voids. Stacks 3 and 4 were chosen for the extreme behaviour shown. Stack 3 is a 3-D volume which is more highly ordered than typically found and Stack 4 is a 3-D volume containing an unusually large void as well as mostly highly ordered regions. All of the particles were frozen in the configuration shown with no particle motion at observable length-scales. Each 3-D volume contains about 30,000 particles. The fast Fourier transforms (FFT) for the four stacks are shown in figure 6.20. The FFTs for the three sheared stacks are different from the quiescent FFT. The FFT of stack 4 has 6 bright regions in a hexagonal configuration. The FFT of stack 3 has two brighter regions at the centre left and centre right. The FFT of stack 2 is similar to stack 3 but less pronounced.

We obtained the particle coordinates for these 4 stacks using the methods described in section 3.4.4. This allows us to compare quantitatively the structures. We calculated the colloid volume fraction Φ_c for each stack from the number of particles, N, located in each stack using equation 2.1. We found that that the quiescent stack (1) that $\Phi_c = 0.43$ which is close to the expected value of $\Phi_c = 0.439$ for Sample D1. For Stack 2 and 3 we found $\Phi_c = 0.44$ and $\Phi_c = 0.46$ for Stack 4.

6.4.1.1 Radial Distribution Functions

We compare the radial distribution functions (RDF) for the three sheared stacks with the quiescent stack to see how the RDF is affected by shear. The x-z and y-z projections appear to show that the particles are arranged in lines corresponding to 2-D planes in the x-y plane. Therefore, we first compare the 2-D radial distribution functions in the three different plane directions (x-y, y-z, x-z) before looking at the full 3-D RDF.

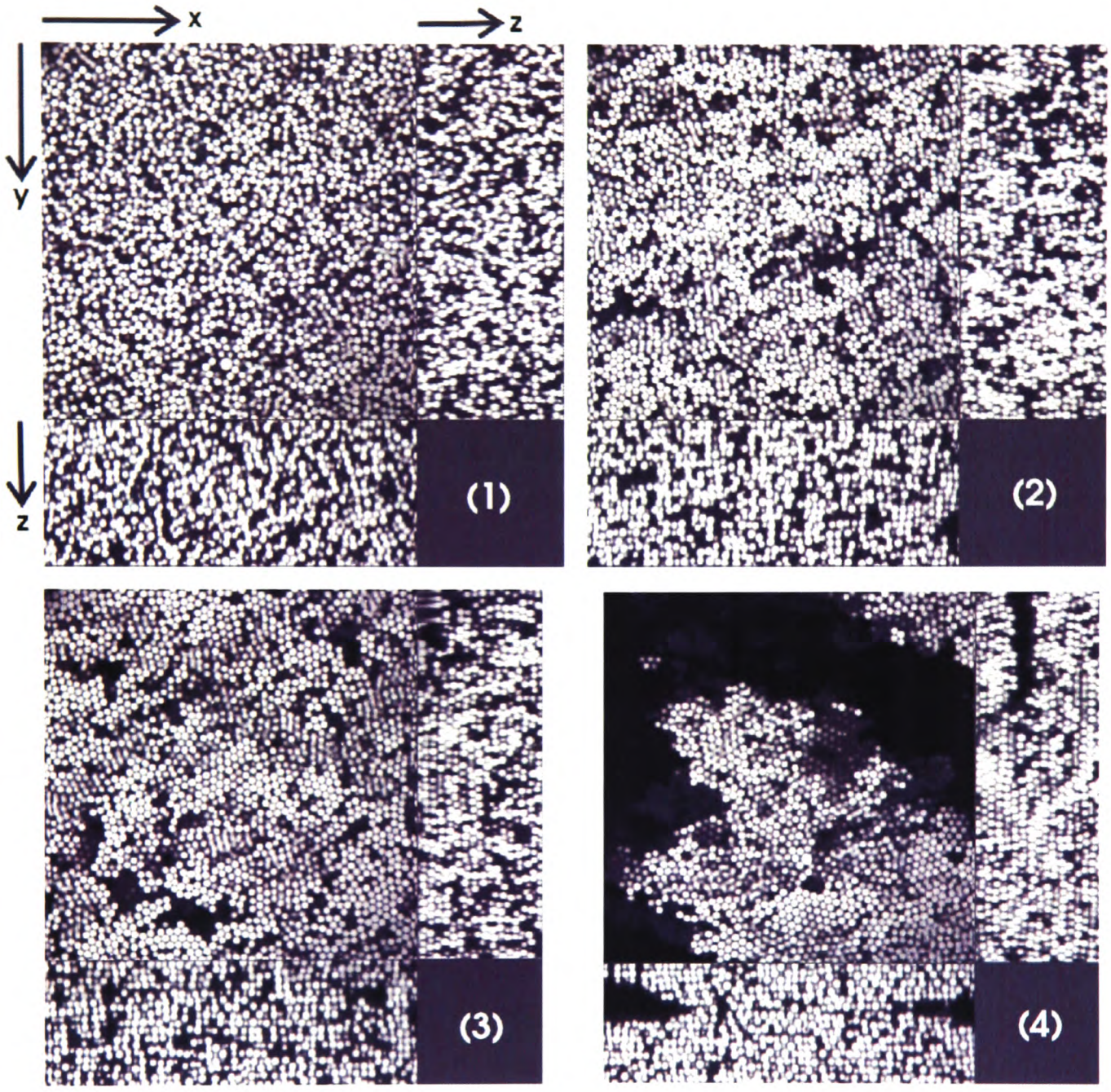

Figure 6.19: 2-D xyz projections of 3-D image volumes used for locating particle centres. Top left image (Stack 1) is the quiescent gel state, before shear. The other three image volumes were recorded after the sample had experienced $\gamma_0 = 0.15$ for 31 minutes at 70Hz. Top right (Stack 2) is a randomly chosen location in the sample. Bottom left (Stack 3) is a highly ordered region. Bottom right (Stack 4) is a region containing a very large void surrounded by ordered regions. (Sample D1). [Image volumes=$103\mu m \times 103\mu m \times 40\mu m$] [square image = x-y plane, projection on right side = y-z plane, projection below = x-z plane],[x = velocity direction (V), z= shear direction (∇), y = $\nabla \times V$

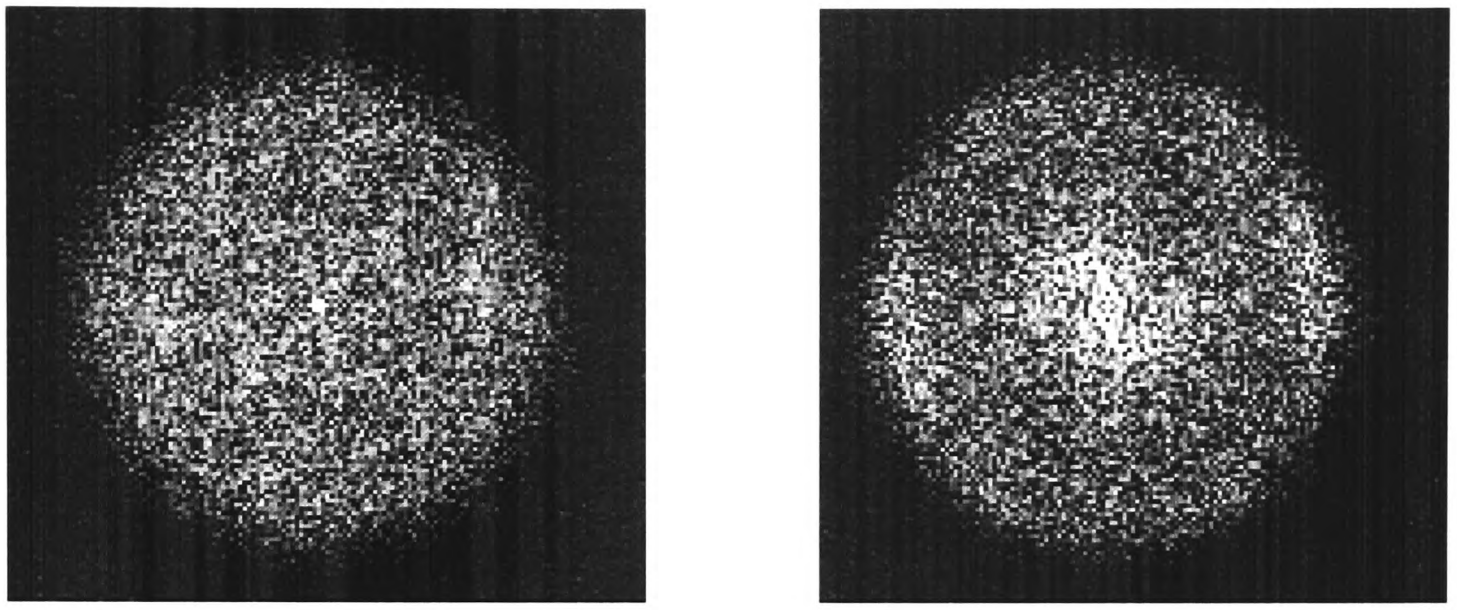

Figure 6.20: Fast Fourier transforms (FFT) of 2-D x-y images for the four different stacks shown in figure 6.19. Note, for Stack 4 a more representative image was chosen for the FFT. (Top left = Stack 1, top right = Stack 2, bottom left = Stack 3, bottom right = Stack 4).

Figure 6.21 (Top) shows the 2-D RDF of the x-y plane for the four stacks. There are many more peaks in $g(r)$ for the three sheared stacks (2-4) compared to the quiescent stack (1) which only has a first peak and very weak second peak. The most striking curve is for stack 4 which has strong peaks in g(r) out to $r = 14R$. The positions of the peaks match well out to $r = 7R$ with the expected positions for a 2-D hexagonal lattice with unit cell size = $2R$ (peaks at $1, \sqrt{3}, 2, \sqrt{7}, 3, 2\sqrt{3}, \sqrt{13}, 4, \sqrt{19}, \sqrt{21}, 5$, in units of $2R$); beyond $r = 7R$ the peaks become smeared together and some expected peaks occur at minima in $g(r)$.

Figure 6.21 (Bottom left) shows the 2-D RDF of the x-z plane for the four stacks. Peaks are observed in the sheared stacks (2-4) but they are quite washed out and noisy (due to the small size of the plane). Even for the most ordered stack (4), the peaks are only visible out to $r = 7R$. The first peaks are about half the height of those in $g(r)$ for the x-y plane. Figure 6.21 (Bottom right) shows the 2-D rdf of the y-z plane for the four stacks. Only stack 4 shows any evidence of a 3rd peak and minimum. Stack 2 and 3 look almost the same as stack 1 (no shear). Some insight can be gained into which orientation of particles contribute to which peak in the 2-D x-y RDF by studying the 1-D pair distribution function (see Appendix B) for different lines of particles at various angles, ϕ which are averaged when the 2-D RDF.

The full 3-D RDF for each stack is shown in figure 6.22. Only for Stack 4 does $g(r)$ show any indication of ordering with a split second peak and a third peak. Stack 2 and 3 do not show obvious peaks, except the 2nd maximum at $r = 4R$.

As one would expect for the quiescent stack (1) the three different plane orientations give the same 2-D RDF, which is the same as the 3-D RDF. However, the same cannot be said for the three sheared stacks. The 2-D RDFs show that there are clear differences in the short range structure between the three different 2-D plane directions. The x-y plane has the longest ranged order and most pronounced peaks in $g(r)$. The x-z plane has shorter ranged order, with weaker peaks in $g(r)$ than the x-y plane. The y-z plane seems to show the weakest and shortest range ordering out of the three plane directions. These findings fit with the direct observations of the stacks as shown in figure 6.19. Stack 4 does indeed have the most ordering, with a larger fraction of ordered particles and larger continuous regions that the other sheared stacks. Stack 2 has the most disordered regions and only small regions of order. In all three stacks much larger regions of order are seen in the x-y planes when compared with the other two plane directions. The x-z plane has more regions of hexagonal order (especially in stack 4) than in the y-z plane. Square particle order rather than hexagonal order is seen in the x-z and y-z planes but it is only very short ranged. The 3-D RDF can be thought of averaging over the three 2-D planes (and all the angles in between). This has the effect of flattening out the strong peaks in $g(r)$ found in

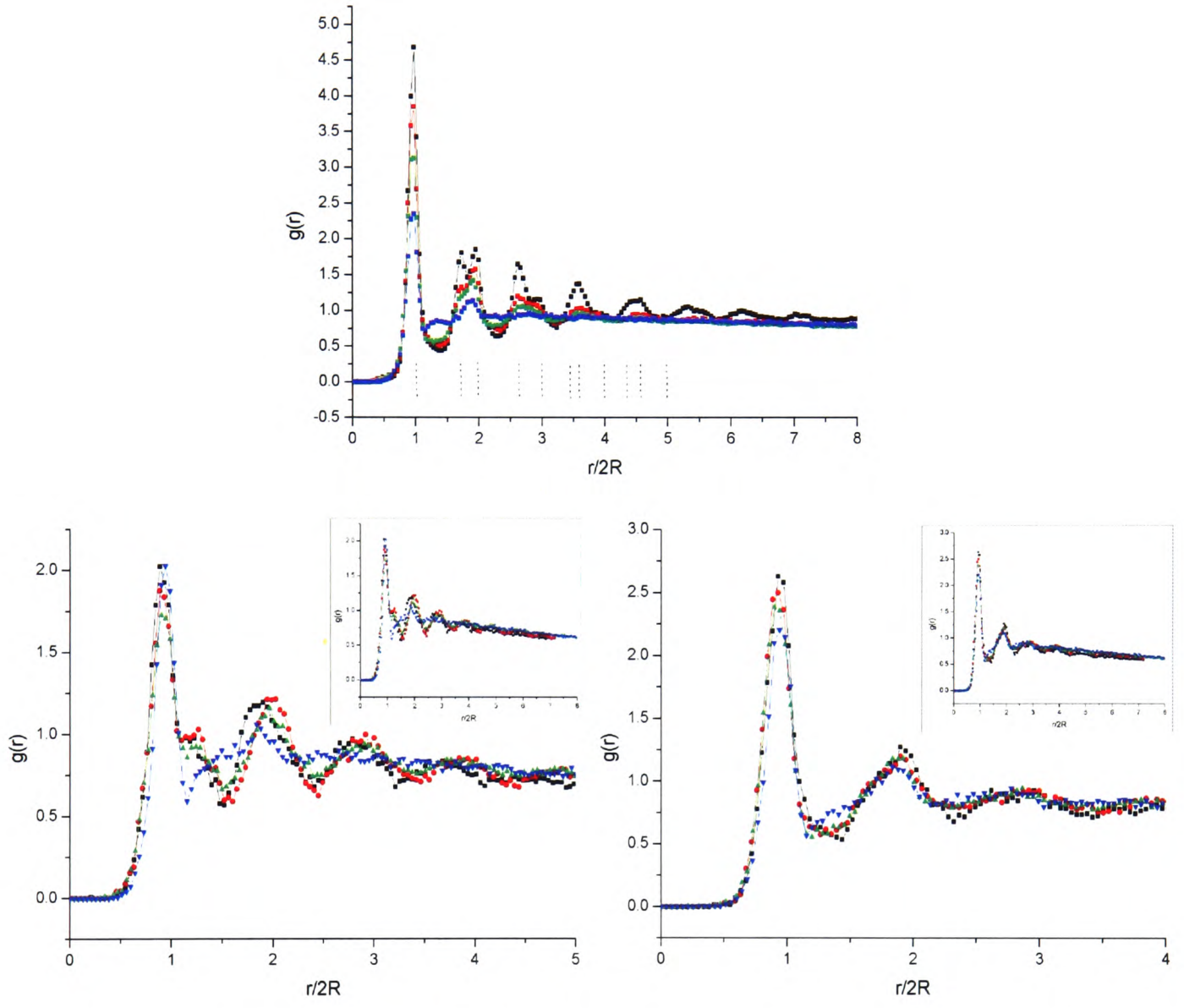

Figure 6.21: Top: 2-D RDF of x-y plane (Top), x-z plane (Bottom left), y-z plane (Bottom right) comparing the local structure of the four stacks described in figure 6.19. (20 plane average, bin-size = 0.1 μm. ■ (black) = Stack 4, • (red) = Stack 3, ▲ (green) = Stack 2, ▼ (blue) = Stack 1.) In the x-y plane RDF the dased lines indicate the positions of the nearest neighbours for a 2-D hexagonal lattice with a unit cell size = 2R. The insets in the bottom plots are the same 2-D RDF's as the main plots but with extended x-axis scale.

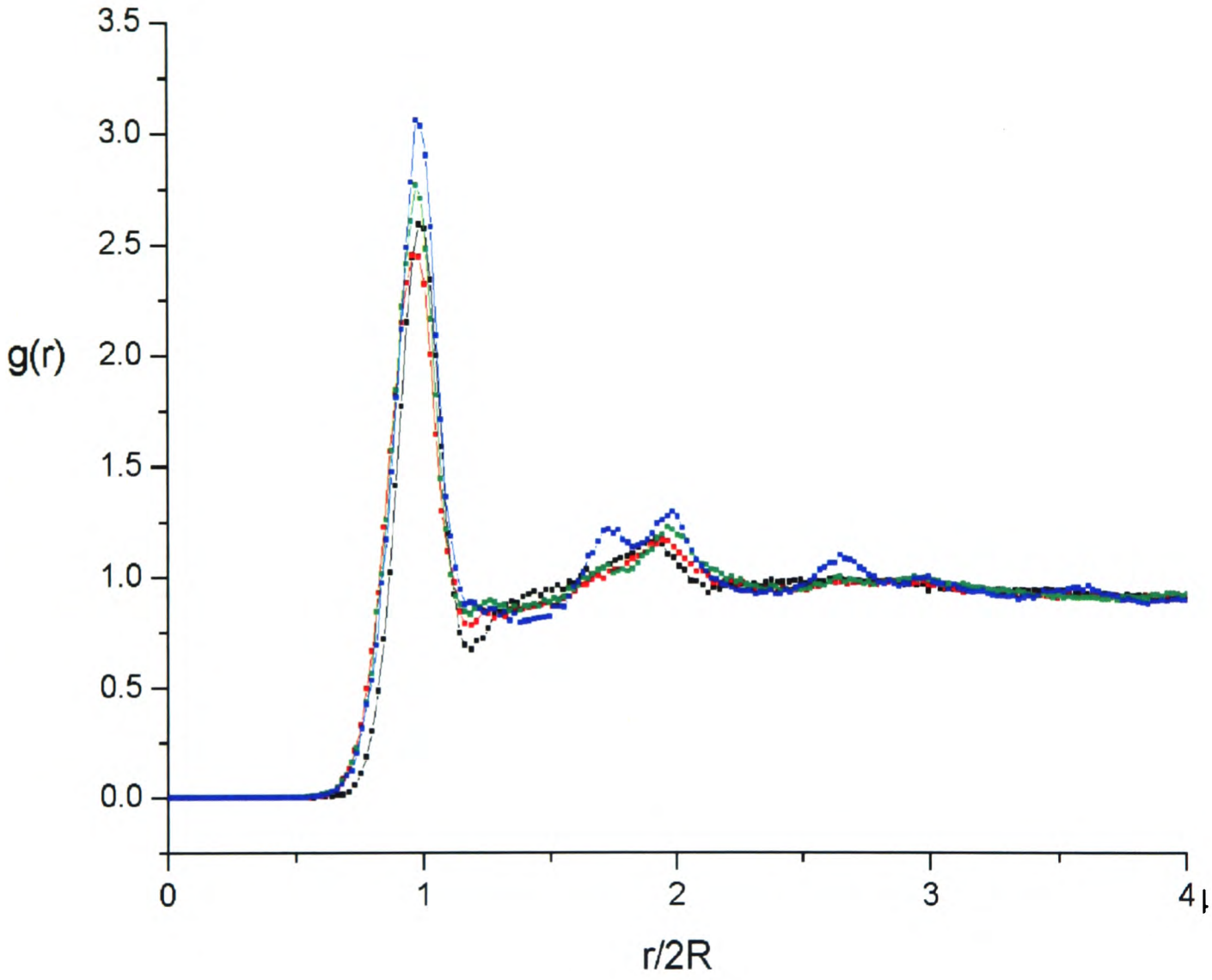

Figure 6.22: 3-D Radial distribution function comparing the local structure of the four stacks described in figure 6.19. (In order of highest first peak height: Stack 4, stack 3, Stack 1, stack 2)

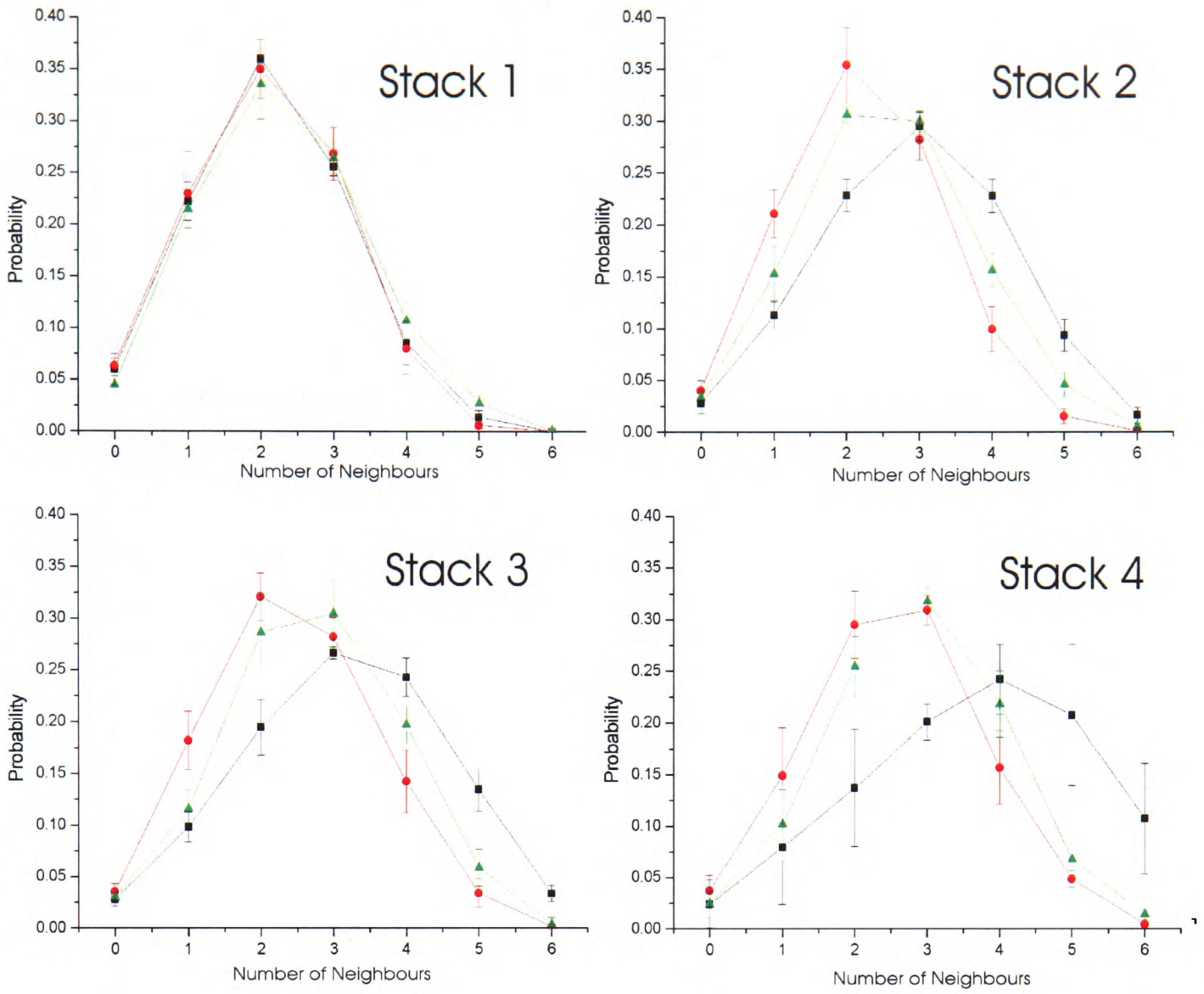

Figure 6.23: 2-D Neighbour distributions comparing the three 2D plane orientations for Stack 1 (Top left), Stack 2 (Top right), Stack 3 (Bottom left) and Stack 4 (Bottom right) from figure 6.19. (x-y plane, = ■, x-z plane = •, y-z plane = ▲)

the x-y plane leading to $g(r) = 1$ for $r > 6R$. There is only very short ranged true 3-D ordering found in these sheared stacks.

6.4.1.2 Neighbour Number and Orientation Angle

We have found in the previous section that a different local structure is found for the different 2-D plane directions. We now look at the neighbour number distributions for the three different plane directions to see if a difference is observed there aswell. We also look at the full 3-D neighbour distribution. Figure 6.23 (Top Left) compares the three 2-D neighbour distributions for the three 2-D plane orientations for Stack 1, the quiescent gel. As expected there is no preferred direction so the neighbour distribution is the same for all three orientations. The

average number of neighbours in a 2-D plane is about 2. No particles have 6 neighbours and very few have 5 neighbours. The error bars represent the standard deviation from the mean due to the varying structure of the 2-D planes used to form the average.

In figure 6.23 are the 2-D neighbour distributions each comparing the three 2-D plane orientations for Stack 2 ,3 and 4 respectively. The number of neighbours varies between the different plane orientations. A similar trend is seen in each stack with the number of neighbours shifting to much higher average neighbour number for the x-y plane. This effect is most pronounced in stack 4 and least pronounced in stack 2, with stack 3 somewhere in between. A lesser shift is found in the y-z plane. The x-z plane is the same as the quiescent state except for stack 4 where a small shift to higher neighbour number is seen. The first peak in $g(r)$ in the 2-D RDFs gives the density of particles at r = 2R, the particles that form the neighbours. The trend of highest to lowest first peak, x-y, x-z then y-z is the same trend as found for the average number of neighbours.

The number of particles with 6 neighbours is taken as a measure of the number of particles within hexagonally ordered regions. As expected the quiescent stack (1) has no particles with 6 neighbours. In stack 2 there is a small number ($\sim 2\%$) of particles with 6 neighbours in the x-y plane, with none in the other planes. In stack 3, $\sim 4\%$ of the particles in the x-y plane have 6 neighbours, whereas none are found for the other two plane orientations. In stack 4 the x-y plane has $\sim 12\%$ of particles have 6 neighbours and in the y-z orientation $\sim 2\%$ of particles have 6 neighbours, again in the x-z no such particle are found.

The 3-D neighbour distribution shown in figure 6.24 compares all four stacks and averages over all 2-D planes including the x-y, x-z and y-z planes shown above. There is a significant shift in the neighbour distribution to higher neighbour numbers for the three Stacks recorded after shear (Stack 2-4) when compared with the quiescent structure (Stack 1). The shift is most pronounced for the stack with the most order (stack 4). The shifts are not as pronounced as in the 2-D neighbour distributions. We can gain additional insight by combining the information about how many neighbours each particle has with the determined particle position in 3-D and producing a 3-D reconstruction (see Appendix B).

We now look at the orientation angle of the neighbours between the particles. We again separate the 3-D volume into 2-D planes, either into x-y, x-z or y-z planes. Figure 6.25 (Top) shows the orientation angle, ϕ, of the neighbours for neighbouring particles in the x-y plane comparing the four stacks described in figure 6.19. The probability of finding a neighbour at any angle is approximately the same for Stack 1 (disordered) as the expected random probability = 1/360 = 0.0028. Stack 4 (most ordered) shows peaks at $\phi = \pm 30°, 90°, 150°$ which is consistent

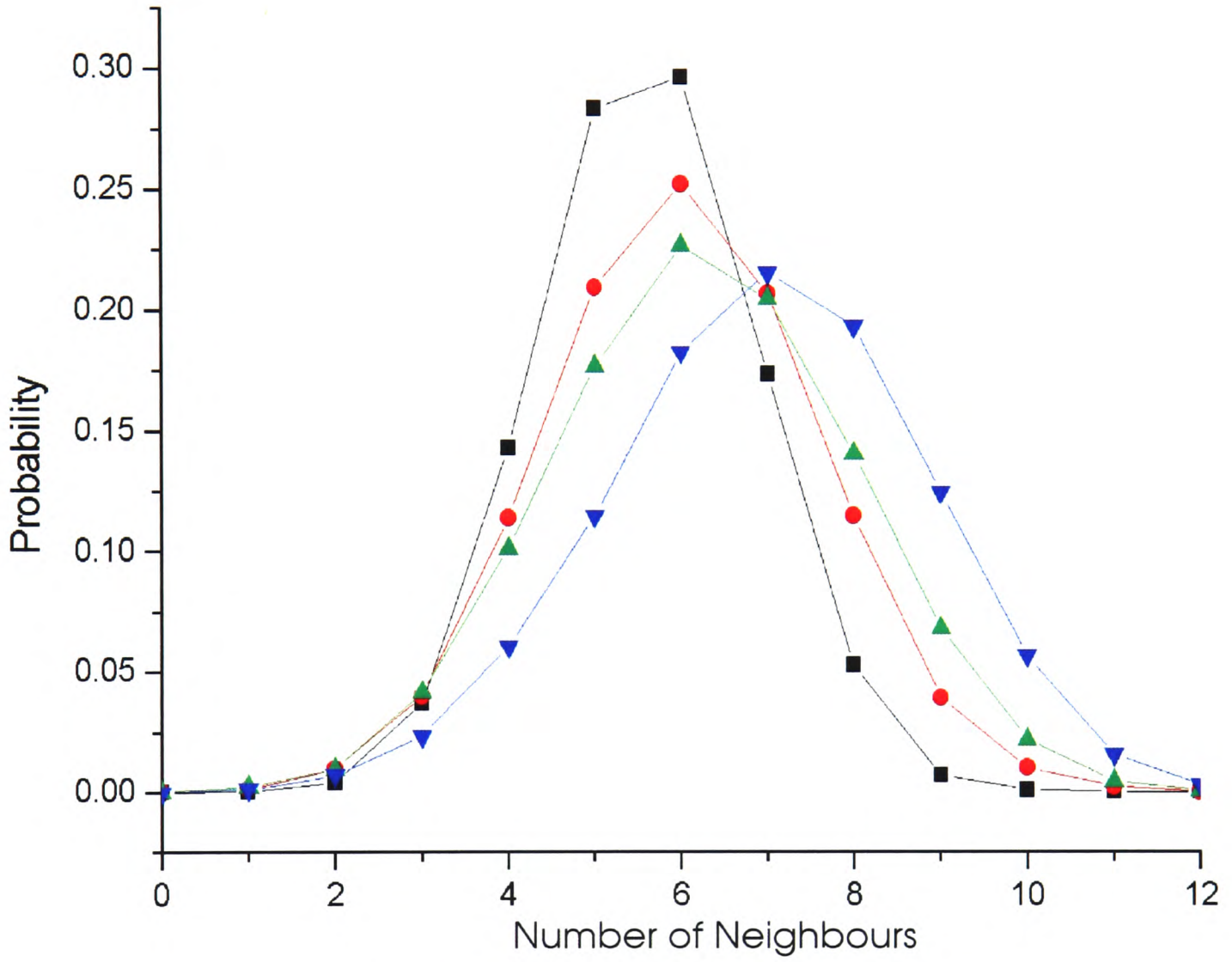

Figure 6.24: 3-D neighbour distribution comparing the four stacks described in figure 6.19 (Stack 1, = ■, Stack 2 = ●, Stack 3 = ▲, Stack 4 = ▼)

with the low strain orientation (straight lines of particles at 90° to the shear direction), with strong minima in between. Similar behaviour is found for Stack 3 and Stack 2 although less pronounced due to the larger amount of disorder present in these stacks. The peaks are in slightly different places, most simply explained by the shear cell not being perfectly parallel to the microscope stage when these stacks were recorded.

Figure 6.25 (Middle) shows the orientation angle, ϕ of the neighbours for particles in the x-z plane. The probability for stack 1 is not completely flat as expected for the quiescent structure. This may indicate some biasing that occurs when the particle coordinates are located that finds particles above each other closer than they should be. Similar behaviour is found for Stacks 2,3 and 4 (sheared) with a very strong peak at $\phi = 0°$ and $\pm 180°$, this corresponds to the lines of particles from the x-y planes stacked on top of each other in the z-direction. More interesting is the other set of peaks at $\phi \sim \pm 90°$. This corresponds to a preference for square particle ordering, with particles in neighbouring vertical planes being found directly above each other, rather than in hexagonal positions. Such square ordering can be clearly seen in the 3-D projections of the image volumes (figure 6.19).

In figure 6.25 (Bottom) the orientation angle ϕ, of the neighbours for particles is shown for the y-z plane. Similar behaviour is found for Stacks 2,3 and 4 (sheared). A very strong peak found at $\phi = 0°$ and $\pm 180°$, this corresponds to the lines of particles from the x-y planes stacked on top of each other in the z-direction. The peaks at $\phi = \pm 60°$ and $\pm 120°$ correspond to a preference for hexagonal ordering, in contrast to the square-ordering seen in the x-z plane. The peaks are less pronounced with increasing disorder in the stack volume.

6.4.2 Summary of other Confocal Shear Experiments

The confocal data presented so far, together with the optical microscopy observation given in section 6.2 and the echo light scattering data in section 6.3, can be made sense of using a shear model, which we introduce in the next section. Here, we summarise the results of a large number of other confocal observations we have made. The details can be found in Appendix C - they contribute little to the shear model developed in section 6.5, but they can form the basis of further, more detailed work on the shear response of gels.

We have found that the critical strain that dense gels respond elastically below also depends on the attraction potential (in addition to the oscillation frequency). Above this critical strain the particles that make up the gel are found to rearrange. The amount of ordering is found to also depend on the colloid and polymer volume fractions (in addition to the strain and frequency).

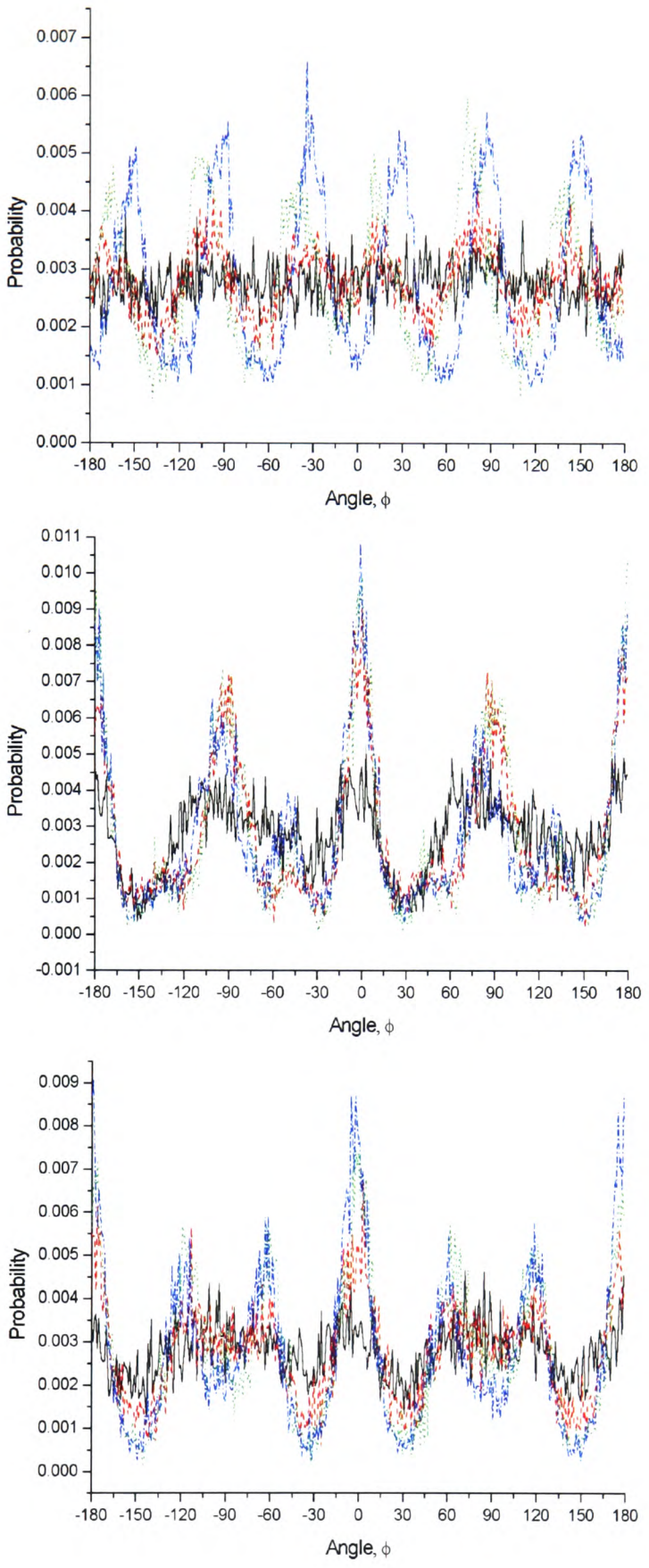

Figure 6.25: The orientation angle ϕ of the neighbours for particles in the x-y plane (Top), x-z plane (Middle) and y-z plane (Bottom) comparing four stacks described in figure 6.19. (ϕ = angle from x-axis towards y-axis [x-y], x-axis towards z-axis [x-z] and y-axis towards z-axis [y-z]) [Stack 1 = solid black , Stack 2 = long dash red, Stack 3 = short dash green , Stack 4 = long-short dash blue]

The results in the appendix (for 70Hz) are brought together in a single 3-D shear phase diagram shown in figure C.17 and contains the observed effect of 70Hz shear for different colloid volume fractions, Φ_c, depletion potential strength (U_0) and strain, γ_0.

6.4.3 Summary

We have discovered that shear induces a new type of colloidal structure in the gel. The shear induced structure of small ordered regions separated by empty voids and disordered regions has never been seen before in any colloidal system. This "swiss cheese" crystal structure is an interesting phenomenon in its own right. We found that the ordered regions are predominantly in 2-D planes and limited to small domains separated by defects, disordered particles or voids.

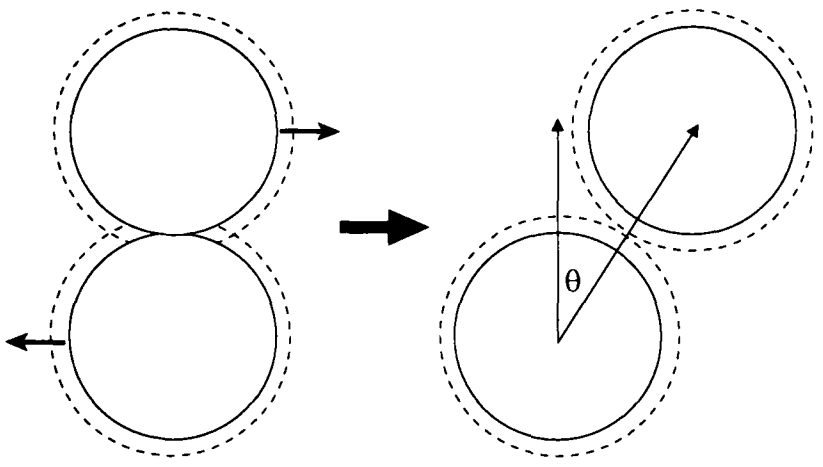

Figure 6.26: Two particles initially in contact are displaced by the shear until their depletion layers (dotted area) no longer overlap.

6.5 Discussion

6.5.1 Shear Model

We now develop a model of the response of dense gels to oscillatory shear. The model can explain many of our gross, qualitative observations reported in the previous three sections. It also makes a number of quantitative predictions, in particular the order-disorder boundary on the 'phase diagram' in figure 6.8, that agree to better than order of magnitude with our results.

We start by imagining the simplest case of two bonded particles, see figure 6.26. We consider the effect of oscillatory shear on these two particles. The two particles will be pulled apart by the shear increasing the distance between them and in turn pulling the particle some way out of the potential well. We therefore define a maximum strain γ_0^{max} at which the particle will have moved further than the range of the potential $\delta = 2\Delta$ where Δ is the thickness of the depletion zone.

$$\gamma_0^{max} = \theta \simeq \sqrt{2\xi^*} \tag{6.3}$$

where $\xi^* = \Delta/R$, the size of the depletion zone Δ divided by the particle radius R. For example, for Sample A1 ($\xi^* = 0.05$) we find $\gamma_0^{max} = 0.32$.

We can estimate the strength of the depletion potential, U at some lower strain $\gamma_0 < \gamma_0^{max}$

$$U(\gamma_0, \xi^*) = U_0 \left(1 - \frac{\gamma_0^2}{2\xi^*}\right) \tag{6.4}$$

Here we have approximated the depletion potential as a linear ramp with depth, U_0. A negative value is used for U, U_0, i.e. $U_0 = -|U_d ep|$.

We now want to determine the timescale with which the particle will escape from the potential well of depth U. We start with the Kramer escape time for a square potential well.

$$\tau_{escape} = \frac{\delta^2}{D_s} e^{-\beta U} \tag{6.5}$$

We have appealed to Arrhenius's law (Rate, $R = R_0 e^{-E}$, where E=Energy ($k_B T$)) with a microscopic attempt frequency $R_0 = D_s/\delta^2$ where D_s is the self-diffusion constant of a particle within the well and δ is the range of the square well ($\beta = 1/k_B T$).

We note that in the Kramer model the particle is escaping over a potential barrier. Therefore, once the particle has escaped there is no chance that it can return in the potential. In our model the particle is escaping from a potential well, so if there were only two particle then there is nothing to stop the particle falling back into the well. However, in the gel there are many other particles nearby the particle that is escaping from the well. So once the particle escapes from the potential well then it is very likely that the particle will become trapped in a different potential well belonging to a different particle. In this way the particle is very unlikely to return to the original potential making the situation equivalent to a potential barrier which is described by the Kramer escape time.

If, instead of a square well, we now assume a ramp potential (which better approximates the depletion potential) then we can find a new expression for τ_{escape} using equation 55 from [53]:

$$\tau_{escape} = \frac{1}{D_s} \int_0^{\delta} dx' e^{\beta U(x')} \int_{-\infty}^{x'} dx e^{-\beta U(x)} \tag{6.6}$$

This gives us, for a linear ramp potential, the following equation for τ_{escape}:

$$\tau_{escape} = \frac{\delta^2}{D_s} \frac{e^{-\beta U} - (1 - \beta U)}{(\beta U)^2} \tag{6.7}$$

Compared to equation 6.5 we now have two additional terms. The reduction in the delay time due to the assumption of a ramp potential rather a square well potential gives the $(\beta U)^2$ term. The rate of escape goes up for a ramp compared to a square well because any particles that are not exactly at the bottom of the ramp will have a smaller potential to escape from. A particle is therefore more likely to escape from a ramp potential compared to a particle in a square well which always experiences the same maximum potential. The $(1 - \beta U)$ term ensures the correct behaviour of the function at small U. This escape time, τ_{escape} can be understood in terms of

an escape attempt frequency and probability of escaping in that attempt. This sets a timescale for local rearrangements of the quiescent gel structure ($\tau_{escape} \sim$ seconds to hours, depending on strength of attraction).

In equation 6.8 we make the important step of replacing the attempt rate with twice the oscillation period of the shear cell ($1/\nu = 2\pi/\omega$). We assume that the particle attempts to escape from the potential well twice per cycle of shear because twice in a cycle the external shear field takes the particle to near the edge of the potential well where it has the best chance of escaping. This allows us to calculate τ_ω the shear escape time in terms of ω and the potential $U(\gamma_0, \xi^*)$ where $\xi^* = \Delta/R$.

$$\tau_\omega = 4\pi\omega^{-1}\frac{e^{-\beta U} - (1-\beta U)}{(\beta U)^2} \tag{6.8}$$

Finally, we substitute the results for $U(\gamma_0, \xi^*)$ from equation 6.4 into equation 6.8 and rearrange for ω giving:

$$\omega = 4\pi{\tau_\omega}^{-1}\frac{e^{-\beta U_0(1-\frac{\gamma_0^2}{2\xi^*})} - (1-\beta U_0(1-\frac{\gamma_0^2}{2\xi^*}))}{(\beta U_0(1-\frac{\gamma_0^2}{2\xi^*}))^2} \tag{6.9}$$

This is our key equation which defines a "shear phase boundary". On one side the particle will not be able escape from the potential well as the frequency and/or strain is insufficient for escape from the potential. On the other side, a high enough frequency and strain allows the particle to escape from the well and thus rearrange. We have τ_ω as a free parameter, the significance of this parameter is discussed below and U_0 as a known parameter but with a large range of uncertainty.

6.5.1.1 Physical Meaning of Timescale, τ_ω

τ_ω is a free parameter in equation 6.9. We believe it corresponds to the timescale needed for the gel structure to rearrange for a given strain. We now calculate an estimate of τ_ω. We start from the well known statement that the addition of sufficient polymer to a colloidal suspension induces phase separation into a colloidal crystalline phase and a colloidal fluid. The addition of more polymer leads to the non-equilibrium behaviour of gelation; the crystallites are unable to form. We suggest that the inability to crystallise can be related to the lack of movement of the particles due to the increased strength of the depletion attraction. The timescale of the

rearrangements of the particles in the lowest polymer volume fraction, Φ_p gel are too slow to allow sufficient free particles for the successful nucleation of crystals. There is then a critical timescale, $\tau_{crystal}$, longer than which crystals can no longer form.

We now return to the shearing of a gel. If the timescale of rearrangement is shorter than this critical timescale, $\tau_{crystal}$, then the particles in the gel will be able to rearrange sufficiently quickly to form crystals. The rearrangement timescale τ_ω of the particles subjected to shear must be as fast as that needed for the particles to crystallise in the highest phase separation mixture. We therefore identify τ_ω with the rate, $\tau_{crystal}$, needed to generate enough free particles for crystallisation to occur within the observed time window.

We can estimate $\tau_{crystal}$ as the Kramer escape time for a colloid-polymer mixture just below the non-equilibrium phase boundary. We first need an estimate of the depletion attraction strength U_0 for this mixture, as well as the self diffusion constant D_s and the depletion potential range δ.

We can calculate the potential providing we can estimate the Φ_p of the non-equilibrium boundary. We can provide a lower estimate of the position of the non-equilibrium boundary on the phase diagram with Mode Coupling Theory using equation 8 from [50]. This gives the transition from fluid to gel occurring at $\Phi_p = 0.1$ for $\Phi_c = 0.4$. An upper estimate is provided by our data that shows that the non-equilibrium boundary must at a lower position on the phase diagram than our lowest Φ_p gel ($\Phi_p = 0.15$). Using $\Phi_p = 0.1$ gives $U_0 = -2.7 k_B T$ calculated using the method described in section 3.2.7.

Now we need to estimate D_s, the self-diffusion constant for this potential. The diffusion constant will be lower than D_0 calculated from the Stokes-Einstein formula as the particle is in a dense suspension. Using the results of Segre et al [54] we can calculate this reduction in D_s due to the high local volume fraction of the suspension. The local volume fraction, Φ_c is estimated as the volume fraction of a homogeneous suspension of particles separated on average by Δ, the range of the potential. This corresponds to $\Phi_c = 0.55$ giving $D_s/D_0 \sim 0.2$. So now we can calculate D_s from D_0 which is calculated from the Stokes-Einstein formula:.

$$D_0 = \frac{k_B T}{6\pi\eta R} \tag{6.10}$$

where η is the viscosity of the solvent, $\eta_{cis-dec} = 3.042 mPas$. For Sample A1, R= 690nm and T=295K this gives, $D_0 = 1.03 \times 10^{-13} m^2 s^{-1}$. Now correcting for the volume fraction effect this gives, $D_s = 0.2 D_0 = 2 \times 10^{-14} m^2 s^{-1}$.

Using $\delta = 2r_g = 2 \times 108nm$ for sample A1 (as dilute polymer regime) we can now calculate $\delta^2/D_s = 0.06s$. Substituting this into equation 6.7 gives:

$$\tau_{escape} = 0.06\frac{e^{-\beta U} - (1 - \beta U)}{(\beta U)^2} \qquad \text{[in s]} \tag{6.11}$$

This gives us $\tau_{crystal} = 0.7s$ which we use as the value for τ_ω in equation 6.9 for the reasons outlined above.

Link to LS-echo experiments We now consider the oscillatory shear experiments with the light scattering echo technique. We can see in figure 6.14 for 70Hz that the timescale, $\tau_{decay} \sim 0.7s$, corresponds to the delay time at which the echo drops to zero height for the same strain at which ordering is observed. This timescale, τ_{decay}, is approximately the same as the calculated value for $\tau_\omega = \tau_{crystal}$. Therefore, we have independent confirmation of the importance of this timescale. We can now interpret it as the timescale within which a typical gel structure (sheared at sufficient frequency and strain amplitude for the shear "phase" boundary to have been crossed) will have been totally rearranged. Figure 6.16, for 10Hz agrees with this interpretation. At the strains studied in this experiment the microscopy results show no ordering. Therefore, we don't expect to find a complete drop in the echos within $\tau_{decay} \sim 0.7s$ at these strains. This is indeed what we find: only a small drop in the echo heights. This suggest that a full drop of the echos to zero height will only occur within timescale, $\tau_\omega = 0.7s$ for a much higher strain (above the strain we were able to measure).

6.5.1.2 Comparing with Results

Dependence on frequency The simple model gives us a prediction for the position of the "phase" boundary on the (ω, γ_0) graph shown in figure 6.8 which plots experimental data from the optical microscopy measurements at frequencies of 1Hz, 10Hz and 70Hz. The experimental frequency versus strain diagram is separated into strains at which no ordering is observed and strains at which ordering is observed. Note that the data shown has an uncertainty of $\gamma_0 \sim 0.03$ from the accuracy of the shear cell calibration. The strain at which the onset of order is observed in the microscope is not sharply defined and thus has an uncertainty of $\gamma_0 \sim 0.05$. We plot the predictions from the theory along with the experimental results in figure 6.27. The curve predicted by the model captures the correct slope of the boundary between the unchanged and ordered structure. The only parameter not fixed in equation 6.9 is the potential strength U_0.

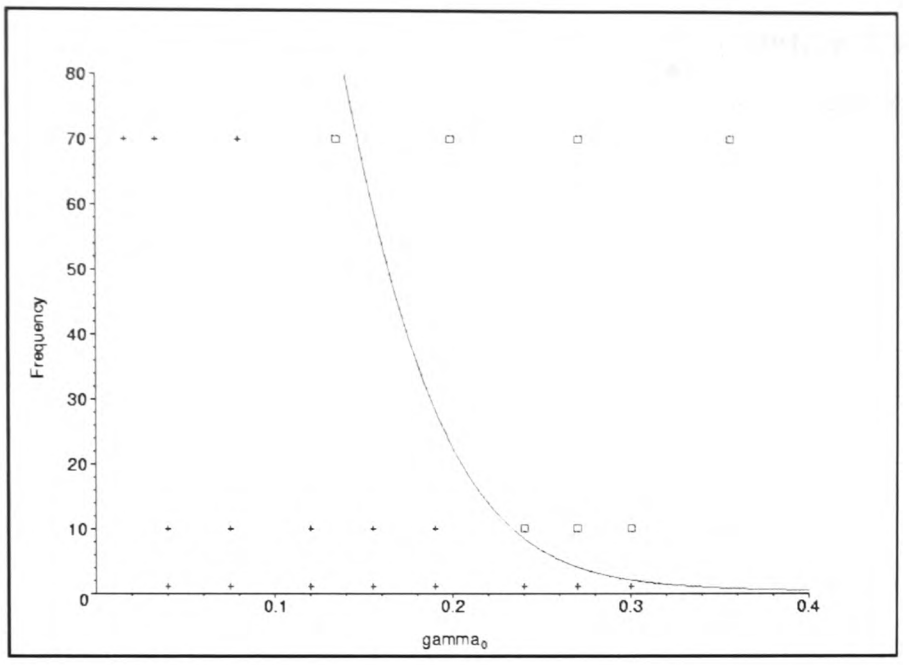

Figure 6.27: Frequency versus strain plot from theory (best fit) compared with experimental optical microscopy data. $U_0 = -9k_BT$, $\tau_\omega = 0.7s$ ('+' = no order, □ = order) [Sample A1]

We have chosen the value of the potential strength that best fits the data, $U_0 = -9k_BT$, which is somewhat lower than the potential strength for sample A1, $U_0 = -22 \pm 8k_BT$. The error range for the potential energy only reflects the uncertainty introduced by the polydispersity of the colloid particle and polymer coils. The unknown systematic error relating to the osmotic pressure correction may account for the difference between the two values. (see section 3.2.7 for more details).

Dependence on U In this section we look at the predictions from the theory for the gel samples used in the confocal experiments (see section 6.4.1 and Appendix C). There is a large range of polymer volume fractions and thus depletion potential strength. The size of ξ also varies between the samples as at low Φ_p the reduction in effective ξ is less pronounced. In figure 6.28 a fixed value of $\tau_\omega = 0.7s$ is used with the predictions for the various samples. Note the depletion potentials used are the potentials corresponding to the values from table 3.4 and are an upper estimate for the reasons discussed in section 3.2.7

The order of the different lines for the different strength gels fall in the matching order to the experimental data (as discussed in Appendix C) for increasing strain. A lower strain is required for a particle to escape from the lower strength gels even with the longer range attraction found at lower polymer concentrations.

The low strain behaviour of the curve for the lowest potential (sample D5) does not seem

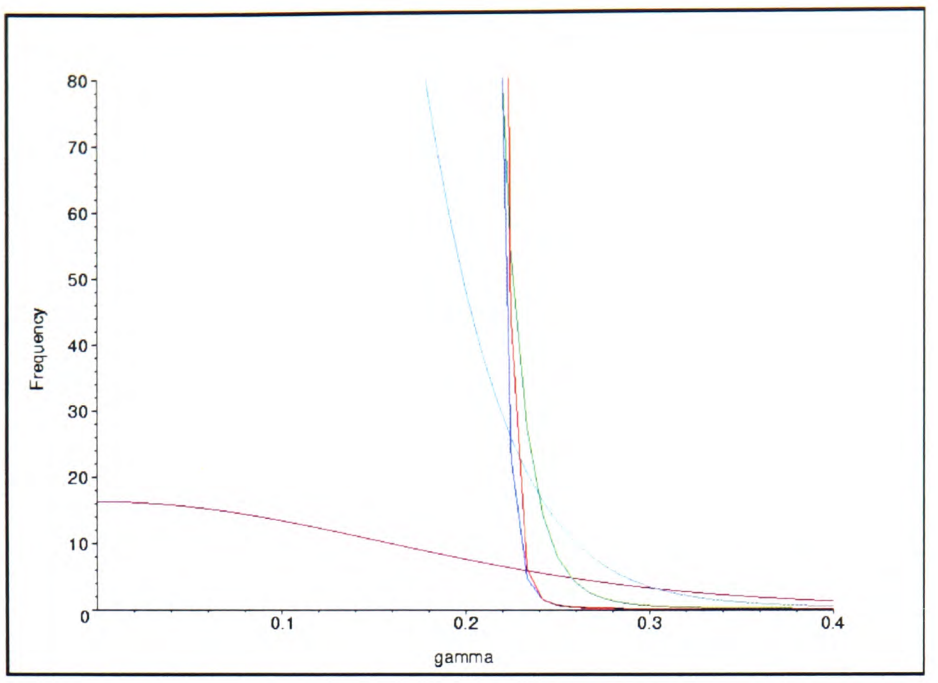

Figure 6.28: Frequency versus strain plots from theory for gels with varying polymer added. Fixed $\tau_\omega = 0.7s$. 'red'= Sample D1, 'blue'= Sample D2, 'green'= Sample D3 , 'cyan' = Sample D4: 'magenta'= Sample D5

quite right. It suggest that at $\gamma_0 = 0$ for high frequencies the particles can rearrange. In the quiescent state, occasionally a particle is observed to rearrange but the vast majority of the particle do not change neighbours. It is worth noting that in all the higher strength gels no particle rearrangement has ever been observed. So the curve is not totally unreasonable but some strain is still needed to see large scale observable changes to the structure.

The position of the curve for the three highest strength gels is very similar. This is consistent with the experimental data. However, it does not capture the difference between ordering and rearrangement detected by the voids changing shape. For sample D3 (the lowest potential of the three) no order is observed at any measured strain but rearrangement of the voids is seen. For samples D1 and D2 some ordered particles are observed.

Decrease in order at higher strains We look again at the "amount of order" phase diagram for 70Hz optical microscopy experiment in figure 6.1. We have understood the transition from no order to some order with the shear model as discussed above. We can link the peak in the amount of ordering observed at $\gamma_0 \sim 0.3$ with the critical maximum strain $\gamma_0^{max} = 0.32$ (for sample A1, calculated from equation 6.3) at which the particle will be pulled out of the potential well, without having to jump out. The amount of rearrangement and collisions will increase above this strain as more bonds are broken per particle. It is possible that this liquefaction of the gel breaks up both disordered and ordered clusters leading to reduction with

increasing strain in the amount of order observed.

6.5.1.3 Physical Interpretation

Our model predicts that a typical particle can escape from the potential well at a certain critical strain (for a given frequency). This escape of the particle allows the particle to rearrange, leading to a small change in the particle micro-structure. The combination of the rearrangement of many, albeit temporarily escaped particles over many cycles of shear will lead to significant rearrangement of the gel micro-structure.

In our model only the breaking of a single inter-particle bond is considered when the particle is trying to escape from the potential. Actually, we have found that a quiescent colloidal gel has multiple bonds per particle (see figure 5.10). We have also found from the confocal experiments that the ordered gel structure is made up of particles arranged in 2-D planes (see figure 6.19). We now attempt to link the model to these observations.

We look for the most important single bond for each particle in the gel; that bond which is most likely to be broken by shear. We assume that this bond is the one between a particle in neighbouring x-y planes. If this particle bond breaks then the two planes will become detached at the point where the two particles were joined. The repeated occurrence of particle bonds breaking between the planes as the consequence of shear will lead to the de-pinning of the x-y planes. Starting at the situation of particles randomly arranged in all 3 dimensions we end up with particles arranged in 2-D planes. When a particle breaks its bond(s) its has freedom of movement within the x-y plane in which it sits. The shear will on average break bonds between the planes. Effectively, in-plane bonds are much more stable/longer lasting than cross-plane bonds. These cross-plane bonds will tend to keep breaking letting the particle try out different local positions. This could account for the shift from a random orientation of neighbours to a preference for neighbours in the x-y plane (see figure 6.23). This increase in neighbours in the planes could give sufficient particles for small ordered regions to form. These ordered regions would be stable under shear, so would be likely on average to stay the same or grow depending on the local environment of particles surrounding them.

Voids that form during shear are typically much thinner in the z-direction (typically a couple of particle diameters) than in x-y (typically order of 10 or so diameters). The large voids that accompany the ordered regions could be simply the extra space created by ordered regions having a higher volume fraction than a disordered gel region.

6.5.1.4 Limitations of the Model

Our model is very simple. The potential is modeled as a linear ramp which gives a potential that is too deep as the strain is increased. Therefore, the particle should be able to escape for larger γ_0 more easily than is found by the model.

This model deals only with a single particle-particle bond and does not deal with the fact that particles may be bonded at different angles initially rather than vertically on top of each other.

6.5.2 Formation of 2-D Planes and Ordered Regions

Why does ordering occur? We observe ordering of the particles in the gel structure in microscopy images recorded after samples experience oscillatory shear. We were unable to study the actual formation of the ordered regions as microscopy images can not be recorded during shear. This prevents us from making significant progress in understanding the mechanism leading to the formation of the ordered regions. We have already argued that the particles must be able to escape from the potential well in which it is trapped, be able to rearrange for ordering to occur. We suggest based on the observation of partly ordered gel regions that the formation of 2-D x-y planes is linked to the ordering process. It is possible that locally dense regions are the first to form ordered clusters that then increase in size.

Comparing 2-d planes i.e. differences in x-y y-z and x-z planes It is reasonable to expect particles to line up into 2-D planes in the x-y direction (as seen in figure 6.19) when experiencing shear as particles would be able to move most easily past each other without collisions. Particles between planes would be more likely to be hit by another particle. Alternatively, ordered regions would be stable in the plane but a disordered particle in between plane would be likely to be knocked by other sheared particles. We find more bonds per particle for a particles in the plane than between planes, and more than in the quiescent gel state. We do not have an explanation for why square ordering is preferred in the x-z plane while hexagonal ordering is preferred in the y-z plane. We can speculate that the planes of particles can move more easily past each other during shear if the particles in one plane are directly above those in the layers above and below. We do find more bonds per particle in the 2-D y-z plane than in the x-z plane due to the denser packing associated with hexagonal ordering.

6.5.3 Comparing with other work

As no other work on the low strain shear of colloid-polymer mixtures exists we can only compare our work with the shear of pure colloidal suspensions. There are the simulations on dense attractive hard spheres but they are only for steady shear.

6.5.3.1 Experiments on Pure Colloid Suspensions

Our limited experiments on a pure colloidal fluid at $\Phi_c = 0.4$ and $\gamma_0 = 0.15$ for 15 seconds agrees with Ackerson [25]. No particle ordering was found in their oscillatory shear experiments at any of the strains studied for fluids of comparable volume fraction. For dense fluids (just below the freezing transition) Ackerson found particle ordering and a transition to the high strain order regime around $\gamma_0 \sim 1$. We did not look at such dense fluids or at such high strains so we are unable to confirm this behaviour. At low freqencies, no ordering was found in the oscillatory shear optical microscopy experiments of Haw *et al* [26] for a colloidal fluid near the freezing boundary. In contrast we do find order in colloidal gels but not in the equivalent volume fraction fluid. The critical shear ordering volume fraction for fluid was found by Ackerson to be just below $\Phi = 0.494$ [25]. It is possible that there is a critical ordering volume fraction for gels near $\Phi_c = 0.4$ as we have found that it is harder to find significant order at $\Phi_c = 0.4$ compared to $\Phi_c = 0.44$ or 0.46. The other possibility is that less order is found with reduced volume fraction but with no sharp cutoff.

There are some similarities between the shear induced structures observed for fluid/crystal coexistence samples studied by Haw [26] and our gel samples. Under the microscope Haw observed regions of crystal order surrounded by disordered fluid whereas we observed regions of crystal order surrounded by voids and frozen disordered gel clusters.

At higher volume fractions, in pure crystal samples Haw observed polycrystalline order at low strains. In the gels the order that is found is polycrystalline aswell. However the defects present in the crystal structure such as vacancies are more similar to those observed in shear induced ordering of colloidal glasses as observed with microscopy by Haw [28]. This could be linked to the fact that both dense colloidal gels and repulsive glasses are both "frozen", preventing any defects being repaired by rearrangement of particles through Brownian motion. The colloidal gels respond elastically to low strains in the same way as found with repulsive glasses [27], [28].

FCC Model We find a preference for low strain orientation ordering in our experiments (see figure 6.25) but mostly restricted to 2-D ordering rather than full 3-D order. The volume fraction we use is $\Phi_c \sim 0.4$, which we note is an average Φ_c as in gels the Φ_c depends on location due to the inhomogeneous stucture. For this average Φ_c, the model predicts that planes can move freely past each other at any strain, so either orientation of order should be stable during shear. For locally denser regions of the gel, $\Phi_c > 0.4$ the low strain orientation is stable up to strains $\gamma_0 \sim 1$.

6.5.3.2 Simulations on Attractive Colloids

Most of the simulation results of Silbert *et al* [29] for attractive hard spheres are not relevant as they consider steady, not oscillatory shear so most of the results are for strains far higher than used in this work. The particle ordering we observe seems to be related to oscillatory shear as for the closest volume fraction in the simulations even at very high strains only string-like order is seen co-existing with disorder. There may be a link between the ordering observed in the microscopy experiments and the intermediate short lived order found at low strains in the simulations. It is possible that if a region of short lived order was subjected to oscillatory shear then it might remain intact rather than immediately disappear.

Chapter 7

Conclusions

The aim of this work was to study the effect of shear on colloidal gels. To make any progress in this area we first had to understand the quiescent structure of our chosen model system, colloid-polymer gels. Secondly we had to develop a suitable shear cell and experimental methods. We limited our study to dense colloidal gels when the wide range of interesting shear induced behaviour in this small part of the colloid-polymer phase diagram became apparent.

7.1 Shear Cells

We set out to design a linear parallel-plate oscillatory shear cell suitable for both light scattering-echo and microscopy experiments on colloidal gels to be conducted with a single shear cell. We successfully developed and tested several different novel models of precision shear cells. The first shear cell was restricted to use with an upright optical microscope and had only three plate gap thicknesses but due to resonances at high frequencies allowed the greatest strain range to be explored, making it best suited to light scattering echo. The second shear cell was the most versatile, allowing use with either inverted or upright microscopes (and LS-echo) and a continuously variable gap size. The third cell was the simplest design with the fewest moving parts. This helped to minimise movement of the sample in the shear cell, making it most suited to the acquisition of 3-D image volumes.

7.2 Quiescent Structure of Dense Colloid-Polymer Gels

We have conducted a systematic study of the quiescent structure of dense colloid-polymer gels with varying strength of attraction. We have found that confocal microscopy provides superior image quality of the particle length-scale structure compared to contrast enhanced optical microscopy. We obtained high quality 3-D images from within the shear cell environment that allowed quantitative comparison of the different gels by the extraction of the 3-D particle coordinates and subsequent calculation of quantitative measures of the local particle structure. We have observed that the gels have a liquid-like, although frozen, short range structure and a very in-homogeneous structure over longer distances. We have found an increase in the average number of neighbours per particle for decreasing attraction strength and for increasing colloid volume fraction. These shifts in neighbour distribution are accompanied by changes in the particle-free void regions which are quantified using the concept of remoteness. Establishing the quiescent gel micro-structure has assisted in the interpretation of the effects of shear on the micro-structure of the different gels by allowing quantitative comparisons between the sheared and quiescent gel structures.

7.3 Dense Gels Under Oscillatory Shear

We have found that the gels respond elastically to strains below a critical value that is dependent on frequency and attraction potential. Above this critical strain the particles that make up the gel are found to rearrange. The use of microscopy and light scattering-echo techniques allowed complementary data to be gathered on the average effect of the shear on the gel and the effect at the local particle level. This is aided by the quantitative analysis of the structures of the gels after shear from the successful acquisition of particle coordinates from 3-D image volumes. Surprisingly, shear induces a new type of colloidal structure in the gel. The shear induced structure of small frozen ordered regions separated by empty voids and disordered regions has never been seen before in any colloidal system. The amount of ordering is found to depend on strain and frequency as well as on the colloid and polymer volume fractions of the gel.

This "swiss cheese" crystal structure is an interesting phenomenon in its own right. We found that the ordered regions are predominantly in 2-D planes and limited to small domains separated by defects, disordered particles or voids. Sufficient strain leads to interesting changes in the void distribution in both samples where particle ordering was observed and in those where it was not. Our results are interpreted by a simple model based on the timescale for a particle to

escape from the potential well. This model captures the essential features of the shear "phase boundary" between the unchanged and rearranged structures but does not differentiate between shear induced ordering and other rearrangements of the gel structure.

7.4 Future Work

It is hoped that our experiments will encourage theoretical developments in this area. Our simple theoretical model could be extended in many ways, for example considering the effect of multiple particles and bonds at different angles.

This work has focused on a limited range of colloid volume fraction around $\Phi_c = 0.4$. It would be interesting to extend the shear experiments to lower colloid volume fractions. This could establish whether ordering of the particles is still observed, for example. The transition between the low density attractive glasses studied here and transient gels could lead to interesting differences in shear behaviour. Likewise, increasing the volume fraction and studying high density glasses would establish whether a similar behaviour is found as expected, with, for example, more ordering with increased volume fraction.

The size ratio, ξ^*, is an important parameter in our model related to the critical strain at which a particle can escape from the potential well. A systematic study of different gels with varying size ratio would be a good test of the applicability of our model to attractive colloids with different ranges of attraction.

A recognised difficulty in this work was accurately estimating the strength of the depletion potential for a dense colloid in a mixture of semi-dilute polymers. A direct measurement of the force required to separate two *in-situ* colloid particles with optical tweezers would give the depletion potential strength while avoiding the uncertainties in the polymer osmotic pressure and depletion layer thickness.

A more detailed study of the formation of the ordered regions and 2-D planes could explain how they form and interact.

On the technical side, a much faster scanning confocal microscopy would allow the study of weaker gels which are not completely frozen. It could also allow the study of the gel during shear rather than having to stop the shear first. This could allow particle tracking (at least in 2-D) and allow the formation of shear induced structures to be studied. This could also be studied with computer simulations of the oscillatory shear of attractive hard spheres.

The shear cells used in this work could be used to conduct oscillatory shear studies of many other soft matter materials and beyond into other areas of science. For example a medical biology study [55] involving the shear response of diseased human knee cells (Chondrocytes) to aid arthritis sufferers is already underway using shear cell 2 combined with confocal microscopy.

Appendix A

Depletion thickness at high polymer concentration

This correction is important if the polymer coils overlap which occurs at high polymer concentrations

The depletion thickness Δ is taken to be the correlation correlation length, $\zeta(C_p^{\text{free}})$ in bulk polymer solution at the same polymer concentration [8]. ζ depends on the free polymer concentration (the quantity we are trying to determine) so we must start with a naive value for C_p^{free}. We use $C_p^{\text{free}} = C_p/(1-\Phi_c)$, i.e. we take the free volume fraction $\alpha = 1 - \Phi_c$, which is equivalent to no overlap of depletion zones.

This allows us to calculate a starting value of ζ using the method described below that we can then use to estimate C_p^{free} more accurately. We repeat the process until a stable value of C_p^{free} and ζ are found. We then take this value of ζ as the Δ to use in the subsequent calculation of the depletion potential.

To calculate the correlation length we first need to determine the reduced concentration, X, which is proportional to C_p/C^*:

$$B_2 C_p^{free} = \frac{9}{16} X \tag{A.1}$$

for $M_w/M_n \leq 1.3$ as obtained by expanding Eq. (8) of [56] to first order in X. B_2 is the second virial coefficient (which for polystyrene is available from [44]).

Wiltzius measured $\frac{\zeta}{r_g}$ for varying X (Fig. 3 of [57]). This allows us to estimate ζ for a given X. At dilute polymer concentrations, the correlation length ceases to be a good measure of the size of the polymer coil. In fact as $\Phi_p \rightarrow 0 \Rightarrow \zeta \sim \frac{r_g}{\sqrt{3}}$. As here we are concerned with polymer volume fractions that are small compared to those in a polymer melt we will scale ζ by $\sqrt{3}$ to give the correct behaviour of $\zeta = r_g$ at low C_p.

Appendix B

Additional Results for 70Hz, 31min $\gamma = 0.15$ Confocal Shear Experiment

This appendix contains additional results for the 31 minutes shear experiment at $\gamma_0 = 0.15$ for sample D1 (section 6.4.1). This includes quantitative analysis, computer generated reconstructions and some interesting confocal images of the sheared gel structure.

1-D Pair Distribution Function

We now consider the 1-D pair distribution function comparing lines of particles at different angles, ϕ (see section 3.4.4) from the x-y plane for Stack 4 from figure 6.19. This is shown in figure B.1 which compares five angles from $0°$ to $90°$. This is to gain some insight into which orientation of particles contribute to which peak in the 2-D RDF. For perfect 2-D hexagonal packing with the parallel lines of particles in the horizontal direction ($90°$) (the low strain orientaion, see figure 2.14). For this low strain orientation we expect peaks (of the same height) for $\phi = 30°, 90°$ at fixed $r = nR$. (with $n \geq 2$) and for $\phi = 0°, 60°$ at $r = n\sqrt{3}R$ (with $n \geq 2$). This is indeed what we find in the 1-d pair distribution. However, we also find a significant peak at r=2R for angles other than $\phi = 30°, 90°$, which we don't expect. For these angles ($\phi = 0°, 60°$) this peak is probably from neighbouring particles not being perfectly ordered as a hexagonal lattice or disordered. The non-uniform peak heights (lower at higher

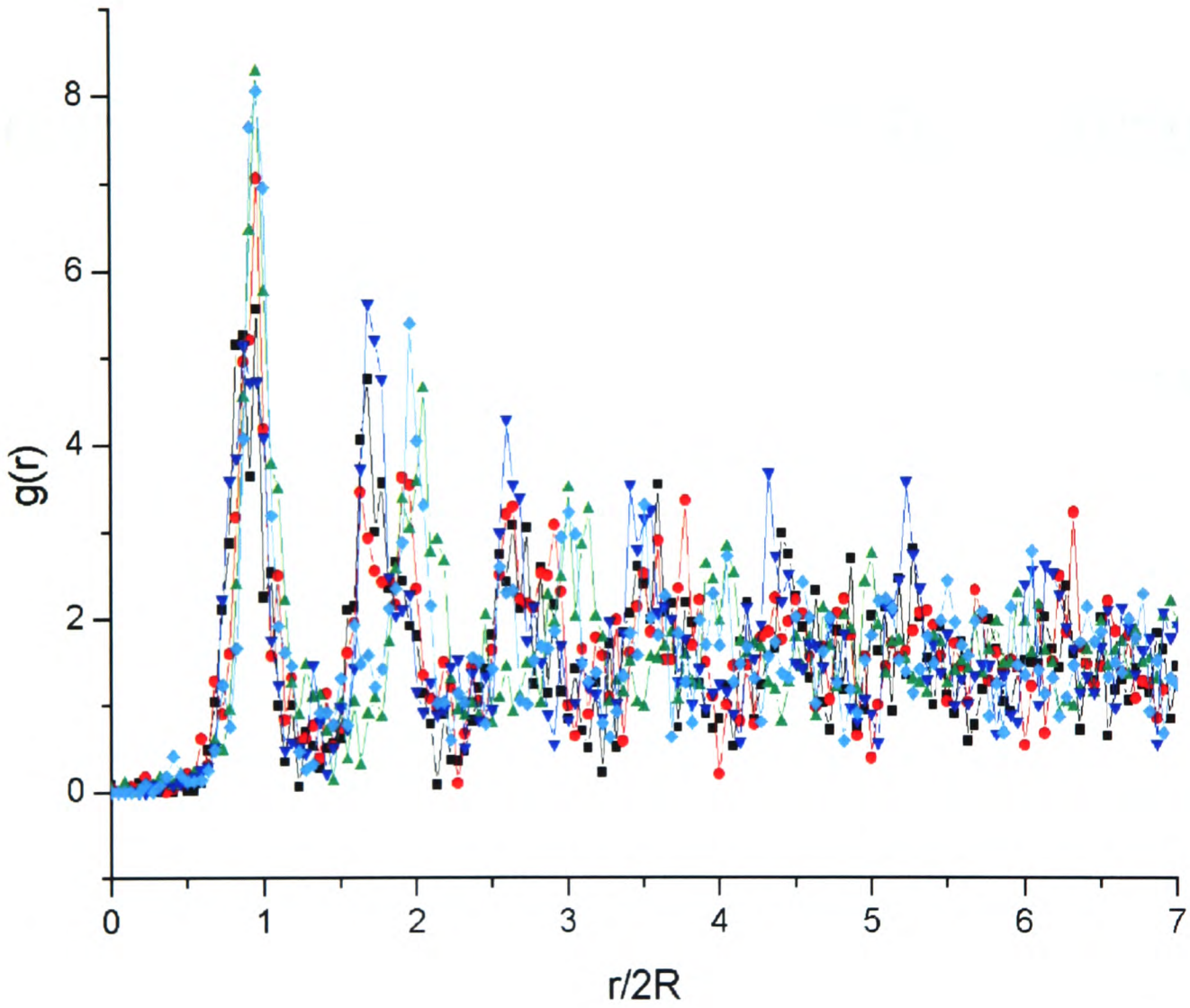

Figure B.1: 1-D Pair distribution function comparing different angles, ϕ in the x-y plane for Stack 4 from figure 6.19. ($0° = \blacksquare, 15° = \bullet, 30° = \blacktriangle, 60° = \blacktriangledown, 90° = \blacklozenge$)

$r/2R$) tells us that the ordered domains are of limited size. By looking at the different positions of the second peak we can see the source of the double peak appearance of the 2nd peak in the 2-D $g(r)$, and why the first part of the double peak is the same if not larger than the second. The average over the different angles gives a greater value of $g(r)$ for the first part of the double peak.

3-D projections

We can gain additional insight by combining the information about how many neighbours each particle has with the determined particle position in 3-D as shown in figure B.2 (a thin 3-D slice of a part of each stack is shown for clarity). Note the neighbour number corresponds to the number of neighbours in 3-D, thus most particles are also neighbours with particles outwith the plane that are not drawn. It is clear that the sheared stacks are whiter than the quiescent stack, showing the shift to higher neighbour number described above. The particles that appear to form an ordered region seem to have higher than average number of neighbours but most do not have as many as 10 neighbours. These particles are not fully enclosed in a 3-D hexagonal crystal. Most of the low neighbour number particles are next to void regions although some high neighbour number particles are as well (at least in this plane).

In figure B.3 a 3-D projection of particles positions reconstructed from part of Stack 4 (figure 6.19) is shown along with the same 3-D projection but only showing particles with 9 or higher neighbours. This shows that a dense region of high neighbour number particles is formed in this case by the shear.

Other Interesting Images

We present here a collection of figures demonstrating the variety of structure found in this single shear experiment. Figure B.4 (Top Left) shows an unusually ordered part of the sample. There are many small domains of ordered particles with different orientations. The small domains of ordered particles are separated by disordered joins and small voids. Note the defects in the crystal structure. The occurance of particle ordering appears to go hand in hand with the appearance of large voids. Such large voids are quite rare. As we observed for stack 4 in figure 6.19 the large void is surrounded by very ordered particles. Figure B.4 (Top Right) shows a region of the gel sample that is quite ordered containing a substantial void (10 by 20 particle

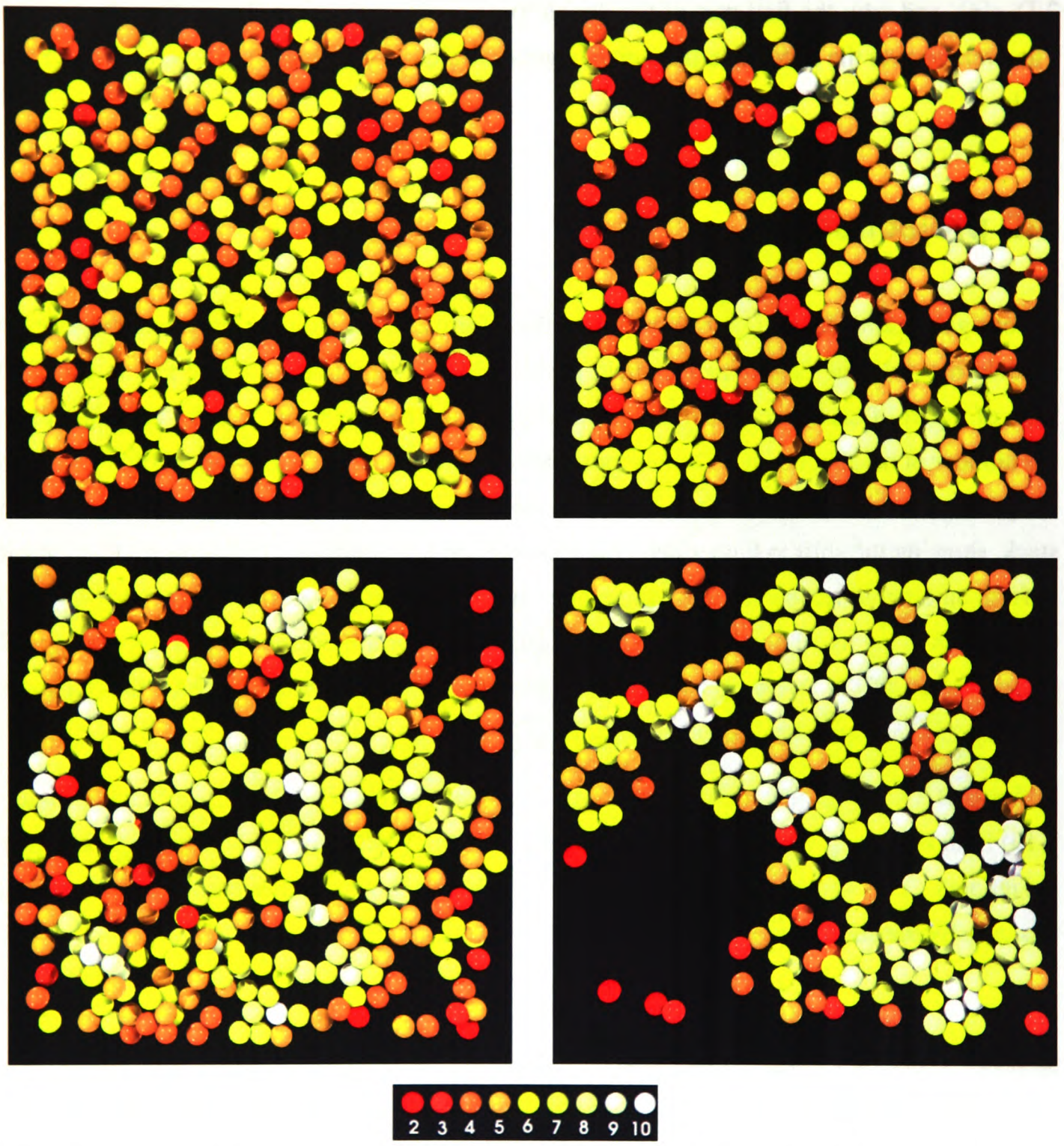

Figure B.2: 2-D plane formed from a 3-D projection of particles positions with particles drawn to scale for portion of stacks shown in 6.19. Colour signifies the number of neighbours (red = low number $->$ white = high number). Particles are neighbours with particles out of the plane (not shown). From top left to bottom right: Stack 1, stack 2, stack 3 and stack 4. [$50\mu m \times 50\mu m$ plane containing all particles with centres within $1\mu m$ thick slice]

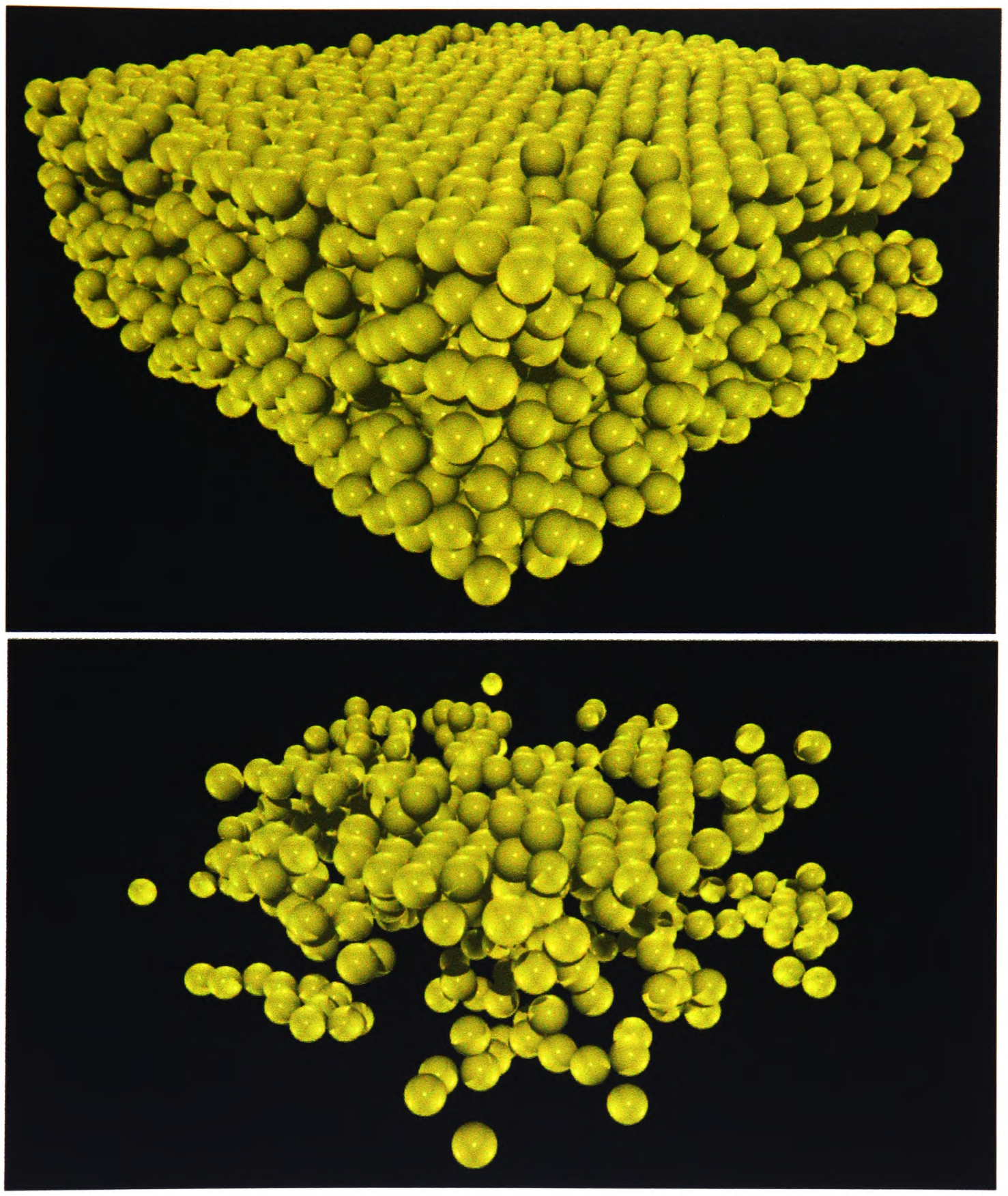

Figure B.3: Top image: 3-D projection of particles positions reconstructed from part of Stack 4 shown in figure 6.19. Bottom image: The same 3-D projection as in the top image but only showing particles with 9 or higher neighbours. Particles drawn to scale. [volume $= 50\mu m \times 50\mu m \times 20\mu m$]

diameters in size). Figure B.4 (Bottom Left) shows a larger void (20 by 30 particle diameters in size) surrounded by ordered regions of particles. In figure B.4 (Bottom Right) we show a huge void that spans more than the viewing area of the objective used (x100). A composite image of the void was made which is about 100 by 150 particle diameters in size. The void is extended in the z-direction but not as far as in the x-y plane (about 10-20 particle diameters depending on position).

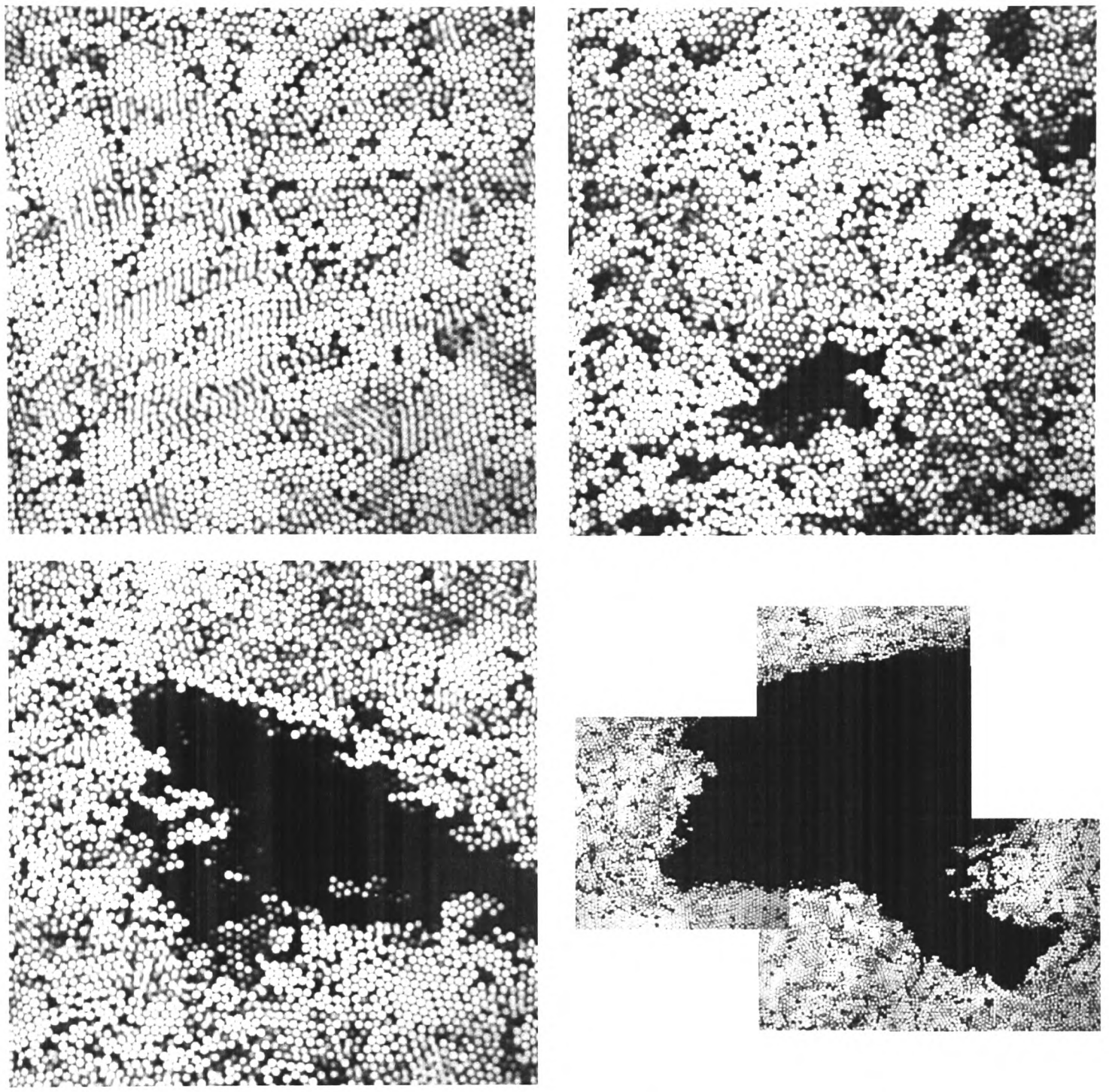

Figure B.4: Selection of interesting 2-D confocal images of the gel after shear ($\gamma_0 = 0.15$ for 31 minutes at 70Hz). Top left: Image of a very ordered region (depth $= 60\mu m$, image size = $103\mu m \times 103\mu m$). Top Right: Image of a quite ordered region of the gel containing a substantial void (depth $= 35\mu m$, image size = $103\mu m \times 103\mu m$). Bottom left: Image of a large void surrounded by ordered regions. Void $\sim 20\mu m$ thick. (depth $= 38\mu m$, image size = $103\mu m \times 103\mu m$). Bottom Right: Composite image of a huge void surrounded by ordered regions. (depth $= 60\mu m$, image size = $250\mu m \times 200\mu m$) . (Sample D1)

Appendix C

Additional Oscillatory Shear Experiments on Dense Gels Studied with Confocal Microscopy

15 Seconds Shear at 70Hz, $\gamma_0 = 0.15$

We present here experiments for a range of samples conducted at a single strain $\gamma_0 = 0.15$ for a short time (15 seconds) at 70Hz.

We look first at the results for high Φ_p sample D1 (see table 3.4). Figure C.1 shows two image volumes recorded after the shear was stopped. Similarly to sample D2 both disordered regions (top stack) and partly ordered regions (bottom stack) were observed in the post-shear sample. The RDF's for this sample showed the same behaviour as in sample D2. For the disordered stack (figure C.2 (Top)) a similar shape for g(r) is seen in all three 2D planes and in the 3-D RDF. In the partly ordered stack (figure C.2 (Bottom)) there is a clear difference between the x-y plane and the other two planes. Clear peaks are seen in g(r) out to $r \sim 10R$. These peaks are again not seen in the 3D rdf.

The neighbour distributions for 3-D (figure C.3 (Top)) and the 2-D planes (figure C.3 (Bottom)) also show the same trends as for the experiment with sample D2. There is no significant difference between the two sheared stacks and the quiescent neighbour distribution. In 2-D, both x-y planes have higher number of neighbours than the other plane orientations. The shift in the ordered stack is larger for this sample with $\sim 4\%$ of particles having 6 neighbours. There

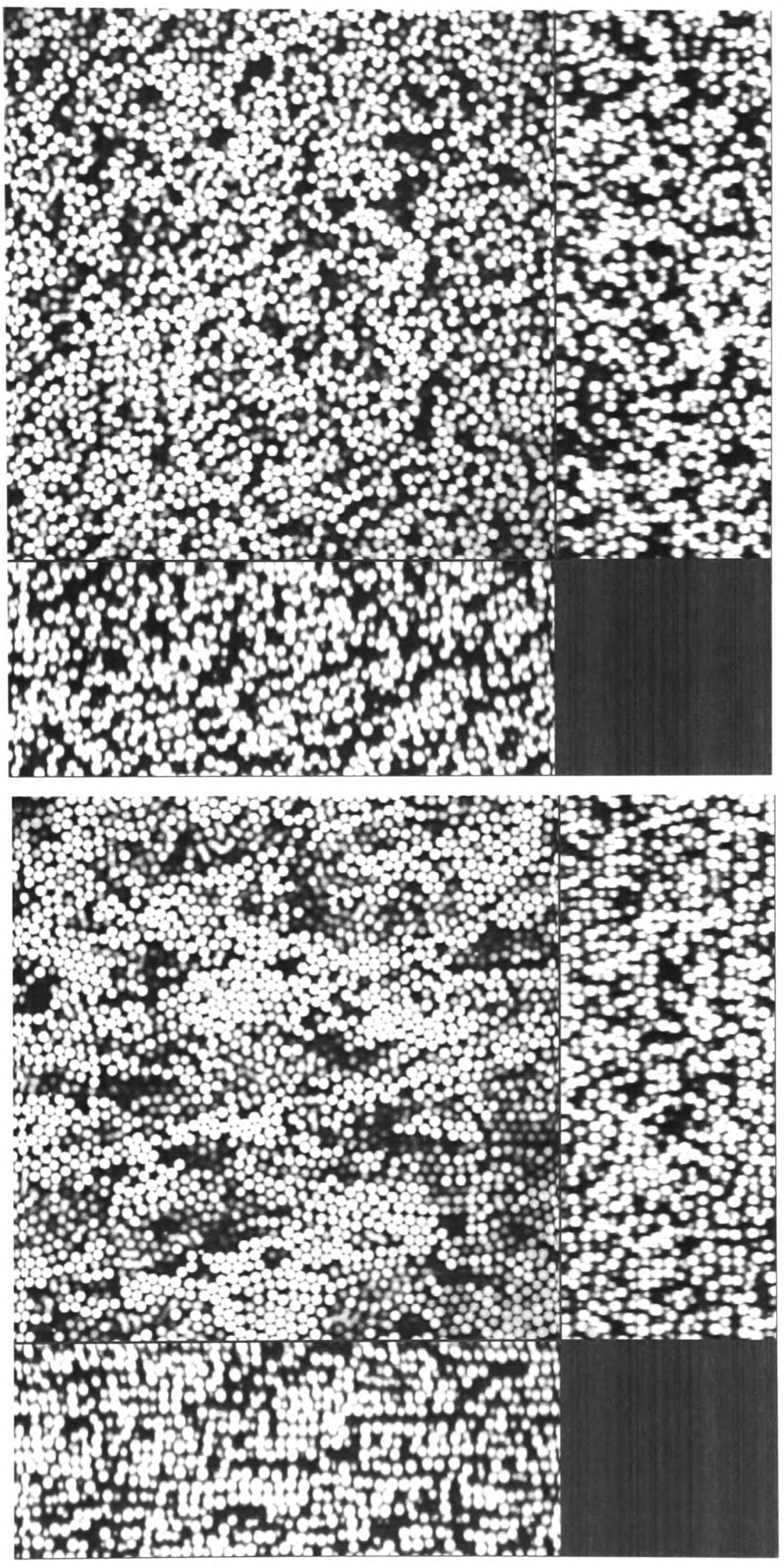

Figure C.1: 2-D projections of 2 different 3-D image volumes of high Φ_p (D1) gel after 15 seconds at $\gamma_0 = 0.15$ at 70Hz. Top image = Typical image of structure in part of sample where no order is evident. Bottom image = Typical image of structure in part of sample where particle order is clearly evident. (Both image volumes = $103\mu m \times 103\mu m \times 40\mu m$)

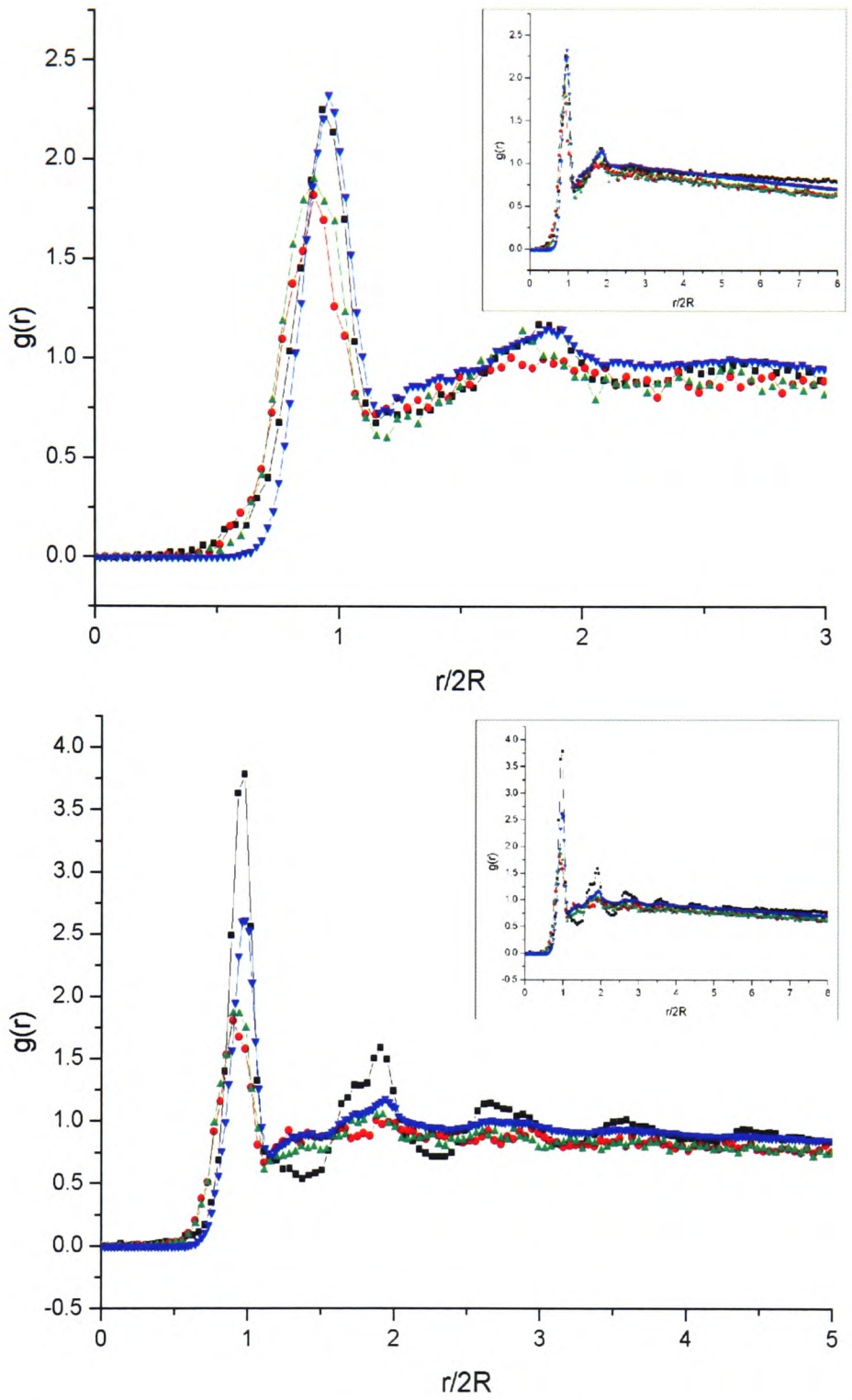

Figure C.2: Radial distribution functions comparing the 2-D planes and the full 3-D volume. The two sets of RDFs compare the local structure of the high Φ_p (note with higher Φ_c as well) gel region in which no order is observed (Top) with the gel region in which order is observed (Bottom). The insets in the two plots are the same RDF's as the main plots but with an extended x-axis scale. [figure C.1: Top and bottom respectively]. (Sample D1) [(x-y plane = ■, x-z plane = •, y-z plane = ▲, 3D = ▼]

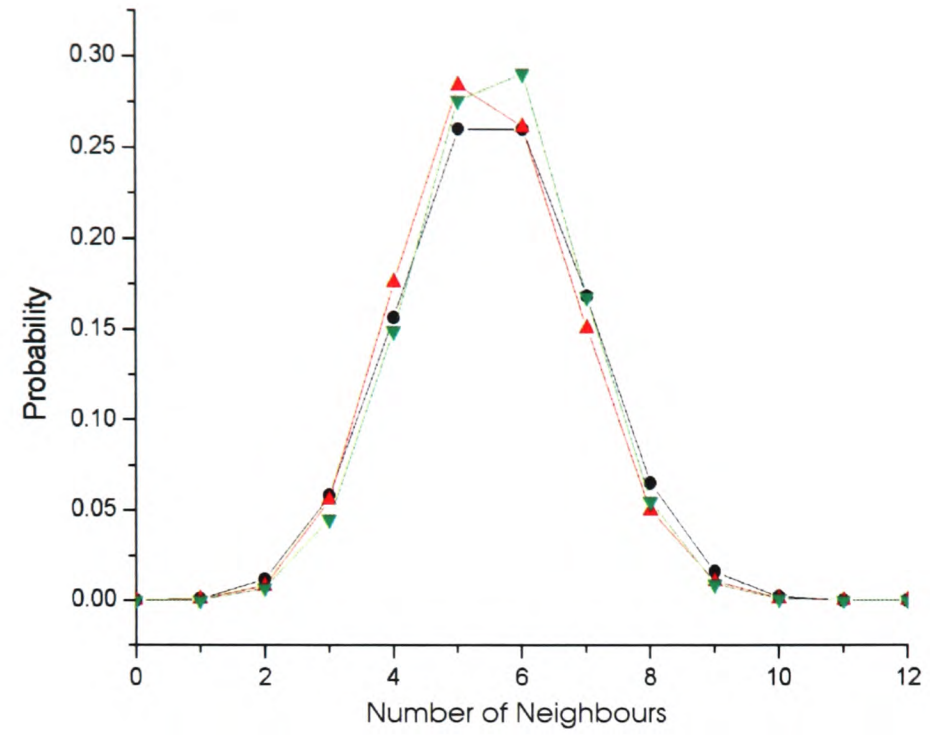

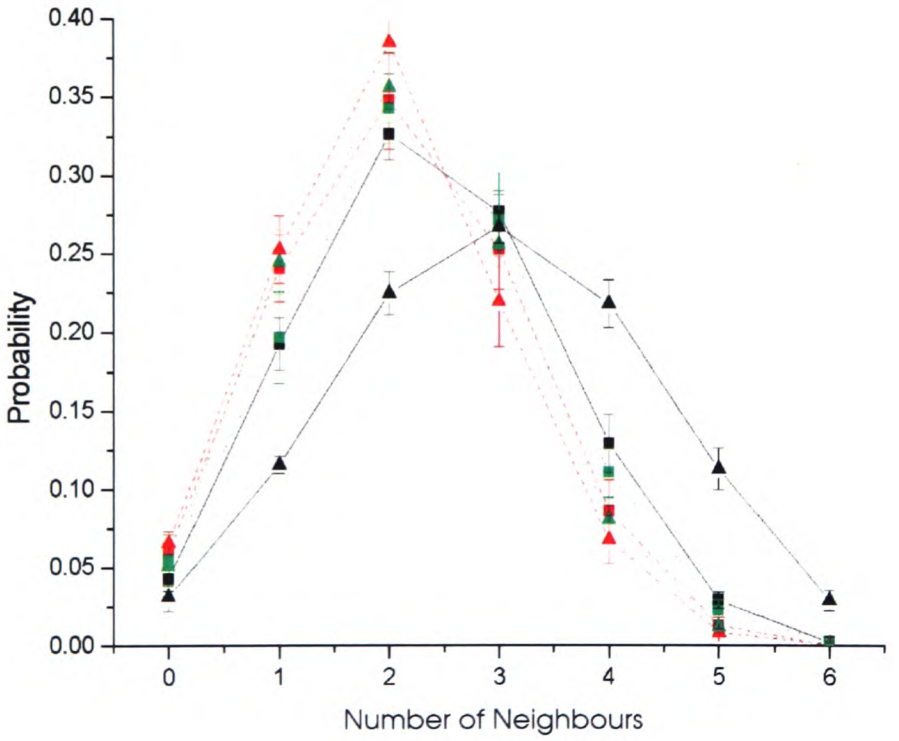

Figure C.3: **Top Plot**: 3-D Neighbour distribution comparing the high Φ_p (note with higher Φ_c as well) gel region containing order (figure C.1: Top= ▲) with the region in which no order is observed (figure C.1: Bottom = •). The average quiescent neighbour distribution (= ▼) is also included. **Bottom Plot**: 2-D Neighbour distribution comparing the high Φ_p (note with higher Φ_c as well) gel region containing order (figure C.1: Top= ▲) with the region in which no order is observed (figure C.1: Bottom = ■).[x-y = solid, x-z = long dash, y-z short dash](Sample D1).

is only a small shift in the sheared stack that does not show obvious ordering and this slight shift is also seen with in the experiment with sample D2, figure C.6(Bottom).

Secondly, we look at the same experiment conducted with high Φ_p sample D2 (see table 3.4). Figure C.4 shows two image volumes recorded after the shear was stopped. Both disordered regions (top stack) and partly ordered regions (bottom stack) of the sample were typically found. In the ordered stack layers of particles orientated in the x-y plane are evident from the lines of particles in the x-z and y-z images. Small 2-D clusters of ordered particles are present separated by voids and the structure is frozen.

The locations of the particles in both 3-D volumes was calculated allowing quantitative analysis of the structure. The three 2-D RDFs are compared with the 3-D RDF for the disordered stack in figure C.5 (Top). A similar shape for g(r) is seen for all three 2-D planes and in 3-D. Figure C.5 (Bottom) shows the same RDFs for the partly ordered stack. There is a clear difference between the x-y plane and the other two planes. Peaks are seen in g(r) for the x-y plane out to $r \sim 10R$. These peaks are not seen in the 3-D RDF.

We also measured the neighbour distributions for both stacks in 3-D and in each of the three 2-D planes orientations. Figure C.6 (Top) compares the 3-D Neighbour distribution for the high Φ_p gel region containing order with the region in which no order is observed. The average quiescent neighbour distribution is also included. There is no significant difference between the two sheared structures or with the quiescent state. However, when the 2-D neighbour distributions (figure C.6 (Bottom)) are considered clear differences emerge between the two sheared stacks. Both x-y planes have higher number of neighbours than the other plane orientations. The shift in the ordered stack is large with $\sim$ 2% of particles having 6 neighbours. There is only a small shift in the x-y neighbour distribution for the sheared stack that does not show obvious ordering and this slight shift is also seen in the experiment with sample D1 in figure C.3 (Bottom).

We now look at the short shear experiment for a medium Φ_p gel (Sample D3, see table 3.4). Figure C.7 (Top left) shows a typical 3-D volume recorded after the shear is stopped. No change in the structure in response to the shear is observed. Quantitative analysis of the sheared stack was conducted. There is no significant difference between the 2D and 3D RDF (figure C.7 (Middle left)) and they all appear the same as the quiescent RDF (see figure 5.9). There is also no significant shift in any of the 2-D neighbour distributions with the applied shear (figure C.7 (Bottom left)).

The short shear experiment for the low Φ_p gel also did not find any change in the structure

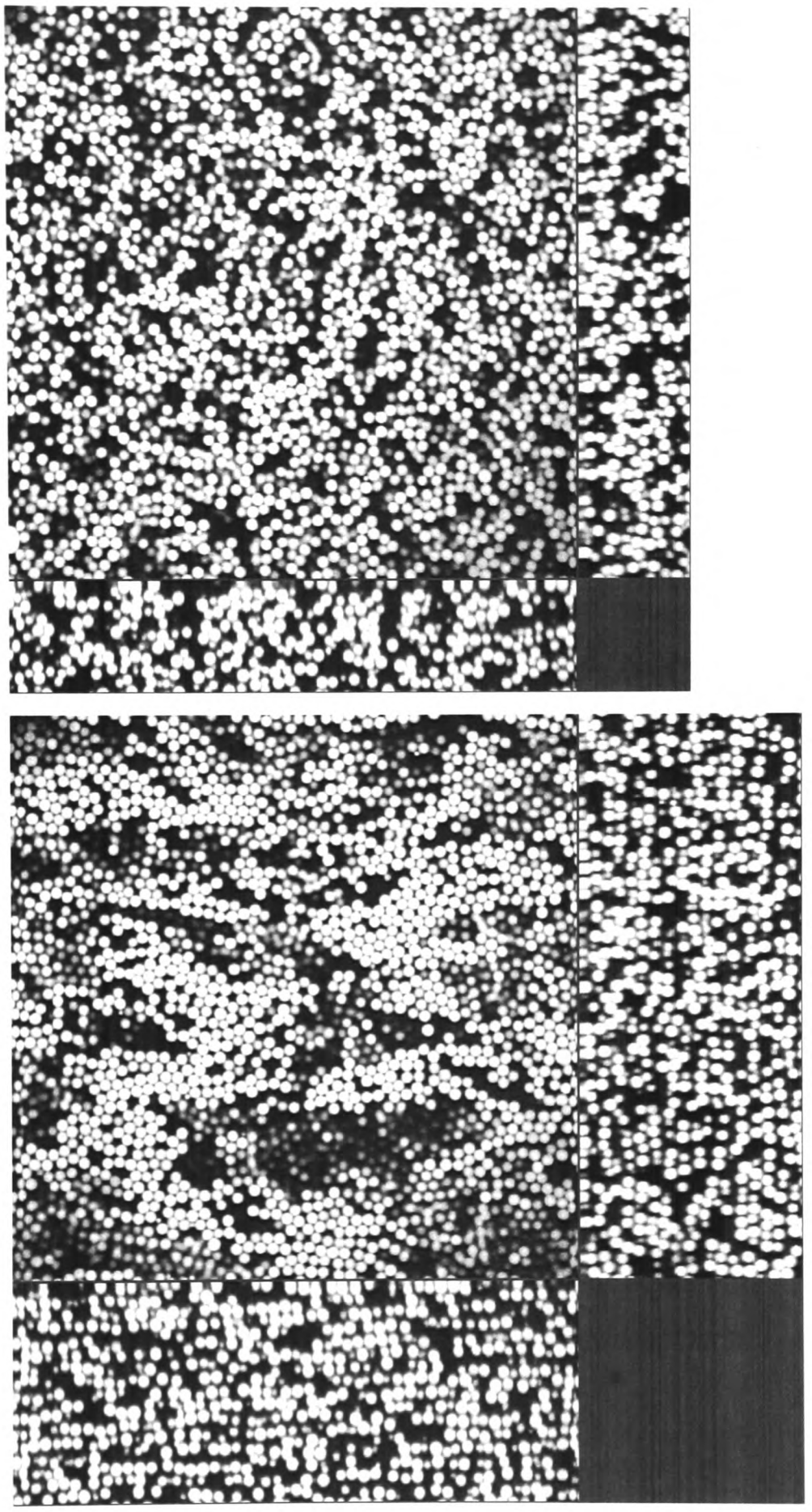

Figure C.4: 2-D projections of 2 different 3-D image volumes of high Φ_p (D2) gel after 15 seconds at $\gamma_0 = 0.15$ at 70Hz. Top image = Typical image of structure in part of sample where no order is evident. Bottom image = Typical image of structure in part of sample where particle order is clearly evident. (Top image volume = $103\mu m \times 103\mu m \times 20\mu m$, bottom image volume = $103\mu m \times 103\mu m \times 40\mu m$)

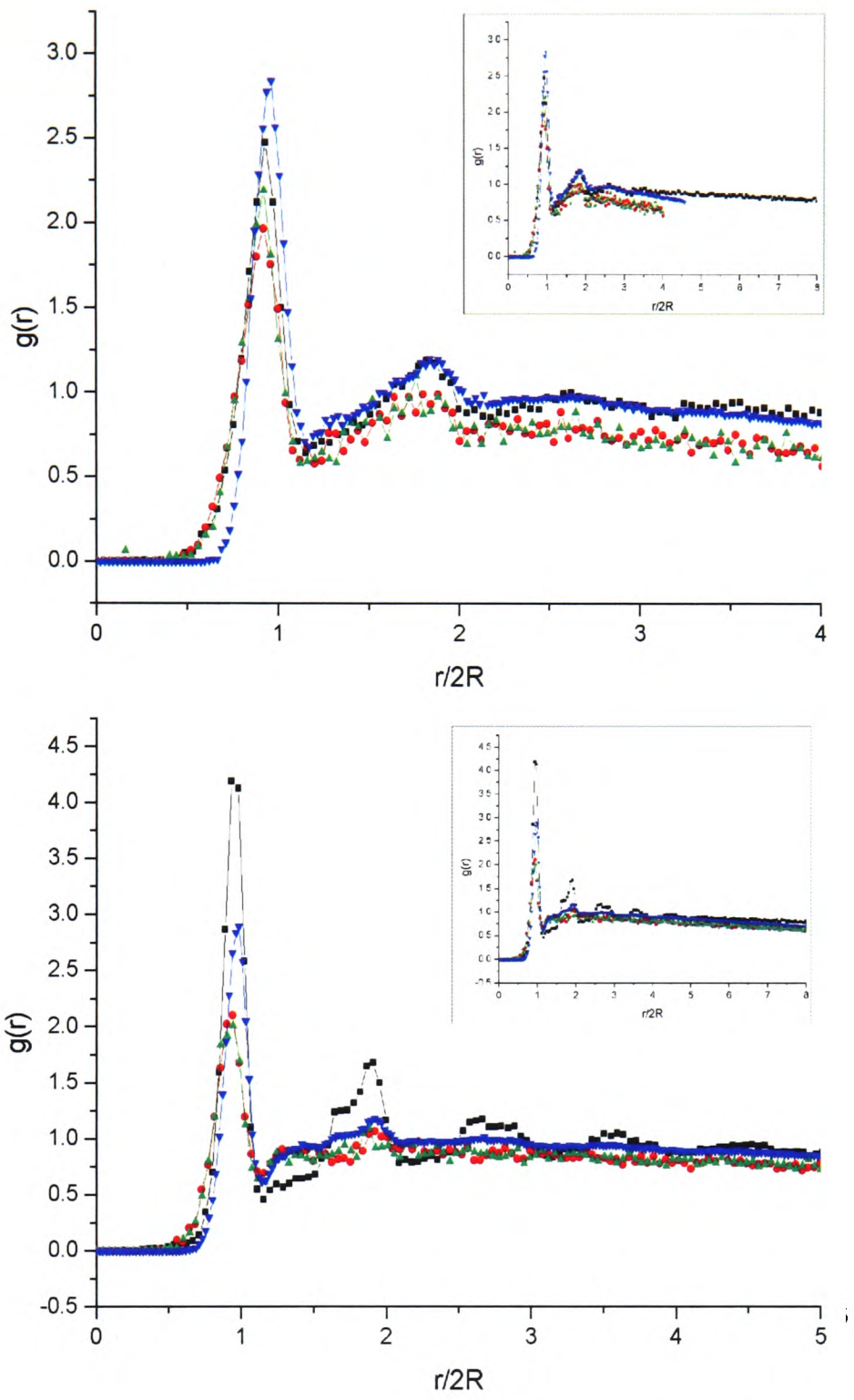

Figure C.5: Radial distribution functions comparing the 2-D planes and the full 3-D volume. The two sets of RDFs compare the local structure of the high Φ_p gel region in which no order is observed (Top) with the gel region in which order is observed (Bottom). The insets in the two plots are the same RDF's as the main plots but with an extended x-axis scale. (figure C.4: Top and bottom respectively). (Sample D2) [(x-y plane = ■, x-z plane = ●, y-z plane = ▲, 3D = ▼]

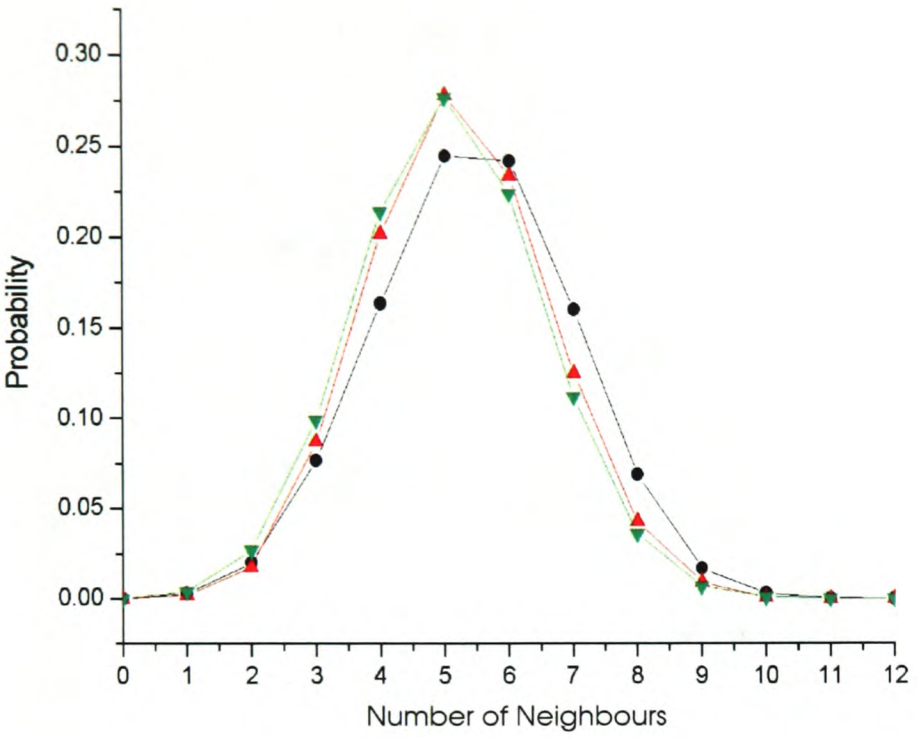

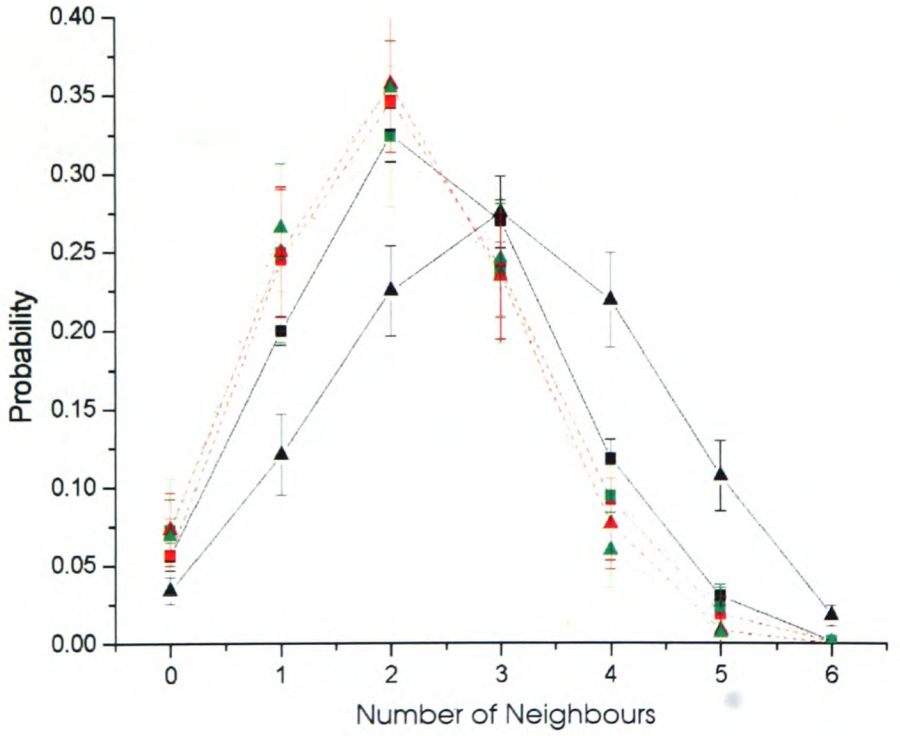

Figure C.6: **Top Plot**: 3-D Neighbour distribution comparing the high Φ_p gel region containing order (figure C.4 : top = ▲) with the region in which no order is observed (figure C.4: Bottom = •) The average quiescent neighbour distribution (= ▼) is also included. **Bottom Plot**: 2-D Neighbour distribution comparing the high Φ_p gel region containing order (figure C.4: Top = ▲) with the region in which no order is observed (figure C.4: Bottom = ■) .[x-y = solid, x-z = long dash, y-z short dash](Sample D2).

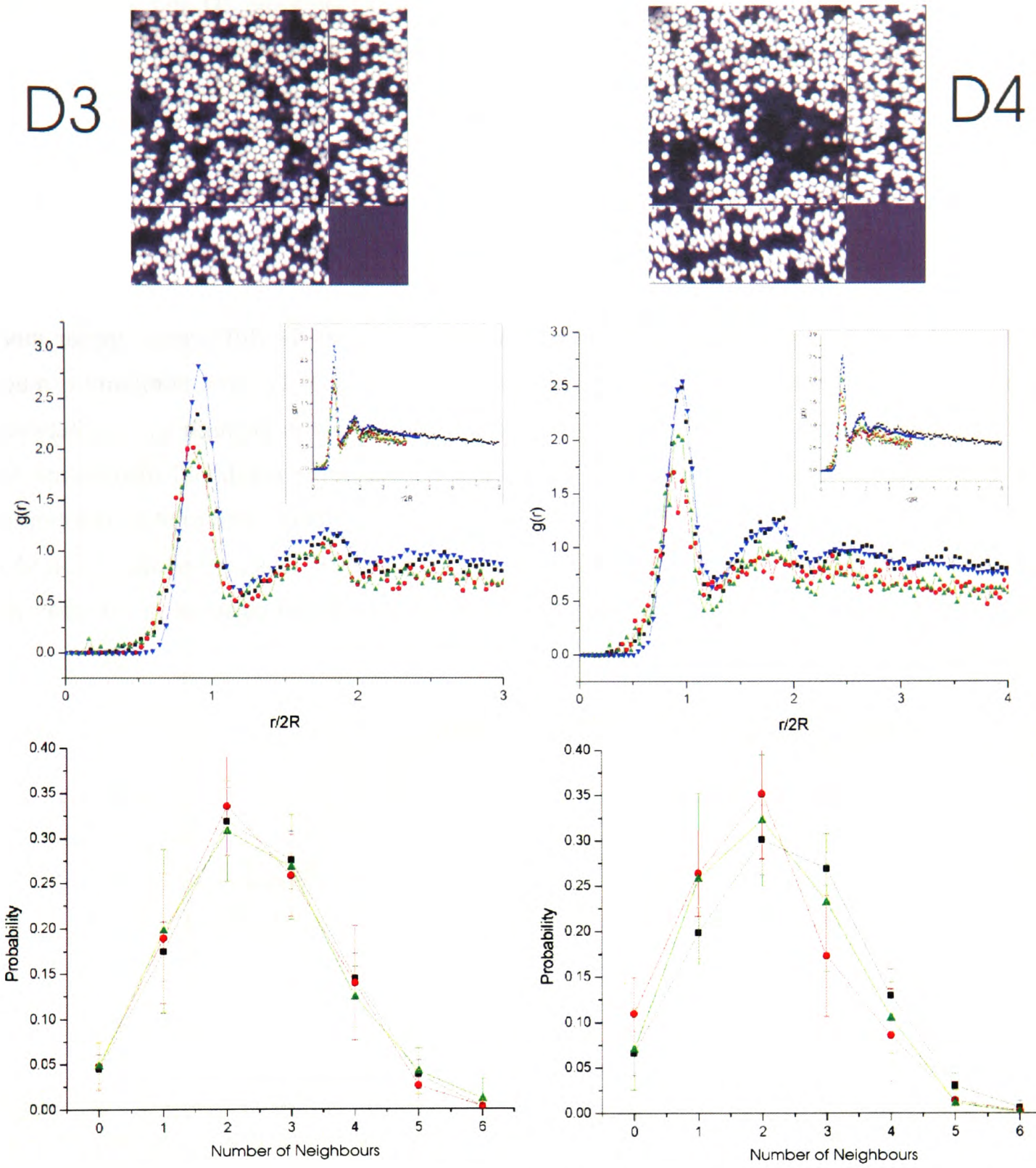

Figure C.7: Results after 15 seconds at $\gamma_0 = 0.15$ at 70Hz for medium Φ_p gel, Sample D3 (Left-hand column) and low Φ_p gel, Sample D4 (Right-hand column).**Top**: 2-D projection of 3-D image volume for both gels (image volume = $51\mu m \times 51\mu m \times 20\mu m$). **Middle**: Radial distribution functions comparing the 2-D planes and the full 3-D volume for both gels. Very noisy and short range due to small size of 3D stack. The insets in the two middle plots are the same RDF's as the main plots but with an extended x-axis scale. [(x-y plane = ■, x-z plane = •, y-z plane = ▲, 3D = ▼] **Bottom**: 2-D Neighbour distributions comparing the different plane orientations for the both gels (x-y plane, = ■, x-z plane = •, y-z plane = ▲).

of the gel after shear (Sample D4, see table 3.4). Figure C.7 (Top right) shows a typical 3-D volume after shear. There is no significant difference between the 2D and 3D RDF (see figure C.7 (Middle right)) and they all appear to have the same shape as the quiescent RDF (see figure 5.9). There is no difference in the 2-D neighbour distribution after shear (see figure C.7 (Bottom right)).

Finally, we consider all of the experiments in this section together. Figure C.8 is a comparison of the 3-D g(r) for the four different gels subject to $\gamma_0 = 0.15$ for 15 seconds at 70Hz. Differences can be seen in the RDF of the high Φ_p gels and the lower Φ_p gels. This is similar to figure 5.9 of the quiescent structure in which similar g(r) but the differences appear more pronounced. The lower Φ_p gels have a much more liquid-like g(r). The first minimum is much wider and more curved than the high Φ_p gels. g(r) is almost linear in the high Φ_p case between the first minimum and the second peak. Figure C.9 compares the neighbour distribution for the four different gels subject to $\gamma_0 = 0.15$ for 15 seconds at 70Hz. The relative position of the different RDFs is similar to the quiescent state (figure 5.10). It is interesting to note that the lower Φ_p gels that are disordered still have more highly ordered particles in 3-D than the ordered gels.

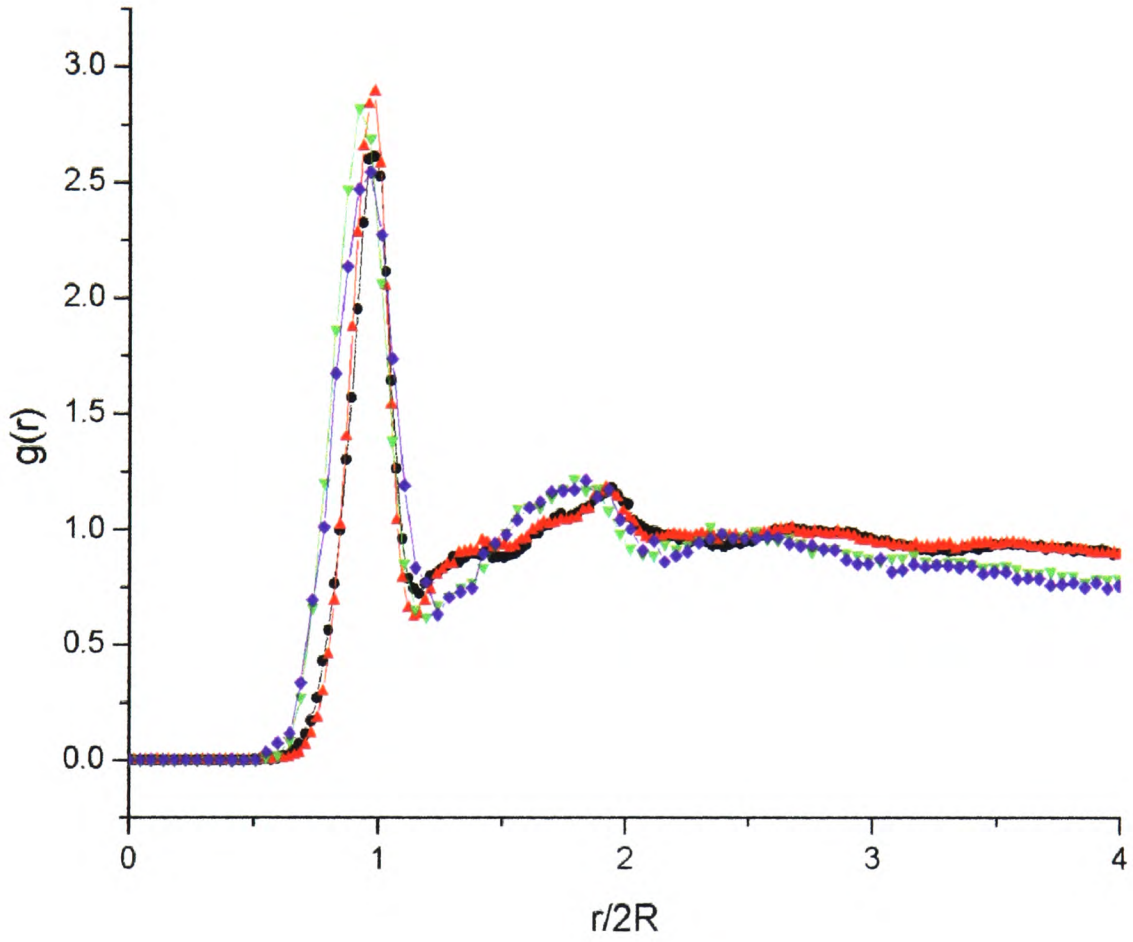

Figure C.8: Comparison of g(r) for the four different gels subject to $\gamma_0 = 0.15$ for 15 seconds at 70Hz. Note, for the high Φ_p gels, g(r) for the partly ordered stacks were used. (● = High $\Phi_p, \Phi_c = 0.44$ (D1), ▲ = High $\Phi_p, \Phi_c = 0.40$ (D2), ▼ = Medium $\Phi_p, \Phi_c = 0.40$ (D3), ♦ = Low $\Phi_p, \Phi_c = 0.40$ (D4))

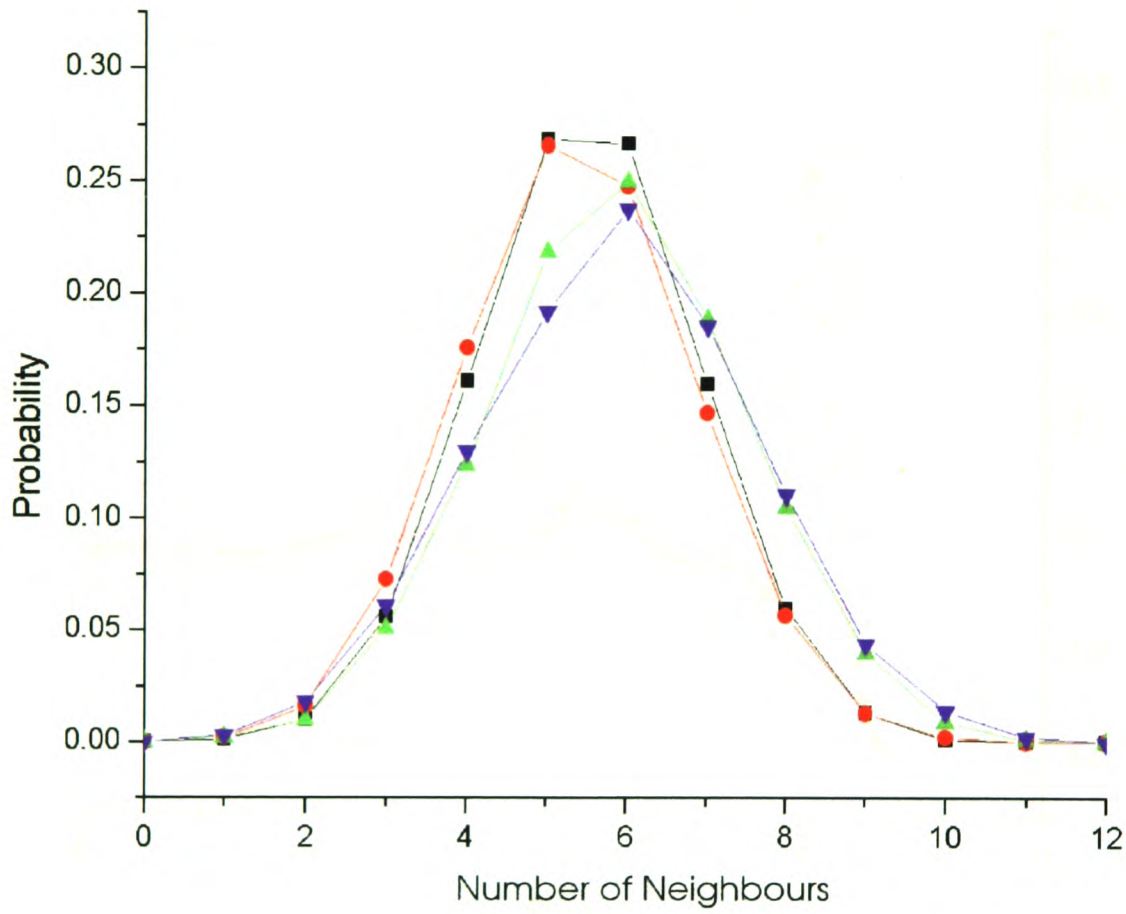

Figure C.9: Comparison of neighbour distribution for the four different gels subject to $\gamma_0 = 0.15$ for 15 seconds at 70Hz. Note, for the high Φ_p gels, the data for the stacks showing order were used. ■ = high $\Phi_p, \Phi_c = 0.44$ (D1), • = High $\Phi_p, \Phi_c = 0.40$ (D2), ▲ = Medium $\Phi_p, \Phi_c = 0.40$ (D3), ▼ = Low $\Phi_p, \Phi_c = 0.40$. (D4))

Step Shear Ramp at 70Hz

In the previous experiments, a strain of $\gamma_0 = 0.15$ has been imposed on a quiescent, freshly loaded sample for some fixed time. In this section we look at experiments where a shear ramp has been used (see figure 3.4). The sample experiences a low strain for a fixed time, then the shear is stopped to allow the sample to be explored and images recorded. A higher strain is then imposed on the sample sample for the same fixed time. The shear is again stopped and images recorded. This process is repeated up to a maximum strain. This method is explained in more detail in section 3.4.3. We look at step shear ramp experiments for a range of samples with varying polymer volume fraction Φ_p.

High Φ_p shear ramp at 70Hz

The high Φ_p gel, sample D2 (see table 3.4) is sheared for 2 minutes at each strain, at a frequency of 70Hz. No change was observed in the structure up to $\gamma_0 = 0.15$. At $\gamma_0 = 0.15$ some very small patches of ordered particles (size of order a few particles) are observed as shown in figure C.10 (Top). However, in general the gel is still disordered at this strain. On increasing the strain further a clear change in the structure is found. There is the emergence of bigger clusters (see figure C.10 (Middle) and very large voids (see figure C.10 (Bottom)) not seen at lower strains or in the quiescent structure (figure 5.8 (B)). Clear evidence of particle rearrangement is seen. However, this is not accompanied in this experiment by any significant particle ordering. The maximum strain available with shear cell 3 used in this experiment was $\gamma_0 = 0.22$.

Medium Φ_p shear ramp at 70Hz

The medium Φ_p gel, sample D3 (see table 3.4) is also sheared at 70Hz, for 2 minutes at each strain. For reference the quiescent structure is shown in figure 5.8 (C). No change in the gel structure is observed up to $\gamma_0 = 0.12$, see figure C.11 (Top). Higher strain does lead to small observable changes in the gel structure. A few very small ordered regions are observed but the gel is basically disordered: see figure C.11 (Bottom). There is some small short-range movement of some particles observed in a time series recorded after the shear was stopped, but most particles remain frozen. The maximum strain available with shear cell 3 used in this experiment was $\gamma_0 = 0.22$.

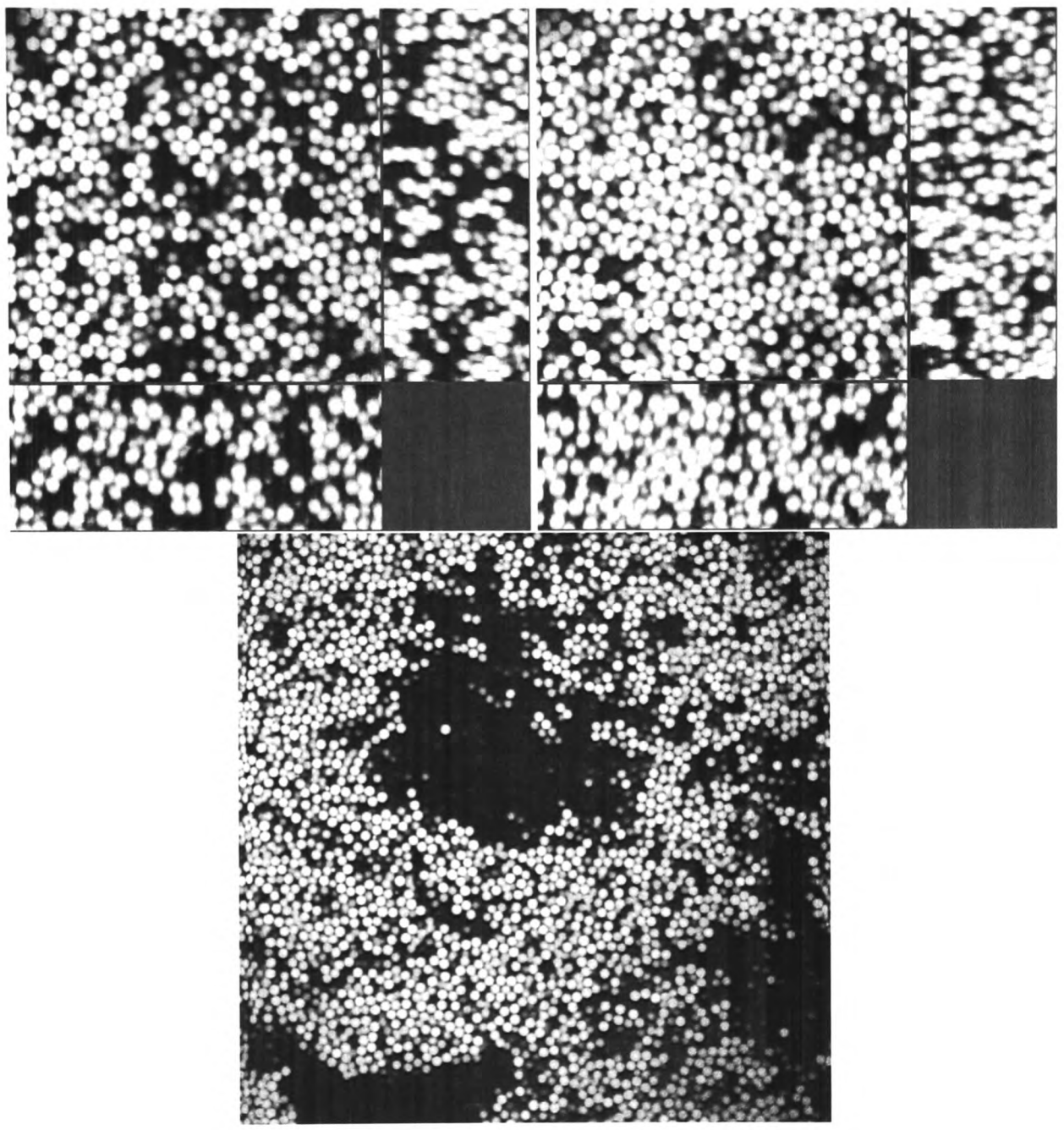

Figure C.10: Typical confocal gel images from High Φ_p gel, 70Hz shear "step-ramp" experiment at a strain of $\gamma_0 = 0.15$ (Top left), $\gamma_0 = 0.22$ (Top right) and (Bottom) . Shear time is 2 minutes at each strain [Top and Middle image volume = $51\mu m \times 51\mu m \times 20\mu m$, Bottom image size = $103\mu m \times 103\mu m$](Sample D2)

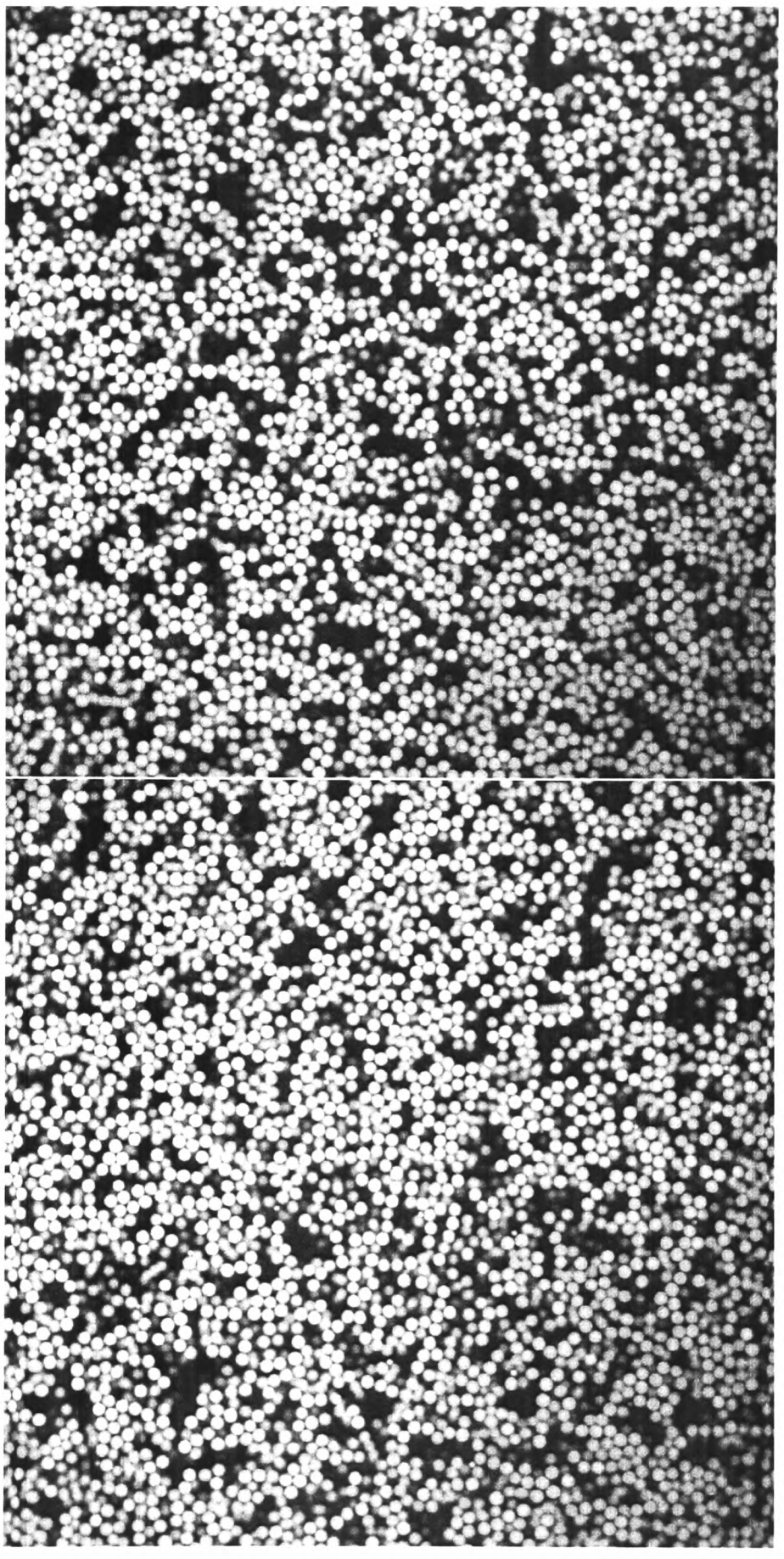

Figure C.11: Typical confocal gel images from Medium Φ_p gel, 70Hz shear "step-ramp" experiment at a strain of $\gamma_0 = 0.12$ (Top) and $\gamma_0 = 0.17$ (Bottom). Shear time is 2 minutes at each strain [box size is 123 $\mu m \times 123 \mu m$](Sample D3)

Low Φ_p shear ramp at 70Hz

The low Φ_p gel, sample D4 (see table 3.4) is sheared at 70Hz for 2 minutes at each strain. For reference the quiescent structure is shown in figure 5.8 (D). No change in the gel structure is observed up to $\gamma_0 = 0.12$ (see figure C.12 (Top Left)). For $\gamma_0 = 0.14$ some changes are observed in the gel structure with larger voids and bigger clusters of particles (see figure C.12 (Top Right). These changes become more pronounced as the shear is increased. Figure C.12 (Bottom Left) shows a typical image for $\gamma_0 = 0.16$. Very large clusters and big voids are observed. Figure C.12 (Bottom Right) shows a lower magnification image of the shear induced structure taken after shear at $\gamma_0 = 0.17$. The maximum strain available with shear cell 3 used in this experiment was $\gamma_0 = 0.22$.

Very Low Φ_p shear ramp at 70Hz

In this experiment the very low Φ_p gel, sample D5 (see table 3.4) is sheared at 70Hz, for 2 minutes at each strain. For reference the quiescent structure is shown in figure 5.6. We observe no change in the gel structure up to $\gamma_0 = 0.05$. Slightly larger voids are evident for figure C.13 (Top left), taken after shear at $\gamma_0 = 0.08$. In a time series recorded after the shear was stopped there was lots of jiggling particles observed within gel structure including some particles breaking bonds and changing neighbours. The amount of particle movement was greater than observed in the quiescent gel. An image from such a time series, but for a higher strain of $\gamma_0 = 0.12$, is shown in figure C.13 (Top right). The image shown is recorded within 2 seconds of the shear being stopped. There is a homogeneous appearance to the particle structure. Voids increase in size over the timescale of a minute to give the structure observed in figure C.13 (Middle left). No further significant change is observed over the timescale observed (a further few minutes). Figure C.13 (Bottom left) shows the gel structure that was recorded for $\gamma_0 = 0.16$. Some bigger voids are observed at this strain. Taken from a time series, figure C.13 (Middle right) was recorded within 2 seconds of shear being stopped at $\gamma_0 = 0.16$. The large void seen here is observed as soon as the shear is stopped. This suggests that it exists while the gel is being sheared. The maximum strain available with shear cell 3 used in this experiment was $\gamma_0 = 0.22$.

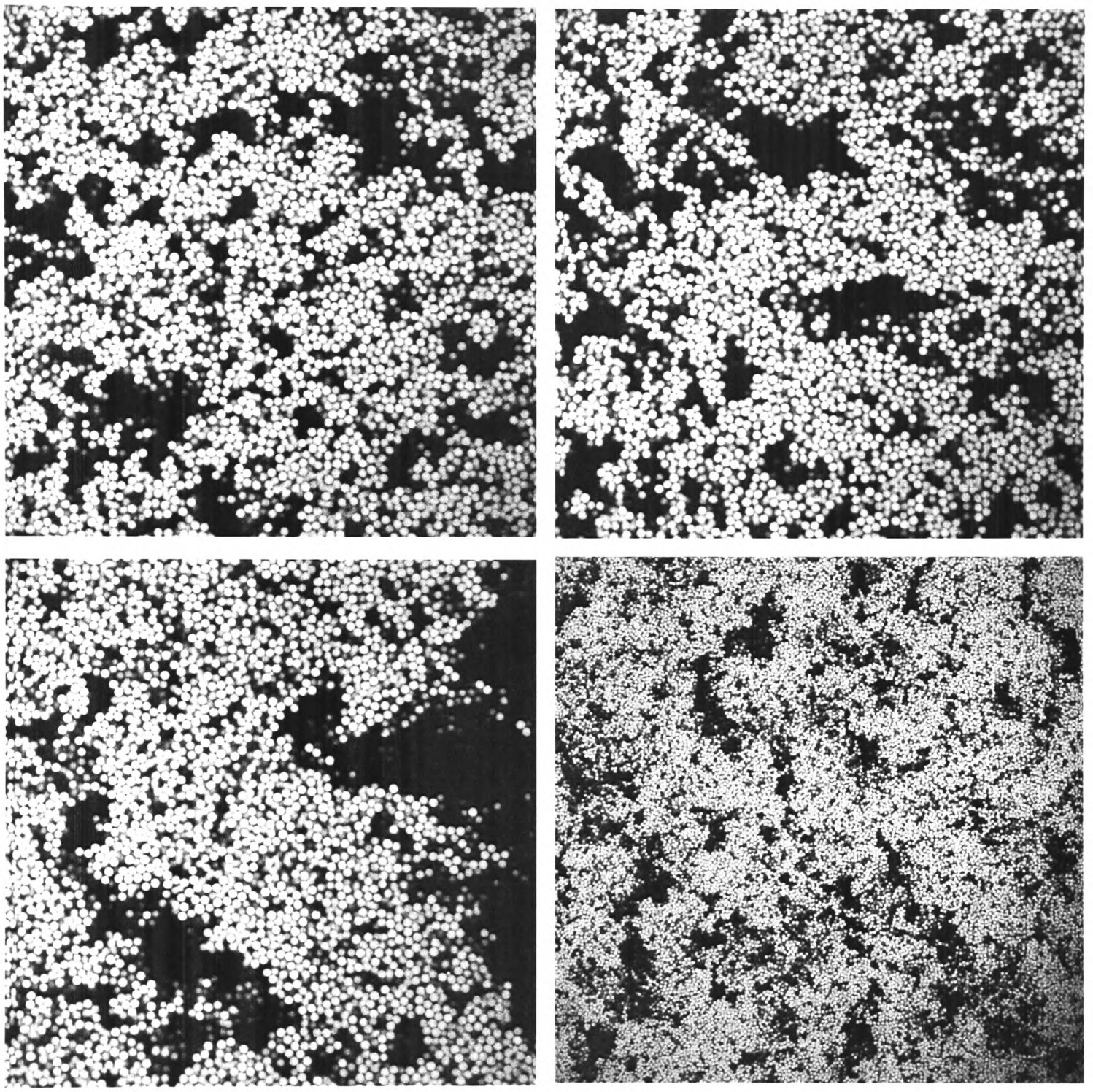

Figure C.12: Typical confocal gel images from low Φ_p gel, 70Hz shear "step-ramp" experiment at a strain of $\gamma_0 = 0.12$ (Top left), $\gamma_0 = 0.14$ (Top right), $\gamma_0 = 0.16$ (Bottom left) and $\gamma_0 = 0.17$ (Bottom right). Shear time is 2 minutes at each strain [box size is 123 $\mu m \times 123 \mu m$] except for Bottom left image where box size is 308 $\mu m \times 308 \mu m$](Sample D4)

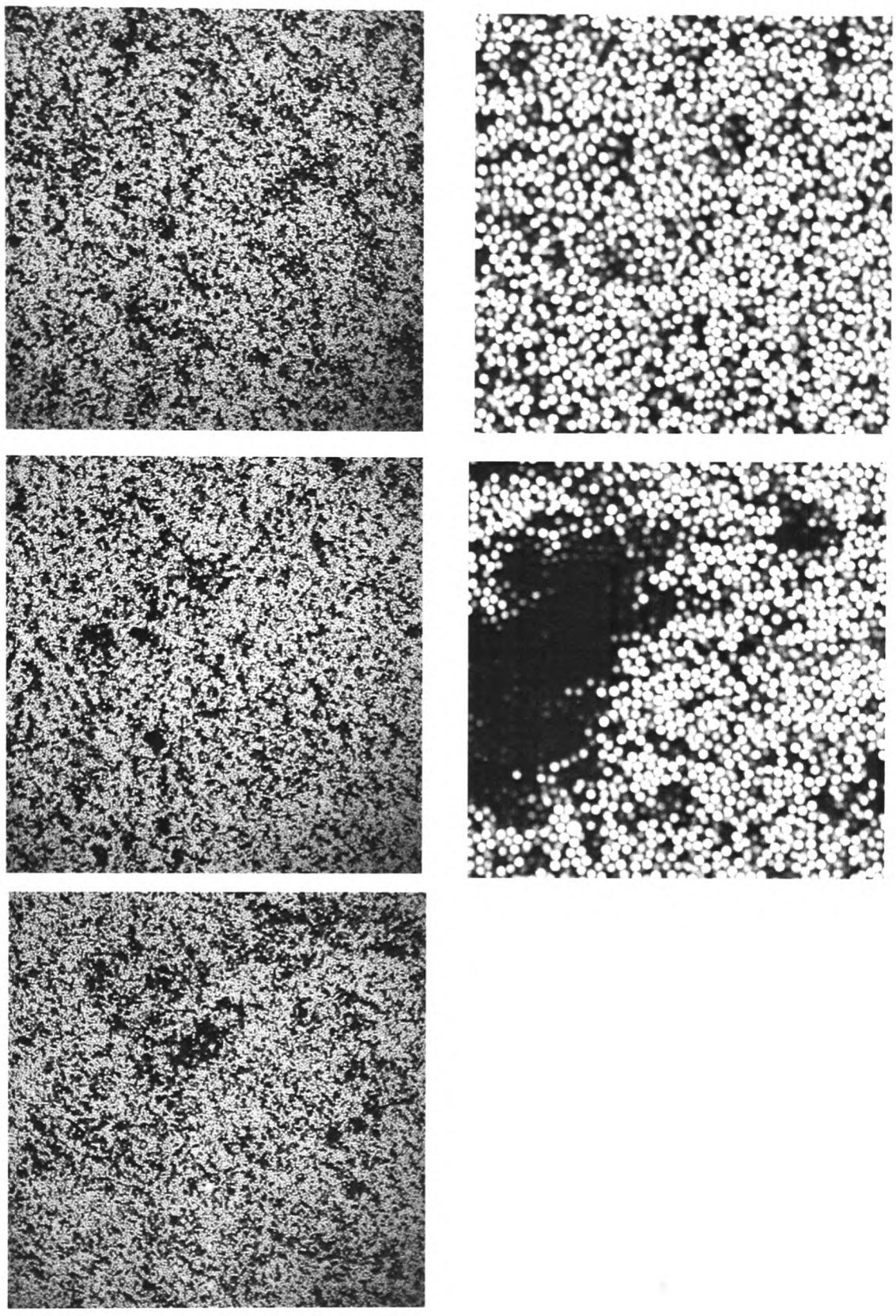

Figure C.13: Typical confocal gel images from very low Φ_p gel, 70Hz shear "step-ramp" experiment at a strain of $\gamma_0 = 0.08$ (Top left), $\gamma_0 = 0.12$ (Top right and Middle left), $\gamma_0 = 0.156$ (Middle right and Bottom left). Shear time is 2 minutes at each strain [Left column images have box size 308 $\mu m \times 308 \mu m$], [Right column images have box size is 88 $\mu m \times 88 \mu m$]],(Sample D5)

Colloidal Fluid at 70Hz ($\Phi_p = 0$)

A pure colloidal fluid with no added polymer was sheared at $\gamma_0 = 0.15$, initially for 15 seconds. No change was observed in the structure for images taken immediately after the shear was stopped. The fluid was sheared for a further 2 minutes. The structure appeare the same to the naked eye. The images recorded appear identical to the quiescent fluid shown in figure 5.7.

Medium Φ_p shear ramp at 70Hz with smaller particles

A shear ramp experiment was conducted with the medium Φ_p gel, sample B2 and with sample B3 which has a higher volume fraction (see table 3.4). The quiescent structure for these gels is shown in figure 5.5. These samples are made with particles half the size of those in the confocal shear ramp experiments already described above.

The medium Φ_p gel, sample B2 is sheared at 70Hz, for 2 minutes at each strain. For $\gamma_0 < 0.10$ no change is observed in the gel structure. At $\gamma_0 = 0.10$ the large voids often found in the quiescent gel (see figure 5.5 (B)) have on average disappeared by this strain. An untypical void is shown in figure C.14 (Top Left) along with small voids and disordered structure. At $\gamma_0 = 0.14$ only small voids remain and very small patches of order begin to appear (see figure C.14 (Top Right)). An unusual part of the sheared gel for $\gamma_0 = 0.18$ is shown in figure C.14 (Bottom Left). There is a "stringy" appearance to the gel structure in this part of the gel and many small voids. As the strain increases small patches of order are still observed as shown in the typical image in figure C.14 (Bottom Right). No significant increase in ordering is seen with increasing strain for this sample (B2) with $\Phi_c = 0.44$.

The same experiment was conducted with sample B3 ($\Phi_c = 0.47$). Similar behaviour was observed up to $\gamma_0 \sim 0.15$. However, in contrast to sample B2 (figure C.14 (Bottom Right)) strains above $\gamma_0 \sim 0.15$ give a lot of ordered regions as shown in figure C.15 (Top). Ordered regions of size ~ 10 particle diameters are found with a variety of orientations separated by voids and disordered regions. Different parts of the sample show a wide spread in the amount of ordering but this image is typical. A closer look at a similar ordered region is shown in figure C.15 (Bottom).

105 Seconds Shear at 10Hz

An experiment was conducted at 10Hz, at the same fixed strain of $\gamma_0 = 0.15$ as the 15 second single strain experiment for the high Φ_p gel at 70Hz. The same number of cycles of shear

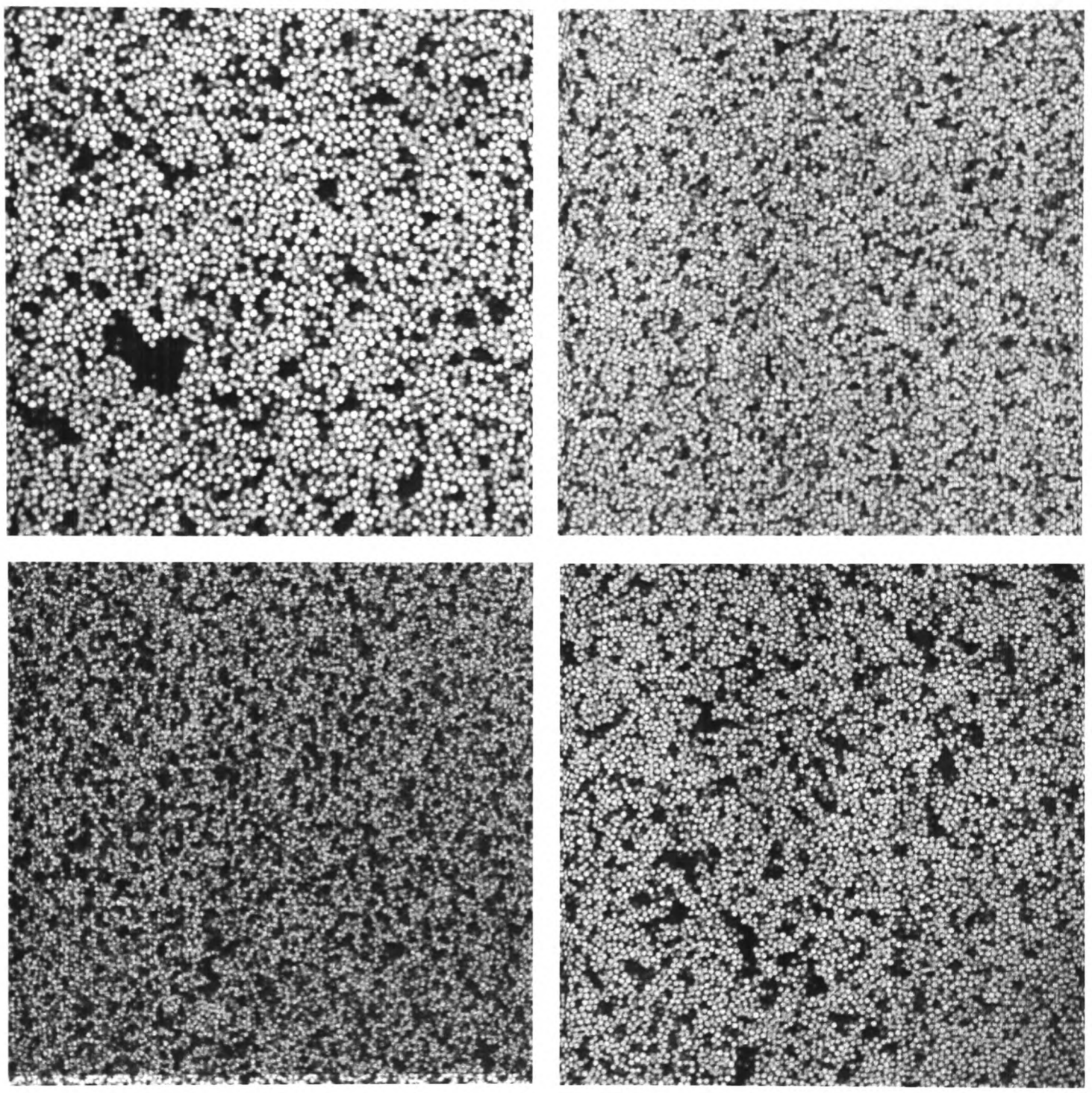

Figure C.14: Confocal gel images from Medium Φ_p gel, 70Hz shear "step-ramp" experiment at a strain of $\gamma_0 = 0.10$ (Top left), $\gamma_0 = 0.14$ (Top right), $\gamma_0 = 0.175$ (Bottom left) and $\gamma_0 = 0.28$ (Bottom right). Shear time is 2 minutes at each strain. [Top left= $62\mu m \times 62\mu m$, Top right = $86\mu m \times 86\mu m$, Bottom left = $93\mu m \times 93\mu m$ and Bottom right = $82\mu m \times 82\mu m$] (Sample B2)

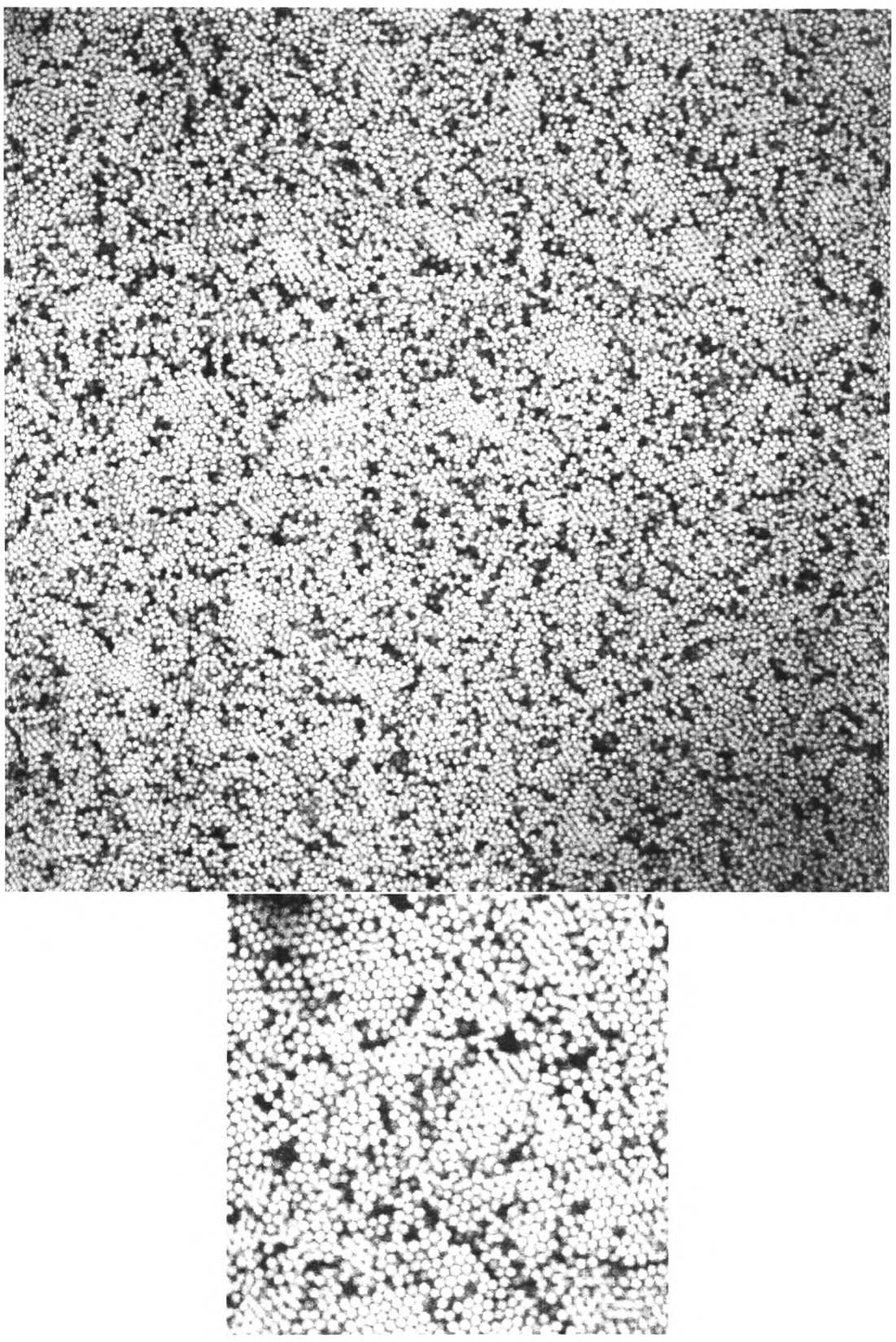

Figure C.15: Typical confocal gel images from Medium Φ_p gel, 70Hz shear "step-ramp" experiment at a strain of $\gamma_0 = 0.17$ with $\Phi_c = 0.467$. Shear time is 2 minutes at each strain. [Top image size = $123\mu m \times 123\mu m$ and Bottom image size = $40\mu m \times 40\mu m$] (Sample B3).

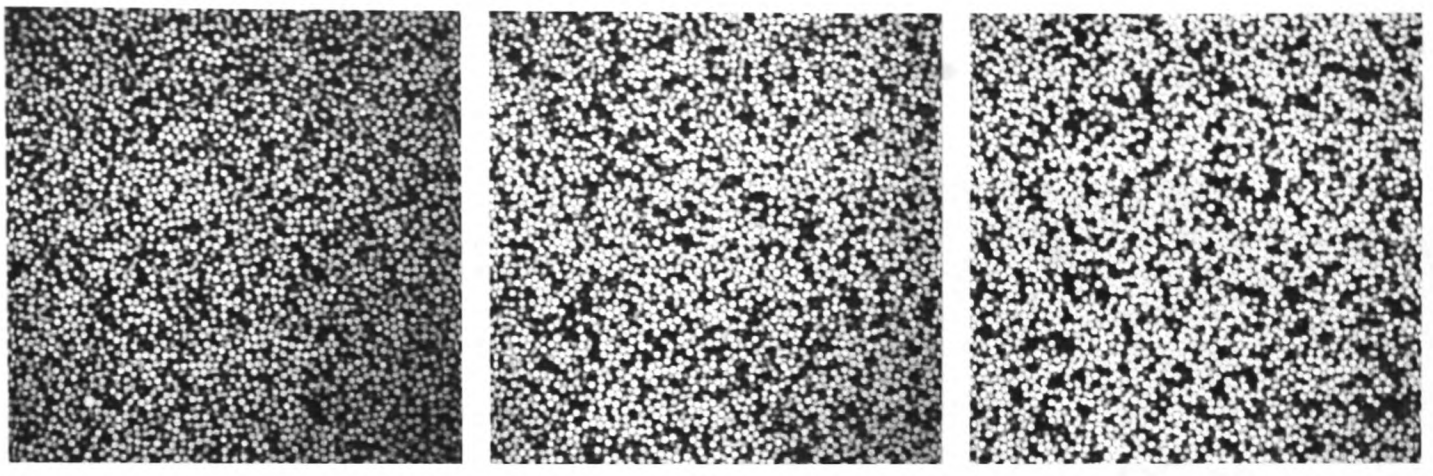

Figure C.16: Typical confocal images. Left Image: Quiescent gel before shear. Middle image: After 105 seconds shear at 10Hz at $\gamma_0 = 0.15$. Right Image: After additional 105 seconds at 10Hz at $\gamma_0 = 0.19$.$\Phi = 0.44, C_p = 0.00366, R = 1.1\mu m$

were used (1050 cycles) as in the 70Hz experiment. This corresponds to an experiment lasting 105 seconds for 10Hz. The experiment was conducted with a high Φ_p gel (Sample D1, see table 3.4). Figure C.16 shows typical images from the experiment. The left most image is the quiescent gel before shear commenced. The middle image is recorded after 105 seconds of shear. The rightmost image is recorded after an additional 105 seconds of shear. The gel appears unaffected by both periods of shear.

Shear Phase Diagram

We bring together all of the confocal shear results for the experiments conducted at 70Hz in a single 3-D shear phase diagram. The shear phase diagram is shown in figure C.17 and contains the observed effect of 70Hz shear for different colloid volume fractions, Φ_c, depletion potential strength (U_0) and strain, γ_0. The depletion potential strength for each of the different Φ_p gels is taken from table 3.4. For a volume fraction $\Phi_c \sim 0.40$ rearrangement is observed at lower strains for lower potential strengths (lower Φ_p). Increasing the volume fraction, $\Phi_c > 0.40$ leads to order being observed when the particles rearrange. For the highest potential, $U_{dep} = 46kT$, a jump to strain $\gamma_0 = 0.15$ leads to order in contrast to no order being seen when the strain is increased from $\gamma_0 = 0$ up to $\gamma_0 = 0.15$ and beyond in steps (the other points at $U_{dep} = 46kT$).

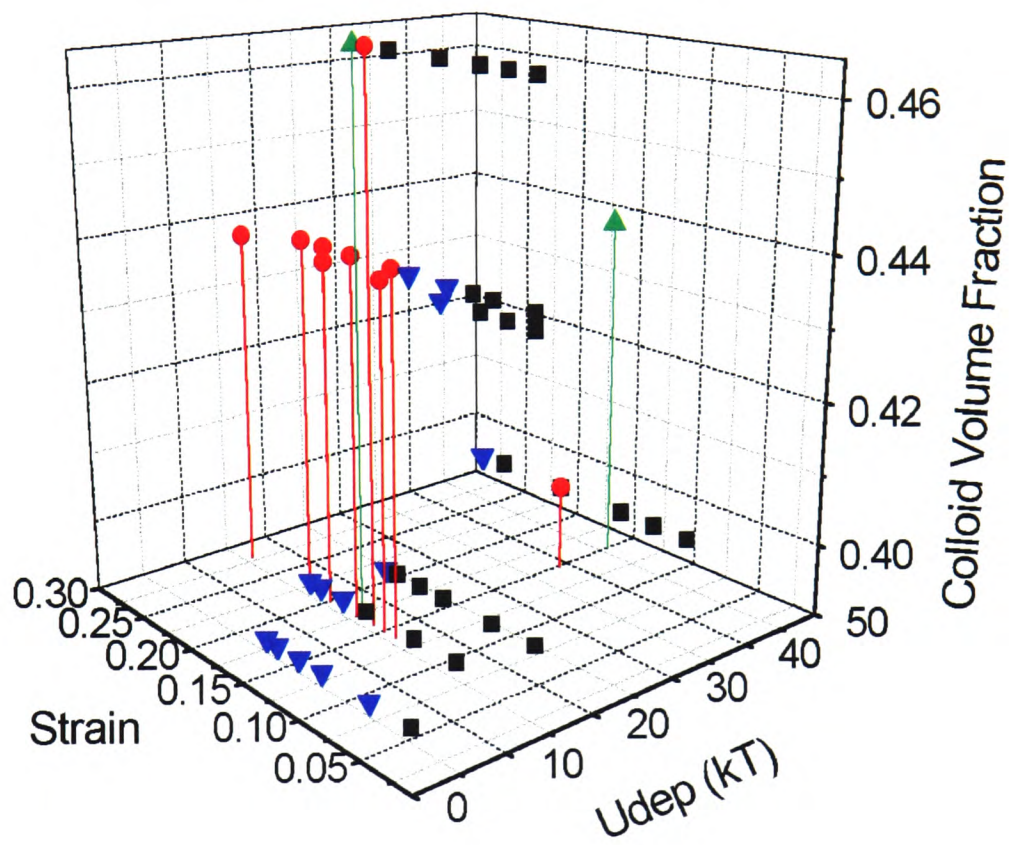

Figure C.17: 3-D shear phase diagram of observed effect of 70Hz shear for different colloid volume fractions, Φ_c, Potential strength (U_0) and strain, γ_0. (figures symbols: No observable change, = ■, Some order observed = ●, Some very ordered areas observed = ▲, Rearrangement of voids observed/ no order = ▼)

Discussion

In this section we bring together all of the separate experiments described in this Appendix. The proportion of ordered particles varies significantly within different parts of a sheared gel sample (e.g. figure 6.19). We also find that the coarse-grained structure of the gel is significantly affected by shear. We find voids in some sheared samples than are much larger than those seen in the quiescent state. We attribute both kinds of structural changes to the inhomogenous structure of the quiescent gel. The inhomogeneous structure has some regions of particles that are more dense and some regions which have more voids (less dense) than average. We have found that ordered regions are more dense and have a higher average number of neighbours (especially in 2-D) than typical quiescent regions. We can only speculate on the formation of the ordered regions but it is possible that particles in denser regions in the quiescent gel would be more likely to order before particles in low density regions. Alternatively, it may be the lower density particles that are more likely to rearrange are also more likely to form ordered regions (of higher final density). Either way ordered regions would be restricted to only some parts of the sample giving the wide difference in the amount of ordering observed in different parts of a sheared gel sample that shows significant ordering on average. Likewise, the voids that are initially larger than the typical size would be more likely to still be found after shear and could grow larger as particles become more densely packed. Although we impose a simple shear profile, there may be local variations in the shear profile experienced by the particles.

We have found that the behaviour of the gel under oscillatory shear is dependent on the oscillation frequency in both microscopy (figure 6.1) and LS-echo experiments (figure (6.17). Optical microscopy shows that higher strains are found to be required to induce ordering in the high Φ_p gel for lower frequencies. The high Φ_p confocal experiments agree with the optical findings. Limited shear step ramp experiments (up to $\gamma_0 = 0.19$) at 10Hz (figure C.16) found no change in the gel structure in contrast to the 70Hz experiment (figure C.10) which found rearrrangement of the gel structure at $\gamma_0 = 0.15$. Similarly, in the LS-echo experiments higher strains are required to lead to a drop in the echo heights (for given delay time), where the drop in the echo height is identified with rearrangement of the gel structure.

The typical amount of order was found to depend on the imposed strain and shear time. In the optical microscopy shear ramp experiment at 70Hz (figure 6.1 (top)) the amount of order was found to increase initially with increasing strain, before decreasing again at higher strains. A comparison of the two experiments conducted at fixed $\gamma_0 = 0.15$ at 70Hz with a high Φ_p gel for different shear times, 31 minutes (1860 seconds) (figure 6.19) and 15 seconds (figure C.1)

show that a longer shear time leads to a larger proportion of ordered regions in the resulting gel structure. This indicates that ordered regions are stable during shear and both the size and fraction of patches of ordered particles grow in time if the sample shear history was "high shear"; sufficient strain to produce particle ordering. In both optical 10Hz experiments (figure 6.7 vs figure 6.6) and confocal 70Hz experiments (figure C.4 vs figure C.10) with high Φ_p gels we find more particle ordering when a shear is suddenly imposed on a new sample than the same shear as part of a strain ramp experiment. This shows that there are different history effects present in the shear ramp experiments. There appears to be a reduced the amount of order observed at a given strain when the sample has been already sheared at a lower strain in comparison to the amount of order observed in a fresh sample sheared at the same strain. We call this the "low shear" sample shear history; longer shear is required to get the same amount of order as found with a "high shear" history.

We now suggest that the greater amount of particle ordering found with the optical compared to the confocal high Φ_p, 70Hz, shear ramp experiment can be explained in terms of the two types of history effect. In the optical experiment, due to the smaller step size used , at $\gamma_0 \sim 0.15$ sufficient time had been spent at "high shear" for the memory of the "low shear" history to be lost. Therefore, further shear at higher strains produced more particle ordering due to the "high shear" history. In contrast, the confocal experiments had less steps so at $\gamma_0 \sim 0.15$ the relevant history was the "low shear" type, leading to less particle ordering being observed.

We have conducted both single strain and shear ramp confocal experiments at 70Hz for gels with varying Φ_p, which corresponds to varying strength of attraction between the particles. The results were summarised in the shear phase diagram in figure C.17. We first consider the 70Hz single strain experiments ($\gamma_0 = 0.15$ for 15 seconds). We only find ordering of the gel structure in the high Φ_p gels (Samples D1, D2); strong peaks are found in g(r) (2-D x-y plane) and an increase in the average neighbour number is found in the 2-D, x-y plane. No evidence of ordering or other rearrangement of particle is observed in the other, lower Φ_p gels (D3, D4, D5) or in the colloidal fluid (Φ_p=0). Quantitative analysis found no significant change compared to the quiescent results for g(r) or the neighbours distribution for the lower Φ_p gels.

Now we consider the 70Hz shear ramp confocal experiments. The strain required to induce changes in the gel structure depends on the Φ_p of the gel but within the strain range used we observed rearrangement of the particle in all of the different Φ_p gels in contrast to the single strain experiment. For samples at high Φ_p (D2) and medium Φ_p (D3, B2, B3) a strain of $\gamma_0 \gtrsim 0.15$ is required for rearrangement to occur. For the low Φ_p gel a slightly lower strain of $\gamma_0 \gtrsim 0.13$ is required. For the very low Φ_p gel a significantly lower strain $\gamma_0 \gtrsim$

0.07 is needed before changes are observed in the gel structure. We note that out of all four confocal shear ramp experiments only in the high Φ_p gel (D2) and in the medium Φ_p gels made with the smaller particles (Samples B2, B3) was any ordering observed. In the other gels the change in the gel structure was detected by observing increased size of disorder clusters and the emergence of large voids, neither of which are found in the quiescent gel structures.

When we consider the colloid volume fraction, Φ_c (particle density) in addition to the polymer volume fraction Φ_p we find a trend in the different kinds of rearrangement found with increasing strain (see phase diagram in figure C.17). In the $\Phi_c = 0.4$ gels (D3, D4, D5) we observe rearrangement of the gel structure but no particle ordering is observed. In contrast, in the experiments with samples with higher $\Phi_c > 0.4$ (B2, B3) we do observe paarticle ordering when the gel structure rearranges. In experiments with samples where we do observe ordering at $\Phi_c = 0.4$ (D2) we find more ordering with increased Φ_c (D1).

This increase in ordering found with increased volume fraction could be due to the locally higher density of the clusters in the gel for a given Φ_p, as a higher number of neighbours. This could lead to a higher probability of an ordered region forming in the first place. Particles could be more likely to line up in planes as collisions between particles are more likely at higher densities if there is a random orientation. We have found that it is possible in some cases for the gel to rearrange without significant ordering of particles being observed.

We do not find any significant particle size related effects in the microscopy experiments. Over the range of strains that the experiments were conducted similar behaviour in response to shear was found with the three different sized particles ($R = 0.5\mu m, 0.7\mu m, 1\mu m$).

List of Tables

List of Figures

Bibliography

[1] W.C.K. Poon and P.N. Pusey. Phase transitions of spherical colloids. In M. Baus, editor, *Observations and Simulations of Phase Transitions in Complex Fluids*, pages 3–51. Kluwer Academic Publishers, 1995.

[2] J. Israelachvili. *Intermolecular and Surface Forces*. Academic Press, second edition, 1991.

[3] W.W. Wood and J.D. Jacobson. Preliminary results from a recalculation of the monte carlo equation of state of hard spheres. *Journal of Chemical Physics*, 27:1207, 1957.

[4] W.G. Hoover and F.H. Ree. Melting transition and communal entropy for hard spheres. *Journal of Chemical Physics*, 49(8):3609–3617, 1968.

[5] S. Asakura and F. Oosawa. *Journal of Polymer Science*, 33(183), 1958.

[6] A. Vrij. Polymer at interfaces and the interactions in colloidal dispersions. *Pure and Applied Chemistry*, 48:471–483, 1976.

[7] J.L. Lebowitz, E. Helfand, and E. Praestgaard. Scaled particle theory of fluid mixtures. *Journal of Chemical Physics*, 43(3):774–779, 1965.

[8] D. G. A. L. Aarts, R. Tuinier, and H. N. W. Lekkerkerker. Phase behaviour of mixtures of colloidal spheres and excluded-volume polymer chains. *Journal of Physics: Condensed Matter*, 14:7551–7561, 2002.

[9] H. N. W. Lekkerkerker, W.C.K. Poon, P.N. Pusey, A. Stroobants, and P. B. Warren. Phase behaviour of colloid + polymer mixtures. *Europhysics Letters*, 20(6):559–564, 1992.

[10] H. B. Callen. *Thermodynamics and Introduction to Thermostatistics*, chapter 9. John Wiley, 1985.

[11] S.M. Illet, A. Orrock, W.C.K. Poon, and P.N. Pusey. Phase behavior of a model colloid-polymer mixture. *Physical Review E*, 51:1344, 1995.

[12] W. C. K. Poon. The physics of a model colloid-polymer mixture. *Journal of Physics: Condensed Matter*, 14:R859–R880, 2002.

[13] W.C.K. Poon, A.D. Pirie, and P.N. Pusey. Gelation in colloid-polymer mixtures. *Faraday Discussions*, 101:65–76, 1995.

[14] S.P. Meeker. *Low shear rheology and Delayed Sedimentation of Colloidal Systems*. PhD thesis, The University of Edinburgh, 1997.

[15] L. Starrs. *Collapse of Transient Gels in Colloid-Polymer Mixtures*. PhD thesis, The University of Edinburgh, 1999.

[16] H. Sedgwick. *Colloidal Metastability*. PhD thesis, University of Edinburgh, 2003.

[17] S. A. Shah, Y-L Chen, S. Ramakrishnan, K. S. Schweizer, and C. F. Zukoski. Microstructure of dense colloid-polymer suspensions and gels. *Journal of Physics: Condensed Matter*, 15:4751–4778, 2003.

[18] K.N. Pham, A.M. Puertas, J. Bergenholtz, S.U. Egelhaaf, A. Moussaid, P.N. Pusey, A.B. Schofield, M.E. Cates, M. Fuchs, and W.C.K. Poon. Multiple glassy states in a simple model system. *Science*, 296:104, 2002.

[19] A .D. Dinsmore and D. A. Weitz. Direct imaging of three-dimensional structure and topology of colloidal gels. *Journal of Physics: Condensed Matter*, 14(33):7581, 2002.

[20] P. Varadan and M. J. Solomon. Direct visualisation of long-range heterogeneous structure in dense colloidal gels. *Langmuir*, 19:509–512, 2002.

[21] T. Vicsek. *Fractal Growth Phenomena*. World Scientific, second edition, 1994.

[22] M.D. Haw. *Computer Simulation of Aggregation and Gelation in Colloidal Suspensions*. PhD thesis, The University of Edinburgh, 1996.

[23] M.D. Haw, M. Sievwright, W.C.K. Poon, and P.N. Pusey. Cluster-cluster gelation with finite bond energy. *Advances in Colloid and Interface Science*, 62:1–16, 1995.

[24] B. J. Ackerson and P. N. Pusey. Shear-induced order in suspensions of hard spheres. *Physical Review Letters*, 61(8):1033–1036, 1988.

[25] B. J. Ackerson. Shear induced order and shear processing of model hard sphere suspensions. *Journal of Rheology*, 34(4):553–590, 1989.

[26] M. D. Haw, W.C.K. Poon, and P.N. Pusey. Direct observation of oscillatory-shear-induced order in colloidal suspensions. *Physical Review E*, 57(6):6859–6864, 1998.

[27] G. Petekidis, A. Moussaid, and P.N. Pusey. Rearrangments in hard-sphere glasses under oscillatory shear strain. *Physical Review E*, 66:051402, 2002.

[28] M. D. Haw, W. C. K. Poon, P. N. Pusey, P. Hebraud, and F. Lequeux. Colloidal glasses under shear strain. *Physical Review E*, 58:4673–4682, 98.

[29] L. E. Silbert and J. R. Melrose. The rheology and microstructure of concentrated, aggregated colloids. *Journal of Rheology*, 43(3):673–700, 1999.

[30] P.N. Pusey. *Liquids, Freezing and the Glass Transition*, chapter 10. Elsevier, 1991.

[31] B. J. Berne and R. Pecora. *Dynamic Light Scattering*. Wiley, 1976.

[32] P. N. Segre, W. van Megen, P. N. Pusey, and K. Schatzeland W. Peters. 2-color dynamic light scattering. *Journal of Modern Optics*, 42(9):1929–1952, 1995.

[33] D. A. Weitz and D. J. Pine. *Diffusing-wave spectroscopy*, chapter 16. Oxford Science Publications, 1993.

[34] G. Maret. Diffusing-wave spectroscopy. *Current Opinion in Colloid and Interface Science*, 2(3):251–257, 1997.

[35] P. Hébraud, F. Lequeux, J. P. Munch, and D. J. Pine. Yielding and rearrangements in disordered emulsions. *Physical Review Letters*, 78(24):4657–4660, 1997.

[36] M.S. Elliot. *The Optical Microscopy of Colloidal Suspensions*. PhD thesis, The University of Ediburgh, 1999.

[37] Savile Bradbury and Peter Evennett. *Contrast techniques in light microscopy*, volume 34 of *Royal Microscopical Society, Microscopy handbooks*. Oxford : BIOS Scientific, 1996.

[38] C.J.R. Sheppard and D.M. Shotton. *Confocal laser scanning microscopy*, volume 38 of *Royal Microscopical Society, Microscopy handbooks*. Oxford : BIOS Scientific, 1997.

[39] R. S. Jardine and P. Bartlett. Synthesis of non-aqueous fluorescent hard-sphere polymer colloids. *Colloids and Surfaces A*, 211:127–132, 2002.

[40] K. Pham. Dynamic light scattering measurements performed by K. Pham at Edinburgh University found the hydrodynamic radius of these colloids to be $1100nm$.

[41] V.C. Martelozzo. *Crystallisation and Phase Separation in Colloidal Systems*. PhD thesis, The university of Edinburgh, 2001.

[42] P. N. Pusey. The effect of polydispersity on the crystallisation of hard spherical colloids. *Journal de Physique(Paris)*, 48(5):709–712, 1987.

[43] A. Yethiraj and A.van Blaaderen. A colloidal model system with an interaction tunable from hard sphere to soft and dipolar. *Nature*, 421:513–517, 2003.

[44] G.C.Berry. Thermodynamic and conformational properties of polystyrene 1:light scattering studies on dilute solutions of linear polystyrenes. *Journal of Chemical Physics*, 44(12):1550–1564, 1966.

[45] V. Prasad. *Weakly Interacting Colloid Polymer Mixtures*. PhD thesis, Harvard University, 2002.

[46] D.J. Fairhurst. *Polydispersity in Colloidal Phase Transitions*. PhD thesis, The University of Edinburgh, 1999.

[47] J. C. Crocker and D. G. Grier. Methods of digital video microscopy for colloidal studies. *Journal of Colloid and Interface Science*, 179:298–310, 1996.

[48] E. Weeks. http://www.physics.emory.edu/~weeks/idl/.

[49] M. D. Haw and R. M. L. Evans. Correlation length by measuring empty space in simulated aggregates. *Europhysics Letters*, 60(3):404–410, 2002.

[50] J. Bergenholtz, W. C. K. Poon, and M. Fuchs. Gelation in model colloid-polymer mixtures. *Langmuir*, 19(10):4493–4503, 2003.

[51] J. P. Hansen and I. R. McDonald. *Theory of Simple Liquids*, chapter 5. Academic Press, second edition, 1990.

[52] M. Jenkins. private communication.

[53] T. McLeish. Rheology of linear and branched polymers. In M. E. Cates and M. R. Evans, editors, *Soft and Fragile Matter: Nonequilibrium Dynamics, Metastability and Flow*, page 102, 2000.

[54] P. N. Segre, O. P. Behrend, and P. N. Pusey. Short time brownian motion in colloidal suspensions. *Physical Review E*, 52(5):5070–5083, 1995.

[55] S. J. Millward-Sadler, S. Romer, P. A. Smith, G. Petekidis, D. M. Salter, and W. C. K. Poon. Imaging of human chondrocytes under shear. to be published.

[56] T. Ohta and Y. Oono. Conformation space renormalization theory of semidilute polymer solutions. *Physics Letters*, 89A(9):460–464, 1982.

[57] P. Wiltzius, H.R. Haller, and D.S. Cannell. Universality for static properties of polystyrene in good and marginal solvents. *Physical Review Letters*, 51(13):1183–1186, 1983.